^{8}B Neutrinos and ^{12}C Resonances

OLIVER SØLUND KIRSEBOM

Department of Physics and Astronomy
Aarhus University, Denmark

Dissertation for the Degree
of Doctor of Philosophy

August 2010

Oliver Sølund Kirsebom
Department of Physics and Astronomy
Aarhus University
Ny Munkegade, Bldg. 1520
8000 Århus C
Denmark
E-mail: oliskir@phys.au.dk

2nd edition, September 2010

This dissertation has been submitted to the Faculty of Science at Aarhus University, Denmark, in partial fulfillment of the requirements for the PhD degree in physics. The work presented has been performed in the period from August 2006 to July 2010 under the supervision of Hans O. U. Fynbo and Karsten Riisager. The experimental work was carried out at the CMAM facility at the Universidad Autónoma de Madrid, Spain, and at the IGISOL facility at the University of Jyväskylä, Finland. The analysis work was mainly carried out at the Department of Physics and Astronomy in Aarhus. The Tokyo Institute of Technology, Japan, is acknowledged for its hospitality in the spring of 2007, and the ISOLDE group at CERN, Switzerland, is acknowledged for its hospitality in the period from February to August 2008.
In the second edition, mainly typographical errors have been corrected.

Contents

Outline

The dissertation is divided into two parts. Part I deals with the measurement of the β decay of ^{8}B performed in January 2008 at the IGISOL facility of the University of Jyväskylä, Finland. Part II deals with the ^{3}He + ^{10,11}B reaction experiments performed in March 2008 at the CMAM facility in Madrid, Spain.

The aim of the IGISOL experiment was to determine the energy spectrum of the neutrinos emitted in the β decay of ^{8}B with an improved accuracy compared to existing measurements. The experimental approach consisted in measuring the energies of the two α particles resulting from the breakup of the daughter nucleus, ^{8}Be. The neutrino spectrum of ^{8}B plays an important role for the physical interpretation of the solar neutrino measurements which, over the past 40 years or so, have deepened our understanding of solar physics as well as our understanding of the fundamental properties of matter.

The discussion is divided into six chapters. Chapter 1 gives an introduction to the subject, first clarifying the astrophysical relevance, then discussing some nuclear physics aspects and finally reviewing the past measurements of the ^{8}B neutrino spectrum. Chapter 2 describes the experimental approach. The setup is introduced and various aspects of the response of the detection system are discussed. Chapters 3–4 concern the analysis of the experimental data. A preliminary neutrino spectrum is extracted and compared to the spectra obtained in past measurements. Chapter 5 concludes and looks to the future. Finally, Chapter 6 presents additional physics results not directly related to the β decay of ^{8}B.

The aim of the CMAM experiment was to measure the properties and the decay of resonances (i.e. excited states) in the ^{12}C nucleus. The ultimate goal, to improve our understanding of nuclear structure, in particular the tendency of the nuclear constituents, the protons and neutrons, to form clusters within the nucleus.

The discussion is divided into seven chapters. Chapter 7 reviews fundamental aspects of nuclear structure in a historical context. The concept of α clustering is introduced and its relevance for the structure of ^{12}C discussed. Chapter 8 concerns the ^{3}He + ^{10,11}B reactions used to populate resonances in ^{12}C. Chapter 9 describes the experimental setup and various aspects of the data analysis including the Monte Carlo simulations. Chapters 10–12 present and discuss the results. Finally, Chapter 13 concludes and looks to the future.

Acknowledgments

Above all, I would like to thank my supervisors, Karsten Riisager and Hans Fynbo, for inspiration and guidance.

Thanks to all the participants at the experiments in Madrid and Jyväskylä who assisted in collecting the data that have kept me busy for the past four years. Thanks, not least, to the operators at the respective facilities, CMAM and IGISOL, who made sure we did not return empty-handed.

A special thanks to Martín Alcorta for the close cooperation on the CMAM experiments and memorable times at conferences, schools and experiments. Thanks to Solveig Hyldegaard for contributing to the analysis of the Jyväskylä data with her *R*-matrix expertise. Thanks to Raquel Álvarez-Rodríguez, Dmitri Fedorov and Aksel Jensen for giving meaning to our measurements through their theoretical input. Thanks to my father, Kim Kirsebom, for proof reading large parts of the manuscript.

Finally, I would like to thank my gymnasium teachers in physics and mathematics, Niels Iver Winstrup Nielsen and Gerhard Offenberg, for getting me interested in physics in the first place. Ultimately, this dissertation represents the product of their inspiring teaching.

Oliver Sølund Kirsebom
Århus, July 2010

List of Publications

I. **O. S. Kirsebom**, M. Alcorta, M. J. G. Borge, M. Cubero, C. Aa. Diget, R. Dominguez-Reyes, L. M. Fraile, B. R. Fulton, H. O. U. Fynbo, S. Hyldegaard, B. Jonson, M. Madurga, A. Muñoz Martin, T. Nilsson, G. Nyman, A. Perea, K. Riisager, and O. Tengblad, *Breakup of ^{12}C resonances into three α particles*. Physical Review C **81**, 064313 (2010).

II. S. Hyldegaard, M. Alcorta, B. Bastin, M. J. G. Borge, R. Boutami, S. Brandenburg, J. Büscher, P. Dendooven, C. Aa. Diget, P. Van Duppen, T. Eronen, S. P. Fox, L. M. Fraile, B. R. Fulton, H. O. U. Fynbo, J. Huikari, M. Huyse, H. B. Jeppesen, A. S. Jokinen, B. Jonson, K. Jungmann, A. Kankainen, **O. S. Kirsebom**, M. Madurga, I. Moore, A. Nieminen, T. Nilsson, G. Nyman, G. J. G. Onderwater, H. Penttilä, K. Peräjärvi, R. Raabe, K. Riisager, S. Rinta-Antila, A. Rogachevskiy, A Saastamoinen, M. Sohani, O. Tengblad, E. Traykov, Y. Wang, K. Wilhelmsen, H. W. Wilschut, and J. Äystö, *R-matrix analysis of the beta decays of ^{12}N and ^{12}B*. Physical Review C **81**, 024303 (2010).

III. **O. S. Kirsebom** , M. Alcorta, M. J. G. Borge, M. Cubero, C. Aa. Diget, R. Dominguez-Reyes, L. M. Fraile, B. R. Fulton, H. O. U. Fynbo, D. Galaviz, G. Garcia, S. Hyldegaard, H. B. Jeppesen, B. Jonson, P. Joshi, M. Madurga, A. Maira, A. Muñoz Martin, T. Nilsson, G. Nyman, D. Obradors, A. Perea, K. Riisager, O. Tengblad and M. Turrion, *Observation of γ-delayed 3α breakup of the 15.11 and 12.71 MeV states in ^{12}C*. Physics Letters B **680**, 44–49 (2009).

IV. S. Hyldegaard, C. Forssén, C. Aa. Diget, M. Alcorta, F. C. Barker, B. Bastin, M. J. G. Borge, R. Boutami, S. Brandenburg, J. Büscher, P. Dendooven, P. Van Duppen, T. Eronen, S. Fox, B. R. Fulton, H. O. U. Fynbo, J. Huikari, M. Huyse, H. B. Jeppesen, A. Jokinen, B. Jonson, K. Jungmann, A. Kankainen, **O. S. Kirsebom**, M. Madurga, I. Moore, P. Navrátil, T. Nilsson, G. Nyman, G. J. G. Onderwater, H. Penttilä, K. Peräjärvi, R. Raabe, K. Riisager, S. Rinta-Antila, A. Rogachevskiy, A. Saastamoinen, M. Sohani, O. Tengblad, E. Traykov, J.P. Vary, Y. Wang, K. Wilhelmsen, H. W. Wilschut and J. Äystö, *Precise branching ratios to unbound ^{12}C states from ^{12}N and ^{12}B*. Physics Letters B **678**, 459–464 (2009).

V. M. Alcorta, **O. S. Kirsebom**, M. J. G. Borge, H. O. U. Fynbo, K. Riisager and O. Tengblad, *A complete kinematics approach to study multi-particle final state reactions*.

Nuclear Instruments and Methods in Physics Research Section A **605**, 318–325 (2009).

VI. H. O. U. Fynbo, R. Álvarez-Rodríguez, A. S. Jensen, **O. S. Kirsebom**, D. V. Fedorov and E. Garrido, *Three-body decays and R-matrix analyses*. Physical Review C **79**, 054009 (2009).

VII. M. Madurga, M. J. G. Borge, M. Alcorta, L. M. Fraile, H. O. U. Fynbo, B. Jonson, **O. S. Kirsebom**, G. Martínez-Pinedo, T. Nilsson, G. Nyman, A. Perea, A. Poves, K. Riisager, O. Tengblad, E. Tengborn and J. Van der Walle, *Evidence of a new state in ^{11}Be observed in the ^{11}Li β-decay*. Physics Letters B **677**, 255–259 (2009).

VIII. M. Madurga, M. J. G. Borge, M. Alcorta, L. M. Fraile, H. O. U. Fynbo, B. Jonson, **O. S. Kirsebom**, T. Nilsson, G. Nyman, A. Perea, K. Riisager, O. Tengblad, E. Tengborn and J. Van der Walle, *Kinematic identification of the βt branch in the decay of ^{11}Li*. European Physical Journal A **42**, 415–419 (2009).

Part I

^{8}B Neutrinos

CHAPTER 1

Introduction

1.1 A Brief History of the Solar Neutrino Problem

The solar neutrino problem emerged in 1968 when Davis and co-workers measured a neutrino flux that was less than half of the solar model prediction. The solution of the problem took more than 30 years. In the words of John N. Bahcall (1934–2005):

> I am astonished when I look back on what has been accomplished in the field of solar neutrino research over the past four decades. Working together, an international community of thousands of physicists, chemists, astronomers, and engineers has shown that counting radioactive atoms in a swimming pool full of cleaning fluid in a deep mine on Earth can tell us important things about the center of the Sun and about the properties of exotic fundamental particles called neutrinos. If I had not lived through the solar neutrino saga, I would not have believed it was possible. [Bah04a]

As we shall see, the ^{8}B nucleus has been and still is one of the great protagonists of the solar neutrino saga. Its production rate through proton capture on ^{7}Be and the energy spectrum of the neutrinos emitted in its decay are essential ingredients to our understanding of the solar neutrino fluxes measured on Earth.

1.1.1 Missing Neutrinos

The basic principles of nucleosynthesis and energy production in stars were laid down in 1957 in the seminal papers of Burbidge, Burbidge, Fowler and Hoyle [Bur57] and, independently, Cameron [Cam57], though nuclear fusion had been generally recognized as the source of stellar energy since the 1930s. In the Sun, hydrogen is converted to helium via a chain of reactions which may be summarized as

$$4p + 2e^- \rightarrow {}^4\mathrm{He} + 2\nu_e + 26.731\ \mathrm{MeV}\ .$$

The primary process is the *pp* chain, shown in Fig. 1.1, which is responsible for 98% of the energy production; the carbon-nitrogen-oxygen (CNO) cycle accounts for the

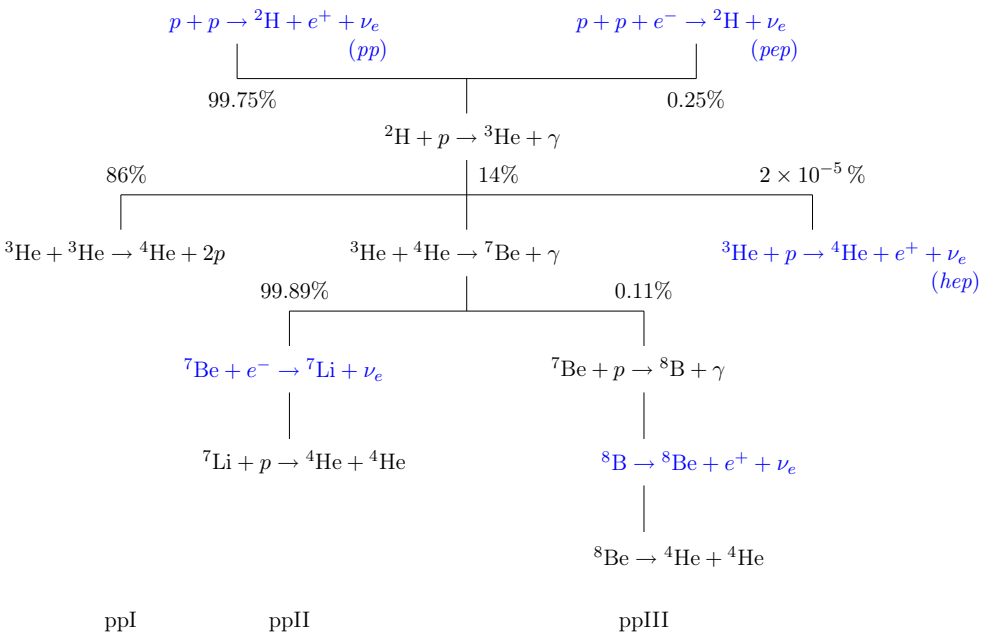

Figure 1.1: The three cycles of the *pp* chain and associated neutrinos. The reactions producing neutrinos are highlighted in blue. The standard solar model branching ratios, in percent, are indicated at the points where pairs of reactions compete. Adapted from [Hax08].

remaining 2%. It was soon realized that the weakly interacting neutrinos, if measured on Earth, could provide direct experimental evidence for the solar model proposed by [Bur57, Cam57]. In 1968, Davis and co-workers reported the result of the first such experiment [Dav68]. Surprisingly, they measured a solar neutrino flux that was less than half of the solar model prediction [Bah68]. The measurement was an impressive accomplishment: ^{37}Ar atoms produced via the capture reaction,

$$\nu_e + {}^{37}\mathrm{Cl} \;\rightarrow\; {}^{37}\mathrm{Ar} + e^- - 0.814\,\mathrm{MeV}\,,$$

at a rate of 0.5 per day, had to be extracted from a tank located deep underground in the Homestake gold mine in South Dakota, USA, containing 615 tons of chlorine-based cleaning fluid (C_2Cl_4), and counted by observing the 2.83 keV Auger electron emitted in the electron-capture decay of ^{37}Ar back to ^{37}Cl.

The solar neutrino energy spectrum predicted by the current standard solar model [Bah04b] is shown in Fig. 1.2. While the total neutrino flux is constrained by the Sun's luminosity, the relative neutrino fluxes depend on nuclear cross sections and the properties of the solar environment such as the temperature, density and com-

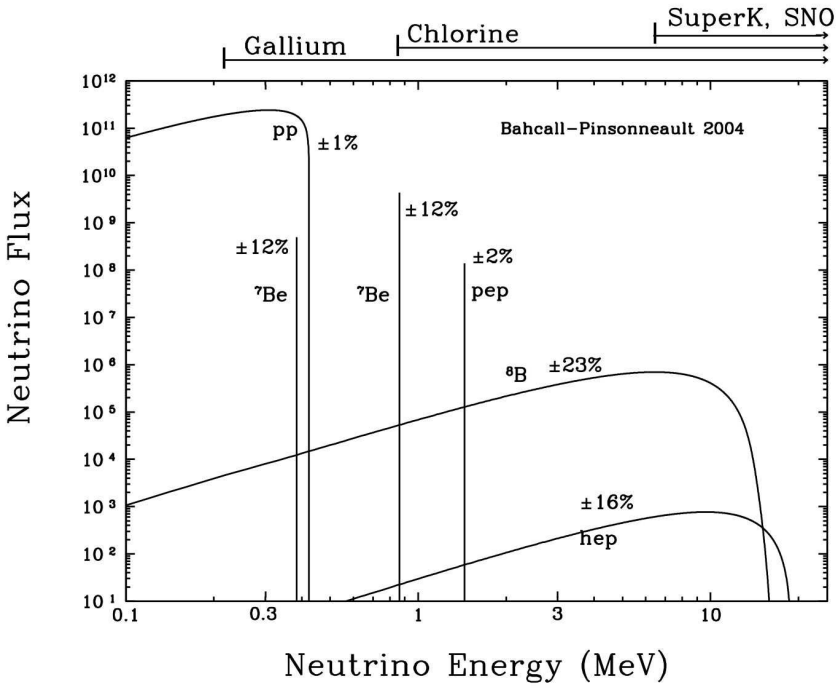

Figure 1.2: The solar neutrino energy spectrum predicted by the standard solar model. For continuum sources, the neutrino fluxes are given in number of neutrinos $\mathrm{cm}^{-2}\,\mathrm{s}^{-1}\,\mathrm{MeV}^{-1}$ at the Earth's surface. For line sources, the units are number of neutrinos $\mathrm{cm}^{-2}\,\mathrm{s}^{-1}$. To avoid complication in the figure, the difficult-to-detect CNO neutrino fluxes have been omitted. The percentages give the theoretical uncertainties. Adapted from [Bah04b].

position. Due to the strong energy dependence of the tunneling probability associated with the Coulomb barrier penetration, the competition between the three *pp* branches is rather sensitive to the solar core temperature. As indicated in Fig. 1.2, the Homestake measurement was primarily sensitive to the ^{8}B neutrinos. The strong dependence of the ^{8}B neutrino flux on the solar core temperature ($\phi \propto T_c^{18}$) meant that the deficit observed in the Homestake experiment could be explained by lowering the central temperature of the Sun somewhat. Furthermore, large error bars were associated with the laboratory measurement of the low-energy cross section for the $^7\mathrm{Be}(p,\gamma)^8\mathrm{B}$ reaction. For these (as well as other) reasons, it was originally believed that the fault lay with the solar models and not with our understanding of neutrino properties [Bah03].

1.1.2 The Multiple Personality Disorder of Neutrinos[1]

The Standard Model of particle physics assumes neutrinos to be massless, but there are no fundamental reasons why this should be the case. If one allows for finite neutrino masses and assumes that the mass eigenstates (eigenstates of the free Hamiltonian) differ from the flavor eigenstates (eigenstates of the weak Hamiltonian), one finds that a neutrino initially produced in a pure flavor eigenstate, for example an electron neutrino produced in a β decay of some nucleus, does not remain a pure flavor eigenstate as it propagates away from the source. This happens because the different mass eigenstates comprising the flavor eigenstate accumulate different phases, a phenomenon known as "vacuum oscillations" and first discussed by Pontecorvo in 1967 [Pon67]. The flavor and mass eigenstates are related by a unitary transformation,

$$\begin{pmatrix} \nu_e \\ \nu_\mu \\ \nu_\tau \end{pmatrix} = \begin{pmatrix} U_{e1} & U_{e2} & U_{e3} \\ U_{\mu 1} & U_{\mu 2} & U_{\mu 3} \\ U_{\tau 1} & U_{\tau 2} & U_{\tau 3} \end{pmatrix} \begin{pmatrix} \nu_1 \\ \nu_2 \\ \nu_3 \end{pmatrix},$$

which is often re-written in terms of three mixing angles, θ_{12}, θ_{13}, θ_{23}, one so-called Dirac phase, δ, and two Majorana phases, ϕ_1, ϕ_2. For negligible θ_{13}, the electron neutrino survival probability in vacuum is given by

$$P_{ee} = 1 - \sin^2 2\theta_{12} \sin^2 \left(\frac{\delta m^2_{12} c^4 x}{4\hbar c E} \right),$$

where x is the distance propagated, E is the neutrino energy and $\delta m^2_{12} = m^2_2 - m^2_1$ is the mass-squared difference. Because the Homestake experiment was sensitive only to electron flavor neutrinos, oscillations to a different flavor would render them invisible.

As pointed out by Wolfenstein in 1978 [Wol78], neutrinos acquire an effective mass in the presence of matter which may be significantly different from the rest mass. In the interior of the Sun, the effective mass of the neutrino reflects the electron density of the surrounding medium; the effective mass acquired by the electron neutrino is larger than that of the muon neutrino due to the enhanced ν_e-e interaction compared to ν_μ-e. In 1985, Mikheyev and Smirnov showed that this could lead to large oscillation probabilities even for small mixing angles [Mik85]. This effect, referred to as matter-enhanced neutrino oscillations or the MSW effect after its discoverers, may be understood as a level-crossing phenomenon [Bet86].

We now know that the mixing angle is, in fact, rather large (contrary to what was generally believed at the time Mikheyev and Smirnov published their work) implying a large oscillation probability even in vacuum. Even so, vacuum oscillations cannot by themselves explain the measured neutrino fluxes. The MSW effect is needed.

[1] This phrase was borrowed from [Bah04a].

Interestingly, the MSW effect also occurs in the Earth leading to a difference in day and night neutrino fluxes. So far this effect has not been observed [Smy10].

1.1.3 Definite Proof

In 1990, the deficit in the solar neutrino flux, first observed by Davis and co-workers in 1968, was confirmed by the Japan-based Kamiokande experiment [Hir90]. Furthermore, it was shown that the neutrinos were indeed coming from the Sun. In the Kamiokande experiment, originally designed for proton-decay search, a tank containing 3 000 tonnes of purified water was used as target. Neutrinos were detected by the Cherenkov radiation produced by elastically scattered electrons. The cross section for ν-e elastic scattering is peaked at forward angles giving Kamiokande directional sensitivity.

During the first half of the 1990s, further evidence supporting the neutrino oscillation interpretation came from the two ^{71}Ga capture experiments GALLEX [Ans95] and SAGE [Abd94], which used the reaction

$$\nu_e + {}^{71}\mathrm{Ga} \;\rightarrow\; {}^{71}\mathrm{Ge} + e^- - 0.233\,\mathrm{MeV}\,,$$

to detect neutrinos. As indicated in Fig. 1.2, these experiments had a lower detection threshold than the ^{37}Cl capture experiment and the water Cherenkov experiment, allowing for the first time a measurement of the numerous *pp* neutrinos. The combination of Cl, Ga and Kamiokande results was found to be incompatible with the temperature dependence of the neutrino fluxes predicted by practically any solar model [Hax08]. In addition, confidence in solar models grew as new helioseismological data appeared that was in perfect agreement with theoretical predictions [Bah03].

The successor of Kamiokande, Super-Kamiokande [Fuk01, Fuk02, Hos06, Cra08, Smy10], started taking data in 1996. Thanks to its much larger size (50 000 tonnes), it quickly confirmed the deficit in the ^{8}B neutrino flux observed in previous experiments and soon surpassed its predecessors in terms of statistics collected. However, conclusive evidence for flavor oscillations was missing. Furthermore, the data could be explained equally well by a number of different parameter choices. There were, however, hints that the so-called large-mixing-angle (LMA) solution might be the right one, one hint being that no significant distortion of the ^{8}B neutrino energy spectrum was observed [Bah99].

Decisive proof came from the Sudbury Neutrino Observatory (SNO) [Ahm01, Ahm02, Ahm04, Aha05, Jel09, Aha10] in the early 2000s. In this experiment, neutrinos were detected as they traversed a tank containing 1 000 tonnes of heavy water

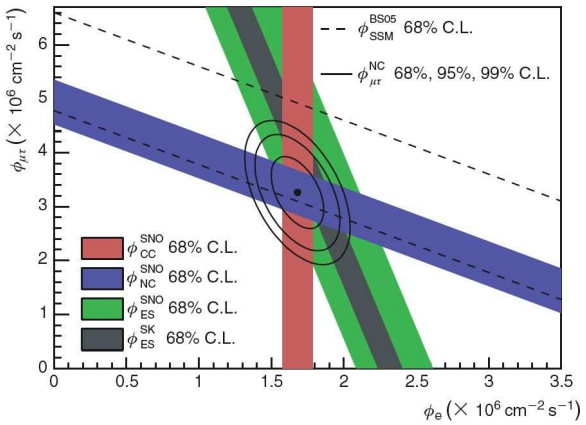

Figure 1.3: The combined flux of muon and tau neutrinos versus the flux of electron neutrinos. CC, NC, and ES flux measurements are indicated by the filled bands. The total ^{8}B solar neutrino flux predicted by the standard solar model [Bah04b] is shown as dashed lines and that measured with the NC channel is shown as the blue band parallel to the model prediction. The narrow gray band parallel to the SNO ES result corresponds to the Super-Kamiokande result reported in [Fuk02]. The nonzero value of $\phi_{\mu\tau}$ provides strong evidence for neutrino flavor transformation. The data point represents ϕ_e from the CC flux and $\phi_{\mu\tau}$ from the NC-CC difference with 68, 95, and 99% C.L. contours included. Adapted from [Aha05].

(worth some 300 million US$) by means of three different reactions:

$$\begin{aligned} \nu_e + d &\rightarrow p + p + e^- - 1.44\ \text{MeV (CC)}\ , \\ \nu_x + d &\rightarrow p + n + \nu_x - 2.22\ \text{MeV (NC)}\ , \\ \nu_x + e^- &\rightarrow \nu_x + e^-\ \text{(ES)}\ , \end{aligned}$$

where $x = e, \mu, \tau$. The charged-current (CC) reaction is only sensitive to electron neutrinos whereas the neutral-current (NC) reaction is equally sensitive to all flavors. The elastic scattering (ES) reaction (the one also used by Super-Kamiokande) is roughly six times more sensitive to electron neutrinos than muon and tau neutrinos. By measuring the electron neutrino flux as well as the total neutrino flux irrespective of the flavor content, SNO could provide direct evidence of flavor oscillations independent of solar models. The neutrino fluxes measured by SNO are displayed in Fig. 1.3. The total flux measured by SNO agrees very well with the predictions of the standard solar model.

Experimentally, one major challenge is the detection of neutrons from the NC reaction. These are detected when re-captured on the deuterons in the heavy water: A 6.25 MeV γ ray is produced which Compton scatters electrons that, if sufficiently

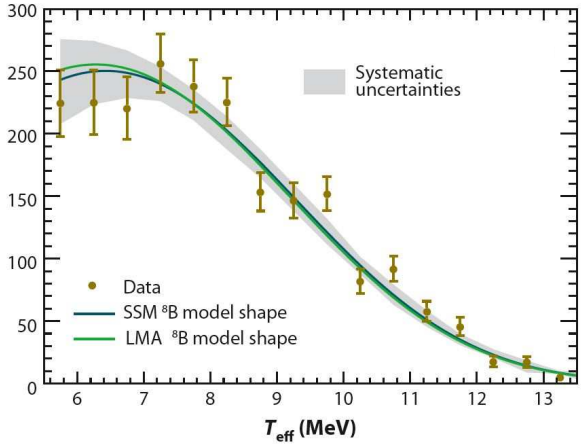

Figure 1.4: Energy spectrum measured by SNO (in the CC reaction) compared to that predicted using an undistorted ^{8}B neutrino spectrum (SSM) and that predicted when the effects of large-angle-mixing flavor oscillations are included (LMA). The error bars on the data points only give the statistical uncertainties. The grey band represents the 1σ uncertainty determined from detector systematic uncertainties. Adapted from [Jel09].

energetic, emit Cherenkov light which may be detected. This technique requires very low cosmic-ray muon backgrounds below 1% of that found in the Super-Kamiokande experiment[2].

Spectral information is best extracted from the CC reaction which produces an electron with an energy nearly equal to that of the incoming neutrino less the Q value of 1.44 MeV. In Fig. 1.4, the energy spectrum obtained by SNO is compared to that predicted using an undistorted ^{8}B neutrino spectrum[3] and that predicted including large-mixing-angle flavor oscillations. Both are seen to be consistent with the SNO spectrum. The error bars on the data points give statistical uncertainties only. The gray band represents the 1σ uncertainty determined from detector systematic uncertainties; it does not include the uncertainties on the laboratory ^{8}B neutrino spectrum.

The most recent spectra published by SNO (Fig. 29 of [Aha10]) and Super-Kamiokande (Fig. 1 of [Smy10]) remain consistent with an undistorted spectrum.

[2]In the second phase of the SNO experiment, two tonnes of NaCl were added to the heavy water so that neutrons would be captured on ^{35}Cl, resulting in a larger cross section and a more easily distinguishable signal. In the third phase, ^{3}He-filled proportional counters for direct neutron detection were installed.

[3]By "undistorted" is meant the neutrino spectrum measured in the laboratory. Here, the laboratory spectrum of [Ort00] was used.

1.1.4 Atmospheric Neutrinos

Evidence for flavor oscillations comes not only from measurements of solar neutrinos. When cosmic rays hit the atmosphere, pions and kaons are produced which decay to electrons, muons and neutrinos. Theory predicts about twice as many muon neutrinos as electron neutrinos. For example $\pi^+ \rightarrow \mu^+ + \nu_\mu \rightarrow e^+ + \nu_e + \bar{\nu}_\mu + \nu_\mu$ gives one electron neutrino but two muon neutrinos. However, in 1998, Super-Kamiokande reported a ratio of muon to electron neutrinos from the atmosphere that was approximately equal to unity [Fuk98a]. The electron-neutrino flux was roughly as expected while the muon-neutrino flux was about half of the expected value, suggesting that something was wrong with the muon neutrinos. The muon-neutrino flux displayed a strong zenith-angle dependence [Fuk98b]. The strongest suppression was observed for neutrinos coming from below, i.e. produced on the other side of the Earth. A plausible explanation was that muon neutrinos oscillate into tau neutrinos which are not seen in Super-Kamiokande because their energy is insufficient to produce tau particles. The strong suppression suggested maximal mixing, i.e. $\theta_{23} \approx 45$ degree, with an oscillation length comparable to the Earth's diameter.

1.1.5 Relevance of Remeasuring the ^{8}B Neutrino Spectrum

Following SNO, new measurements of neutrino oscillations have been made by the Japan-based KamLAND experiment [Egu03]. Its primary goal is to detect antineutrinos produced by nuclear power plants surrounding the experimental location. The antineutrinos are detected in a large tank containing 1 000 tonnes of liquid scintillator through the reaction $\bar{\nu}_e + p \rightarrow n + e^+$. The experimental signal consists of the prompt positron scintillation (which gives the neutrino energy), in combination with the 200 microsecond delayed capture of the neutron on a proton giving a 2.2 MeV γ ray (significantly reducing background). The disappearance of electron antineutrinos observed by KamLAND is consistent with the oscillation interpretation and, as the first experiment, KamLAND observes spectral distortion [Ara05, Abe08]. The energy spectrum measured by KamLAND is consistent with the spectrum predicted by flavor oscillations while inconsistent with the spectra predicted by two alternative models (neutrino decay and decoherence). The current best-fit values combining solar neutrino data with KamLAND reactor data, are $\delta m^2_{12} = 7.59^{+0.19}_{-0.21} \times 10^{-5}$ eV^2 and $\theta_{12} = 34.3^{+1.3}_{-1.2}$ degree.

While primarily designed for measuring reactor antineutrinos, KamLAND will also be measuring ^{8}B neutrinos from the Sun via elastic scattering on electrons, with a reduced detection threshold compared to Super-Kamiokande thanks to the liquid scintillation detection technique. It remains to be seen exactly how far down in energy KamLAND can go. The background levels are expected to be much higher for

the single-scintillation detection of neutrinos than the double-scintillation detection of antineutrinos.

At present, spectral information on solar neutrinos only exists above 4 MeV (Super-Kamiokande and SNO). Given the current oscillation parameters, the spectral distortion is expected to be small in this energy region [Bah99] and has so far not been observed. However, significant spectral distortion is expected around 3 MeV due to the transition from vacuum to matter-enhanced (MSW) oscillations. (The level crossing responsible for the MSW effect only occurs above 3 MeV.) This transition can only be explored if the experimental data is extended to lower energies as KamLAND promises to do.

Another experiment currently extending the solar neutrino data set to lower energies, is the Borexino experiment [Arp08] in Gran Sasso, Italy, which is similar to KamLAND but focuses on the detection of ^{7}Be solar neutrinos. Other on-going neutrino oscillation experiments are K2K, MINOS and OPERA. Many question remain regarding the properties of neutrinos. Most significantly, the absolute masses of the neutrinos are still unknown. An impressive achievement of solar neutrino measurements is a prediction of the temperature at the center of the Sun to an accuracy of 1%. If, in the future, neutrinos from the CNO cycle are measured, the solar core metallicity may also be determined [Hax08].

As Fig. 1.4 demonstrates, present-day solar neutrino experiments are able to measure the neutrino energy spectrum with 1σ uncertainties (statistical as well as systematical) of 10% or less depending on the energy bin. In the future, these uncertainties are likely to diminish making it possible to detect even small distortions of the ^{8}B neutrino spectrum. There is, however, one problem. Two of the most recent laboratory measurements of the ^{8}B neutrino spectrum are in substantial disagreement, in particular for large neutrino energies where they differ by as much as 10% [Win06]. This is clearly unsatisfactory. We, nuclear physicists, may soon find ourselves in the somewhat embarrasing situation that solar neutrino experiments are able to deliver more accurate measurements of the ^{8}B neutrino spectrum than we. In consequence, spectral distortions will be difficult to detect, in particular at high energies obscuring a possible *hep* neutrino signal, i.e. neutrinos from the $^{3}\mathrm{He} + p \rightarrow {}^{4}\mathrm{He} + e^{+} + \nu_{e}$ reaction (see Fig. 1.1).

1.2 Nuclear Physics Aspects

Before proceeding to review the existing laboratory measurements of the ^{8}B neutrino spectrum, we shall briefly discuss some nuclear physics aspects of ^{8}B and its decay.

1.2.1 Decay Modes of the ^{8}B Nucleus

1.2.1.1 β Decay

Our present understanding of the β decay of ^{8}B is that it occurs as a two-step process. First, the ^{8}B ground state decays to ^{8}Be by emitting a positron and an electron neutrino. Second, the unbound ^{8}Be nucleus breaks up in two α particles:

$$^8\mathrm{B} \rightarrow {}^8\mathrm{Be} + e^+ + \nu_e \,, \quad {}^8\mathrm{Be} \rightarrow \alpha + \alpha \,.$$

A schematic illustration is given in Fig. 1.5. Transitions from the 2^+ ground state of ^{8}B to the 0^+ ground state of ^{8}Be or the very broad 4^+ state at 11.4 MeV are second forbidden and hence strongly suppressed. A recent experimental study [Bac07] gives an upper limit of 7.3×10^{-5} for the branching ratio to the ground state. No 1^+ or 3^+ states are energetically accessible. This means that the decay proceeds exclusively by allowed transitions to the 2^+ states. In the discussion that follows, the distribution of excitation energies populated in ^{8}Be will be referred to as the "E_x distribution". The majority of the decays proceed via the broad 3 MeV state, resulting in a broad distribution of α-particle energies peaked around 1.5 MeV.

1.2.1.2 Electron Capture

The ^{8}B nucleus may also decay by capturing one of its atomic electrons (electron capture, EC):

$$^8\mathrm{B} + e^- \rightarrow {}^8\mathrm{Be} + \nu_e \,.$$

Electron capture is irrelevant for all but the highest excitation energies in ^{8}Be because the β^+ transition is much faster. With the excitation energy approaching the endpoint of the β-decay window and the β-decay phase-space factor thus approaching zero, the roles will eventually be reversed with electron capture gaining the upper hand.

Close to the endpoint of the β-decay window, we find two 2^+ states at excitation energies of 16.626 and 16.922 MeV. These states are known to be nearly maximally mixed in isospin. We may therefore assume their β-decay matrix elements to be approximately equal. The lower state is situated 332 keV below the endpoint of the β-decay window; the upper state only 36 keV below. Since the β-decay phase space grows with the fifth power of the β energy, we expect the β-decay rates to have the

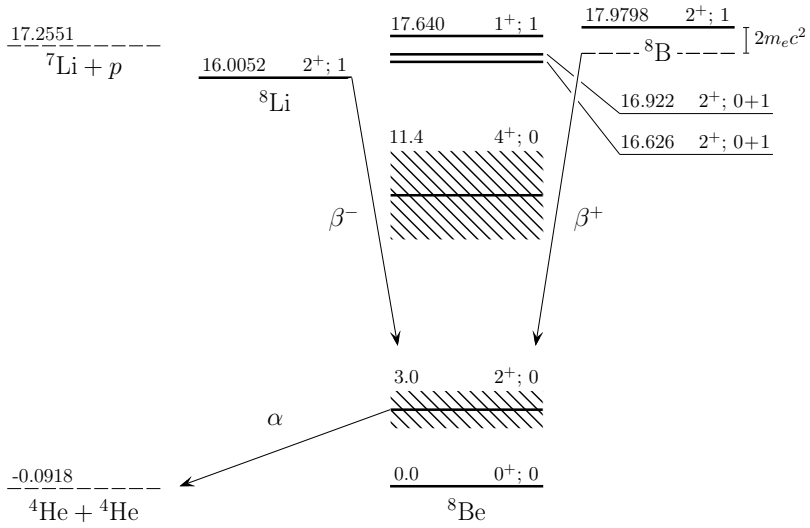

Figure 1.5: Nuclear levels in the $A = 8$ isospin triplet below the ground state of ^{8}B. The levels are labeled by their energy above the ^{8}Be ground state (in MeV), their spin-parity and their isospin. Energies and quantum numbers are taken from [Til04]. The 2^+ doublet found at an excitation energy of 16 MeV is strongly isospin mixed.

ratio

$$\frac{r_\beta(16.922)}{r_\beta(16.626)} \sim \left(\frac{36\ \mathrm{keV}}{332\ \mathrm{keV}}\right)^5 = 1.5 \times 10^{-5}\ .$$

In the absence electron capture, this is the relative intensity with which the two states should be seen in the α spectrum.

1.2.2 Halo Structure of the ^{8}B Nucleus

The existence of so-called halo nuclei, characterized by an unusually large spatial extension, was recognized more than 20 years ago. The large spatial extension of halo nuclei is explained by the presence of one or two loosely bound valence nucleons with a large fraction of their wave function extending into the classically forbidden region. For the wave function of the valence nucleon to extend far into this region, the nucleon must be lightly bound, and Coulomb and centrifugal barriers must be small. This explains why nearly all halo nuclei have been found among the light neutron-rich nuclei.

^{8}B is the only nucleus known to possess a proton halo structure in its ground state [Jon04]. The proton separation energy is only 137 keV. The most compelling evidence for the halo structure of ^{8}B comes from p+^{7}Be breakup reactions at relativistic energies

of 1440 MeV per nucleon on a carbon and lead targets [Sme99]. The halo structure of ^{8}B is inferred from the large one-proton removal cross section as well as the narrow momentum distribution of the ^{7}Be fragment indicative of a large spatial extension. For more recent studies, see [Agu09, Fur09].

The halo structure of ^{8}B has implications for the ^{7}Be + p capture cross section at low energies. In the solar environment, the ^{7}Be + p reaction takes place at a center of mass energy of ~ 20 keV. The proton already encounters the Coulomb barrier at a separation of ~ 50 fm, making the capture cross section highly sensitive to the tail of the ^{8}B ground-state wave function [Rii93]. Long the most uncertain rate in the pp chain, this cross section has recently been determined to an accuracy of 5% [Jun03, Jun10].

The only excited state in ^{8}Be above the β-decay window energetically accessible in electron-capture decay, is the 1^+, $T = 1$ state at 17.640 MeV, see Fig. 1.5. It is situated 385 keV above the p + ^{7}Li threshold and known to decay mainly by proton emission. We may estimate the EC decay rate to this state by picturing ^{8}B as composed of a proton loosely bound to a ^{7}Be core and assuming that the electron is captured on the ^{7}Be core with the proton acting merely as a spectator. From the 53.22(6) day half-life of ^{7}Be and the 89.6% braching ratio to ground state of ^{7}Li, we deduce a capture rate of 1.4×10^{-7} s^{-1} to the ground state of ^{7}Li. (The first excited state in ^{7}Li at 478 keV accounts for the remaining 10.4%.) Assuming that the matrix element for electron capture is unaffected by the presence of the proton, we only have to account for the difference in phase space in the final state. For EC decays, the phase space is proportional to the neutrino energy squared. In the decay of ^{7}Be to the ^{7}Li ground state, the neutrino energy is 862 keV; in the decay of ^{8}B to the 17.640 MeV state in ^{8}Be, it is 340 keV. Therefore, our estimate of the EC decay rate is

$$r_{\mathrm{EC}} \sim 1.4 \times 10^{-7}\ \mathrm{s}^{-1} \times \left(\frac{340\ \mathrm{keV}}{862\ \mathrm{keV}}\right)^2 = 2 \times 10^{-8}\ \mathrm{s}^{-1}\ .$$

In comparison, the total decay rate of ^{8}B, deduced from its 770 ± 3 ms half-life, is 0.9 s^{-1}. The EC decay to the 17.640 MeV state in ^{8}Be has not previously been observed. A measurement of its strength would deepen our understanding of the halo structure of the ^{8}B nucleus.

1.2.3 The 2^+ Continuum in ^{8}Be[4]

The 2^+ continuum in ^{8}Be forms a highly interesting subject for R-matrix analysis [Bar69, War86, Bar89, Bha02, Hyl10a], the ultimate goal set forward by Barker in 1969, being the consistent description of the data obtained from β-decay studies of ^{8}Li and ^{8}B as well as from $\alpha+\alpha$ scattering studies. The R-matrix analysis of the present data is the subject of the PhD dissertation of S. Hyldegaard [Hyl10a]. Here the R-matrix description of the 2^+ continuum will serve, merely, to give an accurate parametrization of the data, useful for the calculation of the neutrino spectrum.

Since many years, the mirror decays of ^{8}Li and ^{8}B to ^{8}Be have been used to study the properties of the so-called "induced weak currents" in nuclei [Gre85] (only surpassed in popularity by the mirror decays of ^{12}B and ^{12}N to ^{12}C). Generally speaking, the term "induced weak currents" designates the modifications to weak processes occurring in nuclei due to the presence of strong interactions, implying that induced weak currents are sensitive to the underlying quark structure of the nucleons. The modifications are of recoil order, which is to say at the 10^{-3} level or below, and are best studied in relative measurements of mirror decays whereby effects of nuclear structure are minimized. More specifically, one compares the β^- and β^+ strength functions [Wil71], or one compares the form of the β-α angular correlations [Sum08]. See also [GM58, Wil00].

[4] By "2^+ continuum" is meant excited states of spin-parity 2^+.

1.3 Laboratory Measurements of the ^{8}B Neutrino Spectrum

The ^{8}B neutrino spectrum cannot be derived theoretically because nuclear theory is unable to give a reliable prediction of the E_x distribution (defined in Section 1.2.1.1). Therefore, measurements are needed.

The best would be if we could determine the ^{8}B neutrino spectrum directly by detecting the neutrino and measure its energy. This approach is not feasible because we are unable to produce ^{8}B in the quantities needed to compensate for the tiny interaction cross-section of neutrinos. The next best solution would be to measure the energy of the positron and the two α particles and use energy conservation to deduce the neutrino energy. In principle, this would be possible. However, in practice, a β-α-α triple-coincidence measurement presents quite a challenge. Not that the three particles cannot be detected and their energies measured. The challenge is to collect enough statistics and, not least, convince any referee that one is in complete control of all experimental effects.

In the first two studies of the β decay of ^{8}B, performed in 1960 [Far60] and 1971 [Wil71], only singles α spectra were measured. The E_x distribution had to be unfolded from the recoil broadening distribution, cf. Section 3.1.2, but this can be done with little uncertainty thanks to the narrowness of the recoil broadening distribution. Small solid-angle detectors were employed to reduce β summing[5]. At low energies, the α singles spectra were affected by the β background. The energy loss of the α particles in the catcher foil and the detector dead layer was a source of systematic uncertainty in the energy calibration of the detectors. More recently, in 1987, the singles β spectrum was measured by [Nap87]. In this case, the E_x distribution had to be unfolded from an even broader β spectrum. In 1996, Bahcall *et al.* compared the existing measurements of the ^{8}B neutrino spectrum and determined what became for some time the standard neutrino spectrum [Bah96].

A measurement of the sum energy (i.e. total energy) of the two α particles provides a direct (no need for unfolding) and hence more reliable determination of the E_x distribution than the singles measurements. Such measurements have only recently become feasible thanks to advances in detector technology.

The first measurement of this type was performed by Ortiz *et al.* in 2000 [Ort00]. In their experiment, the ^{8}B activity was implanted in a thin carbon foil and the α particles were measured in coincidence in two 256 mm^2 Si detectors placed at opposite sides of the foil. A strong magnetic field (3.5 T) was applied to sweep away the positrons which, owing to their smaller momentum, have their trajectories bent

[5] By "β summing" is meant the coincident detection of an α particle and a positron in the same detector, whereby the sum energy (i.e. total energy) of the two particles is measured.

much more easily than the α particles. In this way, β summing and unwanted β-α coincidences were effectively eliminated. The detectors were calibrated using standard ^{148}Gd and ^{241}Am α sources, giving calibration points at 3.2 and 5.5 MeV, corresponding to sum energies of 6.4 and 11 MeV. Corrections had to be made for the energy loss of the α particles in the foil (20–30 μg/cm^2, growing thicker during the experiment) and the detector dead layers (9 ± 2 μg/cm^2 Si). The largest corrections (at E_α = 0.5 MeV) were 25 and 15 keV, respectively. A significant drawback of the setup of Ortiz *et al.* is that the efficiency for detecting the two α particles in coincidence is energy-dependent, decreasing with the α-particle energy. A complicated Monte Carlo simulation which takes into account the bending force exerted by the magnetic field as well as an energy-dependent shift in α trajectory caused by the recoil motion of the ^{8}Be daughter nucleus, is necessary to correct for this effect.

The second measurement of this type was performed by Winter *et al.* in 2003 [Win03, Win06]. In their experiment, 27.3 MeV ^{8}B ions were implanted into a 91 μm thick Si detector and the sum energy of the α particles directly measured. One great advantage of their approach is the complete absence of insensitive layers of material in which the α particles lose energy. One significant drawback is the systematic shift in energy of several tens of keV due to β summing which must be accounted for with simulations. The energy calibration was performed by implanting ^{20}Na in the detector, a β-unstable isotope that decays to unbound states in ^{20}Ne which subsequently break up into α + ^{16}O, thereby giving rise to α groups with well-established energies from 2 to 6 MeV. With this calibration method, Winter *et al.* do not measure the α-particle energy alone but the sum energy of the α particle and the recoiling ^{16}O ion. The different response of Si detectors to α particles and ^{16}O ions must then be taken into account. Additional calibration points between 5 and 9 MeV were provided by an external ^{228}Th α source.

In between the measurements of Ortiz *et al.* and Winter *et al.*, though first published in 2006, another measurement was performed by Bhattacharya, Adelberger and Swanson using a conventional single-α technique [Bha06]. The ^{8}B activity was implanted in a thin carbon foil and the α particles detected in small solid-angle Si detectors to minimize β summing. Standard ^{148}Gd, ^{239}Pu and ^{241}Am α sources were used for calibration. Corrections had to be made for the energy loss of the α particles in the foil (23.5 μg/cm^2) and the detector dead layers ($\sim$50 μg/cm^2 gold).

The results of Winter *et al.* and Bhattacharya *et al.* are in excellent agreement but disagree with the results of Ortiz *et al.* Winter *et al.* and Bhattacharya *et al.* find that the peak of the E_x distribution is narrower and occurs about 50 keV higher in energy than do Ortiz *et al.*, see Fig. 4.3. The uncertainty in the determination of the peak position is quoted as 12 keV by Ortiz *et al.*, 9 keV by Winter *et al.* and 6 keV by Bhattacharya *et al.*

Recently, our collaboration has performed two independent experiments in which the sum energy of the two α particles was measured by different techniques. The first experiment, which forms the subject of the present dissertation, was performed in January 2008 with a setup similar to that of Ortiz *et al.* The α particles are measured in coincidence in separate detectors facing the thin carbon foil in which the ^{8}B activity is implanted. Our setup differs from that of Ortiz *et al.* in that we use segmented Si detectors to reduce β summing and unwanted background from β-α coincidences. Consequently, a strong magnetic field to sweep away the positrons is not needed. This, as already mentioned, was a significant source of systematic uncertainty in their measurement. Like Winter *et al.*, we use the well-known β-delayed α emitter ^{20}Na for energy calibration. By implanting the ^{20}Na activity in the same foil as used for the ^{8}B measurement, we reduce the systematic uncertainties from energy loss corrections compared to Ortiz *et al.* who relied on standard α sources for the energy calibration. Unlike Winter *et al.*, we measure the energies of the α particle and the recoiling ^{16}O ion separately, meaning that we do not have to correct for the different response of Si detectors to α particles and ^{16}O ions.

The second experiment, which is not treated in the present dissertation, was performed at the turn of the year 2008/2009 at the KVI facility in Groningen, The Netherlands, using an implantation technique similar to that of Winter *et al.* The setup was improved by using a 78 μm thick, finely segmented, Si detector with strips only 300 μm wide, whereby the effects of β summing were much reduced [Smi05].

CHAPTER 2

Experiment

Having reviewed past measurements of the ^{8}B neutrino spectrum, we shall now discuss the experimental approach of the present measurement. The apparatus and the experimental techniques are described in Section 2.1. A brief description of the SRIM software used for energy-loss calculations, is given in Section 2.2. Finally, various aspects of the response of the detection system are discussed in Section 2.3.

2.1 Apparatus and Techniques

2.1.1 Overview

The experiment was performed in January 2008 at the IGISOL facility for radioactive beam production at the University of Jyväskylä, Finland. The experiment lasted two weeks. The first week was spent preparing the setup. The actual measurements took place during the second week. The measurement program is shown in Fig. 2.1. To begin with, various calibration measurements were performed using a standard ^{241}Am α source. Then ^{20}Na was measured for 5 hours, followed by ^{23}Al for 8 hours and ^{8}B for 72 hours. Then ^{20}Na was measured again, this time for 10 hours, and ^{23}Al was also measured again, this time for 22 hours. At the end, calibration measurements were performed once more using the ^{241}Am α source as well as an α source prepared on-site containing the α-emitting nuclei of the ^{223}Ra decay chain. From the beginning of the first ^{20}Na measurement to the end of the second ^{23}Al measurement, the vacuum of the experimental chamber was never broken.

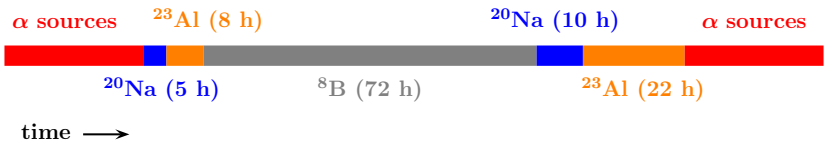

Figure 2.1: Timeline of the IGISOL experiment

Figure 2.2: The University of Jyväskylä, January 2008.

2.1.2 Radioactive Beam Production

2.1.2.1 ^{8}B

The 770 ms half-life of ^{8}B implies that it must be produced and studied on-line. A schematic and simplified illustration of the setup used for producing ^{8}B and measuring its decay is shown in Fig. 2.3. The primary beam consisting of singly ionized $^{3}He^{+}$ ions was accelerated to 15 MeV in the K-130 cyclotron. The beam intensity measured in a Faraday cup located upstream with respect to the ion guide was $\sim 0.5\,\mu$A. The beam energy is accurate to 0.5–1%. To exit the cyclotron beam line and enter the ion guide, the $^{3}He^{+}$ ions had to pass through two windows, one consisting of 4.5 mg/cm^2 Havar (standard alloy of several metals including Ni, Co and Fe), the other consisting of 25.6 mg/cm^2 ^{nat}Ni. A target consisting of 1.95 mg/cm^2 LiF evaporated on a 3.2 mg/cm^2 Al backing was placed inside the ion guide. The Li content was 95% enriched ^{6}Li. ^{8}B ions were produced by the impact of the primary beam on the target through the ^{6}Li(^{3}He, n)^{8}B reaction. According to calculations performed with the LISE++ program [Tar04], the beam energy on target after passage through the two windows as well as the Al backing of the target is 7.0 MeV. The straggling given by LISE++ is 0.3 MeV.

As explained in [Äys01], the basic idea of the ion guide is to use a buffer gas, typically helium, to slow down and thermalize the energetic ^{8}B ions produced by the impact of the primary ^{3}He beam on the LiF target. The collisions with the buffer-gas molecules not only slow down but also change the charge state of the ^{8}B ions, the

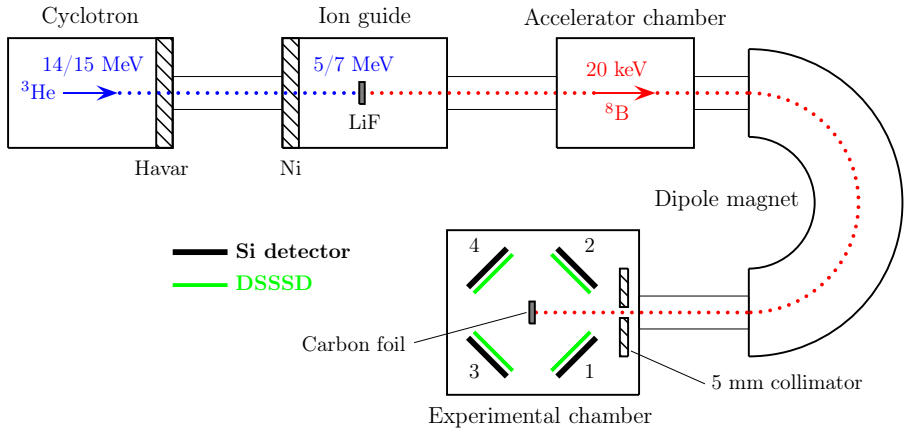

Figure 2.3: Schematic and simplified illustration of the experimental setup at IGISOL.

predominant final charge state being 1^+ (i.e. singly ionized ^{8}B atoms). The ions are transported by the continuous flow of gas and injected into the high-vacuum section of the isotope separator for further acceleration and separation by mass in a dipole magnet. In the present case, the beam was accelerated to 20 keV resulting in the ^{8}B activity being implanted about midway into the carbon foil.

By degrading the energy of the primary beam to 7.0 MeV, we ensure that no ^{8}Li is produced through the ^{7}Li(^{3}He, $2p$)^{8}Li reaction which has a threshold of 8.1 MeV. The presence of ^{8}Li activity in the mass separated beam would constitute a very serious problem. To our setup, the β^- decay of ^{8}Li is essentially indistinguishable from the β^+ decay of ^{8}B. After 24 hours of beam time, the energy of the primary beam was lowered to 14 MeV, resulting in an energy of 5.2 MeV on target. This was done to further lower the risk of accidental ^{8}Li production.

For a couple of hours, we switched to having the primary beam in pulsed mode (on for two seconds, then off for six seconds). The number of β triggers was used to monitor the growth in activity during the two-second beam-on period, and the exponential decline in activity during the six-second beam-off period. A half-life of 766^{+6}_{-16} ms was deduced from these measurements in good agreement with the literature value of 770 ± 3 ms [Til04]. The inclusion of a ^{8}Li component in the fit function with the half-life fixed to 840.3 ms [Sal90] gives an upper limit of $\sim 10^{-5}$ on the ^{8}Li fraction. The small difference between the half-lifes of ^{8}B and ^{8}Li makes it difficult to put better limits on the ^{8}Li fraction.

During 72 hours of measurement, we observe 10.6 million α-α events and 5.2 million single-α events. Given our solid-angle coverage of 30%, we estimate the average

^{8}B implantation rate to be $15.8 \times 10^6/0.30/72$ h $= 2.0 \times 10^2$ ions per second.

2.1.2.2 ^{20}Na and ^{23}Al

^{20}Na and ^{23}Al were produced in the ^{24}Mg$(p, n\alpha)^{20}$Na and ^{24}Mg$(p, 2n)^{23}$Al reactions, respectively. The energy of the primary beam was 40 MeV out of the cyclotron. The target was 4.3 mg/cm^2 $^{\text{nat}}$Mg. In addition to ^{20}Na, the mass separated $A = 20$ beam may have contained small amounts of ^{20}F, a pure β emitter that we need not worry about. From the number of decays observed to the isobaric analog state in ^{20}Ne and the branching ratio of 2.877(42)% given in [Cli89], we estimate the average ^{20}Na implantation rate to 2.2×10^4 ions per second. In addition to ^{23}Al, the mass separated $A = 23$ beam contains vast amounts of ^{23}Mg produced in the ^{24}Mg$(p, pn)^{23}$Mg reaction. The Al-to-Mg ratio is about 1:200 [Per00]. From the number of counts in the peak observed at 817 keV in the β-delayed proton spectrum of ^{23}Al and the branching ratio of 0.22(11)% given in [Per00], the average ^{23}Al implantation rate is estimated to 2.4×10^2 ions per second. In comparison, the implantation rate obtained in 2000, also in Jyväskylä, by Peräjärvi *et al.* was 20 ions per second [Per00]. In both cases, the energy of the mass separated beam was 20 keV.

2.1.3 Detectors

The detection system consisted of four double sided silicon strip detectors (DSSSD) 60 μm thick, each backed by an unsegmented silicon detector 1.5 mm thick. The detectors were placed about 5 cm from the foil in a rectangular configuration as shown in Fig. 2.3 and 2.4. Together, the four detectors cover about 30% of 4π with an angular resolution of ~ 3 degrees. The detectors are numbered 1–4 as shown in Fig. 2.3. Detector 1 is facing 4 and 2 is facing 3, with 1 and 2 placed upstream and 3 and 4 downstream. The detectors are turned 45 degrees relative to the beam axis. The thickness of the DSSSDs is chosen such that the most energetic α particles ($\sim$8.5 MeV) are completely stopped. The unsegmented 1.5 mm thick silicon detectors placed behind the DSSSDs serve to detect β particles.

The DSSSDs measure 5×5 cm^2. Both sides are divided into 16 strips running in perpendicular directions. The front side is p^+ doped, the back side n^+ doped. The p^+ doped layer on the front side is implanted to a depth of only 100 nm. An Al grid covers 3% of the surface. Further details regarding the design and performance of the DSSSDs are given in [Ten04]. A feature that deserves to be emphasized is the very thin dead layer of only 100 nm (over 97% of the surface) which facilitates the detection of low-energy ions. For a general account of silicon detectors, see e.g. [Kno00].

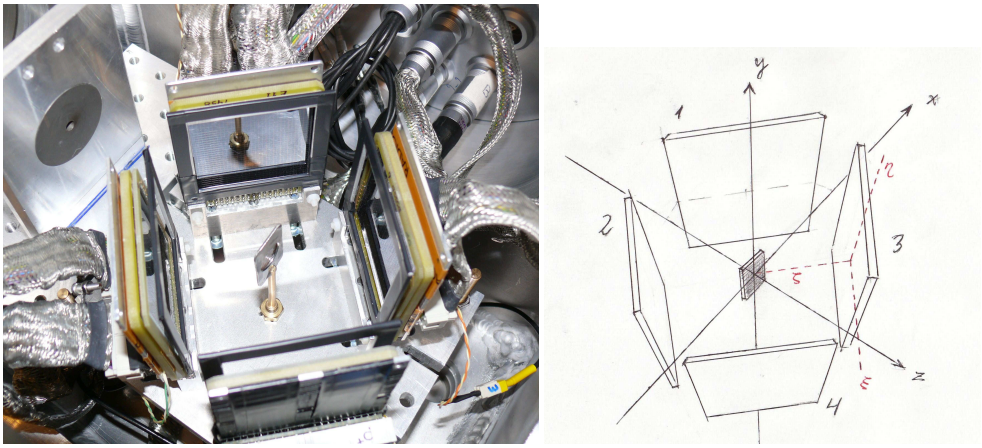

Figure 2.4: (Left) A look inside the chamber containing the final setup: Four DSSSDs backed by unsegmented silicon detectors surrounding the carbon foil in the center. The beam comes in from the left through the 5 mm collimator. DSSSD 2 (bottom left) is seen to be slightly tilted with respect to the vertical axis. **(Right)** Drawing of the setup showing the two coordinate systems, (x, y, z) and (ξ, η, ζ), used in the data analysis.

2.1.4 Electronics and Data Acquisition

The data acquisition system used in the IGISOL experiment and the data acquisition system used in the CMAM experiment share the same basic structure which will be described in connection with discussion of the CMAM experiment, cf. Section 9.2.

2.2 Energy-Loss Calculation

The effects of the passage of charged particles through matter are of paramount importance to any nuclear physics experiment concerned with the detection of charged particles. It is through their interaction with matter that we detect charged particles as well as other kinds of radiation. In the present experiment, electrons, positrons, protons, α particles and ^{16}O ions are detected through the large numbers of electron-hole pairs they create as they are stopped in a silicon crystal.

Here, we employ the SRIM (Stopping and Range of Ions in Matter) program package [Zie08] to perform energy-loss calculations[1]. Sometimes we want to know how much energy is lost by a charged particle in passing through a slab of material of a certain thickness. In other cases we also want to know how this energy is deposited in the material. How much is spent on ionization? How much is transfered to the crystal

[1]The SRIM program package can be obtained from http://srim.org/. The most recent version (2008) is used here.

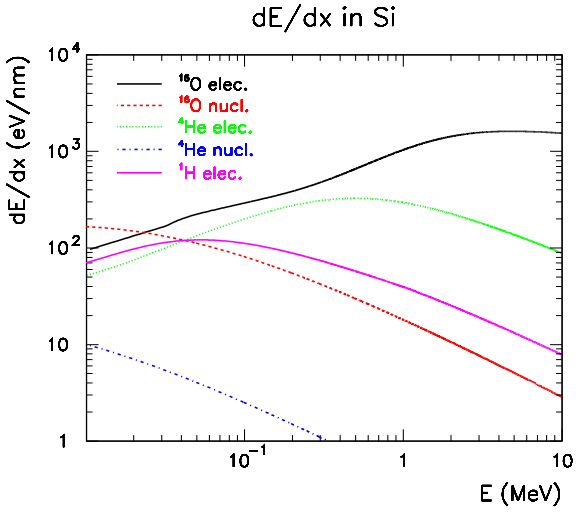

Figure 2.5: Differential stopping powers, $\frac{dE}{dx}$, obtained from SRIM for protons, α particles and ^{16}O ions in silicon divided into electronic and nuclear parts. The nuclear stopping of protons is below the chosen scale.

lattice thereby disrupting its structure? For simple energy-loss calculations, we use the tables given by SRIM containing stopping powers (energy loss per path length) and ranges as a function of particle energy. If we want to know how this energy is deposited in the material, we perform an event-by-event simulation of the stopping process using the TRIM (Transport of Ions in Matter) program. In general, SRIM energy-loss calculations are in good agreement with measurements, see e.g. [Zha02] for a recent comparison, whereas the predictions of TRIM concerning how the energy is deposited in the material, are less reliable.

SRIM stopping powers, $\frac{dE}{dx}$, are shown in Fig. 2.5 divided into electronic and nuclear parts, as explained below. The range of 0–10 MeV α particles in silicon is shown in Fig. 2.6 (a). Using SRIM stopping powers, we calculate the energy loss of protons, α particles and ^{16}O ions in the carbon foil and the dead layers of the detectors by simple numerical integration. As an example, the energy loss of α particles in 100 nm silicon is shown in Fig. 2.6 (b). A fixed step size of 1 nm gives adequate precision. For the ^{16}O ions, which have the largest stopping power, a step size of 0.1 nm is required to obtain sub-keV precision.

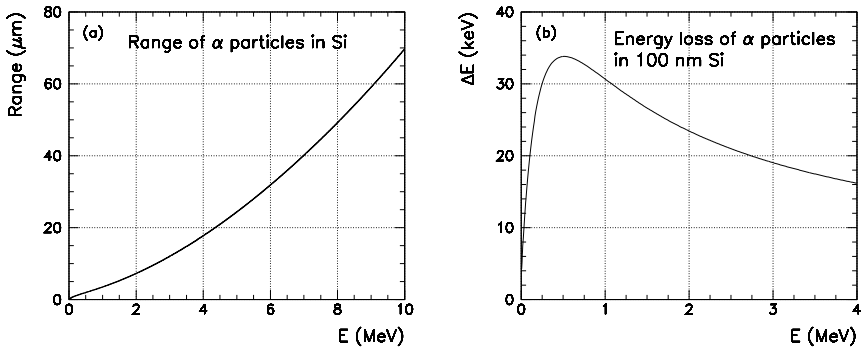

Figure 2.6: (a) Range of α particles in silicon given by SRIM. **(b)** Energy loss of α particles in 100 nm silicon obtained by simple numerical integration of SRIM stopping powers.

2.2.1 Ionizing and Non-Ionizing Energy Loss

The stopping powers given by SRIM are divided into two parts: Electronic and nuclear stopping. The first refers to the energy lost in collisions with the electrons of the target material, the second to the energy lost in collisions with the atomic nuclei of the target material. The stopping powers may be integrated numerically to yield the total energy transfered to the electrons, E_{elec}, and the total energy transfered to the nuclei, E_{nucl}. Fig. 2.7 displays E_{nucl} in percent of the total energy, $E = E_{\text{elec}} + E_{\text{nucl}}$.

The TRIM simulations also divide the energy loss into an electronic part, E_{elec}, and a nuclear part, E_{nucl}. The electrons and the recoiling nuclei may, in turn, deposit the energy acquired in the collision with the incoming ion by three different mechanisms: (i) Ionization, (ii) vacancy formation and (iii) phonon production. Mechanism (i) creates electron-hole pairs which give rise to the electronic signal that we measure. Mechanisms (ii) and (iii), on the other hand, do not contribute to the electronic signal. The fraction of the electronic energy loss subsequently deposited by the two non-ionizing mechanisms (ii) and (iii), is denoted f_{elec}. Similarly, the fraction of the nuclear energy loss subsequently deposited by the two non-ionizing mechanisms (ii) and (iii), is denoted f_{nucl}. Then, the total non-ionizing energy loss is given by

$$E_{\text{non-ion}} = f_{\text{elec}} E_{\text{elec}} + f_{\text{nucl}} E_{\text{nucl}}$$

The non-ionizing fractions, f_{elec} and f_{nucl}, obtained from TRIM simulations for protons, α particles and ^{16}O ions in silicon, are shown in Fig. 2.8–2.10. The electronic non-ionizing fractions, f_{elec}, are below 1%. The nuclear non-ionizing fractions, f_{nucl}, range from 60–80%.

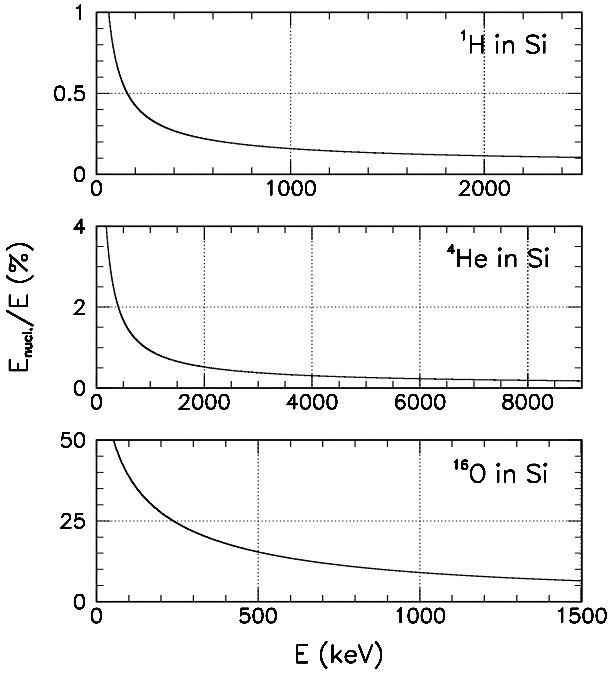

Figure 2.7: Integrated nuclear stopping, expressed as a percentage of the ion energy, for protons, α particles and ^{16}O ions in silicon. Notice the different scales, both on the abscissa and the ordinate.

2.2.1.1 Calculation Details

For ^{16}O ions, the TRIM simulation was performed in the "Detailed calculation with full damage cascades" mode. For protons and α particles, the simulations were performed in the "Surface sputtering/Monolayer collision steps" mode as recommended by TRIM for energetic light ions. This mode differs from the "Detailed calculation with full damage cascades" mode by not using the approximation of "free flight paths" (as a result, the simulation is 10–50 times slower). In all cases, at least 1 000 events were simulated.

In the "Ion distribution and quick calculation of damage" mode, TRIM gives non-ionizing energy losses for ^{16}O ions that agree with [Len86] within 1–2 keV, suggesting that the underlying algorithms and approximations are near identical. In the more comprehensive "Detailed calculation with full damage cascades" mode, TRIM gives values roughly 10 keV below [Len86].

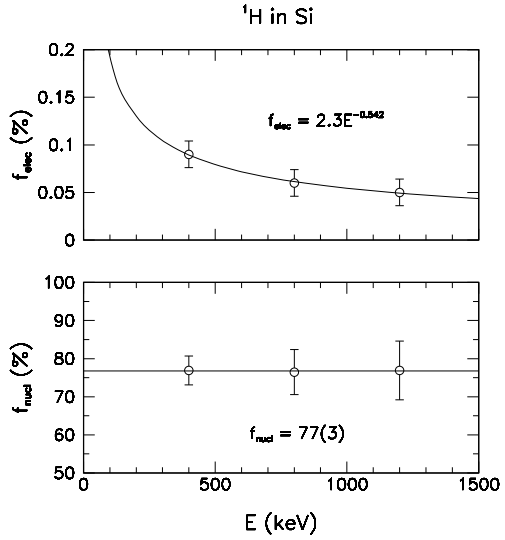

Figure 2.8: Non-ionizing fractions f_{elec} and f_{nucl} in silicon for protons of initial energy E. The data points show the result of the TRIM simulations. The solid line shows the parametrization used in the analysis of the experimental data.

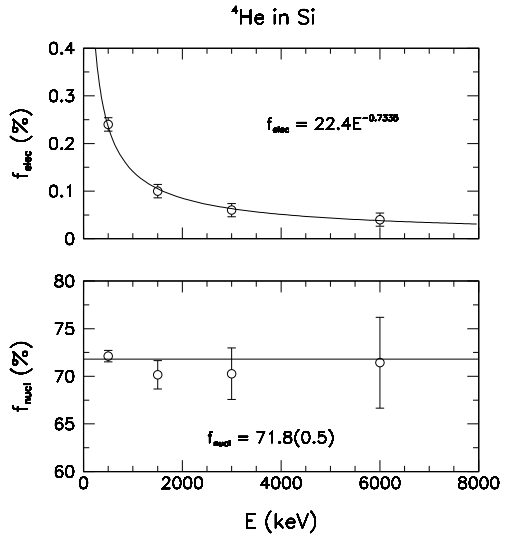

Figure 2.9: Non-ionizing fractions f_{elec} and f_{nucl} in silicon for α particles of initial energy E. The data points show the result of the TRIM simulations. The solid line shows the parametrization used in the analysis of the experimental data.

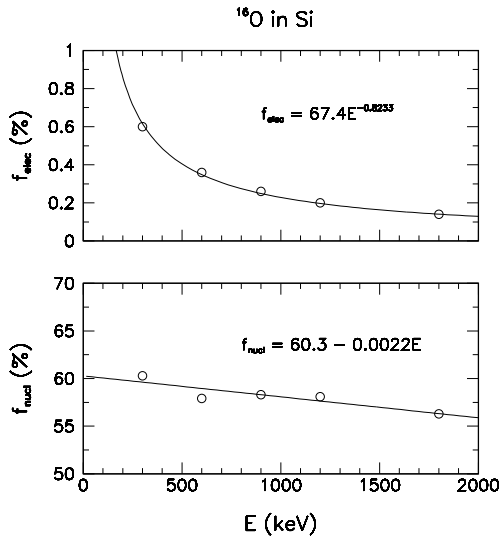

Figure 2.10: Non-ionizing fractions f_{elec} and f_{nucl} in silicon for ^{16}O ions of initial energy E. The data points show the result of the TRIM simulations. The solid line shows the parametrization used in the analysis of the experimental data.

2.3 Calibration

A more descriptive section heading might have been "Getting to know your experimental setup". As used here the term "calibration" should be understood in its most general meaning, i.e. the act of understanding the response of your measuring device to the "forces" it is subject to. Aiming, as we are, for an accuracy comparable to that of the previous experiments of 5–10 keV, we must calibrate our measuring device with great care. All aspects of its response must be investigated. This is the purpose of the present section. Its subsections, each dealing with its own aspect of the detection system, can to a large extent be read independently of one another. The reader who is interested in results but not in complicated data analysis, is advised to proceed to Section 2.3.14 which gives a summary of Sections 2.3.1–2.3.13.

2.3.1 Geometry

Two coordinate systems are used to describe the geometry of the setup. These are illustrated in the drawing of Fig. 2.4. The (x, y, z) coordinate system has its origin at the implantation spot on the carbon foil, the z axis coincides with the beam axis, the y axis points in the vertical direction and the x axis points in the horizontal direction. The (ξ, η, ζ) coordinate system is detector-specific in that it has its origin at the center

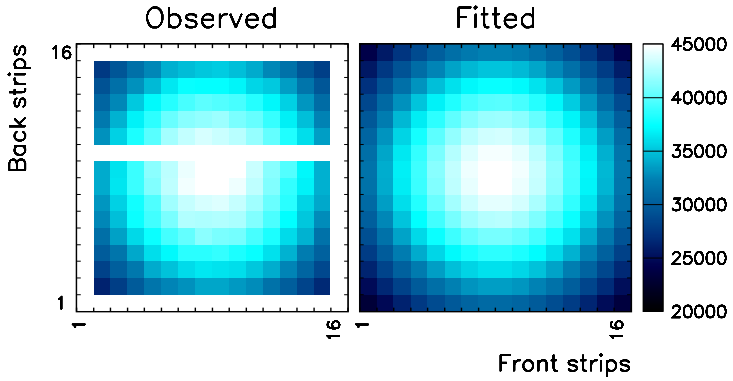

Figure 2.11: Hit pattern of DSSSD 3 (^{8}B data). Observed distribution to the left, fitted distribution to the right. Back strip 10 was not working properly and hence excluded from the analysis. So were the edge strips which were partially covered by a metallic frame.

of the DSSSD. The ζ axis is perpendicular to the detector plane and points toward the carbon foil. The ξ and η axes are parallel to the detector plane and point in the horizontal and vertical direction, respectively.

The exact positions of the detectors relative to the implantation spot are determined from the hit patterns, i.e. the intensity distribution over the surface of the DSSSDs, assuming isotropic emission from a uniform circular region of diameter 7 mm. This is illustrated in Fig. 2.11 which shows the observed and fitted hit pattern of DSSSD 3 using ^{8}B data. Back strip 10 in DSSSD 3 was not working properly and is excluded from the analysis. So are the edge strips which were partially covered by a metallic frame mounted to protect the electronic read-out from the radiation. Edge strips of the other DSSSDs are excluded from the analysis for the same reason. If the finite dimensions of the implantation spot are not taken into account, errors of $\sim$0.2 mm in the determination of ξ and ζ result.

As seen in Fig. 2.4, DSSSD 2 was slightly tilted causing a small error in the determination of its vertical coordinate relative to the implantation spot. The effect of this error is seen in Fig. 2.12 as a shift and broadening of the measured distribution of relative α-α angles in the decay of ^{8}B. By varying the vertical position so as to minimize the shift and broadening, the error is determined to 5.3 $\pm$ 0.5 mm corresponding to a tilt of 7 degrees or, assuming that DSSSD 3 (opposite to DSSSD 2) was tilted too, a tilt of 3.5 degrees for each detector (a closer inspection of Fig. 2.4 suggests that this was indeed the case). DSSSD 1 and 4 were tilted by $<$0.5 degrees.

The geometries deduced for the ^{8}B run and the first ^{20}Na run are given in Table 2.1. The x and y coordinates are consistent within 1 mm. A tiny systematic shift is seen which may be due to different beam optics. The z coordinates, on the other

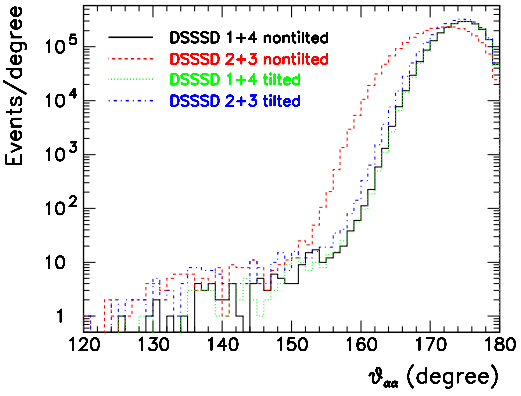

Figure 2.12: Distribution of relative α-α angles measured in oppositely facing pairs of detectors (^{8}B data). Distributions are shown both for tilted and non tilted geometries (see text for explanation).

Table 2.1: Geometry of the detector setup determined from ^{8}B and ^{20}Na data. The coordinates give the position of the center of the DSSSD.

DSSSD	x (mm)		y (mm)		z (mm)	
	^{8}B	^{20}Na	^{8}B	^{20}Na	^{8}B	^{20}Na
1	38.3	38.8	−0.4	0.2	−35.9	−38.1
2	−31.4	−31.8	−0.5	0.5	−29.8	−32.9
3	33.2	34.4	−1.8	−1.2	32.9	38.0
4	−37.4	−36.0	−1.1	−1.0	39.0	38.5

hand, differ by as much as 5 mm. Since the chamber was not opened between the two measurements, there is no reason why the z coordinates should differ. Presently, the origin of this difference is not fully understood.

2.3.2 Linearity of the Electronics

The linearity of the electronics was checked on five occasions during the seven days of data taking by feeding signals from a precision pulse generator to the preamplifiers. A dial on the pulser generator module was used to adjust the size of the signals. The peaks observed in the ADC spectrum were perfectly Gaussian with a typical width of $\sigma \sim 3.5$ channels. Centroids were determined with negligible error.

A quadratic polynomial was used to fit the data. The residuals from the fit are

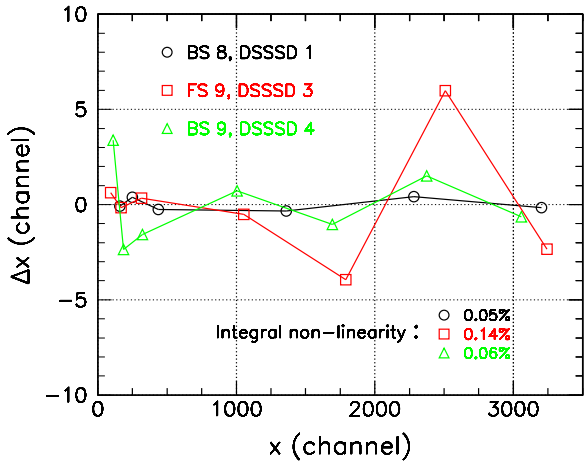

Figure 2.13: Residuals from a quadratic fit to data obtained with a precision pulse generator (three selected strips).

shown in Fig. 2.13 for three individual strips. The behavior of back strip 8 of DSSSD 1 is representative of the behavior found in all back strips of DSSSD 1–3. Similarly, the behavior of front strip 9 of DSSSD3 is representative of the behavior found in all front strips of DSSSD 1–3. The behavior of back strip 9 of DSSSD 4 is representative of the behavior found in all strips of DSSSD 4, front strips as well as back strips.

The data were also fitted with a straight line. The maximum deviation of this fit from the quadratic fit was determined and is given in Fig. 2.13 expressed as a percentage of the full range value (integral non-linearity). The values found are consistent with the ±0.1% specified by the producer corresponding to ±4 channels over the full range.

2.3.3 Method of Energy Calibration

The calibration of the energy scale is based on the two most intense β-delayed α groups of ^{20}Na. Their energies (2 153.3 and 4 433.9 keV) were deduced from the tabulated [Til98] excitation energies of the corresponding states in the β-decay daughter nucleus ^{20}Ne (7 421.9 ± 1.2 and 10 273.2 ± 1.9 keV) using 4 729.84 ± 0.01 keV for the $\alpha + {}^{16}$O threshold energy [Til98].

In calculating the α energies, we neglect the tiny systematic shift caused by the recoil motion of the ^{20}Ne daughter nucleus. The magnitude of the shift is $\frac{1}{5}E_R$ where E_R is the kinetic energy of ^{20}Ne which attains its maximal value when the leptons are emitted in the same direction. To first order, one has $E_{R,max} = (E_0 - E_x)^2/2Mc^2$ where

$E_0 = 13.376\,\text{MeV}$ is the maximum total β energy for decays to the ground state of ^{20}Ne, E_x is the excitation energy in ^{20}Ne and M is the mass of ^{20}Ne. Inserting numbers, one obtains $E_{\text{R,max}} = 0.95\,\text{keV}$ for the 2153 keV α group and $E_{\text{R,max}} = 0.26\,\text{keV}$ for the 4434 keV α group. The corresponding shifts in α energy are one-fifth of these values, 0.19 and 0.05 keV, respectively. When averaged over the lepton angles the shifts become even smaller.

The amount of statistics collected was sufficient to allow for the energy calibration of the strips to be performed on a pixel-by-pixel basis[2]. In each pixel, the positions of the two α groups were determined (most probable values were used). The energy loss experienced by the α particles in the carbon foil and the detector dead layer prior to entering the active volume of the detector was computed. Furthermore, corrections were made for the non-ionizing energy loss in the active volume of the detector as described in Section 2.2.1. (For the 4434 keV α group, the pixels were paired two-and-two to gain enough statistics.) The energy loss in the foil was computed assuming a fixed implantation depth of 32.7 nm neglecting a rather large spread of $\sigma \sim 10\,\text{nm}$ discussed below. The finite size of the beam spot was also neglected. In both cases, the primary effect will be a broadening of the signal; systematic shifts will only occur at the sub-keV level. The geometry of the detector setup was deduced from the hit pattern as discussed in Section 2.3.1. The small quadratic correction, deduced from the pulse generator calibration, was included in the calibration.

2.3.4 Implantation Depth

Fig. 2.14 shows the implantation depth distribution in carbon of ^{8}B, ^{20}Na and ^{23}Al ions at 20 keV obtained from TRIM simulations of 40 000 events. The average implantation depths are 56.1 nm for ^{8}B, 32.7 nm for ^{20}Na and 28.2 nm for ^{23}Al.

For ^{20}Na, we may check the prediction of TRIM by monitoring the apparent shift in energy of the 2153 keV α group with angle in the two upstream detectors (DSSSD 1 and 2). Back strips 7–10 were used in each DSSSD because they span the widest range of angles. For each strip, the angular dependence of the measured α energy (corrected for the energy loss in the dead layer of the detector) was fitted with an expression of the form

$$E(\theta) = 2153.3\,\text{keV} + k + \Delta E_0 \sec\theta \tag{2.1}$$

where θ is the angle with respect to the normal to the foil plane and ΔE_0 is the energy loss at zero degrees. The constant k is included to account for imperfections in the energy calibration. A simultaneous fit was performed to the four strips allowing for

[2]Here, "pixel" refers to the 3×3 mm^2 geometric overlap of front and back strips. The strips are not physically divided into pixels.

different values of k, but with the same value of ΔE_0. In Fig. 2.15 (a), the energy loss in the foil $\Delta E(\theta) = E(\theta) - 2153.3\,\text{keV} - k$ is plotted against $\sec\theta$. Each data point is obtained by averaging over the four strips. The fit yields $\Delta E_0 = 10.2 \pm 0.7$ keV for DSSSD 1 and $\Delta E_0 = 9.6 \pm 0.6$ keV for DSSSD 2. The slope of the straight line superimposed on the data points is the average of these two values, i.e. 9.9 ± 0.5 keV. We may convert this energy loss to an equivalent implantation depth by dividing with the stopping power of 2153 keV α particles in carbon, $\mathrm{d}E/\mathrm{d}x = 1.336\,\text{keV}/\mu\text{g/cm}^2$. The result is $7.4 \pm 0.4\,\mu\text{g/cm}^2$ or, equivalently, 32.9 ± 1.7 nm, in perfect agreement with the TRIM prediction.

2.3.5 Foil Thickness

By monitoring the apparent shift in energy of the 2153 keV α group with angle in the two downstream detectors (DSSSD 3 and 4), we may determine the thickness of the carbon foil less the implantation depth of the ^{20}Na ions. The procedure was explained in Section 2.3.4. The results are displayed in Fig. 2.15 (b). The fit gives $\Delta E_0 = 27.1 \pm 0.8$ keV for DSSSD 3 and $\Delta E_0 = 26.9 \pm 0.9$ keV for DSSSD 4. Taking the average of the two and converting to the equivalent thickness of carbon, we obtain $20.1 \pm 0.4\,\mu\text{g/cm}^2$ or, equivalently, 89 ± 2 nm. By adding the implantation depth determined previously (32.9 ± 1.7 nm) we obtain 122 ± 3 nm for the full thickness of the carbon foil. In comparison, measurements performed with the ^{241}Am α source, with and

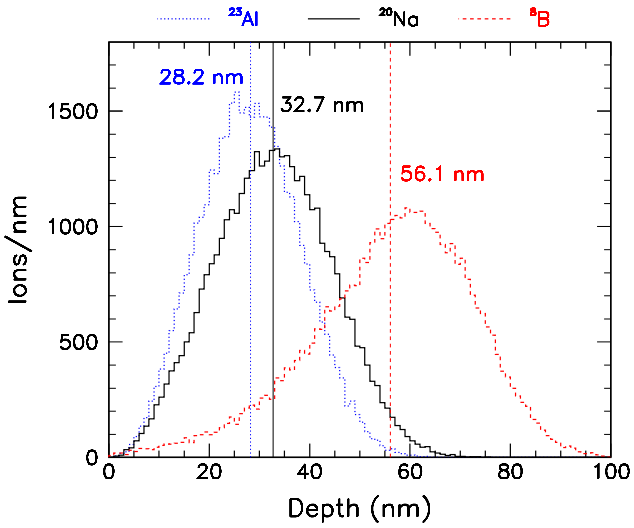

Figure 2.14: Implantation depth distribution of ^{8}B, ^{20}Na and ^{23}Al ions in carbon at 20 keV obtained from TRIM simulations. Mean values of the distributions are given.

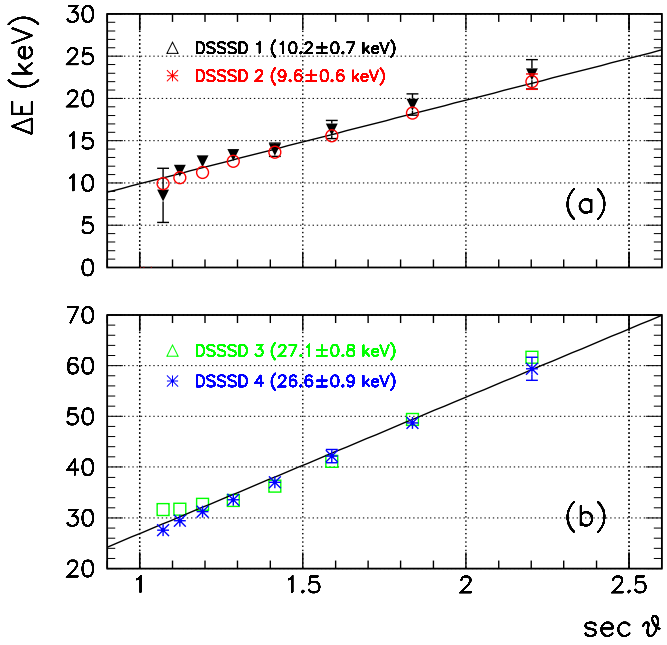

Figure 2.15: Energy loss of 2153 keV α particles in the carbon foil as a function of $\sec\theta$ where θ is the angle with respect to the normal to the foil surface. Given in the parentheses are the slopes of the best fit straight lines corresponding to the energy loss at normal incidence. Their average is used for the straight lines shown on the plot.

without the carbon foil placed between the source and the detector, yield a thickness of 106 ± 2 nm. Though fairly close, the two values certainly do not agree within the quoted error bars indicating the presence of systematic effects at the 10% level not properly accounted for. One such effect could be inhomogenities in the foil. We take their weighted average value, 114 ± 8 nm ($= 25.7 \pm 1.8\ \mu g/cm^2$), as our estimate of the foil thickness with the error bar raised to account for the large spread. This is in good agreement with the $25\ \mu g/cm^2$ specified by the manufacturer.

2.3.6 Detector Dead Layers

Details concerning the design and performance of the DSSSDs are given in [Ten04]. An aluminum grid 600 nm thick that serves to collect the electron-hole pairs created by the penetrating radiation covers 2.9% of the detector surface. Over the remaining 97% of the surface, the dead layer (p^+ doped Si) is only 100 nm thick. The precision of this (mean) value is not stated by the manufacturer (Micron Technology, Inc.). A precision better than 10% seems unlikely. Since the detectors used for the present

Figure 2.16: The short but eventful life of a carbon foil. From left to right: (i) Fishing for the carbon foil, (ii) before exposure, (iii) after one week's exposure to various beams the implantation spot is clearly seen and (iv) its diameter is measured to 7.0 ± 0.5 mm.

experiment were not made from the same Si wafer[3], we expect variations in dead layer thickness at the 10% level.

Dead layers are usually measured with a monochromatic α source by rotating the detector (thereby varying the angle of incidence) while monitoring the shift in energy. Unfortunately, such a measurement was not performed during the present experiment. In principle, dead layers may be determined by monitoring the shift of the 2153 keV α group of ^{20}Na over the length of a single strip. In practice, however, this approach fails for two reasons: First, due to the smallness of the dead layer thickness as well as the limited angular range spanned by the strips (< 25 degrees), the shift is only 3 keV. Second, part of this tiny shift is caused by the varying energy loss in the carbon foil, the contribution of which must be properly subtracted. The same is true for the ^{241}Am calibration data. In this case, it is the energy loss in the source itself that must be properly subtracted.

An attempt was made to determine the dead layers by monitoring the shift of the 1110 keV ^{16}O recoil group with changing angle. With an energy loss of $\approx$ 115 keV in 100 nm silicon, the anticipated shift over an angular range of 25 degrees is $\approx$ 12 keV, enough to allow for a rough determination of the dead layer thickness. We use the four central front strips (vertical) for the analysis. The ^{16}O ions hitting these strips are emitted at 45 degrees relative to the foil plane. The variation over the length of the strip is slightly less than 5 degrees and the corresponding change in effective foil thickness 6 percent.

At 45 degrees upstream (DSSSD 1 and 2), the energy loss of the 1110 keV ^{16}O ions in the foil is $\approx$ 65 keV so the shift in energy due to the varying effective foil thickness over the length of the strip is 0.06×65 keV = 4 keV, which should be compared to the 11 keV expected from the varying effective dead layer. The exact magnitude of this shift may be calculated for each angular bin using SRIM tables. (If, say, the energy loss predicted by SRIM is off by 5 keV, we still get the shift right within $\frac{5}{65}4$ keV = 0.3 keV.)

[3]Our collaboration has a large collection of DSSSDs. The detectors have been purchased over many years, two at a time.

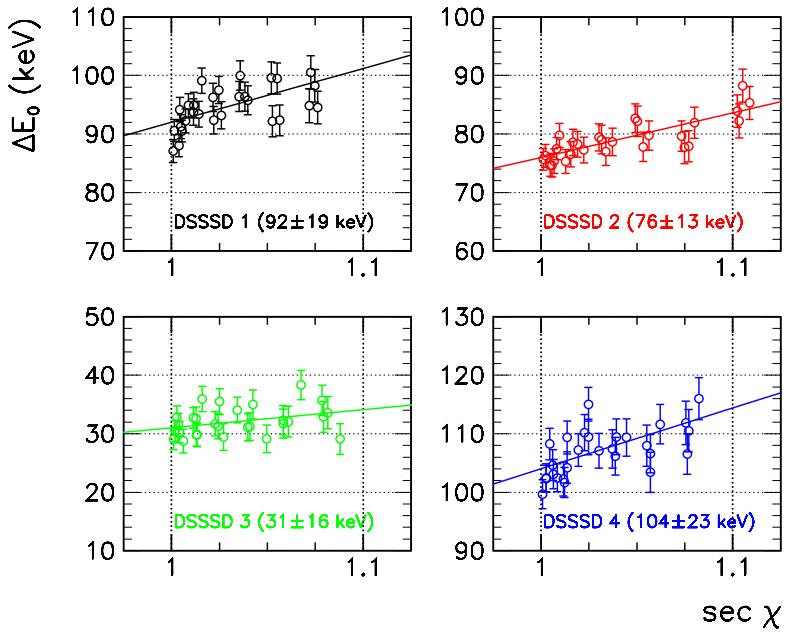

Figure 2.17: Energy loss of 1110 keV ^{16}O ions in the dead layer as a function of sec χ where χ is the angle of incidence relative to the normal to the detector surface. Given in the parentheses are the slopes of the best fit straight lines corresponding to the energy loss at normal incidence.

For DSSSD 3 and 4 the situation is less favorable. At 45 degrees downstream, the energy loss in the foil is ≈ 160 keV implying a shift of 0.06×160 keV $= 10$ keV over the length of the strip with an uncertainty of ± 1.6 keV due to the ± 8 nm uncertainty on the thickness of the foil.

The angular dependence of the measured ^{16}O energy, corrected for the energy loss in the foil, is fitted with an expression similar to Eq. 2.1. For each detector a simultaneous fit is performed to the four strips allowing for different values of k, but with the same value of ΔE_0. The results are displayed in Fig. 2.17. The energy loss in the dead layer at normal incidence is determined to 92 ± 19 keV for DSSSD 1, 76 ± 13 keV for DSSSD 2, 31 ± 16 keV for DSSSD 3 and 104 ± 23 keV for DSSSD 4. The equivalent dead layers (including an additional 10 keV uncertainty on DSSSD 3 and 4 due to the uncertainty on the foil thickness) are 84 ± 17 nm, 70 ± 12 nm, 30 ± 23 nm and 102 ± 29 nm, respectively. For DSSSD 1, 2 and 4 the dead layers are in good agreement with our expectations. The dead layer obtained for DSSSD 3 is unrealistically small. Considering the simplifying assumptions (fixed implantation depth, homogeneous foil and dead layer) made in the analysis, this should cause no worries. A 10% varia-

tion in dead layer thickness over the length of the strips (e.g. due to tiny amounts of dirt covering part of the detector surface) suffices to explain such a result.

As it turns out, the dead layers may be determined rather accurately by requiring the β-delayed proton groups of ^{23}Al at 539 and 817 keV to have the same energy in all four DSSSDs. The logic behind this approach is the following: If, say, 10 nm is added to the dead layer, the energies of the 2153 and 4434 keV α groups of ^{20}Na are reduced by 2.3 and 1.6 keV, respectively (for normal incidence). Since these two α groups provide our energy calibration, the apparent energy of the proton groups will shift too. One finds $\Delta E_p = -2.7$ keV. The increased dead layer implies an energy loss correction for the protons that is slightly larger but only by 0.5 keV so the net shift is -2.2 keV. By adjusting the thicknesses until agreement is obtained between the four DSSSDs, we obtain dead layers of 85, 75, 120 and 105 nm Si for DSSSD 1–4, respectively, in good agreement with expectations and the values obtained by monitoring the shift of the 1110 keV ^{16}O recoil group. The estimated error (statistical) is ±7 nm.

Assuming a certain dead layer thickness in one DSSSD, the requirement of equal proton energies in all four DSSSDs fixes the dead layer thickness in the other three DSSSDs to within ±7 nm. The overall scale, naturally, is free to vary. However, with dead layers ranging from 75 to 120 nm and given the 100 nm specified by the manufacturer, it seems reasonable to assume that the overall scale is correctly determined within ±15 nm.

2.3.7 Detection Thresholds

The range of 5.5 MeV α particles in atmospheric air is 4 cm [Yu03]. So, if we place an ^{241}Am source at a distance of, say, 5 cm from the detector and raise the pressure inside the chamber to near-atmospheric levels, the α particles will have very little energy left by the time they reach the detector. This method was used to study the trigger efficiency close to threshold. The typical rise "time" was $\sim$100 keV (10–90% trigger efficiency). 50% Trigger efficiency was reached at 130–210 keV depending on the channel (henceforth referred to as the trigger threshold). ADC thresholds were 30–200 keV depending on the channel.

2.3.8 Charge-Sharing Phenomena

Given that an α particle hits one of the DSSSDs, what is the overall efficiency for it being recorded in the data stream and identified in the subsequent analysis? Generally speaking, they are good, around 96% for α particles with energies above the trigger and ADC thresholds.

For an α particle to be identified in the analysis, its front-strip energy, E_{f}, and back-strip energy, E_{b}, must agree within a specified tolerance. We refer to this re-

quirement as "front-back matching". The observed distribution of energy differences, $\delta E = E_\mathrm{f} - E_\mathrm{b}$, resembles a Gaussian centered at $\delta E = 0$. At the beginning of the experiment, the width is $\sigma \approx 14$ keV in DSSSD 1–3 and $\sigma \approx 18$ keV in DSSSD 4. During the experiment, the resolution deteriorates considerably (cf. 2.3.12) in the front strips of DSSSD 1 and 2 so that $\sigma \approx 25$ keV at the end of the experiment. In DSSSD 3 the width grows to $\sigma \approx 19$ keV; in DSSSD 4 it remains unchanged. We adopt a tolerance of $\pm 4\sigma$ for the front-back matching with σ increasing linearly with time from its start value to its end value.

Using data from the ^{8}B run, where a continuous distribution of α energies from threshold to 8.5 MeV is measured, one may study the dependence of δE on the particle energy and hence the stopping range. One may also study the dependence on the angle of incidence on the detector. Small systematic variations in δE on the order of ± 2 keV are found in both cases. This may be interpreted as evidence for the charge collection efficiency being weakly dependent on the range of the α particle.

More can be learned by studying two-dimensional plots with E_f on one axis and E_b on the other. An example of such a plot is shown in Fig. 2.23 (a). Only events with a single front-strip signal and a single back-strip signal are shown. Both a vertical, a horizontal and a diagonal response tail is visible. The diagonal response tail is discussed in Section 2.3.10. The horizontal tail is caused by α particles stopped in a front-side inter-strip spacing; the conduction electrons created in the Si crystal are shared between the adjacent front strips but in unbalanced proportions such that only one of the two voltage pulses climbs above detection threshold. Similarly, the vertical tail is caused by α particles stopped in a back-side inter-strip spacing. In this case it is the holes that are shared. Since front strips and back strips run perpendicular to one another, sharing (almost) never occurs on both sides at the same time. Together, the horizontal and vertical tails account for less than 0.1% of the intensity. Notice that the vertical tail (sharing between back strips) extends from the point of maximum intensity on the diagonal whereas the horizontal tail (sharing between front strips) extends from a point on the diagonal somewhat below the point of maximum intensity. The reason for this asymmetry is the presence of an additional dead layer of 0.8–0.9 μm Si equivalent in the inter-strip spacing on the front side.

A more balanced sharing of charge carriers between the adjacent strips gives two above-threshold voltage pulses which, when added up, match the single voltage pulse registered on the opposite side of the DSSSD. This is illustrated in Fig. 2.18 where the sum of the shared energies is plotted versus the non-shared energy. The red circle marks the locus of maximum intensity expected in the event of full charge collection. For sharing between back strips, the observed locus of maximum intensity coincides with the red circle. For sharing between front strips, this is not quite the case due to the aforementioned extra dead layer. Additional off-diagonal intensity is

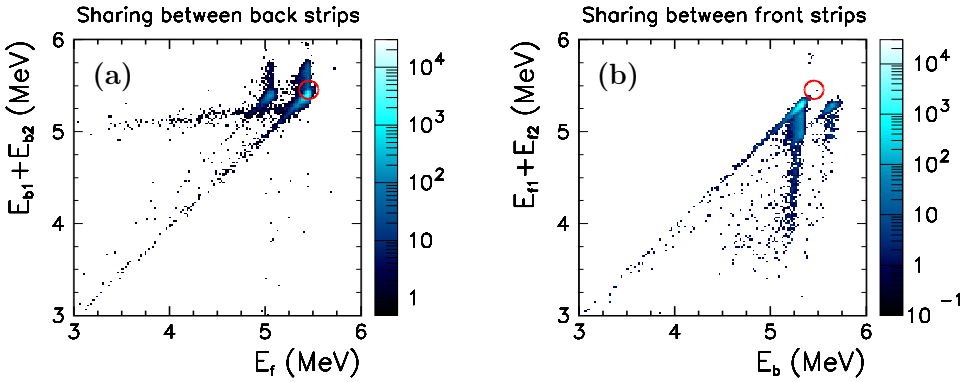

Figure 2.18: ^{241}Am measured in DSSSD 1. **(a)** Sharing between back strips. Events with a single front-side energy signal and two back-side energy signals coming from neighboring strips are selected. The non-shared front-side energy is on the abscissa; the sum of the shared back-side energies is on the ordinate. **(b)** Sharing between front strips. Similar to **(a)** but with the roles of front and back strips reversed.

present in Fig. 2.18 the origin of which has not been investigated. A close inspection reveals that the diagonal intensity is actually slightly off-diagonal: The sum of the shared energies is systematically 30 keV less than the non-shared energy.

The ^{8}B data may be used to study the energy and angular dependence of charge sharing. Using the non-shared *front*-strip energy, we obtain the spectrum of α-particle energies shared between *back* strips. We do not include off-diagonal sharing events. Sharing events with one of the shared energies below detection threshold are not included either. Dividing this spectrum by the full spectrum of α-particle energies one obtains the curves shown in Fig. 2.19 which give the probability for charge sharing to occur between back strips depending on the α-particle energy. The probability for charge sharing to occur between front strips is obtained in a similar way. (In doing so it is necessary to account for the extra dead layer present between front strips.) The probability for charge sharing to occur is found to be similar in front and back strips, both in terms of energy dependence and magnitude (about 1.5%), though minor differences are also observed. The interstrip spacing accounts for 0.1 μm/3.2 μm = 3% of the surface area of the DSSSDs so a sharing probability of 1.5% makes good sense. The charge sharing probability is also found to be weakly dependent on the angle of incidence, the probability being largest for normal incidence. We shall not concern ourselves any further with the phenomena of charge sharing. See [Yor87] for a dedicated experimental study of inter-strip effects in silicon strip detectors. We content ourselves with two observations: The first one is that sharing occurs with a probability of $\approx 2 \times 1.5\% = 3\%$. The second one is that the probability is weakly energy-dependent.

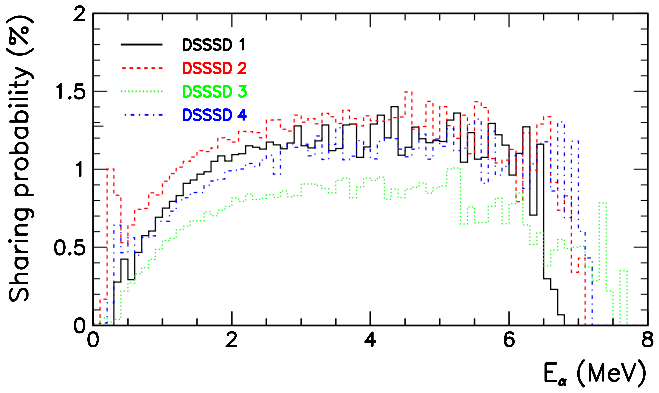

Figure 2.19: Ratio of the spectrum of α-particle energies shared between back strips to the full spectrum of α-particle energies using ^{8}B data.

2.3.9 Single-Particle Detection Efficiency

We have seen that the single-α detection efficiency is reduced by 3% due to charge sharing. The presence of additional experimental effects at the percent level cannot be excluded. Fortunately, the single-α detection efficiency can be determined directly from the ^{8}B data without any need of understanding the underlying effects: Given the arrangement of the detectors and the fact that the α particles from the decay of ^{8}B are being emitted back-to-back, we know with certainty that given the detection of an α particle in one detector a second α particle has to hit the opposite detector. Consequently, the single-α detection efficiency in the opposite detector can be determined by simply keeping count of how often the second α particle is detected.

The ratio of the coincidence α spectrum to the singles α spectrum measured in the central central 6×6 pixels of DSSSD 4 is shown in Fig. 2.20 (a) and (b). We interpret this ratio as the single-α detection efficiency in DSSSD 1. Note that the energy on the abscissa refers to the α particle detected in DSSSD 4. As will be discussed in Section 3.1.4, the α particles from the decay of ^{8}B are not emitted in a perfect back-to-back configuration. To be certain that the second α particle has hit DSSSD 1, we restrict our attention to the central 6×6 pixels of DSSSD 4. Above $\approx$ 0.7 MeV, the trend of the data points is given by the red curve. The efficiency exhibits a weak energy-dependence dropping from $\approx$ 97.0% at 0.7 MeV to $\approx$ 96.3% at 8 MeV. Below $\approx$ 0.7 MeV the efficiency seems to drop rapidly. This is not the case. As illustrated in Fig. 2.20 (c), the rapid drop in the ratio of coincidences to singles is caused by the presence of a low-energy background component in the singles spectrum. If we require $E_\beta = 0$ in the Si detector behind DSSSD 4, the low-energy component is reduced by a factor of two or so, indicating that β particles are responsible for at least part of the observed

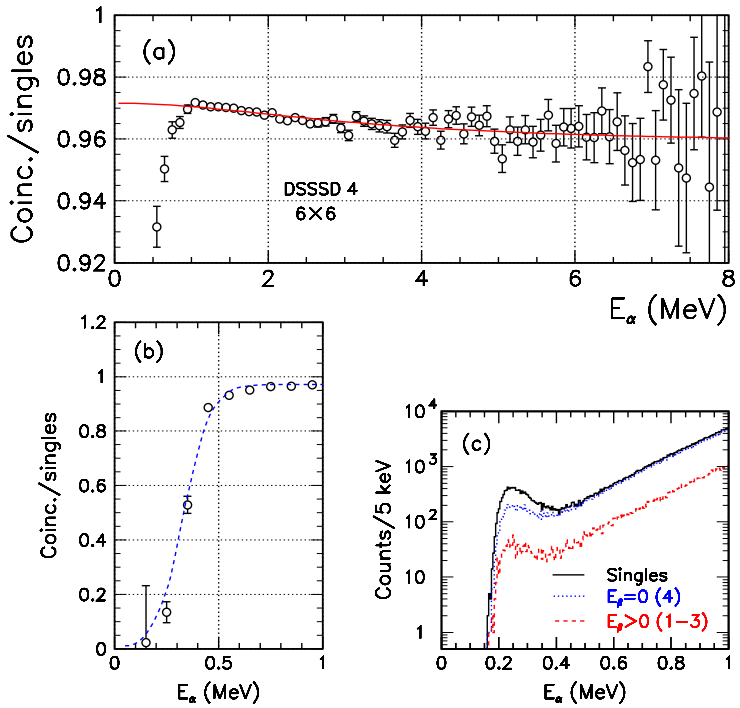

Figure 2.20: (a) and **(b)** Ratio of coincidences to singles in the central 6×6 pixels of DSSSD 4. The curves superimposed on the data points are meant to guide the eye. **(c)** α Spectra measured in DSSSD 4. See the text for explanation of the labels. The low-energy background component is seen to dominate the α spectra below 0.4 MeV and contributes up to 0.7 MeV.

low-energy background. If β particles were the sole source of background, we would expect the low-energy component to disappear all together when we require $E_\beta > 0$ in one of the Si detectors behind DSSSD 1–3. This is seen not to be the case. We conclude that part of the low-energy background component present in the singles spectrum cannot be explained as β particles. The most plausible alternative would seem to be uncorrelated noise, e.g. induced by the laser system at the IGISOL facility. Due to the presence of the low-energy background component in the singles spectrum, we are unable to determine the single-α detection efficiency of our detectors below $\approx$ 0.7 MeV. The single-α detection efficiencies of DSSSD 2–4 are very similar to that of DSSSD 1. The extent of the background component in the singles spectrum does, however, vary somewhat. In DSSSD 1, for instance, the coincidence-to-singles ratio already starts falling around 1.0 MeV.

Background measurements, performed during short interruptions during the 72-

hour long ^{8}B measurement, indicate the presence of a long-lived β-activity in the chamber (half-life on the order of hours) which accounts for about half of the intensity below 0.5 MeV in the singles spectrum. The energy loss of minimum-ionizing β particles in silicon is 0.6 keV/μm. Given that the DSSSDs are 60 μm thick, the typical energy deposited by β particles is only 36 keV. β Particles subject to significant straggling may, however, deposit considerably more energy, thus giving rise to the low-energy background component discussed above.

2.3.10 Response Function

The term "response function" refers to the *distribution* of energies measured from a perfectly monochromatic source due to experimental effects. Below, we discuss how the response function is best extracted from the experimental data.

The β decay of the 2^+, $T = 1$ ground state of ^{20}Na to the isobaric analog state (IAS) in ^{20}Ne, found at an excitation energy of 10 273.2 ± 1.9 keV, is responsible for the second most intense peak in the β-delayed α spectrum found at 4 434 keV. The IAS in ^{20}Ne and the ground state of ^{20}Na have the same quantum numbers and similar structures. The width of the IAS is ≤ 0.3 keV [Til98]. The energy of the α-particles emitted in its decay is smeared out due to the β-decay recoil motion of ^{20}Ne. For a pure Fermi transition, the broadening effect can be approximated by [Bha02]

$$\rho(x) = \begin{cases} \frac{5}{8T_{\max}}(1 - x^4) , & -1 \leq x \leq 1 \\ 0 , & |x| > 1 \end{cases} \tag{2.2}$$

with $x = \delta E / T_{\max}$ where $\delta E = E_\alpha - \langle E_\alpha \rangle$ is the shift relative to the mean α-particle energy. The maximum shift is given by

$$T_{\max} = \frac{m_e}{M}\left[2Qm_\alpha(W_0^2 - 1)\frac{M - m_\alpha - Q}{M - Q}\right]^{1/2} , \tag{2.3}$$

where m_e, m_α and M are the electron, α-particle and ^{20}Na masses; $Q = E_x - 4\,729.84$ keV and $W_0 = (E_0 - E_x)/m_e$ where E_x is the excitation energy in ^{20}Na and $E_0 = 13.376$ MeV is the maximum total β energy for decays to the ground state of ^{20}Na. For the IAS in ^{20}Ne, one obtains $T_{\max} = 29.9$ keV. The transition to the IAS was shown by [Cli89] to be a mixed Fermi and Gamow-Teller type transition. The Gamow-Teller component is, however, rather small so the broadening effect is well described by Eq. 2.2. Only little interference between the IAS and neighboring 2^+ states, which could potentially distort the shape of the 4 434 keV peak, is expected due to the unique structure and $T = 1$ character of the IAS. We conclude that the *physical* shape of the 4 434 keV peak is well understood and hence this provides an excellent case for studying the modifications to the shape introduced by *experimental* effects.

We adopt the parametrization of [Bha06] to describe the line shape caused by experimental effects. It consists of a Gaussian folded through two low-energy exponential tails:

$$\psi(E_0, E) \;=\; \sum_{i=1}^{2} \frac{A_i}{2\lambda_i} \exp\left(\frac{E - E_0}{\lambda_i} + \frac{\sigma^2}{2\lambda_i^2}\right) \mathrm{erfc}\left(\frac{E - E_0 + \sigma^2/\lambda_i}{\sqrt{2}\sigma}\right) , \tag{2.4}$$

where E_0 and E are the nominal and observed energies, λ_i are the exponential decay lengths and erfc is the complement of the incomplete error function. The normalization coefficients are $A_1 = 1/(1 + r)$ and $A_2 = r/(1 + r)$ with r being the relative area of tail 2 compared with tail 1.

The presence of the exponential tails may, in part, be attributed to incomplete charge collection, i.e. not all electron-hole pairs created by the incoming α particle reach the electrodes (or they do, but too late) either due to recombination or trapping. The presence of impurities and structural defects in the crystal lattice enhances the probability of recombination and trapping. The further the charges have to travel to reach the electrodes, the more likely recombination and trapping is to occur. The strength of the electric field also plays a role: A stronger field implies faster charge collection and hence reduced risk of recombination and trapping [Kno00]. We shall not concern ourselves any further with the physical interpretation of the parameters entering Eq. 2.4. We note, however, that the length of the exponential tails may depend on the range and hence the energy and identity of the incoming ion. The matching of front and back-strip energies discussed in Section 2.3.8 eliminates the hits for which incomplete charge collection only occurs for one type of charge carriers. In consequence, only loss phenomena which affect both types of charge carriers equally contribute to the exponential tails.

Ions striking the aluminum grid that covers 3% of the detector surface experience an additional energy loss compared to other ions giving rise to a low-energy "satellite" peak. We model the additional energy loss as a Gaussian distribution with mean E_g and spread σ_g. A spread of 5% is expected from the variation in effective thickness with angle. The complete line-shape formula then reads,

$$\Psi(E_0, E) \;=\; (1 - g)\, \psi(E_0, E) \;+\; g \int \frac{1}{\sqrt{2\pi}\sigma_g} \exp\left(-\frac{(E' - E_g)^2}{2\sigma_g^2}\right) \psi(E_0 - E', E)\, \mathrm{d}E' , \tag{2.5}$$

where g is the percentage of the detector surface covered by the aluminum grid. We refer to Ψ as the "response function" of the detector. It gives the energy distribution measured from a monochromatic source.

The line shape of the 4 434 keV peak in the β-delayed α spectrum of ^{20}Na, including experimental effects, is given by the convolution of the response function, Ψ, with the lepton broadening distribution, $\rho(x)$, of Eq. 2.2. Fits to the measured line shapes

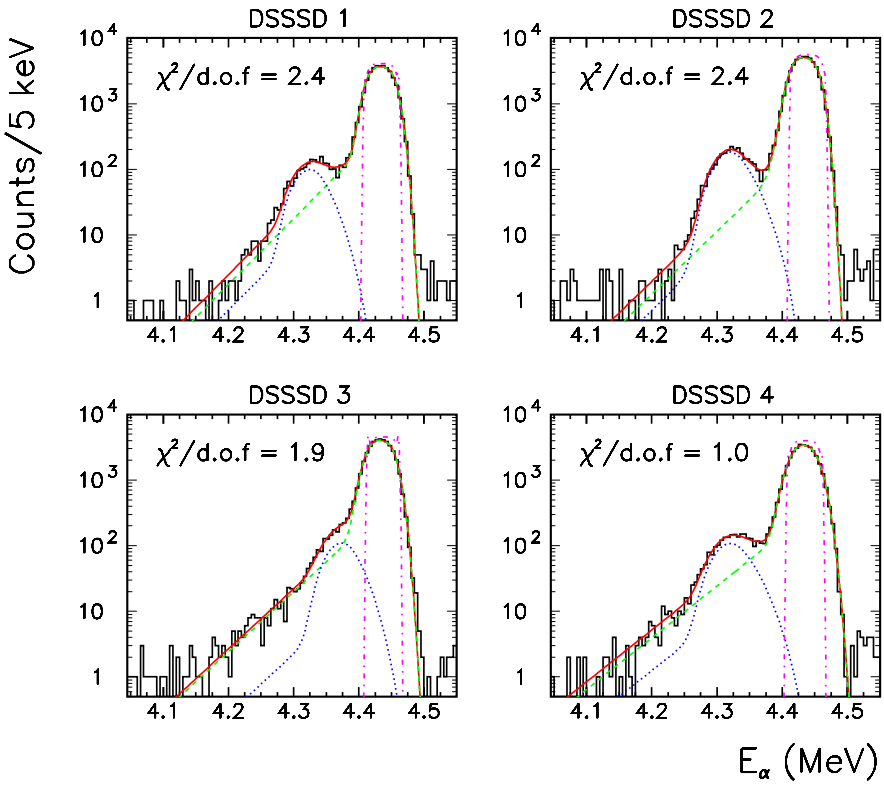

Figure 2.21: Fits to line shape of the 4 434 keV peak in the β-delayed α spectrum of ^{20}Na (first measurement). The fitting function is a convolution of the response function (Eq. 2.5) with the lepton broadening distribution (Eq. 2.2). The fit is shown by the solid red line. The contribution of the main and satellite peak are shown by the dashed green line and the dotted blue line, respectively. The pure lepton broadening distribution is shown by the dash-dotted purple line.

are shown in Fig. 2.21. The α-particle energy is corrected for the energy lost in the foil and the dead layer of the detector on an event-by-event basis taking into account the variation in effective thickness with angle, but assuming a fixed implantation depth of the 20 keV ^{20}Na ions in the foil. The best-fit parameter values are given in Table 2.2. The thickness of the Al grid, x_g, deduced from the energy loss, E_g, is also given. These are used for calculating the energy loss in the aluminum grid at other α-particle energies. The most probable value, $E_{\max}$, of the response function, Ψ, i.e. the energy for which Ψ attains its maximal value, does not coincide with the nominal energy, E_0. The displacement, $\delta E = E_{\max} - E_0$, is given in the last column of Table 2.3; it depends on the length of the exponential tails. Since most probable pulse-height

Table 2.2: Parameter values of the response function obtained from the analysis of the shape of the 4 434 keV peak in the β-delayed α spectrum of ^{20}Na (first measurement).

DSSSD	σ (keV)	λ_1 (keV)	λ_2 (keV)	r	g (%)	E_g (keV)	x_g (μm Al)	σ_g (keV)	δE (keV)
1	8.42	1.21	43.3	0.0942	3.17	86.5	0.49	14.0	-1.3
2	7.42	5.83	45.3	0.0425	4.46	86.9	0.49	16.2	-4.4
3	8.61	4.34	47.5	0.0823	3.14	38.2	0.22	13.3	-3.8
4	11.6	1.56	55.0	0.0875	4.05	83.1	0.47	17.3	-1.6

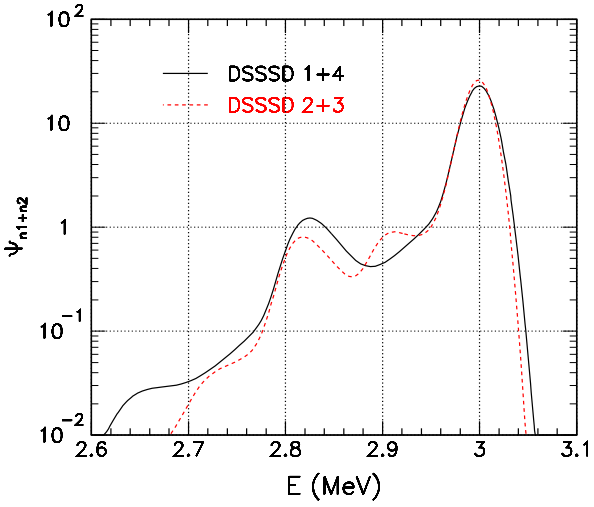

Figure 2.22: E_x Response functions for the two sets of oppositely facing detectors. Relevant to the determination of the ^{8}Be excitation energy, E_x , in the decay of ^{8}B.

values were used for the energy calibration, it is necessary to correct for this displacement. The spread in energy loss caused by the spread in implantation depth (see Fig. 2.14) is estimated from simulations to 4 keV. It contributes in quadrature to the spread, σ , given in the second column of Table 2.2.

In the β decay of ^{8}B, the quantity of interest is the ^{8}Be excitation energy, E_x , computed as the sum of the α-particle energies. We calculate the E_x response function as

$$\Psi_{n_1+n_2}(E) = \int \Psi_{n_1}(E_1)\, \Psi_{n_2}(E - E_1)\, \mathrm{d}E_1 \,, \tag{2.6}$$

where $\Psi_{n_1}(E_1)$ and $\Psi_{n_2}(E_2)$ are the single-α response functions in detectors n_1 and n_2. $\Psi_{n_1+n_2}(E)$ is shown in Fig. 2.22 for the two sets of oppositely facing detectors for a sum energy of 3 MeV. To a first approximation, variations in implantation depth do

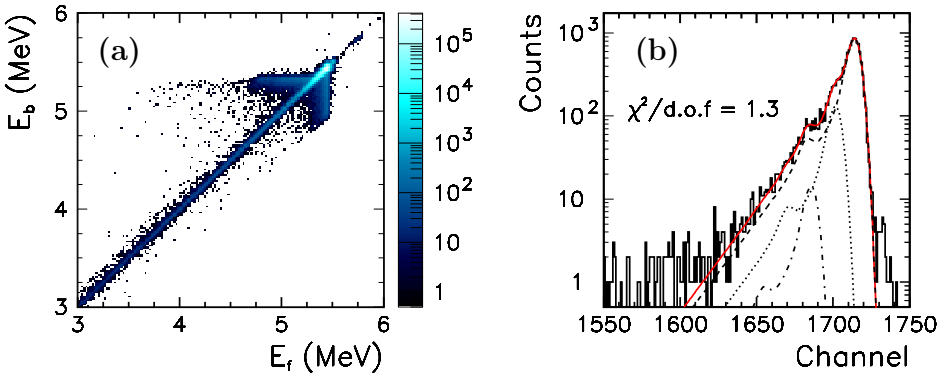

Figure 2.23: (a) Corresponding front and back-strip energies measured with ^{241}Am in DSSSD 1. **(b)** Fit to the ^{241}Am spectrum measured in a single pixel in DSSSD 1. The dashed, dotted and dash-dotted curves show the contribution of the three individual ^{241}Am lines.

not affect the sum energy: The reduced energy loss of one α particles is compensated by the larger energy loss of the other α particle. To account for this correlation, we use $\sqrt{\sigma^2 - (4\text{ keV})^2}$ in stead of σ in the calculation of $\Psi_{n_1+n_2}(E)$ where σ is the spread given in Table 2.2.

The 2 153 keV peak in the β-delayed α spectrum of ^{20}Na can be used to check whether the tails of the response function depend on the energy. Such a check has, however, not yet been performed. The fit to the line shape of the 2 153 keV peak is complicated by the sizeable width, $\Gamma = 15.1 \pm 0.7$ keV [Til98], of the corresponding state in ^{20}Ne. A proper R-matrix description is necessary to account for interference with other 2^+ states in ^{20}Ne.

Initially, before the idea of using the IAS in ^{20}Ne came up, an attempt was made to extract the detector response function from the observed shape of the ^{241}Am peak. This approach was, however, abandoned for reasons that will shortly become clear. Plenty of statistics meant that the analysis could be performed on a pixel-by-pixel basis. Corresponding front and back-strip energies are shown in Fig. 2.23 (a). Only diagonal hits were considered for the analysis. A typical single-pixel ^{241}Am spectrum is shown in Fig. 2.23 (b). ^{241}Am has three sharp α lines at 5486, 5443, and 5388 keV with relative intensities of 85.2%, 12.8% and 1.4%, respectively [Fir96]. As seen in Fig. 2.23 (b), the experimental resolution is not sufficient to separate these three lines. The spectrum was fitted with a function of the form

$$f(E) \propto \sum_{i=1}^{3} c_i \Psi(E_i, E) \,,$$

Table 2.3: Typical parameter values of the response function obtained from the analysis of the line shape of the α spectrum of ^{241}Am.

DSSSD	σ (keV)	λ_1 (keV)	λ_2 (keV)	r	g (%)	E_g (keV)	x_g (μm Al)	δE (keV)
1	12.8	9.7	45	0.50	3.5	108	0.70	-8.7
2	11.0	12.1	51	0.33	4.1	98	0.63	-8.7
3	12.2	13.7	55	0.25	2.9	69	0.45	-9.9
4	16.0	12.5	56	0.24	3.2	93	0.60	-10.4

with the coefficients c_i fixed to the intensities given above and with the energies of the two minor peaks, E_2 and E_3, at fixed positions relative to the major peak, E_1, which was allowed to vary freely. The response function Ψ given in Eq. 2.5 was used with the Gaussian function replaced by a delta function centered at $E' = E_g$. Typical parameter values obtained from the fit are given in Table 2.3. Compared to the IAS in ^{20}Ne, the ^{241}Am peak has a significantly larger spread, σ , and its exponential tails, λ_i , are more pronounced. These differences must obviously be a consequence of energy loss in the ^{241}Am source material though the effect is not fully understood. The energy loss depends on the spatial distribution of the implanted activity and will be affected by material deposited on the surface of the source over years of use.

2.3.11 Measurements with α Sources

The α-particle energy spectrum of ^{241}Am was measured at the beginning of the experiment and at the end. In addition, the α-particle energy spectra of ^{223}Ra and its α-emitting descendants, ^{219}Rn, ^{215}Po and ^{211}Bi, were measured at the very end of the experiment. The spectrum measured in one selected DSSSD is shown in Fig. 2.24 (a). Deviations of the observed peak energies (most probable value) from literature values are shown for all DSSSDs in Fig. 2.24 (b).

The deviation observed for ^{211}Bi, away from a linear trend, may be explained as follows: For each step in the ^{223}Ra decay chain, the recoiling daughter nucleus will, on average, come to a halt slightly deeper into the source because some of them escape. Hence, α particles will experience a slightly larger energy loss. Being the last α-emitting isotope in the decay chain, ^{211}Bi will be buried more deeply than any of the other α-emitting isotopes and its α particles subject to the largest such energy loss. (In the absence of ^{211}Bi this effect would have gone unnoticed: The α energies of ^{223}Ra, ^{219}Rn and ^{215}Po increase with decreasing mass number thereby masking the

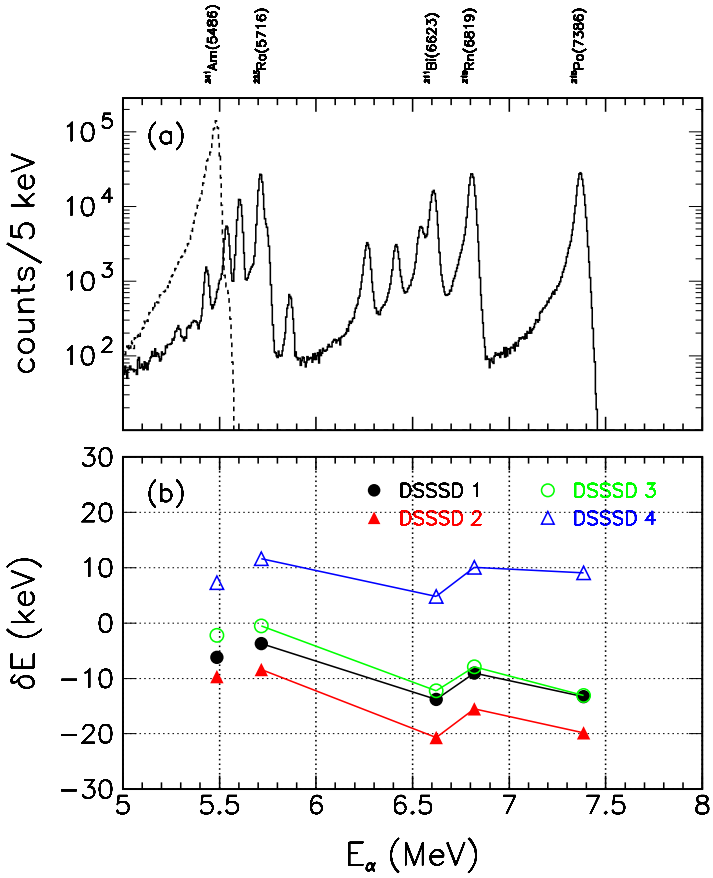

Figure 2.24: (a) Spectrum measured from a "cocktail" of α-particle emitters consisting of ^{223}Ra, ^{219}Rn, ^{215}Po and ^{211}Bi (solid line) and from ^{241}Am (dashed line). **(b)** Deviations from literature values.

increasing energy loss as a calibration issue.)

For ^{241}Am, the energy loss in the source was measured by varying the orientation of the source relative to the detector while monitoring the shift in peak position. We find that the energy lost by α particles exiting normal to the source plane is 7.7 ± 0.4 keV, see Fig. 2.25.

2.3.12 Temporal Variations in Gain and Resolution

A signal from the precision pulse generator was fed to the preamplifiers throughout the entire experiment in order to monitor the stability of the calibration. Fig. 2.26 shows variations in the position (solid, black) and width (dashed, red) of the pulse

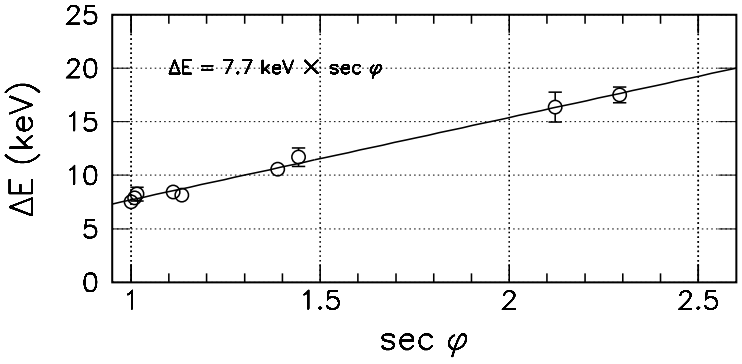

Figure 2.25: Energy loss of ^{241}Am α particles in the source, ΔE, as function of $\sec\varphi$ where φ is the angle out of the source.

generator signal for two selected strips. The sudden big jumps in position can be attributed to interventions where the pulse generator was used for other calibration purposes. However, slow drifts in position (probably due to variations in the electronic gain) are also visible, both in front and back strips. Toward the end of the experiment, the resolution in the front strips of DSSSD 1 and 2 deteriorates considerably. This is clearly seen in Fig. 2.26. In contrast, the resolution of the back strips is unchanged. In DSSSD 4, both front and back strip resolution is unchanged, whereas in DSSSD 3 the resolution worsens over the course of the experiment in both front and back strips, but only by a small amount. Given the deteriorating resolution in the front strips of DSSSD 1 and 2, we only use the back strips for energy determination. For consistency, we do this in all four DSSSDs. The front-strip energies are only used for the front-back matching discussed in Section 2.3.8 where we adopt a time-dependent tolerance to account for the deteriorating resolution in the front strips.

Since we know the implantation depth, the foil thickness and the detector dead layers at the beginning of the experiment and at the end, we can calculate the shift in apparent energy of the 817 keV proton group of ^{23}Al, the 2 153 and 4 434 keV α groups of ^{20}Na and the 5 486 keV α line of ^{241}Am. By subtracting these shifts from the shifts actually observed, we obtain the shift that has occurred in the electronic gain. This is shown in Fig. 2.27 for selected back strips in each DSSSD. The data point at channel ~ 3000 gives the shift of the pulse generator signal, carefully corrected for the big "artificial" jumps observed in Fig. 2.26. The shift in electronic gain is well described as a linear function of pulse height with the exception of the fourth data point (^{241}Am) which is systematically 5 keV above the linear trend.

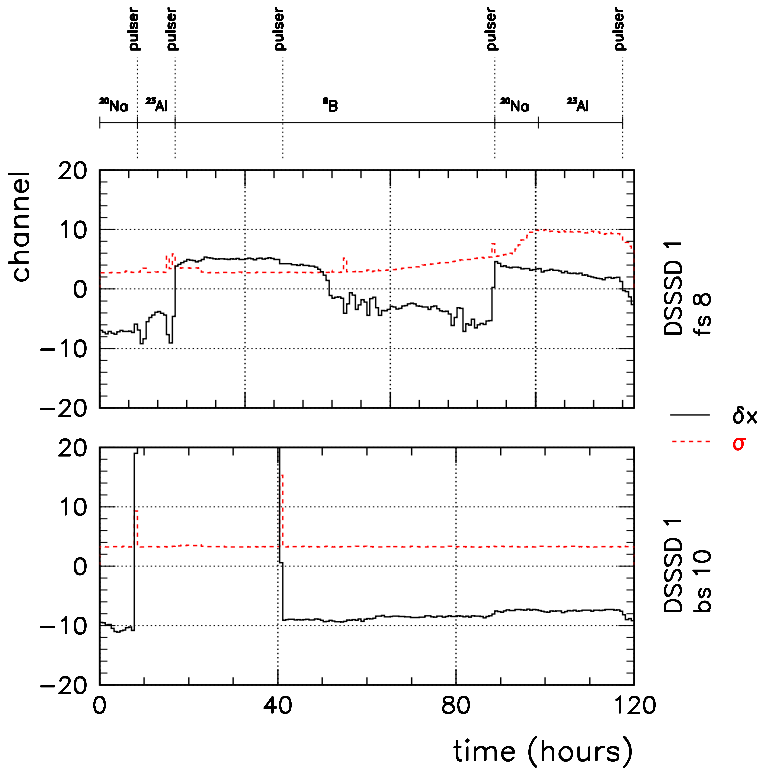

Figure 2.26: Variations in the position (relative to the average), δx, and width, σ, of the pulse generator signal in front strip 8 and back strip 10 of DSSSD 1 during the experiment.

2.3.13 Foil and Dead Layer Growth

Using data from the second ^{20}Na measurement, performed at the end of the experiment, the energy lost by 2 153 keV α particles exiting normal to the foil plane is determined to 10.4 ± 0.2 keV upstream and 36 ± 2 keV downstream. The former value is in good agreement with the value of 9.9 ± 0.5 keV obtained from the first ^{20}Na measurement. The latter value is significantly above the value of 26.9 ± 0.6 keV obtained from the first measurement. Dividing the excess, 9 ± 2 keV, by the stopping power of 2 153 keV α particles in carbon, $\mathrm{d}E/\mathrm{d}x = 1.336$ keV/μg/cm^2, we determine the equivalent growth in foil thickness to 7.0 ± 1.6 μg/cm^2. Using the ^{241}Am source, the foil thickness was measured to 23.9 ± 0.4 μg/cm^2 at the beginning of the experiment and 28.5 ± 1.0 μg/cm^2 at the end, corresponding to a growth of 4.6 ± 1.1 μg/cm^2. Within errors, this agrees with the growth deduced from the ^{20}Na data. The foil thickness deduced from the second ^{20}Na measurement, 35.0 ± 1.5 μg/cm^2, is significantly larger than the thickness deduced from the ^{241}Am measurement. We take their weighted

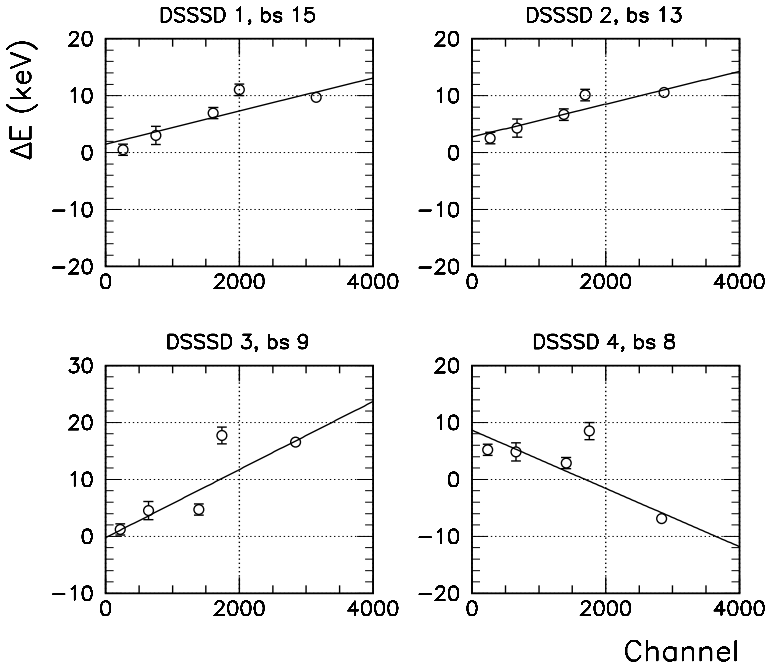

Figure 2.27: Drift in electronic gain in four back strips. ΔE is the change in energy from the beginning of the experiment to the end. The best fit straight line is superimposed.

average, $31 \pm 3\,\mu g/cm^2$, as our estimate of the true foil thickness with the error bar raised to account for the large spread.

The reason for the growth in foil thickness is not obvious. There seems to be two possible explanations: Either a very intense and stable beam component or contaminating gas, e.g. hydrocarbons from pump oil. In the former case, the additional material will be deposited only on the upstream side of the foil whereas in the latter case material will aggregate on both sides of the foil and presumably also on the surface of the detectors. Taking the observed growth ($\Delta x = 7\,\mu g/cm^2$), the time with beam on target separating the two measurements ($\Delta t = 80$ hours), the cross sectional area of the beam ($a \approx 0.4\,cm^2$) and the mass of a single carbon atom ($m = 2.0 \times 10^{-17}\,\mu g$), we obtain $I \sim a\Delta x/m\Delta t = 5 \times 10^{11}$ pps as an estimate of the average beam intensity required to explain the observed growth. The assumed beam content is not important for the estimate, using Si one obtains $I \sim 3 \times 10^{11}$ pps.

A stable beam component of the intensity estimated *and* with the appropriate A/q ratio to pass through the separator, seems very unlikely. Therefore, we conclude that a contaminant gas originating from the pumping system constitutes the most

plausible explanation for the observed growth in foil thickness. In this case, we expect the contaminant gas to condensate not only on the foil but also on the surface of the detectors in amounts similar to that found on the foil, thereby lowering the energy of the 2 153 keV α group by another 9 ± 2 keV. This corresponds to an additional dead layer of 40 ± 9 nm Si. Remarkably, the inclusion of this additional dead layer in the analysis of the second ^{23}Al data set, brings down the energy of the 817 keV proton group from 826 to 817 keV in exact agreement with the energy obtained from the first data set. (Optimal agreement between the four DSSSDs is obtained by increasing the dead layer of DSSSD 1 by 30 nm, that of DSSSD 2 and 3 by 40 nm and that of DSSSD 4 by 45 nm.)

2.3.14 Summary

Before proceeding to the next chapter let us briefly summarize the most important things we have learned about our "measuring device": The geometry has been determined with an accuracy of 1 mm or so. An energy calibration has been performed using the 2 153 and 4 434 keV β-delayed α groups of ^{20}Na. A small quadratic correction, derived from measurements with a precision pulse generator, was applied to the calibration. The foil thickness at the beginning of the experiment has been determined to 25.7 ± 1.8 μg/cm^2 and the thickness of the dead layers of DSSSD 1–4 have been determined to 85, 75, 120 and 105 nm, respectively (see Section 2.3.6 for a discussion of the uncertainties on these values). Trigger thresholds vary from 130–210 keV depending on the channel. Charge sharing between neighboring strips occurs with a probability of 3%. The probability exhibits a weak energy dependence. The single-particle detection efficiency of our setup has been determined above 0.7 MeV by comparing singles and coincidence α spectra from the decay of ^{8}B. The experimental response function has been determined by analyzing the shape of the 4 434 keV peak in the β-delayed α spectrum of ^{20}Na. The additional energy loss experienced by particles striking the electrode grid that covers 3% of the detector surface gives rise to a low-energy satellite peak. The electronic gain drifts by up to 10 keV during the experiment. The foil and the dead layers grow in thickness during the experiment by the equivalent of 7 μg/cm^2 of carbon. These temporal variations are taken into account in the analysis of the ^{8}B data by assuming that they occur linearly in time. Finally, the resolution of the front strips of DSSSD 1 and 2 deteriorates toward the end of the ^{8}B measurement. In consequence, we use exclusively the back strips for energy determination.

CHAPTER 3

Data Analysis

We have presented the experiment and its calibration in the previous chapter. The present chapter is concerned with the data analysis. In section 3.1, we discuss the kinematics of the β decay of ^{8}B and the theoretical description of the β-ν-α angular correlations. This is necessary to determine the recoil correction, E_{R}, and to model the α-α coincidence detection efficiency of the setup. In section 3.2, we extract the E_x spectrum from the experimental data. We correct for detection efficiencies and discuss the uncertainties on the spectrum.

Note: We distinguish between the E_x *spectrum*, which is the observed distribution of excitation energies, and the E_x *distribution*, which is the distribution of excitation energies obtained from the R-matrix fit (Section 4.1), i.e. corrected for the effects of the detector response function (Section 2.3.10).

3.1 Correlations and Kinematics

3.1.1 Kinematics

A schematic illustration of the kinematics of the ^{8}B β decay is given in Fig. 3.1. In the rest frame of the daughter nucleus (recoil frame) the two α particles travel at

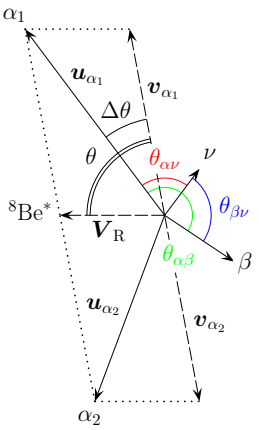

Figure 3.1: Kinematics of the β decay of ^{8}B. In the rest frame of the daughter nucleus ^{8}Be the two α particles travel at equal speeds in opposite directions, i.e. $\boldsymbol{v}_2 = -\boldsymbol{v}_1$. The velocities of the α particles in the rest frame of ^{8}B are obtained by simple vector addition, $\boldsymbol{u}_i = \boldsymbol{v}_i + \boldsymbol{V}_{\mathrm{R}}$, where $\boldsymbol{V}_{\mathrm{R}}$ is the recoil velocity of the daughter nucleus ^{8}Be.

equal speeds in opposite directions, i.e. $\boldsymbol{v}_{\alpha_2} = -\boldsymbol{v}_{\alpha_1}$. The velocities of the α particles in the rest frame of ^{8}B (laboratory frame) are obtained by simple vector addition, $\boldsymbol{u}_{\alpha_i} = \boldsymbol{v}_{\alpha_i} + \boldsymbol{V}_\mathrm{R}$, where $\boldsymbol{V}_\mathrm{R}$ is the recoil velocity of the daughter nucleus ^{8}Be. Squaring and multiplying by $\frac{1}{2}m_\alpha$, we obtain the α-particle kinetic energy in the laboratory frame,

$$\begin{aligned} E_{\alpha_i} &= \tfrac{1}{2}m_\alpha u_{\alpha_i}^2 \\ &= \tfrac{1}{2}m_\alpha v_{\alpha_i}^2 + \tfrac{1}{2}m_\alpha V_\mathrm{R}^2 + m_\alpha \boldsymbol{v}_{\alpha_i}\cdot\boldsymbol{V}_\mathrm{R} \\ &= E_\alpha^* + \tfrac{m_\alpha}{M}E_\mathrm{R} \pm 2\sqrt{\tfrac{m_\alpha}{M}E_\alpha^* E_\mathrm{R}}\cos\theta\ , \end{aligned} \tag{3.1}$$

where $E_\mathrm{R} = \frac{1}{2}MV_\mathrm{R}^2$ is the kinetic energy of the recoiling daughter nucleus and $E_\alpha^* = \frac{1}{2}(E_x + 92\ \mathrm{keV})$ is the α-particle kinetic energy in the recoil frame, E_x being the excitation energy in ^{8}Be. With the angle θ chosen as shown in Fig. 3.1, the plus sign applies to α_1 and the minus sign to α_2. In the present case $\frac{m_\alpha}{M} = \frac{1}{2}$ whereas in the case of ^{20}Na $\frac{m_\alpha}{M} = \frac{1}{5}$.

Adding the two α-particle laboratory energies, we obtain

$$E_{\alpha_1} + E_{\alpha_2} = 2E_\alpha^* + E_\mathrm{R} = E_x + 92\ \mathrm{keV} + E_\mathrm{R}\ , \tag{3.2}$$

owing to the cancellation of the last term in Eq. 3.1. Apart from the small correction given by the recoil energy E_R, the sum energy of the α-particles thus equals the excitation energy in ^{8}Be plus the 92 keV gap that separates the ground state of ^{8}Be and the α+α threshold. The recoil energy attains its maximal value when the leptons are emitted in the same direction. Momentum conservation gives $E_\mathrm{R,max} \approx (E_0 - E_x)^2/2Mc^2$ where $E_0 = 17.4688(10)$ MeV is the maximum total β energy for decays to the ground state of ^{8}Be, E_x is the excitation energy in ^{8}Be and M is the mass of the ^{8}Be nucleus. At $E_x = 3$ MeV one obtains $E_\mathrm{R,max} = 14$ keV. When averaged over the lepton angles, the recoil energy is somewhat reduced. A precise calculation, cf. Section 3.1.4, gives an average recoil energy of 8.5 keV. The dependence of the average recoil energy on E_x is shown in Fig. 3.3.

3.1.2 Recoil Broadening

As discussed in Section 3.1.1, the recoil of the ^{8}Be daughter nucleus causes a small systematic shift of the α-particle energy given by the second term of Eq. 3.1. The third term averages to zero but causes a substantial broadening of the α-particle energy spectrum, i.e. for fixed E_x we measure a *distribution* of α-particle energies in the laboratory. According to [Bha02] the shape of this distribution is well described by the following expression:

$$\rho(x) = \begin{cases} \frac{15}{16T_\mathrm{max}}(1 - 2x^2 + x^4) & -1 \le x \le 1 \\ 0 & |x| > 1 \end{cases} \tag{3.3}$$

with $x = \delta E/T_{\max}$ where $\delta E = \frac{1}{2}(E_{\alpha_1} - E_{\alpha_2})$ is the shift relative to the mean, and $T_{\max}$ is the maximum shift given by Eq. 2.3 with M, in this case, being the ^{8}Be mass; $Q = E_x + 92$ keV and $W_0 = (E_0 - E_x)/m_e$ where $E_0 = 17.4688(10)$ MeV is the maximum total β energy for decays to the ground state of ^{8}Be. The full-width at half-maximum of the recoil energy distribution is FWHM = $1.08\,T_{\max}$.

The broadening observed for 2.8MeV $< E_x <$ 3.0 MeV is shown in Fig. 3.2 (b). The data has been fitted with the theoretical distribution of Eq. 3.3 folded through the following response function:

$$\Psi_{n_1-n_2}(\delta E) = \int \Psi_{n_2}(E_{\alpha_2})\,\Psi_{n_1}(2\delta E + E_{\alpha_2})\,\mathrm{d}E_{\alpha_2}\ ,$$

where Ψ_{n_1}, Ψ_{n_2} are the single-particle response functions introduced in Section 2.3.10 and n_1, n_2 are the detectors in which α_1, α_2 are detected. The only free parameters in the fit are $T_{\max}$ and an overall normalization factor. We restrict our attention to coincidence events in which one of the α particles is detected within the central 6×6 pixels. This is done to eliminate the bias toward small values of δE induced by the preferential selection of decays with the α particles emitted at small angles θ relative to the recoil axis (see Section 3.2.4).

In Fig. 3.2 (a) we compare the FWHM obtained in each excitation-energy bin by the fitting procedure described above with the theoretical prediction. The agreement is seen to be very good. The systematic deviations below ~ 4 MeV are believed[1] to result from the neglect of higher-order terms in the derivation of Eq. 3.3 such as the kinematic terms discussed below. The deviations do not represent a binning effect, nor can they be explained by uncertainties in the response function (this has been checked with simulations). Coincidence data from DSSSD 2 and 3 with one α particle detected within the central 6×6 pixels of DSSSD 3 was used for the present analysis. Coincidence data from DSSSD 1 and 4 has also been analyzed and is found to give practically identical results.

3.1.3 β-ν-α Triple Correlation

Neglecting terms of order E_β/M where E_β is the total β energy and M is the mass of the β-decay daughter nucleus (popularly known as recoil order terms), the β-ν-α triple correlation probability distribution is given by Eq. 5 in [Cli89]. Further neglecting the kinematic terms of order E_β/Mv_α where v_α is the speed of the α particle in the recoil frame one obtains the following approximate probability distribution:

$$w \approx 1 + A\frac{p_\beta}{E_\beta}\cos\theta_{\beta\nu} + B\frac{p_\beta}{E_\beta}\cos\theta_{\alpha\beta}\cos\theta_{\alpha\nu},$$

[1] A thorough analysis will be performed in the near future.

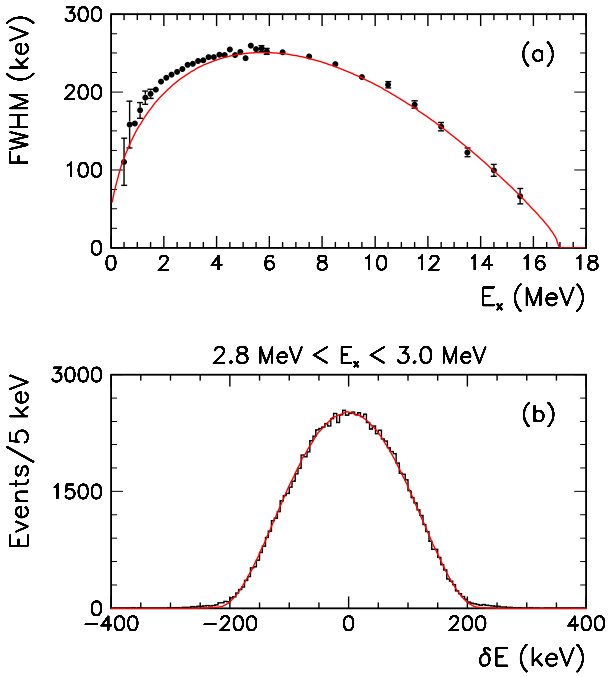

Figure 3.2: Recoil broadening in the β decay of ^{8}B. **(a)** FWHM of the α-particle energy distribution as function of the ^{8}Be excitation energy. The solid red curve superimposed on the data points is the theoretical prediction. **(b)** Quality of the fit to the α-particle energy distribution in one selected excitation energy bin.

where p_β is the β momentum, θ_{xy} is the relative angle of particle x and y as illustrated in Fig. 3.1 and the coefficients A and B are given by

$$A = \frac{g_2}{g_1} - \frac{\xi}{30}\frac{g_{12}}{g_1}\,, \qquad B = \frac{\xi}{10}\frac{g_{12}}{g_1}\,,$$

with

$$\frac{g_2}{g_1} = \tfrac{1}{3}(2a_3 + 1)\,, \qquad \frac{g_{12}}{g_1} = \tfrac{1}{2}\Theta(a_3 - 1).$$

Here a_3 is the so-called triple-correlation coefficient and ξ and Θ are spin-dependent coefficients which for the present spin sequence, $2^+ \to 2^+ \to 0^+$, take on the values 10 and 1, respectively. For pure Gamow-Teller decays, we have $a_3 = -1$ (for pure Fermi $a_3 = 1$). We thus arrive at the following approximate formula:

$$w \approx 1 - \frac{p_\beta}{E_\beta}\cos\theta_{\alpha\beta}\cos\theta_{\alpha\nu}. \tag{3.4}$$

Before proceeding, let us briefly discuss the approximations made. Recoil order terms $E_\beta/M < 17\,\text{MeV}/7.5\,\text{GeV} \sim 2\times10^{-3}$ may safely be neglected. The kinematic terms, on the other hand, are of order E_β/Mv_α where v_α is the speed of the α particle in the recoil frame and hence become large for small E_x. Uncertainties concerning the trigger levels prevent a reliable efficiency correction to be made below $E_x = 1$ MeV. Above 1 MeV we have

$$\frac{E_\beta}{Mv_\alpha} = \frac{E_\beta}{M}\left(\frac{m_\alpha}{E_x + 92\,\text{keV}}\right)^{1/2} < \frac{17\,\text{MeV}}{7.5\,\text{GeV}}\left(\frac{3.7\,\text{GeV}}{1\,092\,\text{keV}}\right)^{1/2} = 0.13\,,$$

indicating that, maybe, the kinematic terms cannot be disregarded in the present case. The neglect of the kinematic terms may possibly explain the deviation observed in Fig. 3.2. Importantly, the E_x distribution is not affected.

3.1.4 Simulation of Recoil Effects

As a consequence of the recoil motion of the ^{8}Be nucleus, the α particles do not travel in completely opposite directions in the laboratory frame. In general, the effect is small but in the particular case of ^{8}B, the effect is enhanced by the combination of a large Q value and a light daughter nucleus. We expect the effect to be most important at small E_x where the recoils are largest. At $E_x = 3$ MeV, for instance, the α-particle energy in the recoil frame is $E^*_\alpha = 1.5$ MeV and the recoil energy of the ^{8}Be nucleus, E_R, varies between 0 and 14 keV depending on the relative angle of the leptons. The shift in α-particle angle, $\Delta\theta$, attains its maximal value when the α particles are emitted at 90 degrees to the recoil axis. From Fig. 3.1 we find

$$\begin{aligned}\Delta\theta_\text{max} &= \arctan V_{\text{R,max}}/v_\alpha \\ &= \arctan\sqrt{m_\alpha E_{\text{R,max}}/ME^*_\alpha} \\ &\approx \arctan\sqrt{0.5\times14\,\text{keV}/1.5\,\text{MeV}} \\ &= 3.9^\circ \end{aligned} \tag{3.5}$$

for the maximal shift corresponding to a relative α-α angle of $\theta_{\alpha\alpha} = 180^\circ - 2\times3.9^\circ = 172^\circ$. The distribution of $\theta_{\alpha\alpha}$ for fixed E_x may be obtained by means of a Monte Carlo simulation:

First, we generate a large sample of $\beta + \nu + \alpha + \alpha$ four-body final states using the following procedure: The directions of the neutrino (ν) and the positron (β) are chosen randomly (independent isotropic distributions) relative to a fixed axis given by the α-particle recoil-frame momentum vector. The β kinetic energy T_β is chosen randomly (uniform distribution) from 0 to the maximum possible value of $E_0 - m_e - E_x = 16.9578\,\text{MeV} - E_x$. Finally, the amplitude of the event $w(E_x; E_\beta, \theta_{\alpha\beta}, \theta_{\alpha\nu})$ is computed from Eq. 3.4.

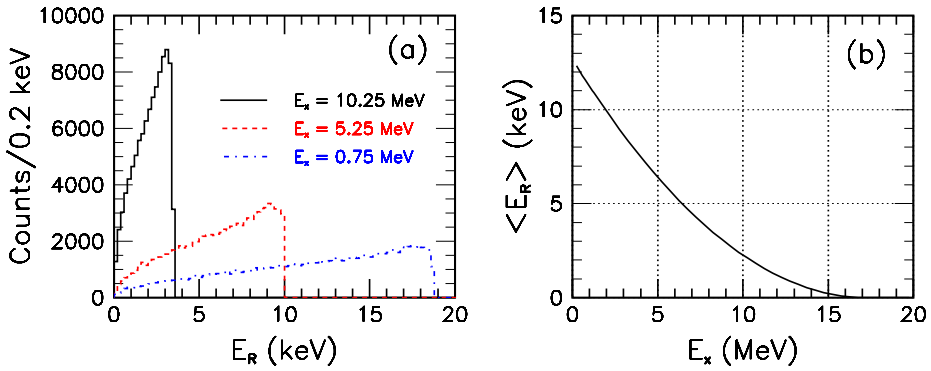

Figure 3.3: **(a)** Recoil energy distribution obtained for three fixed values of E_x. **(b)** Average recoil energy as function of E_x.

Second, we leaf through the sample just generated applying the Von Neumann sampling technique: For each event a random number $0 \leq r \leq 1$ is generated and the event is accepted if $w > rw_{\max}$ where $w_{\max}$ is largest weight assigned to any event of the sample. The neutrino energy is computed as $E_\nu = E_0 - E_\beta$ with $E_\beta = T_\beta + m_e$ being the total β energy. The ^{8}Be recoil energy, E_{R}, is determined by the requirement of momentum conservation, $\boldsymbol{p}_{\mathrm{R}} = -(\boldsymbol{p}_\beta + \boldsymbol{p}_\nu)$. The laboratory velocities of the α particles, $\boldsymbol{u}_{\alpha_i}$, are obtained from the velocities in the recoil frame, $\boldsymbol{v}_{\alpha_i}$, by simple vector addition: $\boldsymbol{u}_{\alpha_i} = \boldsymbol{v}_{\alpha_i} + \boldsymbol{V}_{\mathrm{R}}$ with $\boldsymbol{V}_{\mathrm{R}} = \boldsymbol{p}_{\mathrm{R}}/M$. The relative α-α angle is then obtained from $\cos\theta_{\alpha\alpha} = \boldsymbol{u}_{\alpha_1} \cdot \boldsymbol{u}_{\alpha_2}/u_{\alpha_1}u_{\alpha_2}$.

Examples of $\theta_{\alpha\alpha}$ distributions for two different values of E_x are shown in Fig. 3.9 (a) and (b) by the dash-dotted blue lines. Examples of E_{R} distributions for three different values of E_x are shown in Fig. 3.3 (a). In Fig. 3.3 (b) the average of the E_{R} distribution is plotted as function of E_x.

3.2 E_x Spectrum

Below, we examine the various types of coincidence events found in the data, we discuss how best to determine E_x from the measurement of the individual α-particle energies and we use simulations to evaluate the efficiency of our setup for detecting α-α coincidences and correct the experimental spectra accordingly. Finally, we check the internal consistency of the singles spectrum and the coincidence spectrum and estimate the uncertainty in the determination of E_x. In the end, a summary is given.

3.2.1 Multiple-Particle Events

Fig. 3.4 (a) shows all α-α coincidences detected during 72 hours of measurement. Events within the region defined by the two red lines are used to construct the E_x spectrum.

Neglecting β-α angular correlations and assuming 100% β detection efficiency[2], the probability of the positron being detected in coincidence with the α particles is simply equal to the solid-angle coverage of 30%. As can be seen by inspecting the color scales of Fig. 3.4 (a) and (b), the requirement of a signal from the back detectors ($E_\beta > 0$) reduces the number of α-α coincidences by a factor of six, i.e. twice the reduction expected, indicating that the β detection efficiency has been overestimated. Since we are only interested in the α particles, this is not a cause of concern.

The chances of detecting the positrons in the DSSSDs are slim because the positrons deposit very little energy, on average 0.6 keV/μm $\times$ 60 μm = 36 keV. Only positrons subject to significant straggling deposit enough energy to climb above detection threshold. Therefore only 10 500 α-α-β triple coincidences have been identified, corresponding to one in every thousand positron being detected in the DSSSDs in coincidence with the α particles.

Fig 3.4 (c) and (d) show coincidences where the relative angle deviates substantially from 180 degrees. The horizontal and vertical bands close to the axes correspond to α-β coincidences in the DSSSDs with the second α-particle not detected. The diagonal band may be identified with α-α coincidences where large-angle scattering has occured in the carbon foil. Random coincidences, to be discussed below, also give a small contribution.

[2]With 90% of the intensity in the E_x distribution located below 6 MeV, the large majority of positrons will be minimum ionizing and, on average, deposit 0.6 keV/μm $\times$ 1500 μm = 0.9 MeV in the 1.5 mm thick back detectors. Enough to stay clear of the detection thresholds, thus seemingly justifying the assumption of 100% β-detection efficiency.

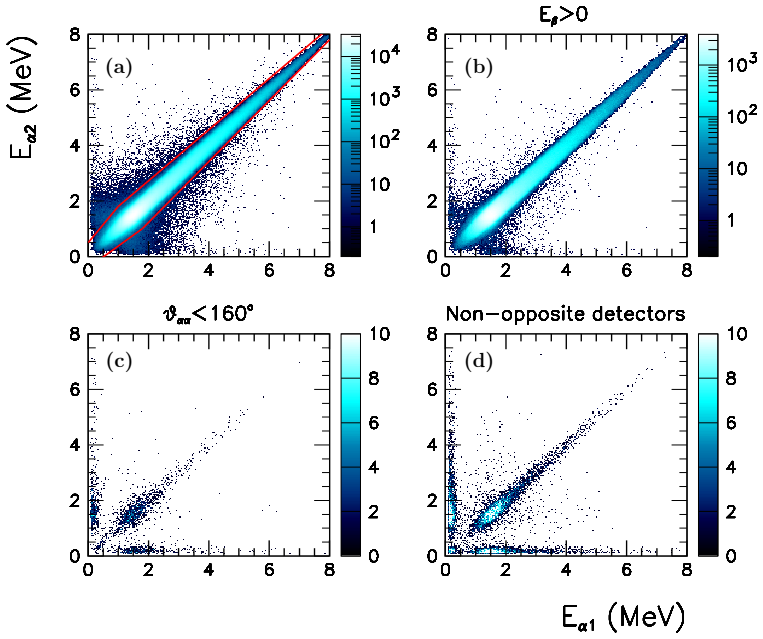

Figure 3.4: Two-dimensional energy spectrum of α-α coincidences from the decay of ^{8}B. The figures **(a)–(c)** display coincidences detected in opposite detectors. In the case of **(b)** and **(c)** additional cuts have been imposed on the data as indicated by the text on top of the figures. Figure **(d)** displays coincidences detected in non-opposite detectors.

3.2.1.1 Random Coincidences

As explained in Section 9.2, random coincidences may occur if two decays take place within less than 2.5 μs of each other, i.e. during the data taking window. The two decays will be recorded to the same event in the data structure even though they represent distinct physical events. It is instructive to compare the length of the data taking window to the typical travel times from decay site to detection. Consider e.g. the breakup of ^{20}Ne to $\alpha + {}^{16}$O. Assuming 4 MeV for the energy of the α-particle and 1 MeV for the energy of the ^{16}O ion, one finds travel times of 3.6 and 14 ns, respectively. The delay between the arrivals of the two particles is seen to be much shorter than the length of the data taking window.

Given the detection of a ^{8}B decay, what is the probability that another decay will occur and be detected within the next 2.5 μs and hence be recorded in the same event in the data stream? With an average ^{8}B implantation rate of 2.0×10^2 ions per second

and a 30% solid-angle coverage, the answer is $2.0\times10^2\ \mathrm{s}^{-1}\times2.5\,\mu\mathrm{s}\times0.3 = 2\times10^{-4}$, i.e. two in every 10 000 events will be random coincidences. Since the decays that come in random coincidence are uncorrelated, exclusion of such events from the analysis will not modify the shape of the E_x spectrum.

3.2.2 β Summing

Neglecting β-α angular correlations, the probability that the positron will hit the same pixel as one of the α particles is only $\sim 2\times9\ \mathrm{mm}^2/4\pi\,(5\ \mathrm{cm})^2 = 6\times10^{-4}$. Assuming an average energy loss of 0.6 keV/μm for positrons in silicon, we estimate the energy shift caused by β summing to $6\times10^{-4}\times0.6\ \mathrm{keV}/\mu\mathrm{m}\times60\,\mu\mathrm{m} = 0.02$ keV , i.e. vanishingly small. One may, however, argue that, for summing to occur, the positron just has to hit the same *strip* as one of the α particles. If, say, the positron and the α particle hit the same back strip but different front strips, their back-side signals will add up while their front-side signals will be read out separately. Typically, the energy deposited by the positron E_β is below detection threshold and hence only one front-side signal (that of the α particle) will be recorded in the data stream. Due to the smallness of E_β, front and back energies will be fairly close, typically close enough to survive the cut placed on the front-back energy difference. Consequently, the β-α coincidence will be identified as a single α particle with an energy of $E_\alpha + E_\beta$ because we use the back-side signal for energy determination. The probability of the positron hitting the same back strip as one of the α particles is 16 times the probability of it hitting the same pixel and hence our estimate of the energy shift caused by β summing is 16×0.02 keV = 0.3 keV, still negligibly small.

3.2.3 Determination of E_x

As we saw in Section 3.1.1, E_x may be computed by simply adding the two α-particle energies provided one corrects for the ^{8}Be recoil energy, E_R. The α-particle momenta offer an alternative way to determine E_x. Subtracting the two α-particle laboratory momenta we obtain

$$\begin{aligned}\boldsymbol{p}_{1-2} &\equiv \boldsymbol{p}_{\alpha_1} - \boldsymbol{p}_{\alpha_2}\\ &= m_\alpha(\boldsymbol{u}_{\alpha_1} - \boldsymbol{u}_{\alpha_2})\\ &= m_\alpha(\boldsymbol{v}_{\alpha_1} - \boldsymbol{v}_{\alpha_2})\\ &= 2m_\alpha\boldsymbol{v}_{\alpha_1}\end{aligned}$$

and consequently,

$$\frac{p_{1-2}^2}{4m_\alpha} = m_\alpha v_{\alpha_1}^2 = 2E_\alpha^* = E_x + 92\ \mathrm{keV} \tag{3.6}$$

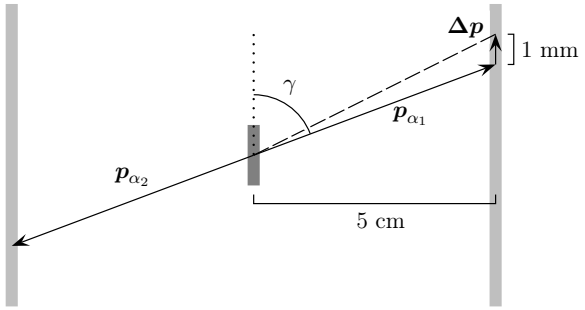

Figure 3.5: Illustration of the effect of a 1 mm error in the assumed placement of the detectors on the deduced α-particle momentum.

The obvious advantage of using this formula rather than Eq. 3.2 to determine E_x, is that it is exact. No need to correct for the systematic and energy-dependent shift caused by the recoil energy term. The disadvantage of using this formula is that it introduces additional experimental uncertainties in the determination of E_x as it relies not only on the energies but also the directions of the α particles. As argued in Section 2.3.1, the placement of the detectors relative to the activity implanted in the foil is known to an accuracy of ±1 mm. This, at least, is true for the coordinates in the plane perpendicular to the axis joining the center of detector and the foil. Let us estimate the effect of a 1 mm error on E_x determined through Eq. 3.6. Given an error $\boldsymbol{\Delta p}$ in the determination of the momentum of α_1 , we have

$$\begin{aligned} \Delta p_{1-2}^2 &= (\boldsymbol{p}_{1-2} + \boldsymbol{\Delta p})^2 - p_{1-2}^2 \\ &= 2\,\boldsymbol{p}_{1-2} \cdot \boldsymbol{\Delta p} + \Delta p^2 \\ &= 2\,p_{1-2}\,\Delta p \cos\gamma + \Delta p^2 \,, \end{aligned} \tag{3.7}$$

where γ is the angle between $\boldsymbol{p}_{1-2}$ and $\boldsymbol{\Delta p}$ as shown in Fig. 3.5. The magnitude of the error $\boldsymbol{\Delta p}$ is approximately given by

$$\Delta p \approx \frac{1\text{ mm}}{5\text{ cm}/|\sin\gamma|}\, p_{\alpha_1} \approx 1 \times 10^{-2}\,|\sin\gamma|\, p_{1-2}\,. \tag{3.8}$$

Combining Eq. 3.7 and 3.8, we obtain

$$\frac{\Delta p_{1-2}^2}{p_{1-2}^2} \approx 2 \times 10^{-2} \cos\gamma\,|\sin\gamma| + 1 \times 10^{-4} \sin^2\gamma\,.$$

When averaged over angles of incidence, the first term vanishes because of the $\cos\gamma$ factor. We conclude that a 1 mm error in the assumed geometry causes a systematic error of only 10^{-4} in the determination of E_x. At 3 MeV this is equivalent to 0.3 keV.

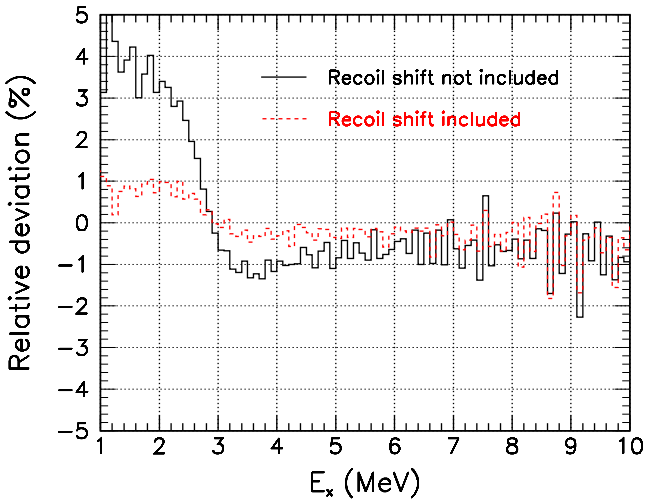

Figure 3.6: Comparison of the E_x spectrum obtained using Eq. 3.6 to the E_x spectra obtained using Eq. 3.2 with and without the recoil-energy term, E_R, included (based on coincidence data from DSSSD 2+3).

A similar analysis may be performed assuming that an error of 5 mm on the distance from the detector to the foil. The resulting systematic error in the determination of E_x is 8 keV. As will be shown below, this is an overestimate of the actual error.

Let Φ_E denote the E_x spectrum obtained from Eq. 3.2 neglecting the recoil energy, E_R. Denote the same spectrum Φ_{ER} when including the recoil. Finally, let Φ_p denote the E_x spectrum obtained from Eq. 3.6. We compare the spectra by calculating:

$$\delta_{p-E} = \frac{\Phi_p - \Phi_E}{\frac{1}{2}(\Phi_p + \Phi_E)} , \quad \delta_{p-ER} = \frac{\Phi_p - \Phi_{ER}}{\frac{1}{2}(\Phi_p + \Phi_{ER})} .$$

These are shown in Fig. 3.6. The relative deviation, $\delta = \frac{\Delta\Phi}{\Phi}$, may be translated into an energy shift, ΔE, using

$$\Delta E \approx \frac{\Delta\Phi}{\Phi}\left(\frac{1}{\Phi}\frac{d\Phi}{dE}\right)^{-1} .$$

At $E_x = 2.4$ MeV, the rate of change of the E_x spectrum is $\frac{1}{\Phi}\frac{d\Phi}{dE} \approx 0.20\%$ per keV and the relative deviations observed in Fig. 3.6 are $\delta_{p-E} = 2.5\%$ and $\delta_{p-ER} = 0.6\%$. It follows that the spectra are shifted by 12 and 3 keV, respectively. We note that the 3 keV discrepancy is consistent with our previous estimates of the systematic error introduced by the uncertainties in the geometry of the detector setup.

In the following analysis, we shall be using Φ_{ER}, i.e. the E_x spectrum obtained from Eq. 3.2 including the recoil energy, unless otherwise stated.

3.2.4 Coincidence Detection Efficiency

In an ideal world, the α-α coincidence detection efficiency would be 100%. In other words, every time an α particle is detected in one detector, its partner α particle is detected in the opposite detector. In the real world things are, as always, more complicated.

First, the detectors are not perfectly aligned, neither with respect to each other, nor with respect to the carbon foil. Second, even if the detectors *were* perfectly aligned, the finite size of the implantation spot would still cause some α particles to miss the opposite detector. Third, as discussed in Section 2.3.8, there is a weakly energy-dependent 3% probability for charge sharing to occur. Such hits are discarded in the analysis (though they can, to a large extent, be recovered if desired). Fourth, the differing trigger/ADC thresholds of the detectors may render a low-energy α particle invisible to one detector even though its partner α particle of nearly equal energy is visible to the opposite detector. These were the experimental effects.

Two physical effects may also be identified. The most important one is the angular shift $\Delta\theta$ caused by the recoil motion of the ^{8}Be nucleus. As can be seen from Eq. 3.5, the shift increases with decreasing E_x, its maximal value exceeding 8 degrees below 3 MeV. Another, less important, effect is the angular straggling that occurs in the carbon foil. At the energies and thicknesses relevant to the present study, the angular spread σ_θ is approximately given by the empirical relation,

$$\sigma_\theta \approx 0.52^\circ \left(\frac{E}{1\ \mathrm{MeV}}\right)^{-1.12} \left(\frac{x}{100\ \mathrm{nm}}\right)^{0.462},$$

where E is the α-particle energy and x is the distance traveled in carbon. This relation was deduced from TRIM simulations.

The combined effect of all these "errors" is seen in Fig. 3.7 which displays the ratio of the coincidence spectrum to the singles spectrum measured in DSSSD 4. The curve labeled 14×14 is obtained by requiring that the α particle seen by DSSSD 4 is within the central 14×14 pixels, the curve labeled 12×12 by requiring that it is within the central 12×12 pixels etc. The ratio of coincidences to singles is seen to drop with decreasing energy. This is a consequence of the increasing recoil shift $\Delta\theta$. The more central we require the hit in DSSSD 4 to be, the more unlikely it is for the partner α particle to miss DSSSD 1. The drop in the ratio of coincidences to singles is correspondingly less marked. For the two most central cuts, 6×6 and 4×4, the drop is essentially absent. The sharp drop around 0.6 MeV that occurs in all spectra is due to the presence of a low-energy background component in the singles spectrum (see Section 2.3.9). Though unaffected by the recoil shift $\Delta\theta$, the 4×4 and 6×6 coincidence-to-singles ratio still exhibits a weak energy dependence. This is understood as resulting from an energy dependence in the single-particle detection efficiency (see Section 2.3.9).

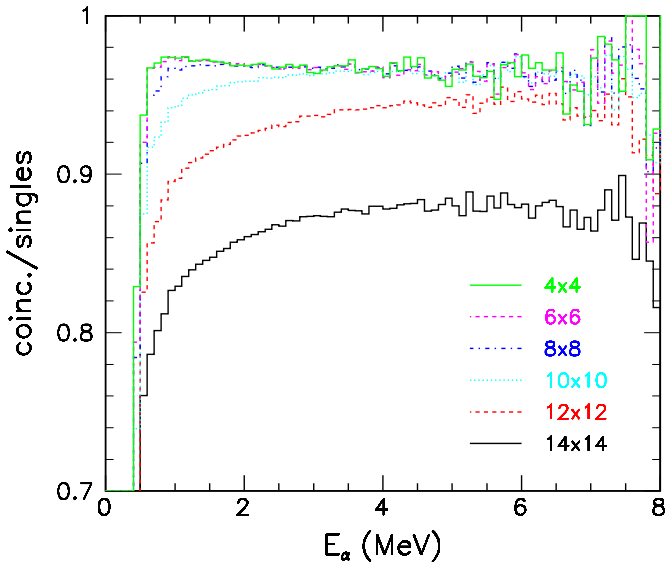

Figure 3.7: Ratio of the coincidence spectrum to the singles spectrum measured in DSSSD 4. The curve labeled 14×14 is obtained by requiring that the α particle seen by DSSSD 4 is within the central 14×14 pixels, the curve labeled 12×12 by requiring that it is within the central 12×12 pixels etc. .

3.2.4.1 Monte Carlo Simulation

A Monte Carlo simulation was performed in order to quantify the effect of the various "errors" discussed in the previous section on the E_x spectrum deduced from the coincidence data. Below, the structure of the simulation program is described.

For a fixed value of E_x, one simulates a large number of ^{8}B decays, say one million, following the method given in Section 3.1.4. The quantities of interest are the α-particle momenta in the laboratory frame, $\boldsymbol{p}_{\alpha_i}$, and the amplitude of the event, w, calculated from Eq. 3.4. From this primary sample, one generates a *realistic* sample with $\sim 10^5$ events by applying the Von Neumann sampling technique (see Section 3.1.4). Next, one chooses a pixel (n, i, j) in one of the detectors identified by detector number n, front strip number i and back strip number j. Assuming that α_1 is detected in this particular pixel, one leafs through the realistic sample, counting the number of times α_2 is detected in the opposite detector. This involves sampling the implantation site (assuming a uniform circular distribution of diameter 1.0 cm) and sampling the angular straggling caused by the passage through the foil. In addition, the energy loss in the foil and the detector dead layer is calculated before checking that the α-particle energy is above detection threshold. The energy-dependence of the single-particle

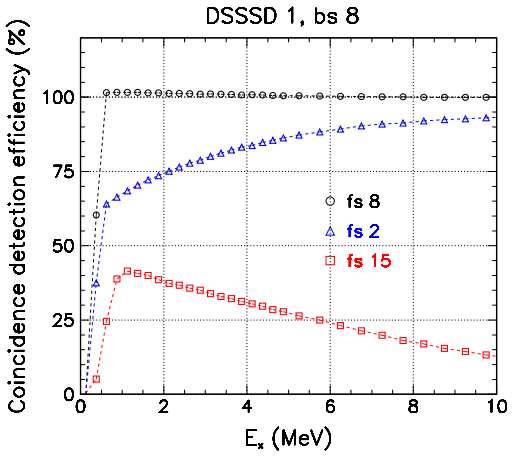

Figure 3.8: Coincidence detection efficiency as a function of ^{8}Be excitation energy in three selected pixels of DSSSD 1 (back strip 8, front strips 2, 8 and 15).

detection efficiency is taken into account twice, both in the detection of α_1 and in the detection of α_2. Finally, the coincidence detection efficiency of the chosen pixel is computed as

$$\varepsilon_{n,i,j}(E_x) = \frac{\text{Number of times both } \alpha_1 \text{ and } \alpha_2 \text{ are detected}}{\text{Size of realistic sample}} .$$

This step is repeated for each pixel (neglecting the edge strips there are $4 \times 14 \times 14 = 784$ pixels in total) for selected values of E_x covering the range of interest. Fig. 3.8 shows $\varepsilon_{n,i,j}(E_x)$ for three selected pixels of DSSSD 1. For pixel $(8, 8)$, the recoil shift, $\Delta\theta$, never becomes large enough for the partner α particle to miss the opposite detector. Consequently, the efficiency is constant. For pixel $(2, 8)$, the efficiency drops with decreasing E_x as the angular shift becomes larger causing more α particles to miss the opposite detector. For pixel $(15, 8)$, the opposite trend is observed. This is due to the detectors not being perfectly aligned. In the absence of any angular shift (large E_x) most α particles miss the opposite detector. With increasing angular shift (small E_x) more α particles have their trajectories bent enough to hit the opposite detector. Below 0.6 MeV, the efficiency drops rapidly due to the trigger/ADC thresholds.

Fig. 3.9 (a) and (b) provide a good check of the simulation. They compare experimental and simulated distributions of relative α-α angles for two different values of E_x. The theoretical distributions which serves as input for the simulations, are also shown. To eliminate bias introduced by preferential selection of events with small recoil shifts $\Delta\theta$, only coincidence events with an α particle detected within the central

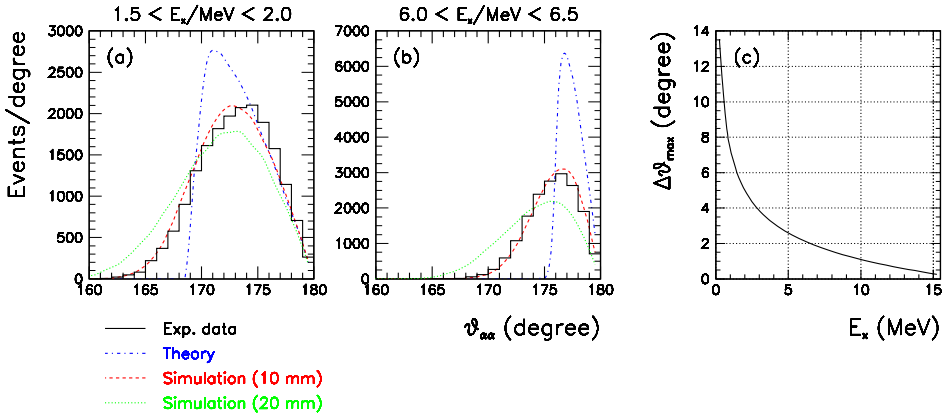

Figure 3.9: (a) and **(b)** Distribution of relative α-α angles at two different values of E_x obtained from coincidence data in DSSSD 1 + 4 selecting only events with an α particle detected within the central 6×6 pixels of DSSSD 4. Simulated distributions were obtained by feeding the output of the simulation program to the same analysis program as used for the experimental data. The lengths in the parentheses refer to the assumed diameter of the implantation area. **(c)** Maximal recoil shift $\Delta\theta_{\max}$ as a function of E_x.

6×6 pixels were selected for the analysis. The simulated distributions were obtained by feeding the output of the simulation program into the same analysis program as used for the experimental data. The simulations were performed with E_x fixed to 1.75 and 6.25 MeV. For the experimental data, 500 keV windows were used.

Simulations were performed for different choices of the diameter of the implantation spot. A uniform circular distribution was assumed in all cases. The best fit to the experimental data was obtained with a diameter of 10 mm in reasonable agreement with the diameter of the visible beam spot, see the photos in Fig. 2.16, which was measured to 7 mm. A Gaussian distribution might seem a more realistic choice. The assumption of a uniform distribution is, however, justified if the ^{8}B beam from the mass separator is badly collimated with a diameter significantly larger than the 5 mm collimator placed at the entrance to the experimental chamber. If this is the case, the effect of the collimator will be to cut off the Gaussian flanks of the beam leaving an essentially uniform distribution.

At $E_x = 6.25$ MeV, the extent of the distribution is almost entirely determined by the experimental resolution. The theoretical distribution is seen to be very narrow. At $E_x = 1.25$ MeV, the roles are reversed with the recoil shift being most important. The simulated distribution is shifted by 1–2 degrees relative to the experimental distribution. This is presumably a binning effect but could also be related to the neglect of the kinematic terms in the derivation of Eq. 3.4.

3.2.4.2 Efficiency-Corrected Spectra

An overall efficiency correction of the E_x spectra is obtained by assigning weight factors $1/\varepsilon_{n,i,j}(E_x)$ to the individual coincidence events. The magnitude of the correction applied to the E_x spectrum obtained from coincidence data in DSSSD 1 + 4, with the requirement that the α particle seen by DSSSD 4 is detected within the central $k \times k$ pixels, is shown in Fig. 3.10 (a), in percent of the uncorrected spectrum. The effects of trigger/ADC thresholds have not been included. They only modify the excitation energy spectrum below 1 MeV. The large fluctuations in the correction applied to the 14×14 E_x spectrum originate from the large weight factors assigned to the edge strips which have rather little statistics.

Fig. 3.10 (b) shows the ratio of the 14×14 E_x spectrum to the 6×6 E_x spectrum before and after the efficiency correction. The agreement between the two spectra is seen to improve when the efficiency correction is applied. Significant discrepancies remain, in particular in the high-energy end of the spectrum. We attribute these to errors in the assumed geometry of the detector setup. The large correlated fluctuations arise because we compare overlapping data sets (the 6×6 data set is a subset of the 14×14 data set).

In the further analysis, we will be using the 6×6 E_x spectrum up to 10 MeV. Above 10 MeV, we will be using the 10×10 E_x spectrum to gain more statistics.

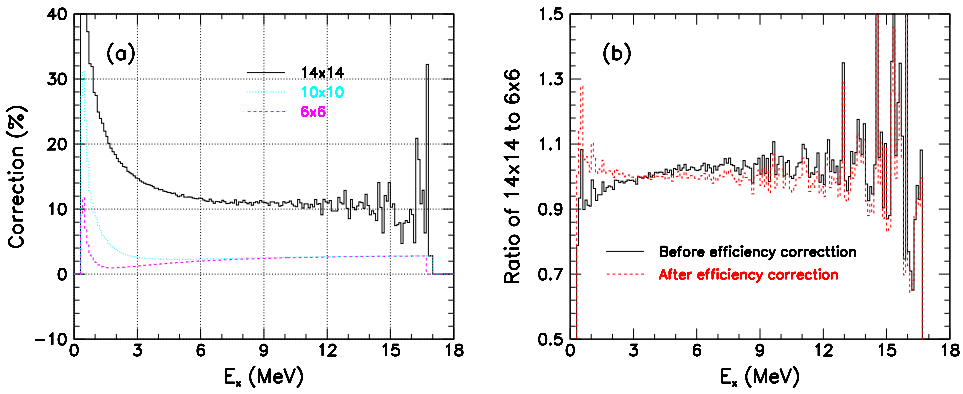

Figure 3.10: (a) Efficiency correction applied to the E_x spectrum obtained from coincidence data in DSSSD 1 + 4, with the requirement that the α particle seen in DSSSD 4 is detected within the central $k \times k$ pixels, in percent of the uncorrected spectrum. **(b)** Ratio of 14×14 E_x spectrum to the 6×6 E_x spectrum before and after the efficiency correction.

3.2.5 Comparison to Single-α Spectrum

Below, we will use the E_x distribution, $f(E_x)$, deduced from the R-matrix fit described in Section 4.1, to derive the single-α energy distribution that we would expect to measure. This will then, as a check of self-consistency, be compared to the one actually measured.

The single-α energy distribution, $g(E_\alpha)$, is obtained by folding the E_x distribution, $f(E_x)$, with the recoil broadening distribution $\rho(x)$ of Eq. 3.3:

$$g(E_\alpha) = \int f(E_x)\, \rho(x)\, \mathrm{d}E_x ,$$

where x depends on both E_α and E_x:

$$x = \frac{E_\alpha - \frac{1}{2}\left[E_x + 92\ \mathrm{keV} + E_\mathrm{R}(E_x)\right]}{T_\mathrm{max}(E_x)} .$$

To obtain the energy distribution, $h(E'_\alpha)$, measured in the detector, we fold the single-α energy distribution, $g(E_\alpha)$, with the response function, $\Psi(E_\alpha, E'_\alpha)$, given by Eq. 2.5:

$$h(E'_\alpha) = \int g(E_\alpha)\, \Psi(E_\alpha, E'_\alpha)\, \mathrm{d}E_\alpha ,$$

taking into account[3] the additional spread in α-particle energy caused by variations in the foil implantation depth (about 10 keV at $E_\alpha = 1.5$ MeV). Finally, we correct for the weakly energy-dependent single-particle detection efficiency. We normalize the distribution obtained to the measured singles spectrum and compute the standardized residuals. These are shown for DSSSD 1 and 4 in Fig. 3.11. Above ≈ 1.6 MeV the residuals look very nice. Between 1 and ≈ 1.6 MeV systematic deviations are present. They can, however, be explained by a mismatch in the energy scales of the reconstructed and measured singles spectra of only 1–2 keV. The downward trend, starting around 1 MeV in DSSSD 1 and around 0.6 MeV in DSSSD 4, is due to the presence of a low-energy background component in the measured singles spectrum (see Section 2.3.9).

[3] Its influence on the calculated distribution is found to be negligible.

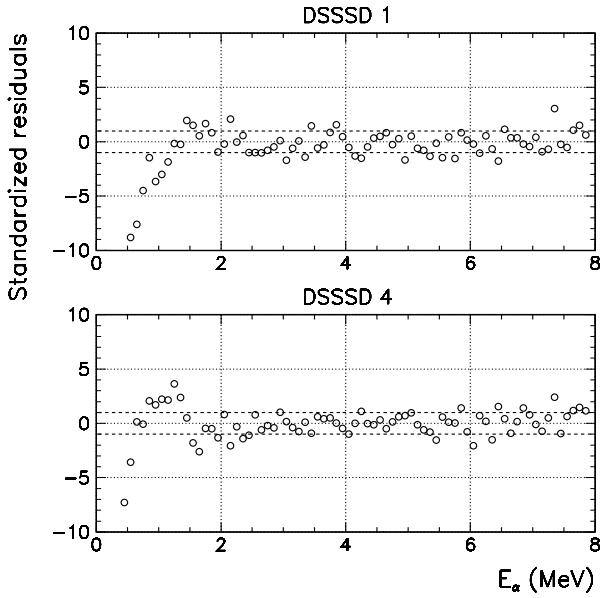

Figure 3.11: Standardized residuals from the comparison of the reconstructed singles spectrum to the measured singles spectrum.

3.2.6 Uncertainty on E_x

Four sources of systematic uncertainty in the determination of E_x may readily be identified:

(i) Uncertainties in the tabulated energies of the α groups of ^{20}Na used for the energy calibration.

(ii) Uncertainties in the energy-loss calculations.

(iii) The drift in electronic gain and growth in foil and dead layer thickness during the experiment.

(iv) Uncertainties in the determination of the E_x response function.

We examine items (i)–(iv) one at the time:

(i) The uncertainties on the tabulated energies of the 2 153 and 4 434 keV β-delayed α groups of ^{20}Na are 1.0 and 1.5 keV, respectively, deduced from the uncertainties on the excitation energies[4] of the corresponding levels in ^{20}Ne. This gives a systematic uncertainty of 1.7 keV on the single-α energy in the peak region. The error is, of

[4]The uncertainty on the α + ^{16}O threshold energy in ^{20}Ne is only 10 eV.

course, the same in all four detectors. Therefore, the contribution to the overall E_x uncertainty is twice as big, i.e. 3.4 keV.

(ii) The systematic uncertainties associated with the energy-loss corrections are greatly reduced by the use of ^{20}Na, implanted in the same foil as ^{8}B, for the energy calibration. In Section 2.3.4 and 2.3.5, the uncertainties on the implantation depth and the foil thickness were estimated to 1 and 8 nm, respectively. One can show that this gives an uncertainty of only 0.3 keV on the single-α energy in the peak region. The uncertainty on the dead layer thickness was discussed in Section 2.3.6. Assuming a certain thickness in one DSSSD, the proton lines of ^{23}Al fix the the dead layer thickness in the other three DSSSDs to within ±7 nm. The uncertainty on the overall scale was estimated to 15 nm. One can show that this gives an uncertainty of 0.4 keV on the single-α energy in the peak region. The combined contribution of foil and dead layer to the overall E_x uncertainty is calculated to 0.9 keV.

(iii) The drift in electronic gain and the growth in foil and dead layer thickness have been taken into account in the analysis of the data by assuming that the changes occur linearly in time. The success of this correction can be seen in Fig. 3.12 (a) which shows the evolution in the maximum of the E_x spectrum during the experiment. The 72 hour long measurement has been divided into 8 bins of approximately 9 hours duration each. To find the energy at which the E_x spectrum attains its maximum value, the spectrum has been fitted between 2 and 4 MeV with a function of the form

$$f(E_x) = \left[\frac{\Gamma}{2\pi} \frac{1}{(E_x - E_0)^2 + \left(\frac{\Gamma}{2}\right)^2} \right] \times A \, [1 + k(E - E_0)] \ ,$$

which attains its maximum value at

$$E_{\max} = E_0 - \tfrac{1}{k} + \left[\tfrac{1}{k^2} + \left(\tfrac{\Gamma}{2}\right)^2 \right]^{1/2} \approx E_0 + \tfrac{1}{2} k \left(\tfrac{\Gamma}{2}\right)^2 - \tfrac{1}{8} k^3 \left(\tfrac{\Gamma}{2}\right)^4$$

Fig. 3.12 (b) and (c) demonstrate the quality of the fit in one selected time bin. After the correction, the maximum of the E_x spectrum is practically constant with time except for the slight upward trend at the beginning of the experiment. Based on Fig. 3.12 (a), the contribution to the overall E_x uncertainty from the drift in electronic gain and the growth in foil and dead layer thickness is estimated to 5 keV.

(iv) The E_x response function (Eq. 2.6) causes the maximum of the E_x spectrum to be shifted 15 keV down in energy relative to the true maximum; the exponential tails give a shift of 6 keV, the satellite peak a shift of 9 keV. By varying the parameters entering Eq. 2.6 within their estimated uncertainties, we find that the contribution to the overall E_x uncertainty is at most 2 keV.

The sources of systematic uncertainty on E_x and their 1σ magnitude in the peak region are summarized in Table 3.1. For a general excitation energy, E_x , the uncertainty

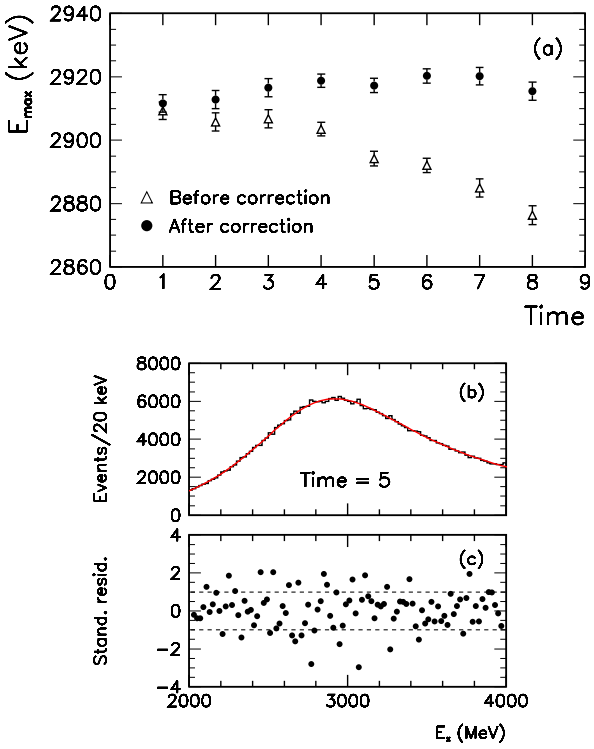

Figure 3.12: Variations in the maximum of the E_x spectrum with time (not corrected for the recoil energy, E_R). **(a)** Maximum as function of time before and after the correction for drift in electronic gain and growth in foil and dead layer thickness. **(b)** E_x spectrum between 2 and 4 MeV for one selected time bin with the fit superimposed. **(c)** Standardized residuals from the fit.

Table 3.1: Sources of systematic uncertainty on E_x and their 1σ magnitude in the peak region. The combined uncertainty is obtained by adding the individual uncertainties in quadrature.

	Source	Magnitude (keV)
(i)	Uncertainties in the tabulated energies of ^{20}Na α groups used for the energy calibration	3.4
(ii)	Uncertainties in the energy-loss correction	0.9
(iii)	Drift in electronic gain and growth in foil and dead layer thickness during the experiment	5
(iv)	Uncertainties in the determination of the E_x response function	2
	Combined uncertainty	6

due to (i) is $(5.5-3.5E_x+0.61E_x^2)^{1/2}$ keV with E_x in MeV. The combined uncertainty due to (ii)–(iv), which we assume to be independent of E_x, is $(0.9^2 + 5^2 + 2^2)^{1/2} = 5.5$ keV. Adding the two in quadrature, we obtain

$$\sigma_{\text{syst.}} = (\,35.3 - 3.5E_x + 0.61E_x^2\,)^{1/2}\ \text{keV}\ , \tag{3.9}$$

as our most conservative estimate of the systematic uncertainty on E_x.

3.2.7 Summary

The correction applied to the E_x spectrum to account for the E_x dependence of the α-α coincidence detection efficiency, has been discussed at length. The correction is largest for small values of E_x where the recoil effects are strongest.

Due to uncertainties in the geometry, we are unable to perform an accurate efficiency correction of the 14×14 E_x spectrum. The 6×6 E_x spectrum, only subject to geometry-dependent corrections below 1.5 MeV, has been selected for the further analysis. Above 10 MeV, the 10×10 E_x spectrum, only subject to geometry-dependent corrections below 7 MeV, is used to gain more statistics. We were able to check the internal consistency of the coincidence and singles spectra down to 1.6 MeV and found good agreement. Below 1 MeV, the E_x spectrum is affected by detection thresholds. Four E_x spectra have been extracted from the data:

I. Coincidence events in DSSSD 1 and 4 with an α particle detected within the central 6×6 (10×10 above 10 MeV) pixels in DSSSD 1.

II. Coincidence events in DSSSD 1 and 4 with an α particle detected within the central 6×6 (10×10 above 10 MeV) pixels in DSSSD 4.

III. Coincidence events in DSSSD 2 and 3 with an α particle detected within the central 6×6 (10×10 above 10 MeV) pixels in DSSSD 2.

IV. Coincidence events in DSSSD 2 and 3 with an α particle detected within the central 6×6 (10×10 above 10 MeV) pixels in DSSSD 3.

The uncertainty on Spectrum III is larger than the other three due to an additional uncertainty associated with the detection efficiency correction[5], and hence this spectrum is discarded. The uncertainty on Spectrum IV is also somewhat larger than the uncertainty on I and II due to some atypical and not fully understood features of the response of DSSSD 3. Therefore, I and II are the preferred spectra. Since their data content overlaps, only one may be selected for further analysis. We randomly chose spectrum II. Spectra I and IV are then used for checks of consistency. Impressively, the maxima of I, II and IV agree to within ±2 keV. Spectrum II is shown in Fig. 4.1

Finally, the systematic uncertainty on E_x in the peak region was estimated to 6 keV.

[5]The additional uncertainty is due to the presence of a dead strip in DSSSD 3

CHAPTER 4

Results and Discussion

Finally, we are able to reap the rewards of our labor. In the present chapter, we unfold the E_x distribution from the E_x spectrum. We compare this distribution to the E_x distributions obtained in previous studies and suggest reasons for the small discrepancies observed. We estimate the effect of these discrepancies on the neutrino spectrum and comment on the implications for the solar neutrino measurements. The neutrino spectrum is calculated making some simplifying assumptions. The complete calculation, following the prescription of Winter *et al.*, remains to be done. In addition, certain systematic effects in the *R*-matrix parametrization of the E_x distribution below 1 MeV remain to be explored. Finally, we present a couple of additional results not related to the determination of the neutrino spectrum.

4.1 *R*-Matrix Description

A parametrization of the E_x distribution is not essential for the purpose of calculating the ^{8}B neutrino spectrum. In practice, however, it is advantageous to calculate the neutrino spectrum from a parametrization rather than from the measured spectrum because it facilitates the propagation of systematic uncertainties. Furthermore, a physically meaningful parametrization allows for a reliable extrapolation to the lowest energies (0–1 MeV) where the measured spectrum is affected by the detection thresholds. Finally, the effects of the detector response may easily be taken into account by folding in the E_x response function (Eq. 2.6).

We adopt a parametrization similar to one used in the previous studies of Winter *el al.* [Win06] and Bhattacharya *et al.* [Bha06] derived from *R*-matrix theory, cf. Section 7.6. The decay is assumed to proceed by allowed transitions to the three known, energetically accessible, 2^+ states in ^{8}Be: The first excited state at 3 MeV and the strongly isospin-mixed doublet around 16 MeV. A satisfactory description of the E_x distribution is, however, only achieved with the inclusion of a fourth, very broad, 2^+ state lying above the β-decay window, but affecting the E_x distribution via its low-energy tail. Our parametrization gives an improved treatment of the 16 MeV doublet compared to that of Winter *el al.* and Bhattacharya *et al.* which is slightly flawed. A detailed account of the parametrization is given in the thesis of S. Hylde-

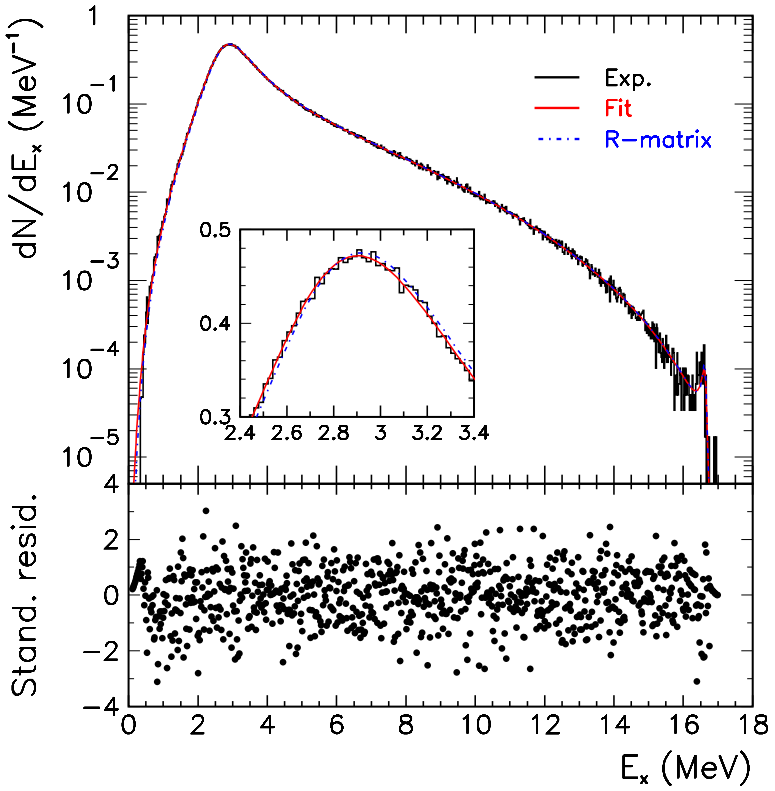

Figure 4.1: E_x Spectrum with the fit (E_x distribution folded with response function, red solid curve) and the E_x distribution (blue dash-dotted curve) superimposed. The inset shows a close-up of the peak region. The 15 keV shift due to the response function is hardly visible. The standardized residuals are shown in the bottom figure.

gaard [Hyl10a] and will not be repeated here. The R-matrix description of the E_x distribution constitutes in itself an interesting problem. The nature of the fourth, higher-lying and very broad, 2^+ state is of particular interest. Is this a genuine state or an artifact of the R-matrix formalism? See the discussion in [Hyl10a].

The E_x spectrum obtained in the present study is shown in Fig. 4.1. The R-matrix function folded with the E_x response function, has been fitted to the spectrum above 1.5 MeV giving an excellent description of the data with χ^2/d.o.f = 0.97. The fit is shown by the red solid curve. The E_x distribution obtained from the fit is shown by the blue dash-dotted curve. The 15 keV shift between the two curves is hardly visible

Relative 1σ statistical and systematic uncertainties on the E_x distribution are shown in Fig. 4.2. The statistical uncertainties were obtained by standard error propagation [Ams08] of the covariance matrix of the fit parameters. To determine the effect of the systematic uncertainty on E_x (Eq. 3.9) on the E_x distribution obtained from the fit, $f(E_x)$, we evaluate $f(E_x)$ at energies $E_x \pm \sigma_{\text{syst.}}$, compute the differences $| f(E_x \pm \sigma_{\text{syst.}}) - f(E_x) |$ and adopt the larger of the two differences as our estimate of the 1σ systematic uncertainty. As pointed out by Winter *et al.*, the choice of channel radius in the R-matrix model represents a source of systematic uncertainty outside the fit region, the effect of which may be estimated by varying the channel radius within realistic limits. Winter *et al.* found that the choice of channel radius is a significant source of uncertainty only for neutrinos at very high ($E_\nu > 15$ MeV) and low ($E_\nu < 0.5$ MeV) energies. The invocation of a fourth, very broad, 2^+ state lying outside the β-decay window, to reproduce the decay strength not accounted for by the three known 2^+ states, represents an additional source of uncertainty not recognized by Winter *et al*. Other models in which the fourth 2^+ state is assumed to reside inside the β-decay window, give equally good fits to the data. To quantify the uncertainty associated with the choice of R-matrix model, we intend to perform fits with a number of models, only differing in their assumptions regarding the whereabouts of the fourth 2^+ state. This analysis remains to be done.

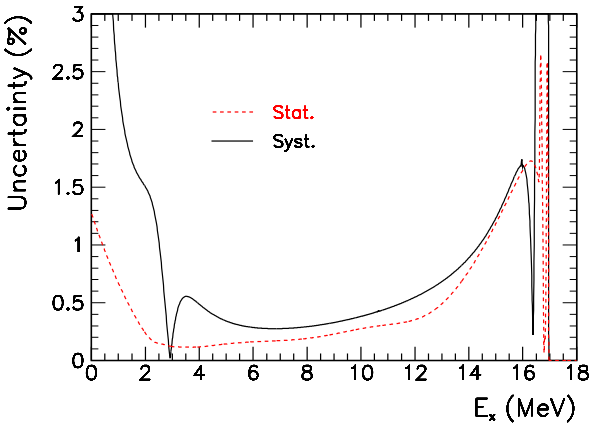

Figure 4.2: Relative 1σ statistical and systematic uncertainties on the E_x distribution in percent of the distribution value. The statistical uncertainties were obtained by standard error propagation of the covariance matrix of the fit parameters. The systematic uncertainties reflect the systematic uncertainties in the determination of E_x.

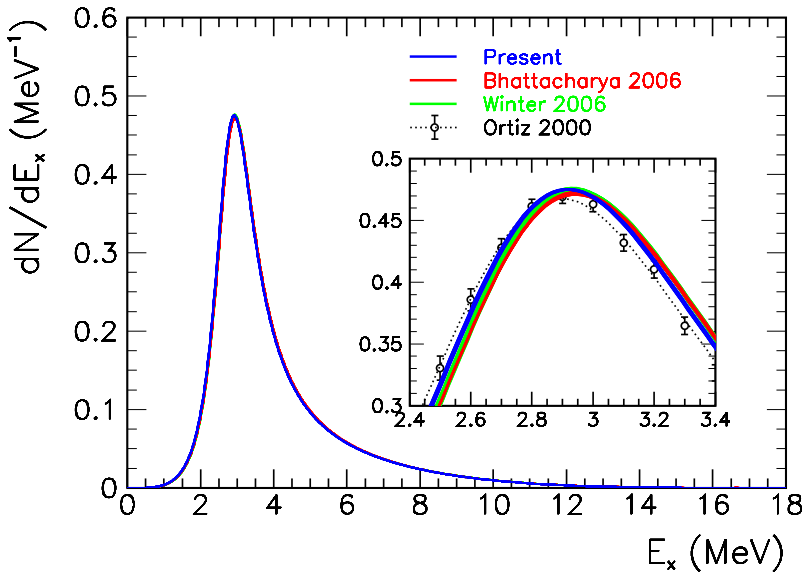

Figure 4.3: Comparison of the E_x distribution obtained in the present study to distributions obtained in previous studies. The distributions of Winter *el al.* and Bhattacharya *et al.* are available online, see references in [Win06] and [Bha06]. The two distributions practically lie on top of each other. The widths of the distributions indicate 1σ uncertainties. The two systematic uncertainties given by Bhattacharya *et al.* were added in quadrature as recommended. The data points show the experimental spectrum of Ortiz *et al.* obtained by private communication with A. Garcia (2010). The error bars represent systematic and statistical uncertainties added in quadrature. The dashed line going through the data points is merely meant to guide the eye. All four distributions have been normalized to unit area.

4.2 Comparison to Past Measurements

In Fig. 4.3, we compare the E_x distribution obtained in the present study to the distributions obtained in the previous studies of Winter *el al.*, Bhattacharya *et al.* and Ortiz *et al.* All distributions have been normalized to unit area. The width of the curves indicate 1σ uncertainties. The statistical and systematical uncertainties on our distributions have been added in quadrature. The maximum of our distribution lies between the maximum of the distribution of Ortiz *et al.* and the maxima of the distributions of Winter *el al.* and Bhattacharya *et al.* which are very close. The precise location of the maxima are given in Table 4.1.

Relative deviations of the distributions of Winter *el al.* and Bhattacharya *et al.* compared to our data, are shown in Fig. 4.4. The gray band indicates the 1σ uncertainty on our distribution obtained by adding statistical and systematic uncertainties

Table 4.1: Spectral maxima of the ^{8}Be excitation energy distribution obtained in the present and previous three studies.

Study	Spectral maximum (keV)	Deviation from present study (keV)	Error on energy scale at maximum (keV)
Ortiz 2000	2899	−19	12
Winter 2006	2943	25	9
Bhattacharya 2006	2939	21	5
Present	2918	0	6

in quadrature. For clarity, the uncertainties on the distributions of Winter *el al.* and Bhattacharya *et al.*, which are comparable to our uncertainties, are not shown. When shifted down in energy by 21 keV, the distribution of Bhattacharya *et al.* is seen to be in reasonable agreement with ours. The dip in relative deviation around 3 MeV shows that their peak is slightly wider than ours, suggesting that experimental broadening effects have not been completely accounted for in their analysis[1]. The curves labeled "DSSSD 1" and "DSSSD 3" show the deviations of *R*-matrix fits of spectra I and IV when compared to the *R*-matrix fit of spectrum II. Within errors, the fits are seen to be consistent.

Starting with Ortiz *et al.*, we are unable to point to a specific reason why their peak energy is 19 keV below ours. We may note, however, that since they, like us, measured individual α energies, an error of 10 keV in the energy calibration is enough to explain the discrepancy. Recently, it was reported [Ade10] that Ortiz *et al.* have recognized that they underestimated the uncertainties related to the energy loss generated by the carbon buildup in their catcher foil, so that a claim of a disagreement with the measurements of Winter *et al.* and Bhattacharya *et al.* no longer should be made. Considering that the largest energy-loss correction made by Ortiz *et al.* was 25 keV (at $E_\alpha = 0.5$ MeV), it seems unlikely that they should have underestimated the energy loss by as much as 20–25 keV (the amount needed to bring their result in agreement with that of Winter *et al.* and Bhattacharya *et al.*)

As for Winter *et al.*, we have identified one possible source of error in their energy calibration which relies on the measurement of the linearly added signals from the ^{20}Na decay products, i.e. α+^{16}O. Essentially, we suspect that they fail to account correctly for the differing response of their Si detector to α particles and ^{16}O ions. Based on our study of the differing response of Si detectors to α particles and ^{16}O ions, as

[1] Alternatively, they may have underestimated the recoil broadening. See the discussion related to Fig. 3.2.

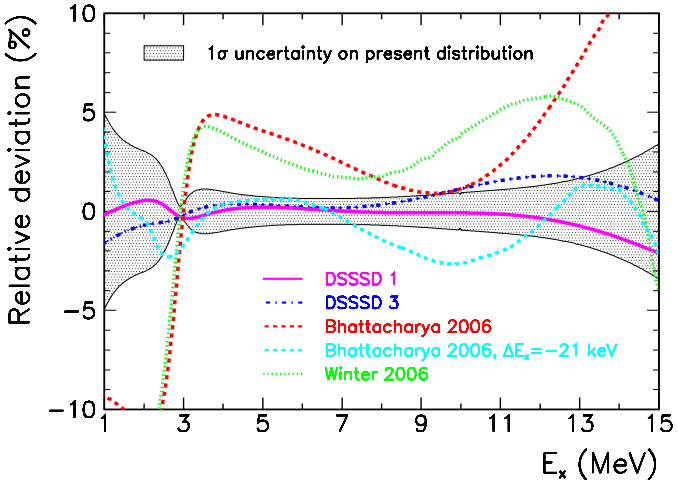

Figure 4.4: Relative deviations of the excitation energy distributions of Winter *el al.* and Bhattacharya *et al.* compared to the present study. The gray band indicates the 1σ uncertainty on our distribution obtained by adding statistical and systematic uncertainties in quadrature. The distributions of Winter *el al.* and Bhattacharya *et al.* have uncertainties similar to ours. The incorrect treatment of the 16 MeV doublet by Winter *el al.* and Bhattacharya *et al.* gives large deviations above 15 MeV which are not shown. The curves labeled "DSSSD 1" and "DSSSD 3" show the deviations of *R*-matrix fits of spectra I and IV compared to the *R*-matrix fit of spectrum II.

well as the study of [Len86], we conclude that the energy calibration performed by Winter *et al.* overestimates the 2α-energy signal by 19 keV at 2.7 MeV (details are given in Section 6.3.3.1). This would seem to explain the 25 keV deviation. Winter *et al.* also used an external ^{228}Th α source for the energy calibration. They state that the α-particle energy loss in the source was taken into account, but it is unclear whether they correct for the different implantation depth of the α emitters in the decay chain of ^{228}Th. As we saw in Section 2.3.11, this effect may distort the energy calibration.

Finally, we suspect that an overestimation, on the part of Bhattacharya *et al.*, of the exponential tails associated with the detector response, may explain why their peak energy is 21 keV above ours. Bhattacharya *et al.* used a standard ^{148}Gd α source to determine their response function which was then folded into the *R*-matrix fit. The effect of the exponential tails is to shift the extracted E_x distribution up in energy. In the present study, we find that the response function determined from the α-source data has much stronger exponential tails than the response function determined from the ^{20}Na data, a difference that may be attributed to energy-loss effects in the α-source material (see Section 2.3.10). Similar effects may be present in the α-source measure-

ment of Bhattacharya *et al.*

4.3 Neutrino Spectrum

Given the E_x distribution obtained from the R-matrix fit, we wish to calculate the corresponding neutrino energy spectrum. The calculation is complicated by the presence of recoil order terms, affecting the neutrino spectrum at the level of 5–10% [Win06]. In addition, radiative corrections affect the neutrino spectrum at the level of 1%. A detailed and comprehensive account of the steps involved in the calculation is given in [Win06]. The uncertainties associated with the recoil order terms introduce uncertainties in the determination of the neutrino spectrum that are roughly half as large as the uncertainties originating from the uncertainties on the E_x distribution of Winter *et al*. Here we limit ourselves to a simpler calculation, the purpose being to estimate how the neutrino spectrum is modified by our—what we believe to be—improved determination of the E_x distribution. A complete calculation, following the prescription of Winter *et al.*, will be performed in the near future.

Neglecting recoil order terms and radiative corrections, the positron energy spectrum, for fixed excitation energy, E_x , is given by,

$$\frac{\mathrm{d}N}{\mathrm{d}E_\beta} \propto p_\beta E_\beta \left(E_0 - E_x - E_\beta\right)^2 F(-Z, E_\beta) \,, \tag{4.1}$$

where p_β and E_β are the positron momentum and total energy, $E_0 = 17.4688(10)$ MeV is the maximum total positron energy for decays to the ground state of ^{8}Be and $F(-Z, E_\beta)$ is the Fermi function which describes the modification of the β phase space by the Coulomb interaction between the positron and the daughter nucleus of charge Z. We evaluate $F(-Z, E_\beta)$ using the analytical expression given in [Bla52] which includes relativistic corrections but does not account for the screening of the nuclear Coulomb field by the atomic electrons. The positron spectrum is calculated by integrating Eq. 4.1 over all excitation energies, E_x , weighted by the E_x distribution. The neutrino spectrum is obtained by the simple substitution $E_\nu = E_0 - E_x - E_\beta$.

Following this simplified procedure, we calculate the neutrino spectrum corresponding to our E_x distribution as well as the neutrino spectrum corresponding to the E_x distribution of Winter *et al*. The neutrino spectrum resulting from our own distribution is shown in Fig. 4.5 (a). The relative deviation with respect to the spectrum of Winter *et al*. is shown in Fig. 4.5 (b). A significant deviation of several percent is seen at high neutrino energies with our spectrum at these energies being the most intense. The odd-looking wiggle around 0.5 MeV is due to the 16 MeV doublet. The larger intensity in our neutrino spectrum at high neutrino energies is a natural consequence of the fact that the maximum of our E_x distribution is shifted 25 keV down in energy compared to that of Winter *et al.*

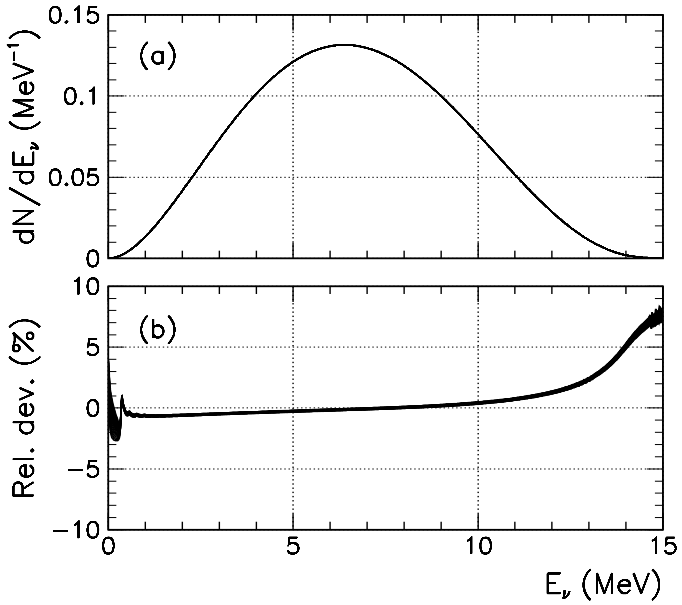

Figure 4.5: (a) Neutrino spectrum calculated from the E_x distribution obtained in the present study neglecting recoil order terms and radiative corrections. **(b)** Relative deviation with respect to the neutrino spectrum calculated from the E_x distribution of Winter *et al.* The width of the band indicates 1σ uncertainties calculated by adding the uncertainties on the two neutrino spectra in quadrature. Only statistical uncertainties were considered in the calculation of the uncertainties on our neutrino spectrum.

Leafing back to the introductory part, we find Fig. 1.4 which shows the current level of uncertainty on the solar neutrino spectrum. A quick reading gives a relative uncertainty of $\approx 10\%$. We therefore conclude that the deviations between us and Winter *et al.* are well below the precision of the existing solar neutrino data except at the very highest neutrino energies ($E_\nu > 13$ MeV) where the deviations may have some implication, in particular for the upper limit, up to now set on the *hep* neutrino signal [Jel09].

4.4 Additional Results

4.4.1 Electron Capture to the 16.922 MeV State

As illustrated in Fig. 4.6, five α-α coincidence events are seen from the decay of the 16.922 MeV state in ^{8}Be. In comparison, roughly 180 coincidence events are seen from the 16.626 MeV state. The ratio of 5/180 = 0.03 is inconsistent with the 10^{-5} ratio of the phase spaces available in the β decay to the two states, cf. Section 1.2.1.2. We therefore believe that the 16.922 MeV state has been populated in electron capture (EC). Notice that it would have been nice to confirm this through the non-detection of the positrons, but their energy is too low (< 36 keV). However, in the following argument on decay rates we show that the EC interpretation very likely is correct.

The matrix elements for β^+ decay and EC are the same. Thus, to get their relative rates, we only need to know the respective phase-space factors f_β and f_{EC}. The β-decay phase-space factor is easily obtained from the parametrization of Wilkinson and Macefield [Wil74]. The EC phase-space factor for capture from the innermost atomic shell may be calculated from the expression given in [Bla52] (allowed decay,

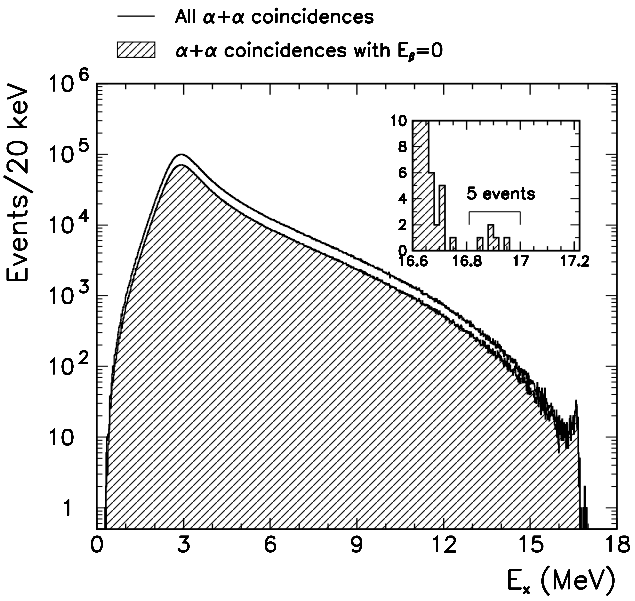

Figure 4.6: E_x Spectrum from all detected α-α coincidence events (10.6 million). The hatched spectrum corresponds to events with $E_\beta = 0$ in all four back detectors.

non-relativistic limit):

$$f_{\mathrm{EC}} \approx 2\pi\alpha^3 Z'^3 \, [\, W_0 + 1 - \tfrac{1}{2}\alpha^2 Z'^2 \,]^2 \, ,$$

with W_0 defined in Section 3.1.2, $\alpha \approx 1/137$ the electromagnetic fine-structure constant and $Z' = Z - 0.3$ where $Z = 5$ is the charge of ^{8}B and -0.3 corrects for the screening of the nuclear Coulomb field by the atomic electrons. For the 16.626 MeV state, we find that β decay dominates: $f_{\mathrm{EC}}(16.626)/f_\beta(16.626) = 0.040$. For the 16.922 MeV state, the roles are reversed: $f_{\mathrm{EC}}(16.922)/f_\beta(16.922) = 75$. For the ratio of the total decay rates $r_{\beta+\mathrm{EC}}$ to the two states, we find:

$$\frac{r_{\beta+\mathrm{EC}}(16.922)}{r_{\beta+\mathrm{EC}}(16.626)} = \frac{f_{\mathrm{EC}}(16.922) + f_\beta(16.922)}{f_{\mathrm{EC}}(16.626) + f_\beta(16.626)} = 2.4 \times 10^{-2} \, .$$

When multiplied with the 180 decays observed to the 16.626 MeV state, this gives 4.3, in very good agreement with the 5 observed decays to the 16.922 MeV state.

4.4.2 Search for the 337 keV Proton Branch

As discussed in Section 1.2.2, it is possible for ^{8}B to decay to p+^{7}Li by electron capture. This decay branch has not previously been observed. Its signature would be a sharp peak in the singles spectrum at 337 keV. The branching ratio is predicted to be on the order of a few times 10^{-8}.

During 72 hours, we observe 15.8×10^6 ^{8}B decays. Taking the 30% solid-angle coverage into account, the total number of ^{8}B decays that have occured is 53×10^6. Given the predicted branching ratio of a few times 10^{-8}, we only expect one or two proton decays to have occured. To look for these protons, we must reduce the intensities of α and β particles as much as possible. Since the decay to $p + {}^7$Li takes place by electron capture, no positrons will be present in coincidence with the protons. Therefore, positron events are removed by requiring zero energy in the back detectors. To reduce the α background, we require that only one particle is detected. We restrict our attention to the central 6×6 pixels of DSSSD 1, 3 and 4 in which the α-α coincidence detection efficiency is maximal. (The α-α coincidence detection efficiency in DSSSD 2 is reduced due to a dead back strip in DSSSD 3.) The spectrum resulting from these cuts is shown in Fig. 4.7. The background component rising up below 300 keV is the same component that caused difficulties in the determination of the single-particle detection efficiency at low energies, see Section 2.3.9. With our attention restricted to the central 6×6 pixels of DSSSD 1, 3 and 4, the angular coverage is reduced to 3.3%.

We fit the data with a Gaussian on top of a smooth background modeled as an exponential decay curve plus a constant offset. We fix the width of the Gaussian to $\sigma = 11.5$ keV which is the typical width of the peaks seen in the β-delayed proton spectrum of ^{23}Al. With the peak energy fixed to 337 keV, the best fit is obtained with

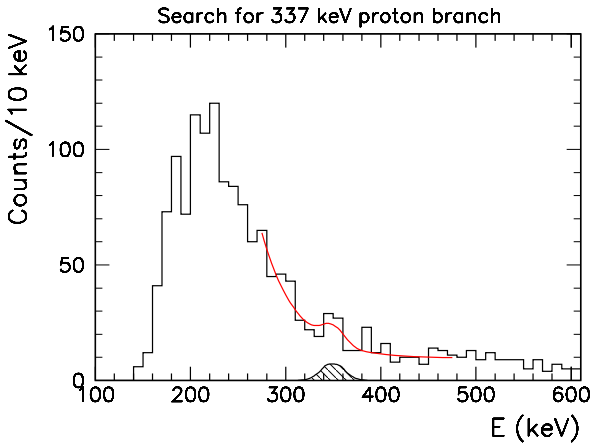

Figure 4.7: Low-energy spectrum of ^{8}B with cuts imposed to reduce the intensities of α and β particles. The red curve was obtained by fitting the data with a Gaussian on top of a smooth background, allowing the peak energy to vary within ±20 keV from the expected value of 337 keV.

no contribution from the peak at all. The 2σ upper limit on the signal is 26 counts. The corresponding limit on the proton branch is 1.5×10^{-5}.

If the peak energy is allowed to vary within ±20 keV from the expected value of 337 keV, the best fit is obtained with the peak centered at 349 keV as shown in Fig. 4.7. The peak integral is 22 counts (branching ratio 1.3×10^{-5}) with a 2σ upper limit of 49 counts (branching ratio 2.8×10^{-5}). The 2σ lower limit is consistent with zero counts.

The existence of a 337 keV proton branch can not be inferred from the present study which puts an upper limit of 1.5×10^{-5} on the branching ratio at 95% confidence level. To reach a sensitivity of 10^{-8}, particle identification seems necessary. This could be accomplished with a Gas-Si type telescope like the ones used by [Tig95] and [Per00] to measure the low-energy β-delayed protons from ^{23}Al. With particle identification, the background could, potentially, be reduced to essentially zero, thereby gaining a factor of ten or so in sensitivity. Another factor of ten could be gained by expanding the solid-angle coverage (presently 3%). To get the last factor of ten needed to reach a sensitivity of 10^{-8}, significantly higher beam intensities are required (due to the difficulties in obtaining beam time).

CHAPTER 5

Conclusion and Outlook

The long-standing puzzle originating from the observation in 1968 by Davis of a 50% deficit in the solar neutrino flux, was solved in the early 2000s by the solar neutrino experiments Super-Kamiokande and SNO: The electron neutrinos produced in the hydrogen-burning reactions in the interior of the Sun oscillate to μ and τ neutrinos rendering them invisible to Davis' detector.

So far, the distortion of the ^{8}B neutrino spectrum due to the transition from matter-enhanced oscillations to vacuum oscillations around 3 MeV has not been observed [Aha10, Smy10]. Above 4 MeV (the detection threshold of Super-Kamiokande and SNO), the distortion is expected to be on the order of 10%. Within a decade, Super-Kamiokande should be able to resolve a 10% distortion with 3σ significance [Smy10].

Using a coincidence-detection technique, we have measured the ^{8}Be excitation energy distribution in the decay of ^{8}B. The main feature of this distribution is a broad peak centered at $E_x \approx 3$ MeV. The distribution obtained in the present study is shifted 20–25 keV toward lower excitation energies relative to the internally consistent distributions of Winter *et al.* and Bhattacharya *et al.* which are held as the current standard [Ade10]. Our measurement gives a more intense neutrino spectrum at high neutrino energies. The deviation reaches 8% at $E_\nu = 15$ MeV. Below $E_\nu = 11$ MeV, our spectrum deviates by less than 1% from the neutrino spectrum of Winter *et al.* and Bhattacharya *et al.* We believe that our experimental approach gives an improved handle on systematical effects compared to the approaches of Winter *et al.* and Bhattacharya *et al.* We have pointed out possible errors in their measurements which may explain the 20–25 keV shift.

The analysis of the KVI experiment (the implantation measurement recently performed by our collaboration) is underway and will provide an important check of the results obtained here. The complete calculation of the neutrino spectrum, following the prescription of Winter *et al.*, remains to be done. However, the conclusions already made regarding the implications of our new measurement for the neutrino spectrum, will not change substantially.

CHAPTER 6

Additional Results

6.1 β-Delayed α Decay of ^{20}Na

The β-delayed α decay of ^{20}Na was measured for calibration purposes, but it is also of great interest in its own right. Below, we discuss various aspects of the β-delayed α decay of ^{20}Na, and we compare our α spectra to the α spectra measured in previous experiments. Notably, we show how the coincident measurement of the α particle and the recoiling ^{16}O ion from the decay of ^{22}Na allows us to establish the existence of three, very weak and hitherto unobserved, α groups below 1.5 MeV.

The decay of ^{20}Na was measured both at the beginning of the experiment and at the end, see Fig. 2.1. We refer to these measurements by the names "first measurement" and "second measurement", respectively.

6.1.1 Introduction

The $J^\pi = 2^+$, $T = 1$ ground state of ^{20}Na decays to ^{20}Ne by positron emission with a half-life of 447.9(23) ms and $Q(\beta^-) = -13\,886(7)$ keV [Til98]. Excited states in ^{20}Ne populated in the β decay of ^{20}Na, with an excitation energy above 4 729.84(1) keV, may break up to $\alpha + ^{16}$O. The α particles originating from such transitions are referred to as β-delayed α particles.

The most recent experimental study of the β decay of ^{20}Na found in the literature is that of Huang *et al.* from 1997 [Hua97]. A much more comprehensive study was carried out by Clifford *et al.* back in 1989 [Cli89]. They performed a β-α coincidence measurement in which the energies and directions of both particles were recorded. By studying the dependence on the β energy of the kinematic shift in α energy for selected relative β-α angles, they were able to determine the ratio of Fermi (vector) to Gamow-Teller (axial-vector) components for a number of allowed transitions including the transition to the $J^\pi = 2^+$, $T = 1$ isobaric analog state (IAS) in ^{20}Ne at 10 273.2(19) keV. The ratio of Fermi to Gamow-Teller components for this transition is of particular interest; together with the measured ft value, it determines the weak vector coupling constant, G_V, thus testing the Conserved Vector Current (CVC) hypothesis. (The CVC hypothesis states that the vector part of the weak charge is conserved under the strong interaction, whereas the axial vector part is not. In other

words, the vector part of the effective weak charge is unchanged by the continuous emission and re-absorption of quark antiquark pairs from the nucleon and other strong processes, whereas the axial-vector part of the effective weak charge is not unchanged by such strong processes.) For a number of allowed transitions to $J^\pi = 2^+$, $T = 0$ states in ^{20}Ne, limits were established on the Fermi contribution and from this, also on the isospin mixing in ^{20}Ne. Finally, ft values were measured and used to determine to what degree the transitions were allowed, and hence indicate the spin and parity of the final state.

The breakup of the IAS in ^{20}Ne to $\alpha + ^{16}$O is reminiscent of the breakup of the IAS in ^{12}C to three α particles (Chapter 11) in that both decays are isospin-forbidden and only occur due to mixing with $T = 0$ states.

The present study is rather limited in scope compared to [Cli89]. Nevertheless, it does bring new results: By measuring the α particle and the ^{16}O ion in coincidence, we are able to identify three new β-delayed α groups below 1.5 MeV that, in the singles spectrum, are buried under the five orders of magnitude more intense ^{16}O recoil groups. In addition, the high level of statistics gathered in the present experiment allows for an R-matrix analysis of the interference feature seen in the β-delayed α spectrum around 3 MeV. The large width of the corresponding states in ^{20}Ne are suggestive of a pronounced $\alpha + ^{16}$O cluster structure. The ft values obtained by [Cli89] suggest that the transitions are first forbidden or allowed, and hence the spin-parity could be 1^-, 2^+ or 3^-. (The observation of α decay from these states excludes unnatural spin-parity.)

6.1.2 Data Analysis

α-^{16}O Coincidences detected in the second ^{20}Na measurement, with the α particle seen in DSSSD 3 and the ^{16}O ion in DSSSD 2, are shown in Fig. 6.1 with the α energy along the abscissa and the ^{16}O energy along the ordinate. The α particle and the ^{16}O ion share the available energy as $E_{^{16}\mathrm{O}}/E_\alpha = m_\alpha/m_{^{16}\mathrm{O}} = 0.25$. Most of the intensity is indeed seen to lie along the diagonal. Weak α-particle response tails are seen extending horizontally from the two most intense peaks. Coincidences in which the ^{16}O ions strikes the aluminum grid that covers 3% of the detector surface, thus losing additional energy before entering the active volume of the detector, are responsible for the satellite peaks seen $\sim$0.6 MeV below the diagonal.

β-Delayed α spectra, summed over all four detectors, are shown in Fig. 6.2. Both singles and coincidence spectra are shown. Only coincidence events which fulfill the requirement $E_{^{16}\mathrm{O}} < 0.25E_\alpha + 75$ keV, i.e. events below the dashed red line in Fig. 6.1, are included. This is done to remove the contribution from the horizontal response tails. Satellite peaks due to the additional energy lost by α particles striking the aluminum grid are visible at the low-energy flank of the two most intense α groups

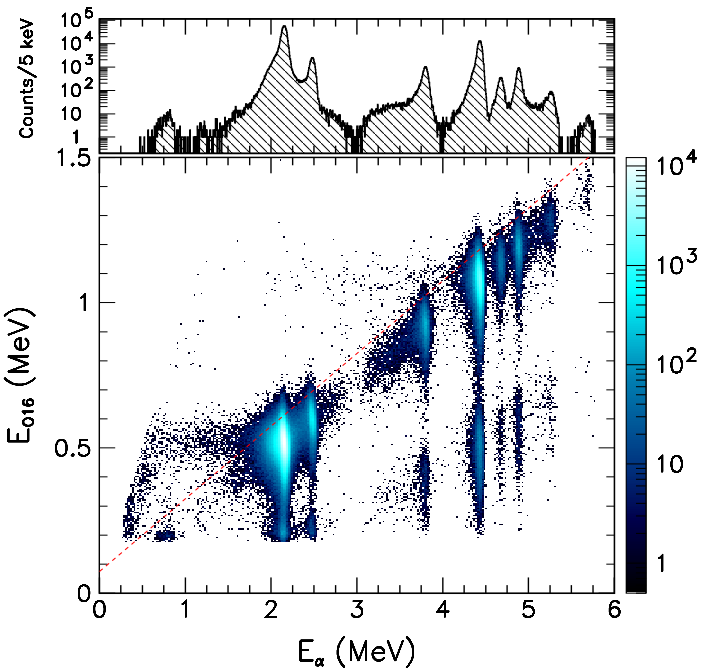

Figure 6.1: α-^{16}O Coincidences with the α energy along the abscissa and the ^{16}O energy along the ordinate. Coincidences in which the ^{16}O ions strikes the aluminum grid that covers 3% of the detector surface are seen below the diagonal. Weak α-particle response tails are seen extending horizontally from the two most intense peaks. The projection of the data below the dashed red line is shown on top.

(5 and 10). The low-energy part of the coincidence spectrum is shown in detail in Fig. 6.3.

The α groups numbered 1–3 are only seen in DSSSD 3. This is because DSSSD 2, which is placed opposite of DSSSD 3, is the only detector with sufficiently low thresholds to detect the coincident ^{16}O ions. As an example, the energy of the ^{16}O ions coincident with the α particles of group 1, is 0.25×688 keV $= 172$ keV. After passage through 30 nm carbon and 75 nm silicon, the energy is reduced to about 120 keV. Unfortunately, DSSSD 3 exhibits some strange behavior, as seen e.g. in the analysis of the line shape of group 10 (Section 2.3.10) and in the analysis of the detector dead layers (Section 2.3.6), indicating that perhaps DSSSD 3 was not fully depleted, in particular toward the end of the experiment.

In the two-dimensional energy spectrum of Fig. 6.1, part of groups 1 and 2 are cut-off by the ^{16}O detection threshold. In consequence, there exists a preference for shallow implantation in the carbon foil. This reduces the energy loss of the ^{16}O ions detected in DSSSD 2 (upstream) and increases the energy loss of the α particles de-

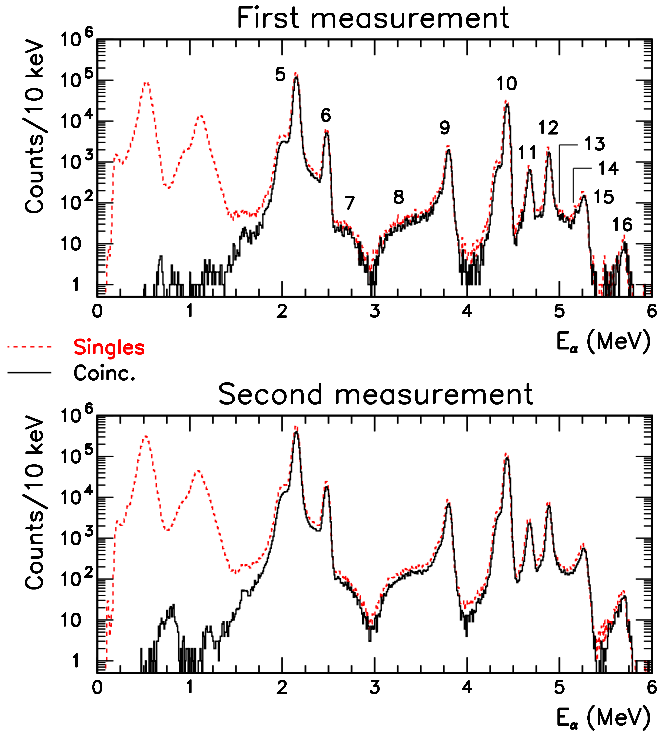

Figure 6.2: β-Delayed α spectra of ^{20}Na. The solid black line is the α-^{16}O coincidence spectrum. The dashed red line is the singles spectrum.

tected in DSSSD 3 (downstream). The bias introduced in the determination of the α-particle energy is estimated to be no larger than −10 keV.

6.1.3 Results

The energies of the 16 α groups identified in the present experiment are given in Table 6.1 along with energies of the α groups identified in the two previous experiments. Group 17, seen by [Hua97] but not by [Cli89], was not seen in the present experiment despite higher statistics[1].

The energies of groups 4–16 obtained in the present experiment are in internal agreement and are consistent with the results of the two previous experiments. The energies of the two most intense α groups, 5 and 10, used for the energy calibration, differ from the energies used in the two previous experiments by a few keV. This is due to the updated value for the α + ^{16}O threshold in ^{20}Ne [Aud03]. The small

[1] A single coincidence event is seen at 5.96 MeV.

Table 6.1: Energies of β-delayed α groups of ^{20}Na identified in the present experiment and in the two most recent experiments described in the literature. Only statistical uncertainties are given on the present results. Statistical uncertainties below 1 keV have been omitted.

α group	Present experiment		[Hua97]	[Cli89]
	1st	2nd		
1	682 ± 5	694 ± 6	∼780[a]	···
2	844 ± 10	795 ± 4		···
3	1 251 ± 10	1 190 ± 11	···	···
4	1 591 ± 7	1 593 ± 6	···	1 580 ± 40
5	2 153[b]	2 153[b]	2 150.4[b]	2 150.4[b]
6	2 481	2 481	2 483.5 ± 2.5	2 479.6 ± 2.1
7	2 600[c]	2 600[c]	2 756 ± 5	2 659 ± 7
8	3 300[c]	3 300[c]	3 325 ± 13	3 570 ± 25
9	3 800	3 800	3 803.0 ± 2.5	3 799 ± 3
10	4 434[b]	4 433[b]	4 432.2[b]	4 432.2[b]
11	4 679	4 678	4 674.6 ± 2.1	4 675 ± 3
12	4 889	4 888	4 884.4 ± 2.5	4 885 ± 3
13	4 900[c]	4 900[c]	4 930 ± 6	4 966 ± 7
14	5 180 ± 10	5 183 ± 10	5 222 ± 47	5 106 ± 7
15	5 265	5 262	5 253.5 ± 2.3	5 249 ± 4
16	5 689 ± 11	5 692 ± 5	5 691 ± 4	5 698 ± 6
17	···	···	5 896 ± 6	···

[a] The evidence presented in [Hua97] for the observation of this α group is meager.

[b] Used for energy calibration.

[c] Broad state. The energy given here is only meant as a rough estimate. Dedicated *R*-matrix fits are necessary to obtain a precise and meaningful value for the energy.

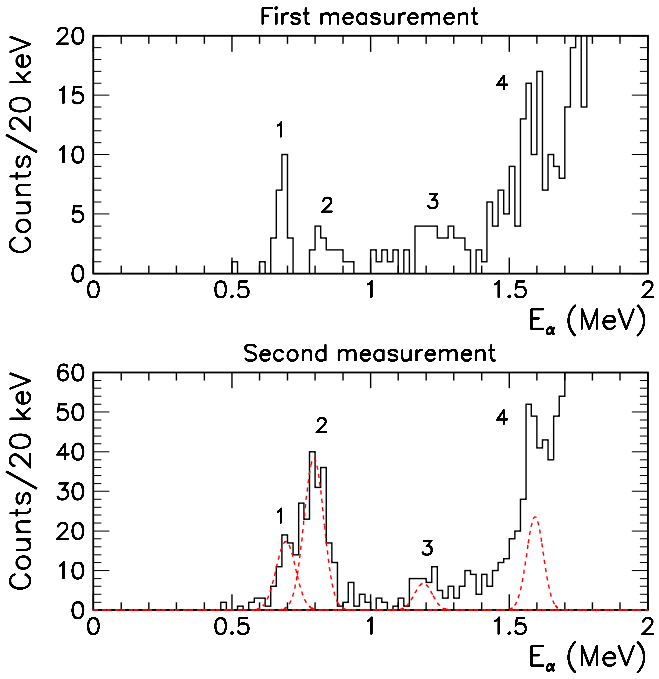

Figure 6.3: Low-energy part of the α-^{16}O coincidence spectrum.

discrepancies seen in the case of group 14 and 15 may be attributed to systematic uncertainties in the determination of the peak position due to the overlap of the two groups as well as the presence of the broad underlying group 13.

In an attempt to identify the excited states in ^{20}Ne responsible for the α groups 1–4, the equivalent excitation energies in ^{20}Ne have been calculated and are given in Table 6.2. The excitation energies have been calculated both assuming population of the ground state in ^{16}O and assuming population of the 0^+ first excited state in ^{16}O at 6 049 keV. Known states in ^{20}Ne relevant to the identification of the α groups 1–4 are listed in Table 6.3.

Group 4 may be identified either with the decay of the state labeled *C* to the ground state in ^{16}O, or with the decay of the state labeled *E* to the first excited state in ^{16}O. The direct population of state *C* requires a second-forbidden transition. The direct population of state *E* could proceed via an allowed transition (assuming that the 2^+ spin-parity assignment holds), but the phase space available is rather limited due to state *E* being situated only 121 keV below the end point of the β-decay window[2].

[2]Electron capture may provide a viable alternative. In any event, one would have to explain why decays

Table 6.2: Low-energy β-delayed α groups of ^{20}Na identified in the present experiment. E_α represents the average of the two values given in column 2 and 3 of Table 6.1, with the error bar raised in the case of group 2 and 3 to account for the large spread. E_x is the corresponding calculated excitation energy in ^{20}Ne assuming that the decay goes to the ground state in ^{16}O. Similarly, E_x^* is the calculated excitation energy in ^{20}Ne assuming that the decay goes to the 0^+ first excited state in ^{16}O at 6 049 keV. The uncertainties on the excitation energies are simply 5/4 times the uncertainties on the corresponding α-particle energies.

α group	E_α (keV)	E_x (keV)	E_x^* (keV)
1	688 ± 4	5 590	11 639
2	820 ± 25	5 754	11 803
3	1 221 ± 31	6 256	12 304
4	1 592 ± 5	6 720	12 769

Table 6.3: Known states in ^{20}Ne, the population of which may explain the low-energy α groups identified in Table 6.2.

Label	E_x (keV)	J^π , T	Γ (keV)	Decay modes
A	5 621.4 ± 1.4	3^- , 0	$(3.3 \pm 0.3) \times 10^{-6}$	γ, α
B	5 787.7 ± 2.6	1^- , 0	$(28 \pm 3) \times 10^{-3}$	γ, α
C	6 725 ± 5	0^+ , 0	19.0 ± 0.9	γ, α
D	12 327 ± 10	2^+ , 0	390 ± 50	α
E	12 743 ± 10	(2^+), 0	61 ± 12	α

However, in both cases the expected ft value is significantly below the ft value actually measured [Cli89]. The alternative explanation proposed by [Cli89] is a weak β branch feeding a hypothetical state at around 11 MeV excitation energy in ^{20}Ne which decays mainly by γ-ray emission to state C. Given the good agreement between the excitation energy of 6 720 ± 6 keV deduced from the present experiment, with much reduced uncertainties compared to [Cli89], and the known energy of 6 725 ± 5 keV of state C, this explanation seems plausible.

The identification of the transitions responsible for the α groups 1–3 is complicated by the shifts in peak position of group 2 and 3 between the two measurements, resulting in large uncertainties on the energy determination. The change in the relative intensity of group 1 compared to group 2 is also a source of concern. Presently,

to the ^{16}O ground state are not seen.

these effects are not fully understood, though they are believed to be explained in part by the aforementioned bias introduced by the requirement of detecting the low-energy ^{16}O recoil in the opposite detector. In addition, the peculiar response of DSSSD 3 may play a role. It seems plausible, however, that group 1 and 2 should be identified with first-forbidden transitions to the states labeled *A* and *B*, subsequently decaying to the ^{16}O ground state. Finally, group 3 can be identified with an allowed transition to state *D*, subsequently decaying to the first excited state in ^{16}O. The large width of state *D* seems compatible with the rather large width of group 3, seen in Fig. 6.3. This does, however, pose the question of why decays from state *D* to the ground state in ^{16}O are not seen. The corresponding α group should be seen at 6.1 MeV.

6.1.4 Continuation—What Next?

The changes in energy and relative intensity of the three low-energy α groups remain to be understood. A plot of the DSSSD hit pattern would be a natural first step in an attempt to clarify the role of the detection thresholds.

The relative intensities of the 16 α groups observed in the present experiment remain to be determined and compared to the literature values. In determining the intensities of the four lowest-energy α groups, the decrease in coincidence detection efficiency due to the ^{16}O ions falling below detection threshold, must be taken into account.

An *R*-matrix analysis is underway, which will pin down the properties of the broad resonances in ^{20}Ne responsible for the interference feature seen in the β-delayed α spectrum around 3 MeV. The β decay of ^{20}Na provides a very clean way to study the properties of the broad resonances in ^{20}Ne in that the initial state and the transition operator are well understood leaving the final state as the only unknown (in the same way that the β decays of ^{12}B and ^{12}N provide a very clean way to study the broad resonances in ^{12}C).

6.2 β-Delayed Proton Decay of ^{23}Al

Like the β-delayed α decay of ^{20}Na covered in the previous section, the β-delayed proton decay of ^{23}Al was measured with the primary objective of obtaining more data points for the energy calibration. Two well-known proton groups with energies of 560(5) and 839(5) keV according to the literature [Tig95], would serve to reduce the uncertainty in the energy calibration at low energies. Later, it was realized that, most likely, the errors on these energies were underestimated. Consequently, the energy calibration was performed without the ^{23}Al proton groups. Even so, these proton groups have been very useful in the data analysis, notably, in constraining the thickness of the detector dead layers.

Below, we present the new physics results that have emerged from the analysis of the ^{23}Al data. Namely, our revised energies for the protons groups previously seen at 560(5) and 839(5) keV, and the observation of several new, less intense, proton groups between 0.9 and 2.1 MeV. We begin, however, with a few introductory remarks about the astrophysical interest in the β-delayed proton decay of ^{23}Al.

The decay of ^{23}Al was measured both at the beginning of the experiment and at the end, see Fig. 2.1. We refer to these measurements by the names "first measurement" and "second measurement", respectively.

6.2.1 Introduction

The proton-rich aluminum isotope ^{23}Al decays to ^{23}Mg by positron emission with a half-life of 0.47(3) seconds and $Q(\beta^-) = -12.243(19)$ MeV [Fir07]. The proton separation energy in ^{23}Mg is 7.5803(14) MeV [Fir07]. If states above this threshold are populated in the β^+ decay of ^{23}Al, they may breakup to $p + {}^{22}$Na. Protons originating from such transitions are referred to as β-delayed protons.

The study of these transitions is relevant to the understanding of the so-called low-temperature rapid proton capture process (rp-process) believed to take place in classical novae at temperatures of 0.1–0.5 billion Kelvins. Classical novae are understood as thermonuclear explosions taking place in the high-temperature hydrogen-rich environment found on the surface of white-dwarf stars which are accumulating material from a nearby companion star. In the rp-process, proton-rich elements are created by successive proton captures with occasional β^+ decays or electron captures back toward stability. The β-delayed proton decay of ^{23}Al is particularly important for the description of the so-called NeNaMg cycle [Boy07].

The β-delayed protons from the decay of ^{23}Al were measured by Tighe *et al.* [Tig95] in 1995. They found four proton groups at 223(20), 285(20), 560(5) and 839(5) keV. The lowest-energy group was attributed to transitions to the $J^\pi = 5/2^+$, $T = 3/2$ isobaric analog state in ^{23}Mg. More recently, Peräjärvi *et al.* measured six proton groups at

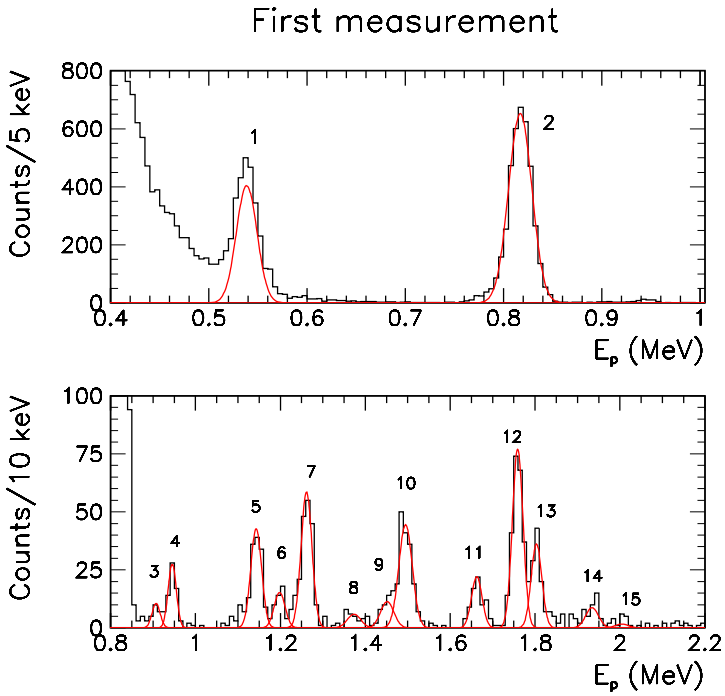

Figure 6.4: β-Delayed proton spectrum of ^{23}Al (first measurement).

200(20), 270(20), 400(20), 554(7), 839(6) and 1931(14) keV, basing their energy calibration on the 560 and 839 keV groups measured by Tighe *et al.* The four other proton groups seen by Peräjärvi *et al.* had poor statistics, see Fig. 1 of [Per00].

6.2.2 Data Analysis and Results

In Jyväskylä we measured ^{23}Al twice. The first time for 8 hours, the second time for 22 hours. In addition to ^{23}Al, the $A = 23$ mass separated beam contains ^{23}Mg which is a pure β emitter and hence gives rise to a large β background below 0.5 MeV. This is seen in the spectra of Fig. 6.4 and 6.5. In addition to the 560 and 839 keV proton groups found by Tighe *et al.*, we find a number of new proton groups between 1 and 2 MeV, the energies and relative intensities of which are given in Table 6.4.

The new proton groups found between 1 and 2 MeV are not of much astrophysical interest because the corresponding center of mass energies are well above the Gamow window of the $p+^{22}$Na reaction at the relevant temperatures. The energies of group 1 and 2 are about 20 keV below the energies found by Tighe *et al.* The reason for this discrepancy is presently not understood. We note that the energy of group 1 has

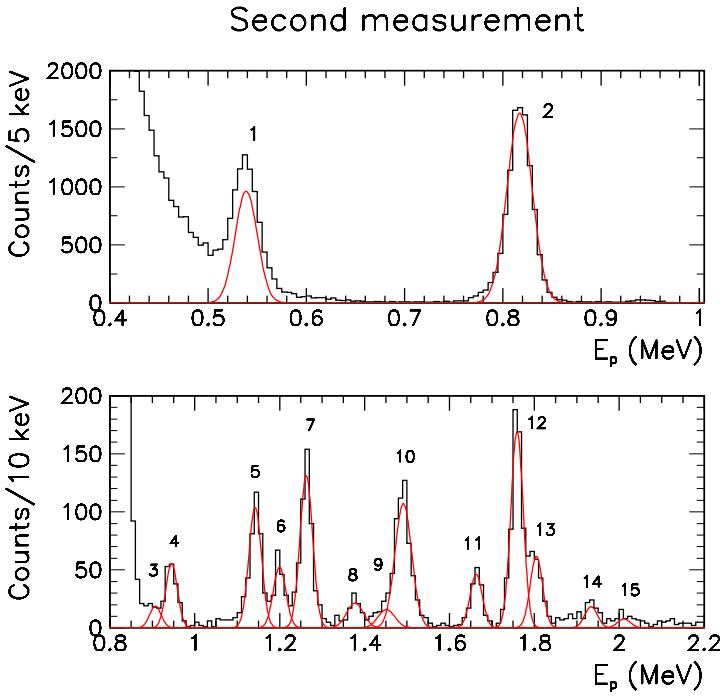

Figure 6.5: β-Delayed proton spectrum of ^{23}Al (second measurement).

been measured to 557(2) keV in a ^{22}Na(p,γ) experiment [Ste96], in agreement with the value of Tighe *et al.*

The 1-to-2 intensity ratio is determined to 50.2(19)% in the first measurement and 44.2(12)% in the second. The discrepancy might be due to the modeling of the background below group 1 or the assumption of Gaussian peak shapes. A thorough investigation has, however, not been conducted. Within 2σ our result for the 1-to-2 intensity ratio is consistent with the ratio of 0.7(1) obtained by Tighe *et al.*

The proton energy E_p and the excitation energy E_x in ^{23}Mg are related by the simple expression

$$E_p = \tfrac{22}{23}(E_x - S_p)\,, \quad S_p = 7.5803(14)\,\text{MeV}\,. \tag{6.1}$$

Using Eq. 6.1, the proton energies measured in the present study have been converted to excitation energies and a quick comparison to the tabulated energy levels of ^{23}Mg has been performed. Proton groups 8, 9, 10, 12, 13 have perfect matches within ±5 keV. Proton groups 4, 5, 7, 11, 14, 15 have matches within ±15 keV. Proton groups 3 and 6 only have matches within ±30 keV. The deviations display no systematic behavior.

Table 6.4: Energies and relative intensities of β-delayed protons from ^{23}Al obtained in the first and second measurement. Only statistical uncertainties are given.

Proton group	E_p (keV)		Rel. intensity (%)	
	1st	2nd	1st	2nd
1	538.5(3)	538.8(2)	28.4(7)	26.0(5)
2	817.2(2)	817.15(13)	56.6(7)	58.7(5)
3	907(3)	907[a]	0.32(7)	0.31(5)
4	945.1(14)	945.5(12)	0.85(11)	0.92(7)
5	1142.9(12)	1142.2(9)	1.76(15)	1.87(10)
6	1198(2)	1199.8(13)	0.63(9)	0.94(7)
7	1261.6(11)	1262.8(7)	2.41(18)	2.37(11)
8	1373(5)	1377(2)	0.30(7)	0.52(5)
9	1452(4)	1452[a]	0.58(13)	0.38(10)
10	1494.9(16)	1491.3(12)	2.26(19)	2.57(14)
11	1663(2)	1662.9(11)	0.89(11)	0.82(6)
12	1759.1(9)	1759.1(7)	3.1(2)	2.99(13)
13	1803.5(15)	1804.7(16)	1.45(15)	1.09(9)
14	1934(3)	1934(2)	0.43(8)	0.33(5)
15	2005(8)	2011(6)	0.08(5)	0.14(4)

[a] Value held fixed.

6.2.3 Continuation—What Next?

A thorough comparison to the tabulated energy levels of ^{23}Mg remains to be done. Some deviations are probably due to the presence of closely separated levels in ^{23}Mg which cannot be resolved due to the experimental resolution of $\approx$ 25 keV (FWHM). Another possible explanation is interference between levels of same spin-parity.

6.3 Response of Si Detectors to α Particles and ^{16}O Ions

The results presented below are the fortunate byproduct of an important effort to make sense of the measured energies of the ^{16}O ions from the decay of ^{20}Na, which were found to deviate by some tens keV from the correct values. As it turns out, the deviations are due to the different responses of Si detectors to different types of ions.

The results presented below do not affect the analysis of ^{8}B data, but they were central in our work to verify the validity of our data. As mentioned earlier, these results may explain why Winter *et al.* measure a ^{8}Be excitation energy spectrum that is shifted 25 keV up in energy with respect to ours.

6.3.1 Introduction

When energetic light ions, like the protons and α particles that we measure in the present experiment, are stopped in silicon, nearly all their energy goes to the creation of electron-hole pairs which, in turn, give rise to a detectable voltage pulse proportional in magnitude to their numbers and hence the energy of the ion. For heavier ions, like ^{16}O, a sizable fraction of the energy is lost in non-ionizing processes, e.g. by causing damage to the crystal lattice structure, and hence does not contribute to the voltage pulse. If not accounted for, this effect will cause us to systematically underestimate the true ion energy.

Past measurements [Len86, Len87, Com92] have shown that, even when the non-ionizing energy loss is taken into account, the pulse heights measured for different ions with the same energy still differ. This residual effect, often referred to as the *pulse height defect*, may be explained by assuming that the average energy required to produce an electron-hole pair in silicon is not constant. Instead, this energy decreases slightly with increasing stopping power $\frac{\mathrm{d}E}{\mathrm{d}x}$ away from its normal value of 3.67 eV/pair observed with particles of low stopping power such as electrons, γ rays or MeV protons [Len86]. We may understand this dependence in the following way: For small stopping powers, the mean free path between the creation of two successive electron-hole pairs is large compared to the atomic spacing and may therefore be considered as independent events. For larger stopping powers, the mean free path becomes comparable to the atomic spacing and the assumption of independence breaks down. Naïvely, we may argue that the creation of the first electron-hole pair perturbs the crystalline order, weakening the electronic bonds in the immediate surroundings thus facilitating the creation of the next electron-hole pair. In practice, this means that protons, α particles and ^{16}O ions create slightly different quantities of electron-hole pairs at the same cost with ^{16}O ions creating the most and protons the fewest (depending on the energy).

Below, we reexamine the measurement made in 1986 by Lennard *et al.* of the pulse

height defect of protons and ^{16}O ions relative to α particles [Len86]. We demonstrate how the pulse height defect of ^{16}O ions may be extracted from our own data and compare our results to those of [Len86] who found that, for energies in the range 0.5–2 MeV, the correction needed amounts to a multiplicative factor of $\xi_{^1\mathrm{H}} = 1.014 \pm 0.002$ for protons and $\xi_{^{16}\mathrm{O}} = 0.979 \pm 0.005$ for ^{16}O ions[3].

6.3.2 Experimental Details

Lennard *et al.* measured the pulse height produced in Si surface barrier detectors by ^{1}H, ^{4}He, ^{7}Li and ^{16}O ions in the energy range 0.5–3 MeV. The energy of the ions was accurately determined by time-of-flight measurements over a distance of 16.25 cm. The energy loss in the detector dead layer was determined by rotating the detector relative to the beam axis while monitoring the change in pulse height with angle. A mixed α source consisting of ^{239}Pu, ^{241}Am and ^{244}Cm was used to establish the energy scale. A precision pulse generator was used to calibrate the linearity of the electronics. Data relevant to the pulse-height analysis is given in Table 1 of [Len86].

We can extract equivalent data from our coincidence measurement of the breakup of ^{20}Ne to α + ^{16}O following the β decay of ^{20}Na. In order to reduce the variations in energy loss experienced by particles emitted at different angles, we restrict our attention to the central four pixels in each detector. We examine the pulse height spectrum recorded in the two center-most pixels of back strips 8 and 9 in DSSSD 1–3. The front-strip spectra are not used due to the large differential non-linearity of their response, cf. Section 2.3.2. DSSSD 4 is excluded for the same reason. We identify the two most intense α groups of ^{20}Na (E_α = 2 153 and 4 434 keV) and their corresponding ^{16}O recoil groups ($E_{^{16}\mathrm{O}}$ = 538.8 and 1 109.5 keV) and determine the pulse height at peak value. (Lennard *et al.* used mean pulse-height values. For our data, the pulse height at peak value differs from the mean pulse height by less than 0.5 channels or, equivalently, 1.5 keV.) The pulse heights are, in all cases, determined with negligible statistical error. We use the α-particle data to calibrate the energy scale. The energy loss of the ions in the carbon foil and the detector dead layer is computed using SRIM stopping powers assuming a foil thickness of 114 nm, a fixed implantation depth of 32.7 nm and dead layers of 85, 75 and 120 nm Si in DSSSD 1–3, respectively. The combined energy loss of the ^{16}O ions in the foil and the detector dead layer ranges from 100–280 keV.

[3] $\xi_{^{16}\mathrm{O}} = \frac{C(^1\mathrm{H})/C(^{16}\mathrm{O})}{C(^1\mathrm{H})/C(^4\mathrm{He})} = \frac{0.965 \pm 0.005}{0.986 \pm 0.002} = 0.979 \pm 0.005$ using values and notation of [Len86].

6.3.3 Data Analysis

We begin with a few definitions:

E_i	=	Ion energy
ΔE_f	=	Energy loss in foil
ΔE_{dl}	=	Energy loss in detector dead layer
E'_i	=	Energy deposited in the active volume of the detector
E_m	=	Energy measured
δE	=	E_m - E'_i (energy deficit)
ΔE_n	=	Non-ionizing energy loss

We calculate the energy that is deposited in the active volume of the detector as $E'_i = E_i - \Delta E_{dl}$ for the data of Lennard *et al.* and as $E'_i = E_i - \Delta E_{dl} - \Delta E_f$ for our own data. The energy deficit δE, i.e. the difference between the energy measured and the energy deposited, is shown in Fig. 6.6. The error bars on our data points include the uncertainties from the energy calibration as well as the uncertainties from the determination of ΔE_f and ΔE_{dl} due to the uncertainty on the foil thickness (±8 nm) and dead layer (±7 nm). The ±15 nm uncertainty on the overall scale of the dead layers gives an additional uncertainty in the determination of δE not shown in Fig. 6.6. The uncertainty is ∓6 keV for the 538.8 keV ions and ∓12 keV for the 1109.5 keV ions (same shift in all DSSSDs).

The assumption of a fixed implantation depth made in the calculation of ΔE_f is well-justified as long as the energy loss is linear in distance, i.e. $\Delta E \approx \frac{dE}{dx}\Delta x$, as is the case for protons and α particles. For the ^{16}O ions, however, the energy loss constitutes a sizable fraction of the ion energy and the linear approximation is less accurate. This may introduce small systematic errors (at the 5 keV level or below) in the calculation

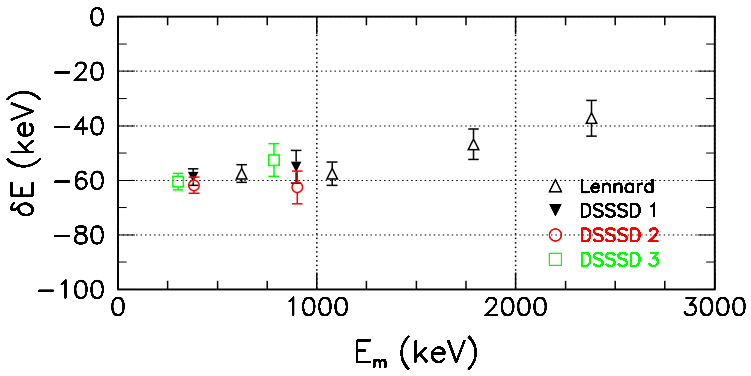

Figure 6.6: The energy deficit δE versus the energy measured E_m for ^{16}O ions.

of ΔE_f.

Ideally, one should calibrate the detector with the same type of particles that are measured in the experiment. Fig. 6.6 clearly demonstrates that an energy calibration performed with α particles cannot be directly applied to ^{16}O ions. A parametrization of the error made is needed.

6.3.3.1 Non-ionizing Energy Loss

Part of the deficit observed in Fig. 6.6 may be attributed to the large non-ionizing energy loss, ΔE_n, of ^{16}O ions compared to α particles. Lennard *et al.* used standard energy-loss algorithms to calculate ΔE_n in silicon for α particles and ^{16}O ions, see [Len86] for details. We may determine ΔE_n at the energies measured in our study by a second-degree polynomial extrapolation (or interpolation, depending on the energy) of their calculations. Correcting the energy deficit δE for the non-ionizing contribution, we obtain Fig. 6.7. The residual deficit observed in Fig. 6.7 represents the aforementioned pulse height defect. As argued by Lennard *et al.*, it can be understood by assuming that the average energy required to produce an electron-hole pair in silicon depends on the stopping power.

Note that the α-particle energies, used for the calibration of the energy scale, have been corrected for the non-ionizing energy loss as well. This lowers the measured energy of the ^{16}O ions, E_m, by roughly 10 keV.

The dashed line superimposed on the data points is the best-fit straight line to the four data points of Lennard *et al.* The slope $\alpha = 0.019 \pm 0.004$ is related to the multiplicative factor, ξ, introduced by Lennard *et al.* through the simple relation $\alpha =$

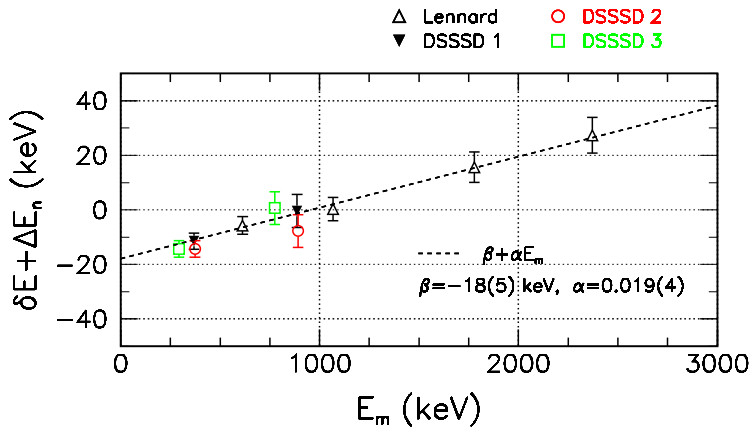

Figure 6.7: The energy deficit δE corrected for the non-ionizing energy loss ΔE_n versus the energy measured E_m for ^{16}O ions. ΔE_n was obtained from [Len86].

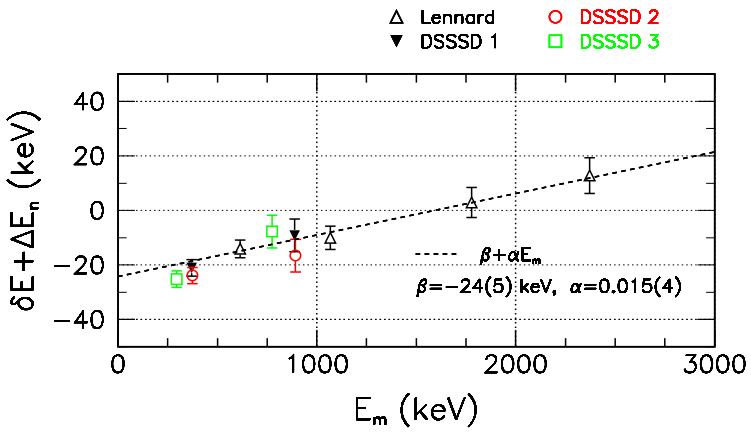

Figure 6.8: The energy deficit δE corrected for the non-ionizing energy loss ΔE_n versus the energy measured E_m for ^{16}O ions. ΔE_n was obtained from TRIM simulations.

$1-\xi$. Inserting the value of $\xi_{^{16}O} = 0.979 \pm 0.005$ obtained by Lennard *et al.*, one obtains $\alpha = 0.021 \pm 0.005$ in excellent agreement with our result. This is expected since we have obtained our value repeating the analysis originally performed by Lennard *et al.*

The non-ionizing energy loss of α particles and ^{16}O ions in silicon calculated by Lennard *et al.* has been checked against the results of TRIM simulations. For α particles they agree within 1 keV, but for ^{16}O ions TRIM gives non-ionizing energy losses that are 10–15 keV below those calculated by Lennard *et al.* Using the non-ionizing energy losses given by TRIM, one obtains the deficits shown in Fig. 6.8.

6.3.4 Conclusion

Based on the reanalysis of [Len86] as well as the analysis of our own data, we propose the following calibration scheme: The α particle data is used for calibrating the energy scale. In doing so, the energy losses in the foil and the detector dead layer are taken into account and corrections are made for the non-ionizing energy loss of α particles in silicon (as given by TRIM). Using this calibration, the measured pulse heights of the ^{16}O ions are converted to energies, E_m , which are corrected for the pulse height defect observed in Fig. 6.8 by a simple linear transformation:

$$E_m \rightarrow (1-\alpha)E_m - \beta, \quad \beta = -26 \pm 5 \text{ keV}, \quad \alpha = 0.015 \pm 0.004 \,. \tag{6.2}$$

Finally, corrections are made for the non-ionizing energy loss of ^{16}O ions in silicon (as given by TRIM) and for the energy losses in the dead layer and the foil. A similar procedure should be applied to protons with $E_m \rightarrow E_m/\gamma$ replacing Eq. 6.2, where

$\gamma = 0.986 \pm 0.002$ as obtained by Lennard *et al.*

Our scheme differs from that of Lennard *et al.* in two respects. First, and most importantly, we include the non-zero offset that Lennard *et al.* considered consistent with zero. Second, we use the newest version (2008) of TRIM to calculate the non-ionizing energy loss, ΔE_n. In this way, we obtain values of ΔE_n for ^{16}O ions that are 10–15 keV below the values obtained by Lennard *et al.*

In a experiment like that of Winter *et al.* [Win03], or our own KVI experiment for that matter, where the activity is implanted in the detector, one measures the combined pulse height of the α particle and the ^{16}O ion. Therefore, the total energies, $2153.5 + 538.8 = 2692.1$ keV and $4433.9 + 1109.5 = 5543.4$ keV, are used for the energy calibration. If the non-ionizing energy loss of α particles and ^{16}O ions in silicon is taken into account, but the pulse height defect observed in Fig. 6.8 is ignored, one obtains an energy calibration that overestimates the 2α energy from the decay of ^{8}B by $\approx 26\,\text{keV} - 0.015 \times 500\,\text{keV} = 19$ keV at 2.7 MeV. This may be the reason why Winter *et al.* measure a ^{8}Be excitation energy spectrum that is shifted 25 keV up in energy with respect to ours.

Part II

^{12}C Resonances

CHAPTER 7

Introduction

7.1 Paradigm of Nuclear Physics

To the nuclear physicist, the basic building blocks of the atomic nucleus are the proton and the neutron, commonly referred to as nucleons. Forgetting about their composite nature and finite size, we treat the proton and the neutron as fundamental particles whose properties (mass, electric charge, magnetic moment etc.) and mutual interaction give rise to the observed properties of atomic nuclei. This, one may say, constitutes the *classical paradigm* of nuclear physics. Its justification and usefulness stems from the different energy scales of *nuclear* excitations (0.1–10 MeV) and *nucleon* excitations (0.1–1 GeV). If a measurement of a nuclear property is made which contradicts the predictions of the current nuclear model, we first try to improve the nuclear model *within* this paradigm, i.e. we try to find a meaningful way in which to accommodate our observation within the picture of the nucleus as composed of inert neutrons and protons, interacting via some two-body potential. When nuclear physicists say a phenomenon can be explained as a "nuclear structure effect" this is, roughly speaking, what they mean. Only if our attempts to explain the new observation as a nuclear structure effect fail, do we invoke the internal structure of nucleons in our explanation [Wil95].

One property that *cannot* be understood within the classical paradigm is the Δ resonance observed e.g. at ≈ 300 MeV in photoabsorption on many nuclei [Ahr85,Sch03]. The underlying reaction is

$$N + \gamma \rightarrow \Delta \rightarrow N' + \pi$$

where an individual nucleon (N) in the nucleus is brought to its first excited state (the Δ isobar) by the absorption of a photon (γ), implying that nucleons possess internal structure. In addition to proton and neutrons, today's *extended* paradigm of nuclear physics makes room for Δ isobars as well as mesons in the nuclear medium. The nuclear force is understood as resulting from the exchange of mesons between nucleons. The effect of Δ isobars and mesons on nuclear phenomena is described sometimes explicitly, other times indirectly through the use of three-body potentials. Many properties of nuclei can be understood within the classical paradigm of nuclear physics. Even more within the extended paradigm.

7.2 Nuclear Structure

Within less than a decade of Chadwick's discovery of the neutron in 1932, two very different descriptions of nuclear structure were formulated: The independent particle model [Hei32a, Hei32b, Hei33] and the liquid drop model [Boh37, Boh39]. Their common starting point is a nucleus composed of protons and neutrons, held together by a strong, short-range, nuclear force acting against the Coulomb repulsion of the protons. The liquid drop model considers the nucleons as strongly correlated, and hence its focus is on the bulk properties of the nucleus, i.e. degrees of freedom which involve correlated motion of nucleons such as rotation and vibration. The independent particle model takes the complete opposite stance by replacing the nucleon-nucleon force with an effective central potential in which the nucleons occupy states of fixed energy, orbital momentum and spin, according to the Pauli principle. The independent particle model developed into the shell model which, with the inclusion of a strong spin-orbit coupling, is able to predict many important nuclear properties such as the ground-state spins of even-even and odd-A nuclei as well as the observed magic numbers. In view of the saturation property of the nuclear force, *viz.* its short range, the great success of the shell model came as a surprise [Bet56]. Over the years, the shell model has been greatly extended. The addition of residual interactions and the use of non-spherical potentials has even allowed for the description of collective degrees of freedom.

7.3 The α Cluster Model

The idea that α particles should exist as separate entities in the nucleus dates back to before Chadwick's discovery of the neutron [Gam30]. As noted by J. Hans D. Jensen (1907–1973) in his Nobel lecture[1] from 1963:

> At that time one was tempted to consider alpha particles as basic building blocks of nuclei. However, from those days a warning from Schrödinger still persists in my mind. During the late twenties he chided the participants in a Berlin seminar for their lack of imagination. In his impulsive manner he said: "Just because you see alpha particles coming out of the nucleus, you should not necessarily conclude that inside they exist as such." [Jen63]

The notion of α particles as nuclear building block was, however, not entirely abandoned. Inspired by molecular physics where the basic building blocks (atoms) are

[1] Jensen shared half of the 1963 Nobel Prize for Physics with Maria Göppert-Mayer (1906–1972) for their proposal of the shell model.

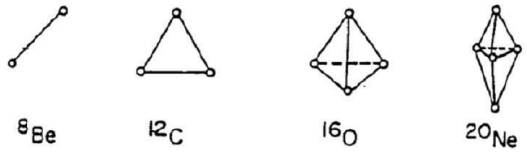

Figure 7.1: Structure of the ground states in ^{8}Be, ^{12}C, ^{16}O, ^{20}Ne according to the original α-cluster model. The α particles are arranged so as to maximize the number of α-α bonds. Adapted from [Fre07a].

themselves composite systems that interact through effective forces, the α cluster model of the nucleus was proposed in the late 1930s [Bet36, Wef37, Whe37, Wei38] as an alternative to the liquid drop model and the independent particle model. The closed-shell configuration gives the α particle its inert character: A large binding energy of 28.3 MeV, spin-parity of 0^+ and a first excited state at 20.2 MeV. These properties of the α particle gave reason to believe that it should be able to exist as a stable sub-unit of the nucleus.

At first, the α cluster model was applied to nuclei composed of an integer number of α particles, i.e. ^{8}Be, ^{12}C, ^{16}O, ^{20}Ne, ^{24}Mg, etc. Their ground states were pictured as geometric configurations with the binding energy proportional to the number of bonds between the α particles, see Fig 7.1. In the case of ^{12}C which can have at most three bonds and has a binding energy of 7.275 MeV (relative to the 3α threshold), we obtain a per-bond binding energy of 2.4 MeV. Similar per-bond energies were found for ^{16}O, ^{20}Ne, ^{24}Mg, ^{28}Si and ^{32}S [Haf38]. However, for the simplest of them all, ^{8}Be, unbound by 92 keV, the model fitted badly. The α cluster model was soon extended to encompass nuclei consisting of an integer number of α particle plus-minus one nucleon [Haf38], e.g. $^{9}\mathrm{Be} = \alpha + \alpha + n$ with the neutron acting like the glue between the α particles much like the electron in a covalent bond between atoms.

Building on work of, among others, Morinaga, a new understanding of the α cluster model emerged in the 1960s [Ike68]. It was realized that, as suggested by the case of ^{8}Be, the α-α bond is indeed very weak. In consequence, nuclei only exhibit α-cluster structure in excited states close to the α-decay threshold. This is illustrated in Fig. 7.2. For ^{12}C, ^{16}O, ^{20}Ne, etc., ground-state configurations more stable than the α-cluster structure exist. In the words of Ikeda "the alpha particle loses its identity in the compact nucleus" [Ike68]. This is perhaps not so surprising when one considers that the binding energy *per nucleon* of the α particle is 7.1 MeV, i.e. no greater than the typical binding in stable nuclei. The structure of the α particle is thus easily susceptible to the nuclear environment.

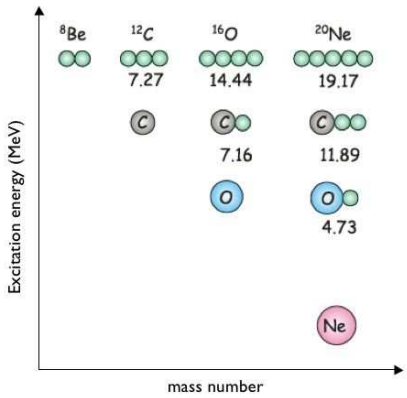

Figure 7.2: Ikeda diagram showing the emergence of cluster-structure at particle-decay threshold. Adapted from [Fre07a].

7.4 A Brief Digression

In 1983, the European Muon Collaboration (EMC) discovered that the quark momentum distribution is changed when the bare nucleon is put into a nucleus [Aub83], since dubbed the EMC effect. Recently, the EMC effect was measured in the light nuclei ^{3}He, ^{4}He, ^{9}Be and ^{12}C [See09]. For ^{3}He, ^{4}He and ^{12}C the observations were consistent with models where the EMC effect scales with the average nuclear density, but ^{9}Be shows an abnormally large effect compared to its average density. One explanation given by [See09] invokes the $\alpha + \alpha + n$ cluster structure of the ^{9}Be ground state: While most nucleons are found in the dense environment of the compact α-particle structure, the average density is much lower due to the α particles and the additional neutron orbiting in a larger volume. Thus, the average density does not reflect the local environment.

This brief digression serves to illustrate the importance of understanding nuclear structure, in this particular case the phenomenon of clustering in light nuclei, in order to use the nucleus as a "laboratory" for particle-physics measurements. It also reminds us that the nucleons, whose properties ultimately determine nuclear structure, are not invariable entities. Their properties depend on the nuclear environment.

7.5 The ^{12}C Nucleus

7.5.1 The Hoyle State

The 0^+ Hoyle state in ^{12}C, famous for its astrophysical importance and named after Fred Hoyle (1915–2001) who predicted its existence [Hoy53], is situated only 379 keV above the threshold for decay to three α particles, making it a plausible candidate for an α-cluster state. Its large size (the radius of the Hoyle state extracted from inelastic electron scattering is 1.3–1.5 times that of the ground state [Che07]) and its large reduced width (comparable to the Wigner limit) support the cluster-structure interpretation.

In 1956, shortly after the experimental discovery of the Hoyle state [Dun53], Morinaga proposed that its structure resembles a linear chain of three α particles [Mor56]. Similar 0^+ states were identified in ^{16}O, ^{20}Ne and ^{24}Mg. The rotation of such a structure would lead to a band of excited states with spin-parity 2^+, 4^+,... on top of the rotationless 0^+ state. Vibrations would give additional energy levels. Using a simple model in which the linear α-particle chain was treated as a rigid rotator with a fixed moment of inertia, Morinaga gave rough estimates of the energy of the 0^+ states and the spacing of the rotational excitations. Reasonable agreeement was found for ^{16}O, ^{20}Ne, and ^{24}Mg, but experimental evidence was not conclusive. As for ^{8}Be and ^{12}C, little was known experimentally at the time. The calculations indicated, however, that a 2^+ excitation of the Hoyle state should be found at ≈ 9.7 MeV. Due to its α-cluster structure, it had to be a rather broad state.

In 1958, a broad state was indeed observed at 10.1(2) MeV [Coo57]. It was populated in the β decay of ^{12}B which implied it had to be 0^+, 1^+ or 2^+. In 1966, its existence was confirmed in another β-decay experiment [Sch66] which determined its energy to 10.3(3) MeV and found that it decayed via the ground state of ^{8}Be, leaving 0^+ and 2^+ as the only possible spin-parity assignments. Soon after, Morinaga suggested that this could be the 2^+ rotational excitation predicted by his model [Mor66]. However, β-decay studies performed by our own collaboration have shown 0^+ to be the correct assignment [Fyn05, Dig05] in agreement with recent ^{12}C$(\alpha,\alpha')^{12}$C experiments [Joh03, Ito04].

Experimental observations indicating the existence of a 2^+ rotational excitation of the Hoyle state have been reported [Joh03, Ito04, Fre07b, Fre09], but a consistent picture has not yet emerged. The R-matrix analysis of our most recent β-decay study give evidence for a 2^+ state around 11 MeV [Hyl10b]. However, the large natural width of cluster states and the presence of several broad overlapping states in the energy region of interest makes the search for the 2^+ excitation very challenging

7.5.2 Level Structure

The level-structure of ^{12}C below 16 MeV according to the most recent compilation [AS90] is reproduced in Table 7.1. Appreciation for the unusual character of the 0^+ Hoyle state may be gained from a simplified shell-model analysis of the level structure of ^{12}C in terms of single-nucleon excitations in the jj coupling scheme. The ground-state configuration of ^{12}C is illustrated in Fig. 7.3. The six protons and six neutrons fill the $1s_{1/2}$ and $1p_{3/2}$ orbitals with their spins coupled to 0^+. If a single nucleon is excited to the the $1p_{1/2}$ orbital, it may couple with the unpaired nucleon left behind in the $1p_{3/2}$ orbital to give 1^+ and 2^+; if excited to the $1d_{5/2}$ orbital, it may couple to give 1^-, 2^-, 3^-, 4^-; if excited to the $2s_{1/2}$ orbital, it may couple to give 1^-, and 2^-. Thus, we conclude that 0^+ states cannot be generated by simple single-nucleon excitations. (Excitation of a single $1s_{1/2}$ nucleon to the $2s_{1/2}$ orbital can give a 0^+ state, but this is energetically very expensive.) A qualitative description of the 0^+ Hoyle state within the shell-model picture in terms of many-nucleon excitations can be given, see e.g. [Coh65]; for a similar description of even-parity states in ^{16}O, see [Bro66].

A 4^+ state also cannot be generated from single-nucleon excitations. A 4^+ state does, however, arise naturally as the second member of the rotational band $(2^+, 4^+, \dots)$ build on top of the 0^+ ground state. The fact that the energies of the 2^+ and 4^+ rotational excitations of the ground state give a ratio of $14.04/4.44 = 3.3$ in beautiful agreement with the ratio of $2(2+1)/4(4+1) = 3.2$ expected for a rigid rotator, $E_J \propto J(J+1)$, was already recognized early on.

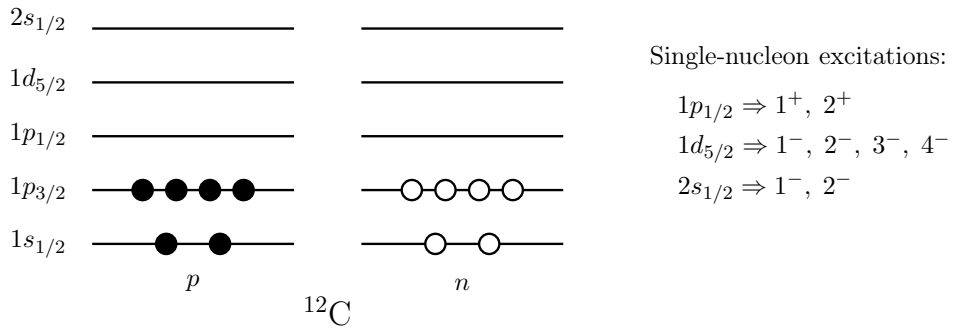

Figure 7.3: Simple shell-model description of the low-level structure of ^{12}C in terms of single-nucleon excitations.

Table 7.1: Level-structure of ^{12}C below 16 MeV according to the most recent compilation [AS90]. The threshold for proton decay is 15.96 MeV. Brackets indicate tentative assignments.

E_x (MeV ± keV)	$J^\pi; T$	Γ (keV)	Decay[a]
g.s.	$0^+; 0$	⋯	stable
4.43891 ± 0.31	$2^+; 0$	$(10.8 \pm 0.6) \times 10^{-6}$	γ
7.6542 ± 0.15	$0^+; 0$	$(8.5 \pm 1.0) \times 10^{-3}$	γ, π, α
9.641 ± 5	$3^-; 0$	34 ± 5	γ, α
10.3 ± 300	$(0^+); 0$	3000 ± 700	α
10.844 ± 16	$1^-; 0$	315 ± 25	α
(11.16 ± 50)	$(2^+); 0$	430 ± 80	
11.828 ± 16	$2^-; 0$	260 ± 25	γ, α
12.710 ± 6	$1^+; 0$	$(18.1 \pm 2.8) \times 10^{-3}$	γ, α
13.352 ± 17	$(2^-)^b; 0$	375 ± 40	γ, α
14.083 ± 15	$4^+; 0$	258 ± 15	α
15.110 ± 3	$1^+; 1$	$(43.6 \pm 1.3) \times 10^{-3}$	γ, α
15.44 ± 40	$(2^+; 0)$	1500 ± 200	
16.1058 ± 0.7	$2^+; 1$	5.3 ± 0.2	γ, p, α

[a] π means e^-e^+ pair creation.

[b] The Dalitz plot analysis of Chapter 12 firmly establishes the spin-parity of this state as 4^-.

The existence of two types of nucleons, namely, the proton and the neutron that are identical to the nuclear force, have nearly equal masses and only differ in their electric charge and magnetic moment, is reflected in the existence of pairs of states with same spin-parity but different isospin, T. A good example is provided by the 1^+ states at 12.71 MeV ($T = 0$) and 15.11 MeV ($T = 1$) which we may identify with isospin-symmetric and isospin-antisymmetric superpositions of single-proton and single-neutron excitations to the $1p_{1/2}$ orbital:

$$|15.11\rangle = \tfrac{1}{\sqrt{2}} \left(|\uparrow\downarrow\rangle + |\downarrow\uparrow\rangle \right) ,$$
$$|12.71\rangle = \tfrac{1}{\sqrt{2}} \left(|\uparrow\downarrow\rangle - |\downarrow\uparrow\rangle \right) ,$$

with $|\uparrow\rangle$ corresponding to the proton and $|\downarrow\rangle$ to the neutron. In reality, the 12.71 and 15.11 MeV states are not pure isospin states. The Coulomb interaction mixes the $T = 0$ and $T = 1$ states causing them to repel each other[2]. Physically, we may interpret the lowering of the $T = 0$ state as it having acquired an excess proton excitation[3]. The $T = 1$ state acquires an equivalent excess neutron excitation. Put more simply, the 12.71 MeV state looks more like $p + {}^{11}$B and the 15.11 MeV state more like $n + {}^{11}$C. This has observable consequences for the one-proton and one-neutron removal cross sections to the 12.71 and 15.11 MeV states [Ade77]. The 16 MeV doublet in ^{8}Be (Section 1.2.1.1) provides an extreme example of isospin mixing. Here, the two states are nearly fifty-fifty $T = 0$ and $T = 1$.

7.5.3 Microscopic Cluster Models

In the excitation region just above the triple-α threshold, one finds states of both shell-model and α-cluster character, prime examples, respectively, being the 1^+ state at 12.71 MeV and, of course, the 0^+ Hoyle state at 7.65 MeV. The coexistence of two such different excitation modes makes the theoretical description of ^{12}C particularly interesting.

α-Cluster models such as the one of [ÁR08b] which we return to later, *assume* the existence of α particles in the nucleus, i.e. ^{12}C is described as a three-body system. The microscopic cluster models do not make this assumption. They treat the nucleons on an individual basis. A realistic[4] two-nucleon potential plus a three-body potential is used to describe the interaction of the nucleons. The eigenstates of the twelve-body system are obtained by variational calculation using Gaussians for the single-

[2]This statement is true in general: When an interaction mixes two quantum states they repel each other.

[3]Proton excitation lowers the Coulomb energy because the time spent by the excited proton in the vicinity of the three protons left behind in the $1p_{3/2}$ orbital is reduced (to be precise, the overlap of their wave functions is reduced).

[4]By "realistic" is meant that the potential reproduces the phase shifts measured in nucleon-nucleon scattering and the properties of the deuteron.

nucleon wave functions. The α-cluster structure then *emerges* from the calculations, see e.g. [Che07].

α-Cluster states are difficult to describe in shell-model type approaches such as that of [Nav07], because large model spaces are required. See [For09] for recent progress in the shell-model description of losely bound nuclei. Microscopic cluster models such as antisymmetrised molecular dynamics (AMD) [KE07] and the closely related fermionic molecular dynamics (FMD) [Rot04], have been more successful in combining shell-model and cluster structures. Many reviews of the subject exist in the literature, see e.g. [Fre07a] and [Oer06].

By measuring the properties of ^{12}C resonances[5] we provide data against which the predictions of the various theoretical models can be tested thereby advancing our understanding of clustering phenomena and nuclear structure in general.

[5]By "resonance" is meant an excited state above particle-decay threshold. We shall be using the terms "resonance" and "excited state" interchangeably in the discussion that follows.

7.6 Concepts of *R*-Matrix Theory

Many of the energy spectra found in the present dissertation exhibit broad features which look very different from the standard Breit-Wigner distribution. *R*-matrix theory [Lan58, Vog04] provides a framework in which these broad features can be described in terms of physically meaningful parameters.

The short-range nature of the nuclear force plays a central role in the formulation of *R*-matrix theory. Consider the nuclear decay $A \rightarrow B + C$ (or, conversly, the fusion reaction $B + C \rightarrow A$). The short range of the nuclear force implies that beyond a separation of a few fm, B and C only interact electromagnetically. Accordingly, we divide space in two regions: An external region, $r > a$, where B and C only interact electromagnetically and an internal region, $r < a$, where the nuclear force is felt.

In the external region, we are dealing with a two-body Coulomb problem which we know how to solve. A solution exists for any energy $E > 0$. The wave function describing the relative motion of B and C in the external region may be written as a linear combination of an ingoing and outgoing wave. Formally, $\psi \sim xI + yO$. The ultimate goal is to determine the relative size and phase of the amplitudes x and y. Losely speaking, if the amplitude of the outgoing wave, y, is large compared to that of the incoming wave, x, the $A \rightarrow B + C$ decay amplitude is large and vise versa.

To determine x and y, we need to know what happens to the wave function in the internal region. Here the relative motion of B and C is governed by the Hamiltonian $H = K + V$ where V is the unknown nuclear potential. Unaware of the form of V, we cannot determine the eigenstates, $HX_\lambda = E_\lambda X_\lambda$, but we know that they exist and form a complete basis. Formally, we may write the internal wave function as a linear combination of the basis states, $\Psi = \sum C_\lambda X_\lambda$.

The information about what goes on in the internal region is mediated to the external region by the matching of the internal and the external solutions at the boundary $r = a$. The information, it turns out, is essentially contained in two quantities: The eigenenergies of the internal region, E_λ , and the surface integral,

$$\gamma_\lambda = \left(\frac{\hbar^2}{2\mu a}\right)^{1/2} \int_S X_\lambda^* \varphi \, \mathrm{d}S \, ,$$

where μ is the reduced mass of B and C and φ is the (energy-independent) angular part of the external wave function, ψ. The integral is to be performed over the boundary sourface. In *R*-matrix theory, we refer to the E_λ's as the *resonance energies* and to the γ_λ's as the *reduced widths*. Knowledge of the E_λ's and the γ_λ's enables us to calculate the ingoing and outgoing amplitudes, x and y, for a given energy, E. Conversly, a measurement of the these amplitudes, *viz.* the decay spectrum or reaction cross section, enables us to determine the E_λ's and the γ_λ's.

In the simple case of a single isolated level, *R*-matrix theory gives a parametrization similar to the standard Breit-Wigner form,

$$\rho(E) = \frac{1}{\pi} \frac{\frac{1}{2}\Gamma}{(E - E_\lambda + \Delta E)^2 + \left(\frac{1}{2}\Gamma\right)^2} , \tag{7.1}$$

with,

$$\Gamma = 2P_l(E)\gamma_\lambda^2 , \quad \Delta E = [S_l(E) - S_l(E_\lambda)]\gamma_\lambda^2 .$$

Here l is the orbital angular momentum of the relative motion of B and C, P_l is the penetrability which gives the probability for tunneling through the Coulomb and centrifugal barrier, and S_l is the so-called shift function. The penetrability, P_l, has a dramatic effect on states located close to the particle-decay threshold. Due to the smallness of P_l close to threshold, an intrinsically broad state, i.e. with a large reduced width, γ_λ, may appear as a very narrow state to the "outside world". The 0^+ Hoyle state in ^{12}C and the 0^+ ground state of ^{8}Be provide good examples of this effect. States close to particle-decay threshold may have an assymmetric shape with a reduced low-energy shoulder and an enhanced high-energy shoulder. The multiplication of the increasing penetrability factor with the decreasing Breit-Wigner tail may even result in the apperance of a "ghost state" [Bar62, Bar68, Bec81, Szc91] above the main peak, as shown in Fig. 7.4 and also beautifully illustrated in Fig. 1.7 of [Alc10]. Both the 0^+ Hoyle state in ^{12}C and the 0^+ ground state of ^{8}Be have associated ghost states.

In the presence of multiple levels of the same spin and parity, intereference effects occur which may significantly affect the shape of the spectrum, e.g. causing the

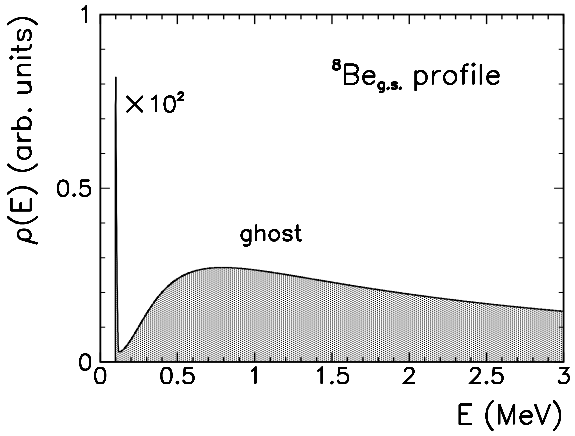

Figure 7.4: Profile of the ^{8}Be ground state calculated from Eq. 7.1 using E_λ = 92 keV, γ_λ^2 = 896 keV, l = 0 and r_0 = 1.41 fm. The very narrow ground-state peak has been replaced with a Gaussian of width σ = 10 keV of the same area and scaled down by a factor 100.

spectral maximum to be shifted compared to the "true" resonance energy, E_λ. The destructive interference around 3 MeV in the β-delayed α spectrum of ^{20}Na (Fig. 6.2) gives a striking example of such intereference phenomena.

The radius[6], a, enters the calculation of P_l and S_l. The choice of a is a source of concern in all applications of R-matrix theory aiming for the determination of physically meaningful levels energies, E_λ , and, in particular, reduced widths, γ_λ; see the discussion in [War86, Hyl10a]. One usually takes $a = r_0(A_B^{1/3} + A_C^{1/3})$ where A_B and A_C are the mass numbers of B and C and $r_0 = 1.4 - 1.5$ fm.

7.6.1 The Wigner Limit γ_W

In the classical picture of α decay, the decay rate has three contributions: (i) The probability for the α particle to be formed, (ii) the rate at which it collides with the barrier and (iii) the probability for it to tunnel through the barrier. In R-matrix theory, the penetrability, P_l, accounts for (iii) while the reduced width, γ_λ, accounts for (i) and (ii).

The Wigner limit, $\gamma_W^2 = \frac{\hbar^2}{\mu a^2}$, gives a rough upper limit on the reduced width. In the classical picture of α decay, the Wigner limit corresponds to setting the probability for the α particle to be formed equal to unity. Then, the reduced width simply equals the collision rate. If an excited nuclear state has a reduced width comparable to the Wigner limit, it is indicative of it possessing α-cluster structure.

An order-of-magnitude derivation of the Wigner limit can be made by placing the α particle in the ground state of a infinite nuclear well of radius a. Then, its energy is $E \sim \hbar^2/ma^2$ and its velocity $v \sim \hbar/ma$, meaning that it collides with the barrier at a rate of $v/a = \hbar/ma^2$, corresponding to a width of $\hbar^2/ma^2$.

[6] The radius, a, is often referred to as the *channel radius*.

CHAPTER 8

Reactions Induced by ^{3}He on ^{10}B and ^{11}B

To study the properties of ^{12}C resonances, we must first find a way to populate them. Below, we discuss how ^{12}C resonances are populated by shooting a beam of ^{3}He ions on targets of ^{10}B and ^{11}B. Kinematical curves are used to identify competing reaction channels. The angular distributions of the reaction products are used to shed light on the reaction mechanism leading to the formation of ^{12}C.

8.1 Reaction Channels

The following four-body final-state reactions (with the Q value given in MeV) were measured,

$$\begin{aligned} &\text{(i)} && {}^3\mathrm{He} + {}^{10}\mathrm{B} \;\rightarrow\; p + \alpha + \alpha + \alpha + 12.4 \\ &\text{(ii)} && {}^3\mathrm{He} + {}^{11}\mathrm{B} \;\rightarrow\; d + \alpha + \alpha + \alpha + 3.2 \\ &\text{(iii)} && {}^3\mathrm{He} + {}^{7}\mathrm{Li} \;\rightarrow\; n + p + \alpha + \alpha + 9.6 \end{aligned}$$

at beam energies of 4.9, 8.5 and 2.45 MeV respectively. The reactions were measured in complete kinematics, meaning that all four final-state momenta were determined experimentally. Neither of the three reactions have previously been measured in complete kinematics. Reaction (iii) offers the possibility to study the decay of ^{9}Be resonances populated in the $^3\mathrm{He} + {}^7\mathrm{Li} \rightarrow p + {}^9\mathrm{Be}$ reaction. It differs from (i) and (ii) by the presence of a neutron in the final state which is not detected with the present detector array. The present discussion deals only with reactions (i) and (ii).

In the center of mass system (CM), the combined kinetic energy of the beam and the target is

$$E_{\mathrm{CM}} = \frac{M}{m+M} E_{\mathrm{beam}} \,,$$

with E_{beam} denoting the beam energy and m and M denoting the masses of the beam and the target. It follows that the CM kinetic energies in reactions (i) and (ii) are $\frac{10}{13}4.9 = 3.8$ MeV and $\frac{11}{14}8.5 = 6.7$ MeV, respectively. These energies may be compared

to the Coulomb barrier height,

$$B = \frac{1.4zZ}{r} \text{ MeV fm} ,$$

where z and Z are the electric charges of the beam and the target; r is the sum of the nuclear radii which we here approximate as $r \approx 1.2(a^{1/3} + A^{1/3})$ fm, where a and A are the mass numbers of the beam and the target. Inserting numbers, we find $r \approx 4.4$ fm and $B \approx 3.2$ MeV, showing that reactions (i) and (ii) both occur above the barrier.

Reaction (i) has previously been studied by Waggoner *et al.* in 1966 [Wag66] at beam energies of 2.45 and 6.0 MeV with an experimental setup that allowed for the coincident detection of two final-state particles. The reaction was found to proceed to the four-body final state by three different channels:

$$^{3}\text{He} + ^{10}\text{B} \rightarrow \left\{ \begin{array}{l} p + ^{12}\text{C} + 19.7 \\ \alpha + ^{9}\text{B} + 12.1 \\ ^{5}\text{Li} + ^{8}\text{Be} + 10.4 \end{array} \right\} \rightarrow p + \alpha + \alpha + \alpha ,$$

with Q values given in MeV. Our primary interest is with the first channel, $p + ^{12}$C, which holds information on the resonance structure of ^{12}C. Excited states in ^{12}C populated in the $p + ^{12}$C reaction, appear as peaks in the CM energy spectrum of the proton. Similarly, excited states in ^{9}B populated in the $\alpha + ^{9}$B reaction, appear as peaks in the CM energy spectrum of the primary α particle. Narrow states give rise to sharp peaks whereas broad states give rise to broad features that are not easily recognizable. Channels involving very broad resonances ($\Gamma \sim 1$ MeV) often overlap kinematically, meaning that they are indistinguishable on the event-by-event basis. Having measured the four-body final state in complete kinematics, we are in a better position than Waggoner *et al.* to disentangle these broad channels, cf. Chapter 10.

Reaction (ii) has previously been studied only through measurements of the deuteron singles spectrum [Hin61, Mil69, Rey71]. Referring to reaction (i), we expect reaction (ii) to proceed to the four-body final state by the following channels,

$$^{3}\text{He} + ^{11}\text{B} \rightarrow \left\{ \begin{array}{l} d + ^{12}\text{C} + 10.5 \\ \alpha + ^{10}\text{B} + 9.1 \\ ^{6}\text{Li} + ^{8}\text{Be} + 4.6 \end{array} \right\} \rightarrow d + \alpha + \alpha + \alpha$$

Again, our primary interest is with the first channel, $d + ^{12}$C.

The maximum orbital angular momenta involved in the ^{3}He$+^{10,11}$B reactions may be estimated by assuming that for reactions to occur, the surface of the two nuclei must touch, i.e. the impact parameter can be no larger than the sum of the nuclear radii, $r \approx 4.4$ fm. Then,

$$L_{\text{max}} \approx r\mu v ,$$

where $\mu = \frac{mM}{m+M}$ is the reduced mass of the beam and the target and $v = (2E_{\mathrm{CM}}/\mu)^{1/2}$ is their relative velocity. Inserting numbers, we find $L_{\max} \approx 2.8\hbar$ for the ^{3}He + ^{10}B reaction at 4.9 MeV and $L_{\max} \approx 3.5\hbar$ for the ^{3}He + ^{11}B reaction at 8.5 MeV. Given the ground-state spins of the nuclei involved (^{3}He is $\frac{1}{2}^+$, ^{10}B is 3^+ and ^{11}B is $\frac{3}{2}^-$), we conclude that excited nuclear states with spins up to 6–7$\hbar$ are within reach. Parity conservation imposes no further constraints: Any combination of spin and parity is allowed. Finally, it is easily verified that in isospin conserving reactions only $T = 0, 1$ states in ^{12}C are accessible in the ^{3}He + ^{10,11}B reactions.

8.2 Kinematical Curves

In any two-body reaction, $1 + 2 \rightarrow 3 + 4$, the CM energies of the reaction products, E_i^*, are uniquely determined by energy and momentum conservation. When transformed to the laboratory system (in which particle 2 is assumed to be at rest), the energies depend on the angle relative to the beam axis. The correspondence between the laboratory energies, E_i, and the laboratory angles, θ_i, is one-two-one if CM velocity of particle i is larger than the boost velocity, i.e. the velocity of the laboratory system relative to the CM system. If, on the other hand, the CM velocity of particle i is smaller than the boost velocity, two energies are possible for each angle (but only one angle for each energy). In both cases, the relation between E and θ can be represented as a continuous curve, referred to as the kinematical curve. The result of a classical derivation is

$$E_3 = \frac{m_1 m_3}{m_2^2} E_1 \left\{ \frac{\cos\theta_3 \pm \left[\left(1 + \frac{m_1}{m_2}\right)^2 \frac{m_2^2}{m_1 m_3} \frac{E_3^*}{E_1} - \sin^2\theta_3 \right]^{1/2}}{1 + \frac{m_1}{m_2}} \right\}^2 ,$$

where $Q = m_1 + m_2 - m_3 - m_4$ is the Q value of the reaction (with $c = 1$) and

$$E_3^* = \frac{1}{1 + \frac{m_3}{m_4}} \left(\frac{1}{1 + \frac{m_1}{m_2}} E_1 + Q \right)$$

is the CM kinetic energy of particle 3. When the CM velocity of particle 3 is smaller than the boost velocity, both signs are allowed. When the CM velocity of particle 3 is larger, only the plus sign is allowed, in which case E_3 is a decreasing function of θ_3 from 0 to 180 degrees. This corresponds to the situation encountered in Fig. 8.1 which shows the proton energy versus angle in the ^{3}He + ^{10}B reaction. A multitude of kinematical curves are seen in the singles spectrum (a). Restricting our attention to events in which three α particles are detected in coincidence with the proton (b), we find that only kinematical curves due to the p + ^{12}C channel survive. Each curve may be identified with the population of a certain excitation energy in ^{12}C as indicated

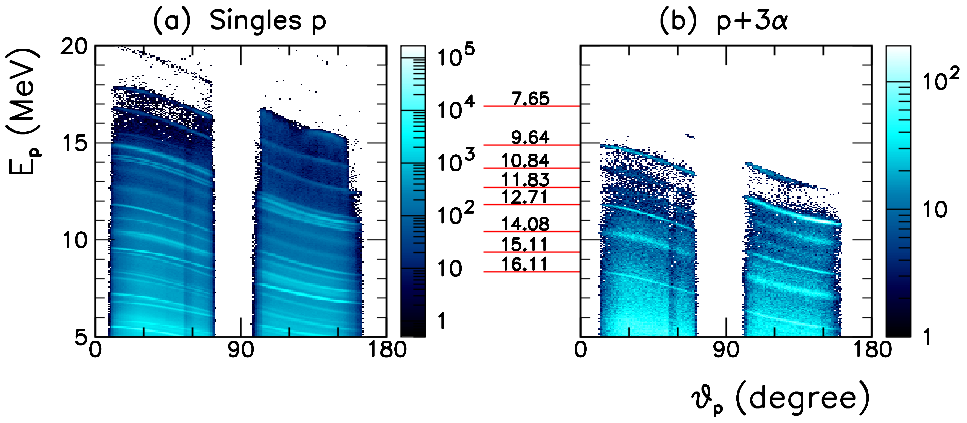

Figure 8.1: (a) Proton energy versus angle using singles data from the ^{3}He + ^{10}B reaction. **(b)** Proton energy versus angle using multiplicity four data (p+3α) from the ^{3}He+^{10}B reaction. The kinematical curves present in both spectra are due to the p + ^{12}C channel. The corresponding excitation energies in ^{12}C are indicated.

in the figure. The kinematical curves corresponding to the population of the ground state and first excited state in ^{12}C are not seen in (b) since these states are bound. The addition kinematical curves, present only in the singles spectrum, are due to reactions on ^{11}B (present at the level of 10% in the ^{10}B target) and reactions on the carbon backing:

$$^{3}\mathrm{He} + {}^{11}\mathrm{B} \rightarrow p + {}^{13}\mathrm{C}$$
$$^{3}\mathrm{He} + {}^{12}\mathrm{C} \rightarrow p + {}^{14}\mathrm{C}$$
$$^{3}\mathrm{He} + {}^{13}\mathrm{C} \rightarrow p + {}^{15}\mathrm{N}$$

The heavier the recoil nucleus, the shallower the kinematical curve.

8.3 Reaction Mechanism

Though not our primary interest, the reaction mechanism leading to the formation of the ^{12}C resonances that we wish to study, cannot be completely disregarded.

The reaction mechanism manifests itself most strongly in the CM angular distributions of the protons and deuterons. This is seen in Fig. 8.2 which displays angular distributions corresponding to the population of two selected states in ^{12}C, namely, the 0^{+} Hoyle state at 7.65 MeV and the 1^{-} state at 10.84 MeV. The angular distributions have been extracted from the singles data by gating on the corresponding

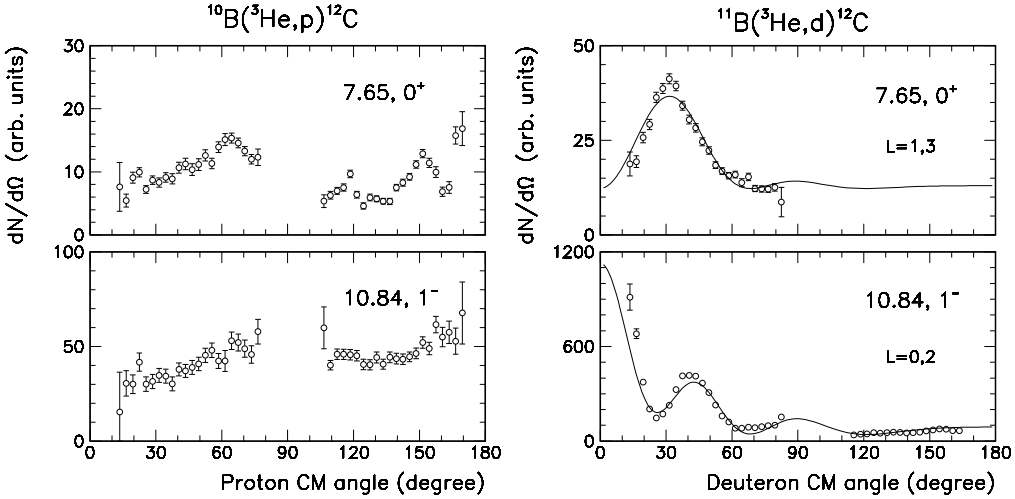

Figure 8.2: Proton and deuteron CM angular distributions in the ^{10}B(^{3}He, p)^{12}C and ^{11}B(^{3}He, d)^{12}C reactions, populating the 0^+ Hoyle state at 7.65 MeV and the 1^- state at 10.84 MeV. The deuteron angular distributions were fitted with the simple model outlined in Section 8.3.1.

kinematical curves in the E-θ plot and have been corrected for experimental effects through the use of simulations. The background contribution from overlapping channels was estimated by examining the E-θ plot and subtracted. It was not possible to extract the deuteron angular distribution at backward angles for the Hoyle state due to it overlapping with the much more intense ^{10}B(^{3}He, d)^{11}C$_{gs}$ channel. The deuteron angular distributions are peaked at forward angles and exhibit a diffraction pattern characteristic of direct reactions, in this case a one-proton transfer. The proton angular distributions, in contrast, are rather uniform, indicating a dominant compound contribution over the entire angular range.

From our point of view, the most important aspect of the angular distributions are their effect on the complete kinematics detection efficiency: The three α particles resulting from the decay of ^{12}C are kinematically focused by the motion of the ^{12}C nucleus. Consequently, the probability of detecting the α particles depends on the direction of motion of the ^{12}C nucleus which, in turn, is determined by the direction of motion of the proton/deuteron, *viz.* the proton/deuteron angular distribution. The effect may be an overall increase or reduction in the probability of detecting the 3α decay of a certain ^{12}C resonance in complete kinematics. This is relevant to the determination of the γ-branching ratios in Chapter 11. The effect may, however, also be a distortion of the observed α-particle energy distributions. This is relevant to the

Dalitz plot analysis in Chapter 12. The effects are accounted for by including the angular distributions extracted from the data in the Monte Carlo simulations (Section 9.4).

The reaction mechanism may also manifests itself in spin degrees of freedom, i.e. as alignment/polarization of the ^{12}C nuclear spin, giving rise to angular correlations between the proton/deuteron and the orientation of the $^{12}\mathrm{C} \rightarrow 3\alpha$ decay. Such correlations are indeed observed in the $^{3}\mathrm{He} + {}^{11}\mathrm{B} \rightarrow d + {}^{12}\mathrm{C}$ reaction proceeding via the 3^- state at 9.64 MeV. The correlations are primarily seen at forward angles (where the direct reaction mechanism is dominant) whereas correlations are essentially absent at backward angles (where the compound mechanism is dominant). This difference in behavior is not surprising. The effects of angular correlations induced by spin alignment/polarization are discussed in relation to the Dalitz plot analysis (Chapter 12).

8.3.1 Diffraction-Pattern Analysis

The diffraction pattern seen in the angular distribution resulting from a direct reaction is characteristic of the orbital angular momentum transfers, L, involved in the reaction. The steep rise seen at small angles in the case of the 10.84 MeV state is, for instance, characteristic of an $L = 0$ transfer.

The angular momentum transfer, L, is, in turn, related to the spin and parity of the resonance populated in ^{12}C. This may be seen in the following way: Let $\boldsymbol{S_\alpha}$ and $\boldsymbol{L_\alpha}$ denote the total spin and orbital angular momentum in the entrance channel. Similarly, let $\boldsymbol{S_\beta}$ and $\boldsymbol{L_\beta}$ denote the total spin and orbital angular momentum in the exit channel. Angular momentum conservation demands $\boldsymbol{S_\alpha} + \boldsymbol{L_\alpha} = \boldsymbol{S_\beta} + \boldsymbol{L_\beta}$. Rearranging, we obtain

$$\boldsymbol{L_\alpha} - \boldsymbol{L_\beta} = \boldsymbol{S_\beta} - \boldsymbol{S_\alpha} \, .$$

The momentum transfers, $\boldsymbol{L} = \boldsymbol{L_\alpha} - \boldsymbol{L_\beta}$, allowed by angular momentum conservation thus are

$$L = |S_\beta - S_\alpha|, \ldots, |S_\beta + S_\alpha| \, . \tag{8.1}$$

The spins in the entrance channel may couple to $S_\alpha = 1, 2$ and the parity in the entrance channel is $(-1)^{1+L_\alpha}$ (^{3}He is $\frac{1}{2}^{+}$ and ^{11}B is $\frac{3}{2}^{-}$). Considering first the 0^+ Hoyle state at 7.65 MeV, we find that the only possible spin in the exit channel is $S_\beta = 1$ and the parity is positive (d is 1^+). Invoking parity conservation and using Eq. 8.1, we conclude that the possible angular momentum transfers are $L = 1, 3$. Applying the same analysis to the 1^- state at 10.84 MeV, we find that the possible momentum transfers are $L = 0, 2$.

In a crude approximation [Sat90], the transition amplitude, T, for a single angular momentum transfer, L, is proportional to the spherical Bessel function of the corre-

sponding order,

$$T \propto j_L(qR) .$$

Here, R is the collision radius and q is the momentum transfer:

$$q = |\boldsymbol{q}| = |\boldsymbol{k_\alpha} - \boldsymbol{k_\beta}| = k_\alpha^2 + k_\beta^2 - 2k_\alpha k_\beta \cos\theta ,$$

with θ being the scattering angle and $\boldsymbol{k_\alpha}$ and $\boldsymbol{k_\beta}$ being the initial and final-state relative momenta in units of $\hbar$. Allowing for the coherent contribution of the two lowest permitted momentum transfers, L and $L + 2$, we obtain the following expression for the angular distribution,

$$\frac{\mathrm{d}N}{\mathrm{d}\Omega} \propto |T|^2 \propto |\, j_L(qR) + re^{i\phi} j_{L+2}(qR)\,|^2 ,$$

with $0 \leq r \leq 1$. Fits to the experimental angular distributions, including a constant offset to account for the compound contribution, are shown in Fig. 8.2. In general, the diffraction patterns are well reproduced. This is true also for the other states populated in ^{12}C. The radius was allowed to float and $R \approx 4.0$ fm was consistently obtained.

The spin-parity information that can be extracted from the angular distributions in an analysis this simple is rather limited. Nonetheless, it nicely complements the information extracted from the Dalitz plot analysis. The present experimental setup was not optimized for angular-distribution studies. In this respect, the singles measurements performed back in the 1960s and 1970s [Hin61, Mil69, Rey71] were more sophisticated, both in terms of the experimental approach and in terms of the theoretical analysis.

CHAPTER 9

Experiment and Data Reduction

The experiment was performed at the Centro de Microanálisis de Materiales (CMAM) located at the Universidad Autónoma de Madrid, Spain. Pilot studies were conducted in 2005 and 2006. Drawing on the experience gathered from these studies [Kir08], the experimental setup was improved before a final study was conducted in March 2008.

Section 9.1 and 9.2 give a brief description of the 2008 experimental setup. For a comprehensive account, see the PhD dissertation of M. Alcorta [Alc10]. Section 9.3 gives an overview of the initial part of the data analysis, concerned with the transformation of raw data into physics events. The various cuts imposed on the data are introduced. As a check of self consistency, random coincidence rates are extracted from the data and compared to the rates expected. The internal calibration of the geometry and the E detectors is discussed. Finally, Section 9.4 gives a brief description the Monte Carlo simulations which constitute an indispensable tool for the data analysis.

9.1 Beam, Targets and Detectors

The $^3He^-$ ions were produced through the use of a duoplasmatron ion source and accelerated to their final energy in a 5 MV tandem accelerator, providing a very stable beam with a energy resolution of a few tens of eV. Typical beam intensities on target were 1–2 nA.

The targets, prepared to us by J. Chevallier at Aarhus University, were made as thin as possible to minimize the energy loss of the reaction products. Their thickness and composition is given in the table of Fig. 9.1.

The detection system consisted of four, 60 μm thick, double sided silicon strip detectors (DSSSD), backed by unsegmented silicon detectors of varying thickness, from 1.0 to 1.6 mm. The intrinsic resolution of the DSSSDs was 35 keV (FWHM) and the intrinsic resolution of the back detectors was 40–50 keV (FWHM). The detectors were arranged as shown in Fig. 9.2 about 4 cm from the target, with two of them covering 7–75 degrees to the beam and two others covering 98–170 degrees, thereby obtaining a total solid-angle coverage of 38% of 4π. One DSSSD had 32×32 strips

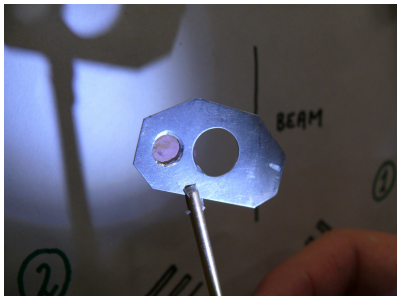

Target	Thickness (μg/cm^2)	Composition
^{10}B	18.9	90% enriched in ^{10}B
^{11}B	22.0	natural B
^{7}Li	33.1	natural LiF

All targets have a 4 μg/cm^2 carbon backing.

Figure 9.1: Table giving the thickness and composition of the three targets and picture of the ^{10}B target prior to beam exposure. During transport from Aarhus to Madrid, the foil had detached from the support frame. O. Tengblad saved the experiment from failure by drilling a new smaller hole in the support frame over which the intact part of the foil was placed.

of 2 mm width, the other three 16×16 strips of 3 mm width, resulting in an angular resolution of 2 and 3 degrees, respectively. The detectors were arranged to maximize multi-particle detection. This entailed placing two detectors as close as possible to zero degrees in order to detect α particles with low center of mass energies which are strongly kinematically focused in the forward direction. The limit to how close to zero degrees we can place the detectors, is set by the large flux of Rutherford scattered beam. Placing the detectors too close to zero degrees results in too many random coincidences and may even damage the detectors.

The arrangement consisting of a thin detector in front of a thick detector, enables particle identification through the ΔE-E method (Section 9.3.3). The thin detector placed in the front is sometimes referred to as the ΔE detector, and the thicker detector placed behind is referred to as the E detector. The combined arrangement is referred to as a ΔE-E telescope.

The three 16×16 DSSSDs used in the present setup are of the same novel design as the four 16×16 DSSSDs used for the ^{8}B experiment in Jyväskylä, Finland, with an Al grid covering only 3% of the surface. The 32×32 DSSSD is of the standard design with an Al layer covering the entire surface. An account of the design and performance of the novel-design DSSSD is given in [Ten04]. For a general description of silicon detectors, see e.g. [Kno00].

Energy calibrations were performed with the standard α sources ^{148}Gd and ^{241}Am, giving calibrations points at 3.2 and 5.5 MeV, respectively. The α-particle energies were corrected for the energy loss in the detector dead layers. The calibrations of the E detectors were found to be inaccurate at the level of a few tens of keV when applied to the most energetic proton and deuteron groups which deposit over 10 MeV. To correct for this, the E detectors were recalibrated as described in Section 9.3.7.

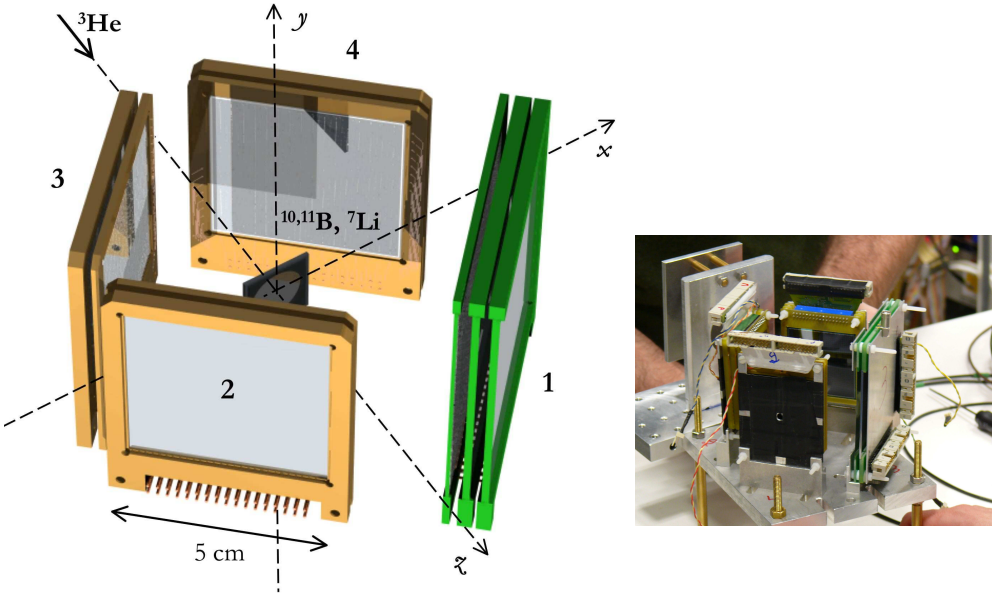

Figure 9.2: Detector setup: Four ΔE-E telescopes (numbered 1–4) surrounding the target with the beam coming in from the top left corner. The xyz coordinate system is used in the analysis. The picture shows the fully assembled detector setup prior to insertion into the chamber.

9.2 Electronics and Data Acquisition

The description of the data acquisition system given below is deliberately simplified and omits many details. The intention is to give an overview of the *modus operandi* of the data acquisition system and explain the basic functions of the electronic modules. For a detailed account, see [Alc10].

A schematic and simplified diagram of the data acquisition system is shown in Fig. 9.3, along with a picture showing what the data acquisition system looks like in real life. The electronic signal from the detector is fed to the preamplifier, the output of which is a fast-rising few-millivolts pulse with a long tail on the order of 100 μs. This signal is fed to the amplifier for further amplification and shaping. The output of the amplifier is a few-volts Gaussian pulse with a width on the order of 1 μs, referred to as the energy signal, which is fed to the ADC (Analog-to-Digital Converter). To eliminate noise, the amplifier has a built-in discriminator which checks that the signal is above the chosen threshold level.

In addition to the energy signal, the amplifier generates two logic signals. One signal, referred to as the timing signal, is fed, with a delay, to the TDC (Time-to-Digital

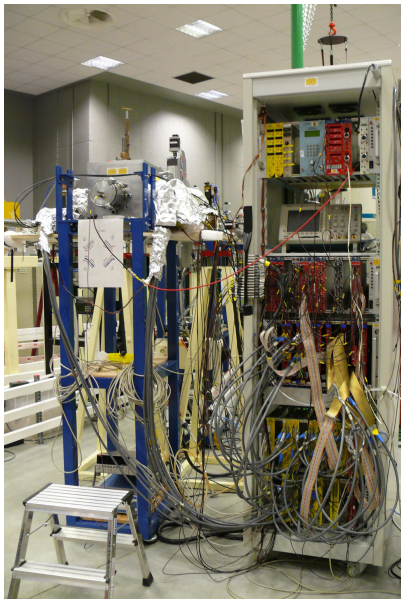

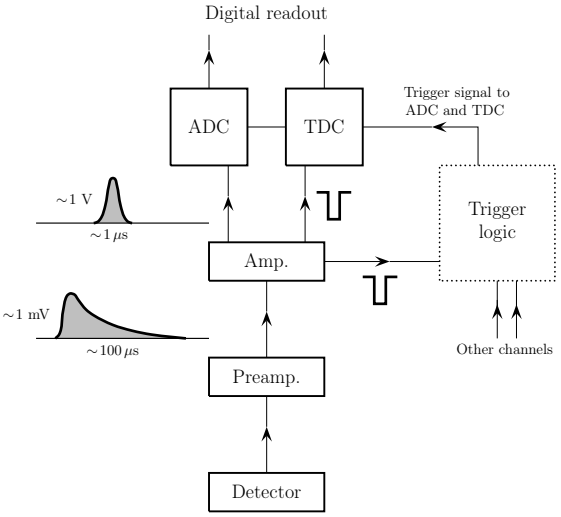

Figure 9.3: Left: Picture of the experimental setup. The chamber is positioned on top of the blue support, flanked by the preamplifiers wrapped in aluminum foil to reduce noise. Amplifiers, ADC and TDC modules as well as other electronic modules are located in the gray rack. **Right:** Schematic, simplified, diagram of the data acquisition system.

Converter). The other signal is fed to a system of standard electronic modules which constitute the trigger logic of the data acquisition system. Here it meets with equivalent signals from other channels. Simple AND and OR operations are performed and, if accepted, a trigger signal is sent to the ADC and TDC modules with the purpose of notifying them of the impending arrival of the energy and timing signals. Following the receipt of this message, the ADC and TDC modules are alert for 2.5 and 2.15 μs, respectively. All signals arriving during this time span are processed by the ADC and TDC modules which, in the case of the ADC, entails determining the pulse height (proportional to the energy deposited in the detector) and, in the case of the TDC, entails determining the time difference between the trigger signal and the timing signal (giving the relative arrival times of the particles). At the closing of the data taking window, the contents of the ADC and TDC modules are converted to digital form and read out. During this 5.7 μs long period, the data acquisition system is effectively blinded (dead time).

In the present experiment, the four E detectors and the two DSSSDs positioned at backward angles (DSSSD 3 and 4) provided the trigger signals. A logic AND was imposed between signals from the front and back sides of the DSSSDs and a logic OR

between the DSSSDs and the E detectors. The forward-angle DSSSDs (1 and 2) were removed from the trigger due to the large flux of Rutherford scattered beam.

One important message to take away from this, admittedly very simplified, description of the data acquisition system is that all particles striking the detectors during the 2.5 μs long data taking window are recorded to the same event in the data structure, even though the particles may originate from distinct physical events. Fortunately, the timing information from the TDC modules can be used to discriminate between such random coincidences and real coincidences. Our ability to discriminate between random and real coincidences is, however, somewhat reduced because the amplifiers used in the present experiment employ a leading-edge-type discriminator. This causes an effect known as "walk" in the timing signal and results in a time resolution of 100 ns (FWHM). In comparison, a resolution on the order of 1 ns can be achieved with constant-fraction-type discriminators.

9.3 Data Reduction

9.3.1 TDC gate

The TDC (timing) information is used to clean the data for random coincidences. Given the 2.5 μs length of the data taking window and the 100 ns width of the TDC gate, all but 4% of the random coincidences are removed. The trigger/TDC thresholds were around 550 keV both for the DSSSDs and the E detectors. The ADC thresholds were set considerably lower, typically around 200 keV, meaning that energy signals between 200 and 550 keV can be detected, provided a coincident signal above 550 keV triggers the data acquisition system[1]. Sub-trigger signals do not give TDC information and hence should not be made subject to the TDC gate.

The rise in trigger efficiency, ε, is found to be well described by a Fermi function,

$$\varepsilon(E) = \frac{\varepsilon_0}{1 + \exp[-(E - E_0)/w]} \,,$$

with $\varepsilon_0 \approx 100\%$ and $w \sim 35$ keV, corresponding to a rise "time" of 150 keV (10–90%). The threshold levels quoted above refer to E_0, i.e. the energy at which the efficiency has reached 50%.

9.3.2 Front-Back Matching

The technique of matching energy signals from the front side and the back side of the DSSSDs has already been discussed in relation to the ^{8}B experiment (Section 2.3.8). The matching is more complicated for the high-multiplicity events encountered in

[1] This is possible because the pulse *height* is used for the trigger while the pulse *area* gives the energy.

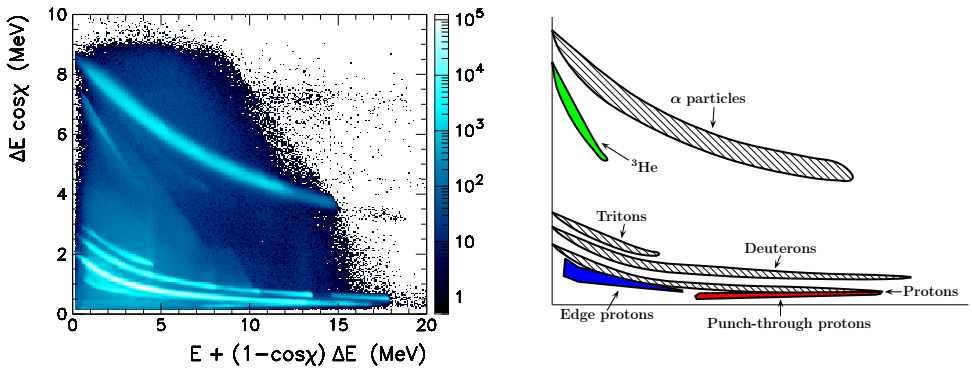

Figure 9.4: ΔE-E plot used for particle identification in the study of the ^{3}He + ^{11}B reaction at 8.5 MeV. The data is from detector 2.

the present analysis, but the basic approach is the same. Charge sharing between neighboring strips (Section 2.3.8) and summing (two particles hit the same strip) are responsible for a sub-class of events where the matching of front and back strips becomes particularly challenging. With two uncorrelated particles hitting the same detector the probability of them hitting the same strip is roughly 10%. In some special cases, notably the breakup of the ground state of ^{8}Be to two α particles, the probability of summing is increased due to the small relative velocity of the two α particles.

Charge sharing and summing are taken into account—to the extent to which we understand these phenomena—in the simulations (Section 9.4).

9.3.3 Particle identification by the ΔE-E method

Since the stopping power, $\frac{\mathrm{d}E}{\mathrm{d}x}$, of charged particles in matter depends on their charge, q, and velocity, $v = E/m$, we may uncover their identity by letting them deposit their energy in two slabs of silicon in stead of just one: The larger their stopping power, the larger a fraction of their energy they deposit in the first slab of silicon. This is the basic idea behind the ΔE-E method (ΔE is the energy deposited in the first slab of silicon and E is the energy deposited in the second slab of silicon).

Applying the ΔE-E method to the ^{3}He+^{11}B data from detector 2, we obtain Fig. 9.4. The DSSSD energy, ΔE, is along the ordinate, multiplied by $\cos\chi$ where χ is the angle of incidence on the detector ($\chi = 0°$ corresponds to normal incidence). To first order, the factor $\cos\chi$ removes the dependence of ΔE on the effective detector thickness. The energy deposited in the E detector, also corrected to first order, is along the abscissa. Bands of increased intensity (sometimes referred to as "bananas" owing to their characteristic shape) corresponding to protons, deuterons, tritons and

α particles are clearly seen. The most energetic protons punch through the E detector without depositing their full energy. Protons hitting the edge strips of the DSSSD may also fail to deposit their full energy. Some Rutherford scattered ^{3}He ions are seen forming a straight line of slope -1, corresponding to a fixed total energy of ≈ 8 MeV and suggesting that the ^{3}He ions have channeled through the DSSSD [Sig06].

In Fig. 9.4, the E-detector energy has been matched with all ΔE energies measured in the DSSSD, i.e. if a proton and an α particle of energies E_p and E_α hit the DSSSD depositing in it the energies ΔE_p and $\Delta E_\alpha = E_\alpha$, and the proton continues into the E detector depositing the rest of its energy $E = E_p - \Delta E_p$, then both the correct match $(E, \Delta E_p)$ and the wrong match $(E, \Delta E_\alpha)$ are shown in Fig. 9.4. In the large majority of such cases, the wrong match $(E, \Delta E_\alpha)$ falls outside the bananas so that an unambiguous identification can be made. If both matches fall inside a banana, we cannot tell which is the correct match so we usually discard the event. In multiplicity three and four events, such ambiguities can often be resolved by checking for energy and momentum conservation.

9.3.4 Energy-Loss Corrections

Having identified the particles, we can correct for their energy loss in the target and the dead layers of the detectors as described in Section 2.2. In calculating the energy loss in the target, we assume the reactions to occur uniformly throughout the thickness of the target. The dead layer on the front side of the 16×16 DSSSDs is only 100 nm thick[2]. The dead layer on the front side of the 32×32 DSSSD which is of the standard design with an Al layer covering the entire surface, is estimated to 0.9 μm. If the particle penetrates into the E detector, we must also correct for the 1 μm dead layer on the back side of the DSSSD and the 0.7 μm dead layer on the front side of the E detector.

9.3.5 Kinematical Cuts

The 100 ns width of the TDC gate allows for $\approx 4\%$ of the random coincidences to slip through. In addition, the TDC gate cannot be used to identify random coincidences involving particles with energies below the trigger level (≈ 550 keV). The complete kinematical information allows us to impose kinematical cuts on the multiplicity three and four events whereby the "left overs" from the TDC gate are significantly reduced.

[2]From the analysis of the ^{8}B experiment, we know that detector-to-detector variations of ± 20 nm occur. The effects of these variations are too small to be of any importance for the present study.

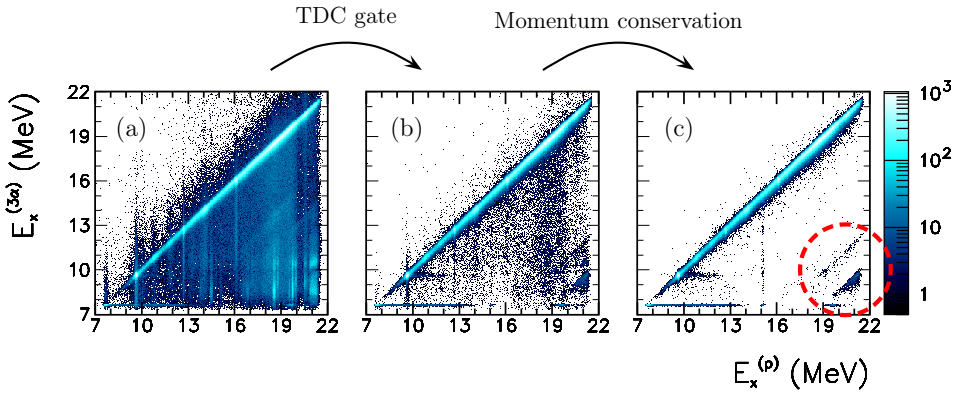

Figure 9.5: Cleaning the multiplicity-four data from the ^{3}He + ^{10}B reaction using the TDC gate and momentum conservation. **(a)** All p + 3α events. The ^{12}C excitation energy determined from the momentum of the proton, $E_x^{(p)}$, is along the abscissa and the ^{12}C excitation energy determined from the momenta of the three α particles, $E_x^{(3\alpha)}$, is along the ordinate. **(b)** p + 3α events surviving the TDC gate. **(c)** p + 3α events surviving both the TDC gate and the requirement of momentum conservation. The encircled events result from reactions on ^{11}B, present at the level of 10% in the ^{10}B target.

9.3.5.1 Multiplicity-Four Events

In multiplicity-four events, we always require the total momentum to be conserved,

$$\boldsymbol{p}_{^3\mathrm{He}} = \boldsymbol{p}_{p,d} + \boldsymbol{p}_{\alpha_1} + \boldsymbol{p}_{\alpha_2} + \boldsymbol{p}_{\alpha_3} \ .$$

Unless we are looking for γ transitions, cf. Chapter 11, we also require the energy to be conserved,

$$E_{^3\mathrm{He}} + Q = E_{p,d} + E_{\alpha_1} + E_{\alpha_2} + E_{\alpha_3} \ ,$$

where $Q = m_{^3\mathrm{He}} + m_{^{10,11}\mathrm{B}} - m_{p,d} - 3m_\alpha$ is the Q value (with $c = 1$).

The effect of the requirement of momentum conservation imposed on the p + 3α data sample, is shown in Fig. 9.5. The ^{12}C excitation energy determined from the momentum of the proton, $E_x^{(p)}$, is along the abscissa, and the ^{12}C excitation energy determined from the momenta of the three α particles, $E_x^{(3\alpha)}$, is along the ordinate. The TDC gate removes many of the random coincidences seen contaminating the plot away from the diagonal, but is unable to remove them all. With the added requirement of momentum conservation, the random-coincidence background is essentially gone. The encircled events in the bottom-right corner of Fig. 9.5 (c) result from reactions on ^{11}B, present at the level of 10% in the ^{10}B target. The higher-lying band is due to d + 3α final states with the deuteron wrongly identified as a proton.

The lower-lying band is due to $n + p + 3\alpha$ five-body final states with the neutron unobserved. The separation between the two bands is 2.2 MeV, equal to the binding energy of the deuteron. The two bands extending horizontally from the diagonal at $E_x^{(3\alpha)} = 7.65$ MeV and $E_x^{(3\alpha)} = 9.64$ MeV and the thin vertical band at $E_x^{(p)} = 15.11$ MeV are discussed in Chapter 11.

If, additionally, energy conservation is imposed, all the non-diagonal events in Fig. 9.5 (c) disappear. The combined effect of requiring momentum and energy conservation is to reduce the multiplicity-four data sample by roughly 7%.

9.3.5.2 Multiplicity-Three Events

We only consider multiplicity-three events in which the proton/deuteron is one of the three detected particles. The energy of the third, unobserved, α particle can be determined, either from momentum conservation,

$$E_{\alpha_3} = \frac{p_{\alpha_3}^2}{2m_\alpha} \qquad \boldsymbol{p}_{\alpha_3} = \boldsymbol{p}_{^3\mathrm{He}} - (\boldsymbol{p}_{p,d} + \boldsymbol{p}_{\alpha_1} + \boldsymbol{p}_{\alpha_2}) \,,$$

or from energy conservation,

$$E_{\alpha_3} = E_{^3\mathrm{He}} + Q - (E_{p,d} + E_{\alpha_1} + E_{\alpha_2}) \,.$$

The kinematical cut imposed on multiplicity-three events consists in requiring the two methods to yield the same answer within 0.5 MeV. This cut is not quite as efficient in removing the random coincidences left over from the TDC gate as the multiplicity-four cut. It reduces the multiplicity-three data sample by roughly 20%.

The ^{10}B(^{3}He, $p\alpha\alpha\alpha$) and ^{11}B(^{3}He, $d\alpha\alpha\alpha$) reactions often proceed via the narrow (Γ = 5.6 eV) ground state ^{8}Be, situated 92 keV above the 2α threshold. Experimentally, this is seen as a narrow peak at 92 keV in the ^{8}Be excitation energy spectrum shown in Fig. 9.6. The width of the peak represents the experimental resolution. *A priori*, we do not know which two α particles out of the three α particles in the final state, originate from the breakup of the ^{8}Be ground state. For each of the three possible combinations, we compute the corresponding ^{8}Be excitation energy by the invariant-mass method [Ams08]. If we combine the two observed α particles, α_1 and α_2, the spectrum labeled "Measured" in Fig. 9.6 results. The width of the peak is 40 keV (FWHM). If we combine either of the observed α particles with the unobserved α particle, α_3, the peak gets wider. If we use momentum conservation to determine the direction of the unobserved α particle but energy conservation to determine its energy, we get the very wide spectrum labeled "Energy". The width of the peak is 330 keV (FWHM). If we only use momentum conservation, we get the spectrum labeled "Momentum". The width of the peak is reduced to 80 keV (FWHM).

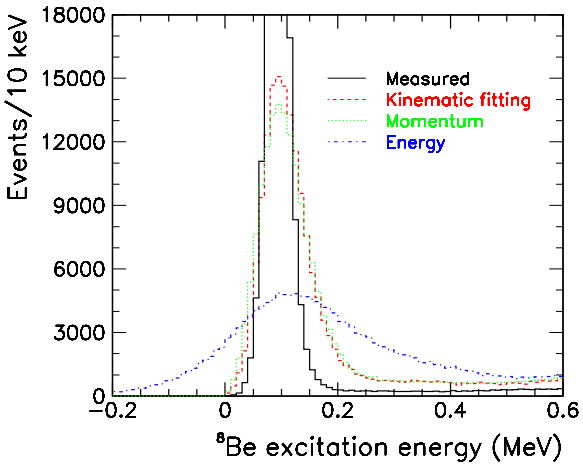

Figure 9.6: ^{8}Be excitation energy spectra extracted from multiplicity-three events ($p + 2\alpha$). The spectrum labeled "Measured" was obtained by using the two observed α particles. The other three spectra were obtained by using either of the observed α particles in combination with the unobserved α particle. The momentum of the observed α particle was reconstructed by three different methods (see text) giving different resolutions in the determination of the excitation energy as seen from the width of the ground-state peak.

The resolution may be further improved to 75 keV by performing *kinematic fitting*, a technique well known to particle physicists[3]. The general idea behind kinematic fitting is to use the know properties (constraints) of a given physical process to improve the measurements describing the process. In the present case there are three unknowns, namely, the three momentum components of the unobserved α particle, and four constraints from energy and momentum conservation. Typically, the three momentum components that satisfy momentum conservation will not also satisfy energy conservation, i.e. the problem is over constrained. The solution offered by kinematic fitting is simple: Roughly speaking, kinematic fitting consists in finding the three momentum components that best satisfy the four constraints while allowing for the measured quantities (the momenta of the proton/deuteron and the two other α particles) to vary within their estimated uncertainties, see [Fro79].

[3] I am indebted to Tord Johansson, Uppsala University, for introducing me to this technique.

9.3.6 Random Coincidences

Below, we examine random-coincidence rates with the purpose of checking the self consistency of the analysis.

First, we consider random coincidences between true[4] $p + 3\alpha$ coincidences and Rutherford scattered ^{3}He. These constitute multiplicity-five events, with one proton identified in the ΔE-E plot and four particles stopped in the DSSSDs. Energy and momentum conservation is used to decide which is the ^{3}He ion. We find 1.8×10^3 such random coincidences in the ^{3}He + ^{10}B data. How many should we expect to find? We observe a total of $Y = 7.1 \times 10^5$ true $p + 3\alpha$ coincidences. Based on the beam current measured in a Faraday cup, the target thickness and Monte Carlo simulations performed to account for geometric acceptance, we estimate the count rate due to Rutherford scattered ^{3}He to $R = 2.3 \times 10^4$ s^{-1}. (The count rate could not be directly measured because the forward-angle DSSSDs were not included in the trigger.) Since the TDC gate of the DSSSDs is 100 ns wide, we expect to see $Y \times R \times 100$ ns $= 1.6 \times 10^3$ random coincidences. This is in good agreement with the number observed.

Second, we consider reaction-reaction coincidences such as $(p + 3\alpha) + (p + 3\alpha)$ corresponding to an event with two protons and six α particles detected. To calculate the expected number of such random coincidences, we need to replace the rate of Rutherford scattered ^{3}He incident on the detectors, R, with the rate at which we detect true $p+3\alpha$ coincidences. We took data for 17.6 hours and observe $Y = 7.1 \times 10^5$ true $p+3\alpha$ coincidences so the rate is Y/17.6 hours $= 11$ s^{-1}. Then, using the slightly narrower TDC gate of the E detectors (70 ns), the expected number of $(p+3\alpha)+(p+3\alpha)$ random coincidences is $Y \times 11$ s$^{-1} \times 70$ ns $= 0.5$. We identify 0 in the data. Following the same line of reasoning, the expected number of $(p + 3\alpha) + (p + 2\alpha)$ random coincidences is $2.3 \times 10^6 \times 11$ s$^{-1} \times 70$ ns $= 1.8$, in good agreement with the 3 such events observed in the data.

This random coincidence identification technique can be used to extract true particle coincidences from higher multiplicity events. Given an event with a higher multiplicity than four, due to a beam-reaction or a reaction-reaction coincidence, we use momentum and energy conservation to extract the true four-particle coincidence, thereby increasing our multiplicity-four event sample. For example, be cleaning up the beam-reaction coincidences, we increase our sample by about 1%.

[4] The term "true coincidence" is used to designate coincidences surviving the kinematical cuts.

9.3.7 Internal Calibration

The energy calibration of the E detectors was performed with the standard α sources ^{148}Gd and ^{241}Am, giving calibrations points at 3.2 and 5.5 MeV. When extrapolated to 15 MeV which is the energy deposited by the most energetic protons and deuterons, the calibration was found to be inaccurate at the level of a few tens of keV. The geometry of the detector setup was measured with a standard ruler, but the delicate nature of the detectors makes it difficult to achieve accuracies better than 5 mm. Therefore, it was necessary to perform an internal calibration of the E detectors and the geometry of the setup.

In principle, the problem is easily solved: Find a number of observables that depend on the geometry and the E-detector calibration. Then vary the geometry and the calibration until all observables have the correct value. One such observable are the $p + {}^{12}$C kinematical curves of Fig. 8.1 which are sensitive to the E-detector calibration as well as the position of the individual detectors relative to the target. Another useful observable is the total momentum measured in multiplicity-four events which is sensitive to the geometry, while only weakly sensitive to the E-detector calibration. The difficulty is merely practical: It takes 5–10 minutes to execute the data analysis program and hence 5-10 minutes to evaluate the effect of every change in geometry or E-detector calibration on the observables.

Below, we describe one way to overcome this difficulty. Consider a particle of mass m and laboratory (lab) energy E emitted at an angle θ relative to beam axis. Since the CM energy, E^*, is a function of both E and θ, the change in E^* due to a change in lab energy, ΔE, and a change in lab angle, $\Delta\theta$, is

$$\Delta E^* = \frac{\mathrm{d}E^*}{\mathrm{d}E}\Delta E + \frac{\mathrm{d}E^*}{\mathrm{d}\theta}\Delta\theta \ .$$

Using non-relativistic kinematics, one easily finds,

$$\frac{\mathrm{d}E^*}{\mathrm{d}E} = 1 - \left(mv^2/E\right)^{1/2}\cos\theta \ , \qquad \frac{\mathrm{d}E^*}{\mathrm{d}\theta} = \left(2mv^2E\right)^{1/2}\sin\theta \ , \tag{9.1}$$

where v is the speed of the CM system relative to the lab system. As an example, $\frac{\mathrm{d}E^*}{\mathrm{d}E} = 0.91$ and $\frac{\mathrm{d}E^*}{\mathrm{d}\theta} = 22$ keV/degree for a 10 MeV proton emitted at 45 degrees.

Consider the CM energy spectrum measured in a single DSSSD pixel. As our observable, we select the CM energy of a proton group corresponding to a narrow state in ^{12}C, e.g. the 12.71 MeV state. Then, we have both θ and E fixed and may evaluate the derivatives using Eq. 9.1. These tell us how our observable, the CM energy of the proton group, is affected by changes in the calibration (ΔE) and changes in the geometry ($\Delta\theta$). Performing a simultaneous optimization to several states in all pixels, we get nice constraints on the geometry and the E-detector calibrations.

9.4 Monte Carlo Simulations

Monte Carlo simulations are indispensable for a quantitative comparison of experimental results to theory. To mention a few examples, we use simulations to determine the detection efficiency for the various γ branches studied in Chapter 11, and to determine the modification of the Dalitz plot intensity distributions studied in Chapter 12 due to experimental effects.

The simulations are structured in three parts: First, the physical description of the reaction process. Second, the simulation of the effects of the detection system. Third, the application of the analysis program to the simulated data.

In general, we describe the reaction process in terms of a sequential model: A path of dynamically independent two-body decays leads from the initial to the final state. Angular correlations may be present due to conservation of angular momentum and parity. The functional form can often be derived from theory [Bie53]. In the study of the $^{12}C \rightarrow 3\alpha$ breakup, other models than the sequential are also used. We obtain the angular distributions of the proton/deuteron from the experimental data and include them in the simulation. Intermediate resonances are usually described by the Breit-Wigner formula, but the effects of the penetrability in the entrance and exit channels are included when needed.

The second part of the simulation program, the one concerned with the detection of the final-state particles, takes into account the geometry of the detector setup and the response of the individual detectors to charged-particle radiation. The intrinsic energy resolution is described by a Gaussian function. We include effects of summing between coincident particles and charge sharing between neighboring strips. Energy losses in the target material and the detector dead layers are calculated using tabulated values of the stopping power of ions in solids [Zie08]. We correct for the pulse height defects of the different types of ions. Finally we include the experimental trigger logic and detection thresholds.

Simulated and physical events are saved in identical data structures. This makes it possible to pass the simulated data through exactly the same analysis program as used for the physical data, hence correcting for any bias introduced by the various cuts and gates imposed on the data.

CHAPTER 10

Reaction Channels and Resonances

In Section 10.1 and 10.2, the complete kinematics data is analyzed using two-dimensional energy spectra with the purpose of identifying the reaction channels leading to the $p + 3\alpha$ and $d + 3\alpha$ four-body final states. It is found useful to divide the reactions into two groups: Those that do proceed via the narrow ^{8}Be ground-state peak and those that do not. In Section 10.3, the energies and widths of the ^{12}C resonances observed in the present study are determined and compared to literature values. In Section 10.4, α-decay branching ratios to the ^{8}Be ground state are extracted. The role played by the "ghost" of the ^{8}Be ground state is discussed in detail. Finally, in Section 10.5, the $^{12}\mathrm{C} \rightarrow p + {}^{11}\mathrm{B}$ decay channel is briefly considered.

10.1 The ^{10}B(^{3}He, $p\alpha\alpha\alpha$) Reaction

As noted in the introduction (Chapter 8), this reaction was observed by [Wag66] to proceed via three different two-body channels: $p + {}^{12}$C, $\alpha + {}^9$B and ^{5}Li + ^{8}Be. In a two-dimensional spectrum with proton CM energies on the abscissa and α-particle energies on the ordinate, the $p + {}^{12}$C channel gives rise to vertical bands of increased intensity, corresponding to the proton CM energy being fixed. Similarly, the $\alpha + {}^9$B channel gives rise to horizontal bands of increased intensity, corresponding to the α-particle CM energy being fixed. The ^{5}Li + ^{8}Be channel gives rise to diagonal bands of increased intensity, corresponding to the total CM energy of the proton and the α particle from the breakup of ^{5}Li being fixed.

A 100 keV wide gate is placed on the ^{8}Be ground-state peak. The three α particles may be paired in three ways. For each combination, we calculate the ^{8}Be excitation energy. If any of the three combinations give an energy within the ground-state gate, we assume that the reaction did indeed proceed via the ground state of ^{8}Be. Then, the energy of the α-particle not originating from the $^8\mathrm{Be}_{\mathrm{gs}} \rightarrow 2\alpha$ breakup, is the one shown on the ordinate. If none of the three combinations give a ^{8}Be excitation energy within the ground-state gate, the α-particle energy is chosen at random[1].

[1] Other choices may be more instructive: If one is mainly interested in the α+^{9}B channel at low excitation

Reactions found to proceed via the ground state of ^{8}Be, are shown in Fig. 10.1. Reactions found *not* to proceed via the ground state of ^{8}Be, are shown in Fig. 10.2. The two-dimensional energy spectrum (c) is divided by the dashed vertical line into two regions: Region I corresponds to events in which the proton is stopped in the ΔE detector and hence has to be identified by kinematical cuts. Region II corresponds to events in which the proton penetrates into the E detector allowing for unambiguous identification by the ΔE-E method. The reduced intensity in region I reflects the reduced efficiency for identifying protons using kinematical cuts. Vertical and horizontal bands indicating the population of resonances in ^{12}C and ^{9}B, are clearly seen. Corresponding peaks are seen in the projected spectra (a) and (d). The diagonal band in Fig. 10.1 (c) corresponds to the population of the unbound $\frac{3}{2}^-$ ground state of ^{5}Li through the ^{5}Li + ^{8}Be channel. The equivalent band in Fig. 10.2 (c) is much more spread out due to the broad distribution of excitation energies populated in ^{8}Be. The ^{5}Li ground-state peak is clearly seen in the p-α relative energy spectrum (b). The $^5\text{Li}_{\text{gs}}$ + ^{8}Be contribution to the proton and α spectra has been attempted removed by gating on the ^{5}Li ground-state peak in the p-α relative energy spectrum, giving the blue dotted curve in the proton and α spectra. In general, the interpretation of the structures in Fig. 10.2 (c) is complicated by the random choice of the α-particle energy shown on the ordinate.

The proton and α groups observed in the projections of Fig. 10.1 and 10.2 are listed in Table 10.1 and 10.2. Starting with the protons, we note that all proton groups can be identified with known states in ^{12}C. The excitation energies, E_x , and quantum numbers, J^π; T, given in Table 10.1 are from the most recent $A = 12$ compilation [AS90]. Decays not proceeding via the ^{8}Be ground state are most often assumed to proceed via the 2^+ first-excited state at 3 MeV, even though the large width of this state makes the notion of a sequential decay rather problematic, an issue we shall return to in Chapter 12. The few decays of the Hoyle state ($E_x = 7.65$ MeV) not proceeding via the ^{8}Be ground state, represent intensity "leaking out" of the ground-state gate due to the experimental resolution, hence the brackets in Table 10.1.

Continuing with the α particles, we note that all four α groups can be identified with known states in ^{9}B. The few decays of the ^{9}B ground state not proceeding via the ^{8}Be ground state, represent intensity "leaking out" of the ground-state gate, hence the brackets in Table 10.2. Decays not proceeding via the ^{8}Be ground state are often described as proceeding via either the broad 2^+ state in ^{8}Be or the equally broad ground state in ^{5}He, see e.g. [Pre05, Pap07, Bro07, ÁR08a]. Again, the notion of a sequential decay is rather problematic.

Together, the proton groups of Table 10.1, the α groups of Table 10.2 and the $^5\text{Li}_{\text{gs}}$ +

energies, better choices, assuming a direct reaction mechanism, would be the most energetic α particle or the smallest-angle α particle.

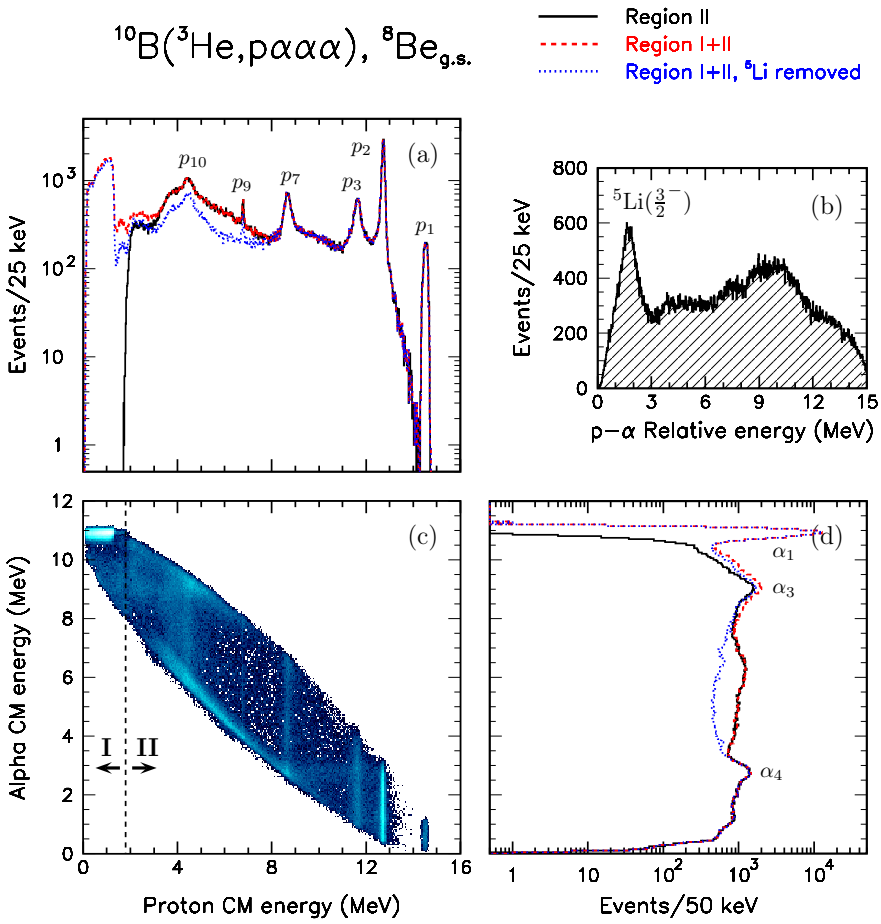

Figure 10.1: ^{10}B(^{3}He, $p\alpha\alpha\alpha$) complete kinematics data (multiplicity-four events only) with gate on the ^{8}Be ground-state peak. **(a)** Proton CM energy spectrum. **(b)** p-α Relative energy spectrum. **(c)** Two-dimensional energy spectrum with the proton CM energy on the abscissa and the α-particle CM energy on the ordinate. The intensity scale is logarithmic. Region I corresponds to events in which the proton is stopped in the ΔE detector and hence has to be identified by kinematical cuts. Region II corresponds to events in which the proton penetrates into the E detector allowing for unambiguous identification by the ΔE-E method. **(d)** α-Particle CM energy spectrum.

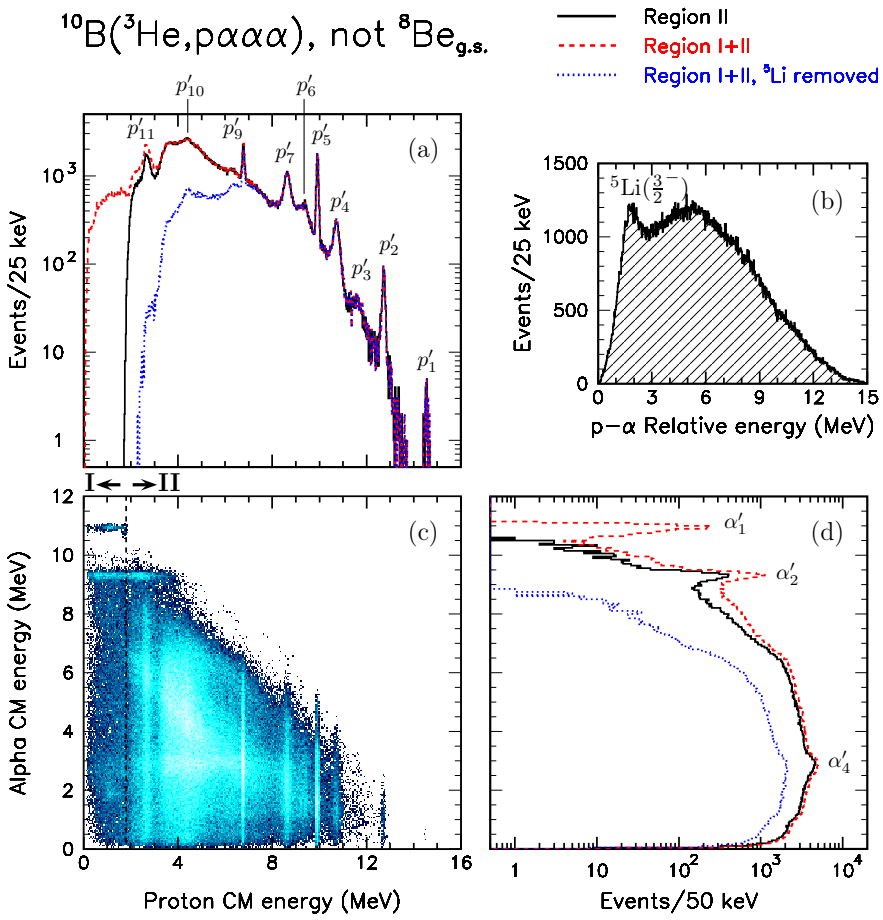

Figure 10.2: ^{10}B(^{3}He, $p\alpha\alpha\alpha$) complete kinematics data (multiplicity-four events only) with *anti*gate on the ^{8}Be ground-state peak. See the caption of Fig. 10.1 for details.

Table 10.1: Proton groups observed in the $^3\text{He} + {}^{10}\text{B} \rightarrow p + {}^{12}\text{C} \rightarrow p + 3\alpha$ reaction. Excitation energies, E_x , and quantum numbers, $J^\pi; T$, are from the most recent $A = 12$ compilation [AS90].

p Group	$E_{p,\text{CM}}$ (MeV)	E_x (MeV)	$J^\pi; T$	$^8\text{Be}_{\text{gs}}$	Not $^8\text{Be}_{\text{gs}}$
1	14.59	7.65	$0^+; 0$	×	(×)
2	12.76	9.64	$3^-; 0$	×	×
3	11.65	10.84	$1^-; 0$	×	×
4	10.74	11.83	$2^-; 0$		×
5	9.93	12.71	$1^+; 0$		×
6	9.33	13.35	$(2^-)^a; 0$		×
7	8.66	14.08	$4^+; 0$	×	×
8[b]	7.71	15.11	$1^+; 1$		
9	6.79	16.11	$2^+; 1$	×	×
10	4.39	18.71	[c] ; (1)	×	×
11	2.69	20.55	$(3^+; 1)$		×

[a] The Dalitz plot analysis of Chapter 12 firmly establishes the spin-parity of this state as 4^-.
[b] Only observed in the singles spectrum.
[c] Natural parity.

Table 10.2: α Groups observed in the $^3\text{He} + {}^{10}\text{B} \rightarrow \alpha + {}^9\text{B} \rightarrow p + 3\alpha$ reaction. Excitation energies, E_x , and quantum numbers, $J^\pi; T$, are from the most recent $A = 9$ compilation [Til04].

α Group	$E_{\alpha,\text{CM}}$ (MeV)	E_x (MeV)	$J^\pi; T$	$^8\text{Be}_{\text{gs}}$	Not $^8\text{Be}_{\text{gs}}$
1	11.01	0.00	$\frac{3}{2}^-; \frac{1}{2}$	×	(×)
2	9.38	2.36	$\frac{5}{2}^-; \frac{1}{2}$		×
3	9.08	2.79	$\frac{5}{2}^+; \frac{1}{2}$	×	
4	2.95	11.65	$\left(\frac{7}{2}\right)^-; \frac{1}{2}$	×	×

^{8}Be channel account for most of the intensity in the two-dimensional energy spectra. The intensity not accounted for may be due to broad resonances in ^{5}Li, ^{9}B and ^{12}C or some more direct reaction mechanism leading to the four-body final state without the formation of intermediate resonances. In any case, the concept of sequential reactions via very broad intermediate resonances must be approached with great care.

10.2 The ^{11}B(^{3}He, $d\alpha\alpha\alpha$) Reaction

The analysis of ^{11}B(^{3}He, $d\alpha\alpha\alpha$) reaction is essentially identical to the analysis of the ^{10}B(^{3}He, $p\alpha\alpha\alpha$) reaction presented in the previous section, with p replaced by d, ^{9}B by ^{10}B and ^{5}Li by ^{6}Li. The two-body channels leading to the $d + 3\alpha$ final state are: $d + ^{12}$C, $\alpha + ^{10}$B and ^{6}Li + ^{8}Be. The two-dimensional energy spectra with associated projections and the d-α relative energy spectrum are shown in Fig. 10.3 and 10.4. The deuteron groups are listed in Table 10.3. The α groups will not be discussed. The narrow peak in the d-α relative energy spectrum corresponds to the formation of the 3^+, $T = 0$ first excited state in ^{6}Li, situated 2.186 MeV above the ground state.

Together, the identified deuteron groups, α groups and the ^{6}Li(3^+) + ^{8}Be channel account for most of the intensity in the two-dimensional energy spectra of Fig. 10.3 and 10.4. A broad diagonal structure (indicated by the red arrow) is seen in Fig. 10.3. Its position fits with the broad 2^+ and 1^+ states in ^{6}Li at 4.31 and 5.65 MeV, with

Table 10.3: Deuteron groups observed in the $^3\text{He} + ^{11}\text{B} \rightarrow d + ^{12}\text{C} \rightarrow d + 3\alpha$ reaction. Excitation energies, E_x , and quantum numbers, $J^\pi; T$, are from the most recent $A = 12$ compilation [AS90].

d Group	$E_{d,\,\text{CM}}$ (MeV)	E_x (MeV)	$J^\pi; T$	$^8\text{Be}_{\text{gs}}$	Not $^8\text{Be}_{\text{gs}}$
1	8.14	7.65	$0^+; 0$	×	(×)
2	6.43	9.64	$3^-; 0$	×	×
3	5.40	10.84	$1^-; 0$	×	×
4	4.55	11.83	$2^-; 0$		×
5	3.80	12.71	$1^+; 0$		×
6	3.25	13.35	$(2^-)^a; 0$		×
7	2.62	14.08	$4^+; 0$		
8[b]	1.74	15.11	$1^+; 1$		
9	0.89	16.11	$2^+; 1$	×	×

[a] The Dalitz plot analysis of Chapter 12 firmly establishes the spin-parity of this state as 4^-.
[b] Only observed in the singles spectrum.

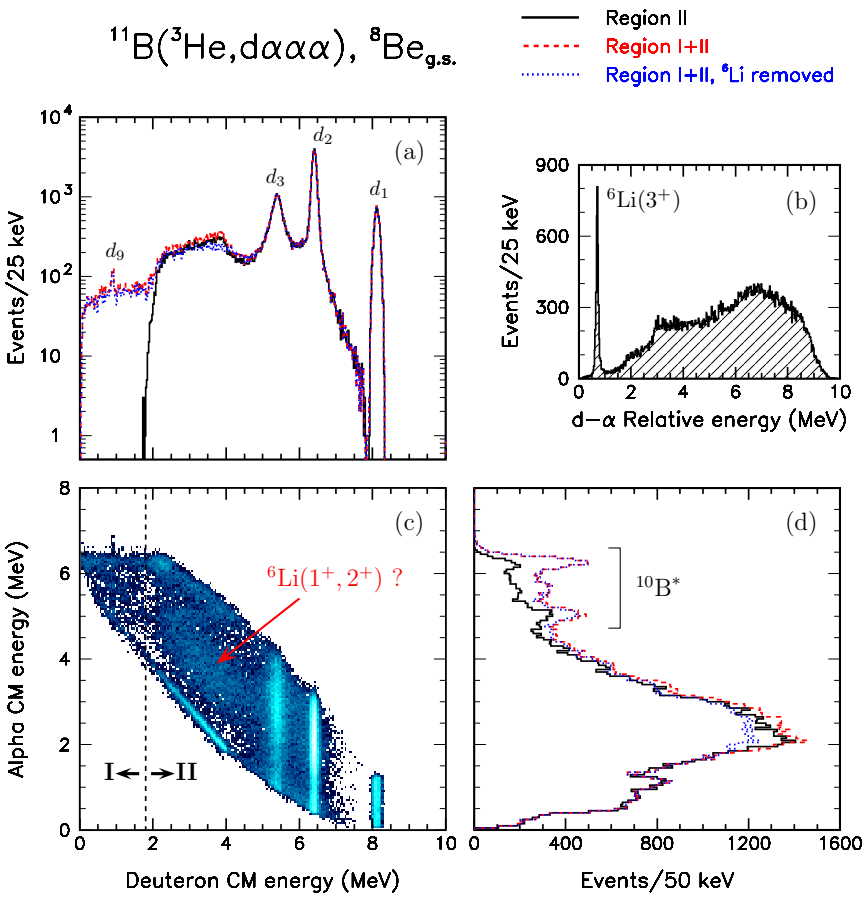

Figure 10.3: ^{11}B(^{3}He, $d\alpha\alpha\alpha$) complete kinematics data (multiplicity-four events only) with gate on the ^{8}Be ground-state peak. **(a)** Deuteron CM energy spectrum. **(b)** d-α Relative energy spectrum. **(c)** Two-dimensional energy spectrum with the deuteron CM energy on the abscissa and the α-particle CM energy on the ordinate. The intensity scale is logarithmic. Region I corresponds to events in which the deuteron is stopped in the ΔE detector and hence has to be identified by kinematical cuts. Region II corresponds to events in which the deuteron penetrates into the E detector allowing for unambiguous identification by the ΔE-E method. **(d)** α-Particle CM energy spectrum.

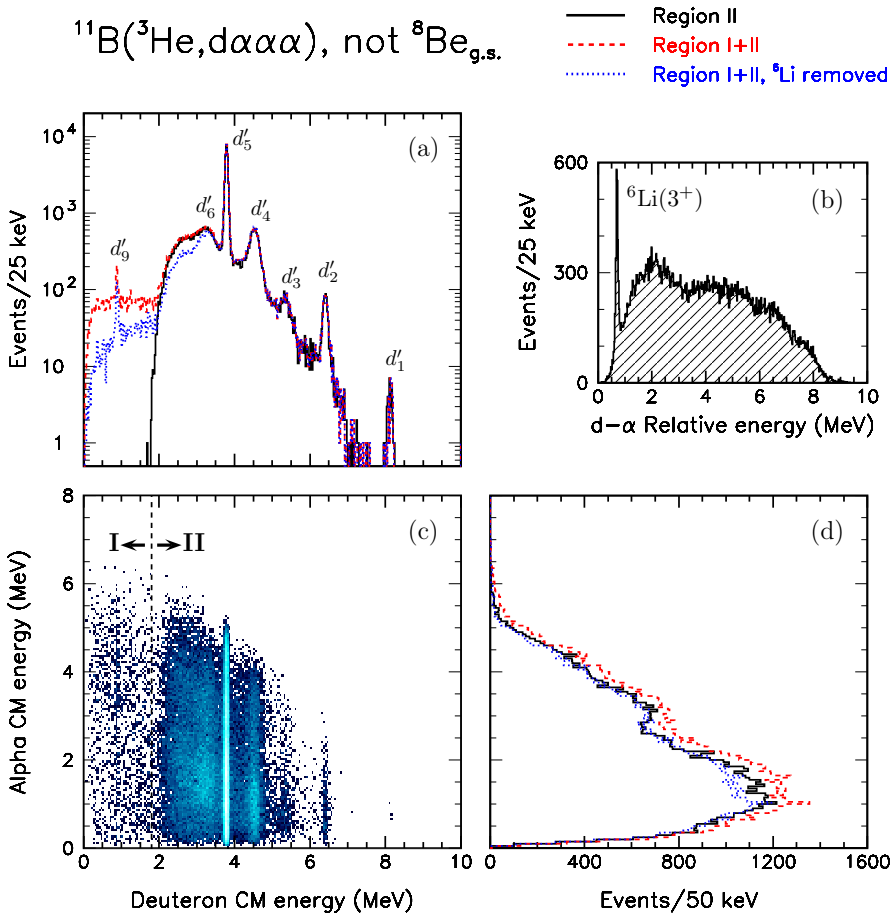

Figure 10.4: ^{11}B(^{3}He, *dααα*) complete kinematics data (multiplicity-four events only) with *anti*gate on the ^{8}Be ground-state peak. See the caption of Fig. 10.3 for details.

respective widths of 1.3 and 1.5 MeV. These states are both $T = 0$ and are known to decay by deuteron emission. Simulations based on a simple sequential description give longitudinal intensity distributions that differ from that observed, but this could be due to angular correlations which were not taken into account in these simulations.

The $^3\text{He} + ^{11}\text{B} \rightarrow d + ^{12}\text{C} \rightarrow d + 3\alpha$ reaction is seen to offer a cleaner probe of the 7–12 MeV excitation region in ^{12}C than the $^3\text{He} + ^{10}\text{B} \rightarrow p + ^{12}\text{C} \rightarrow p + 3\alpha$ reaction which overlaps with α group 4. In both cases, background from very broad resonances formed in the competing two-body channels or from some direct reaction mechanism may be present.

10.2.1 Simple Analysis of the ^{3}He + ^{11}B → d + ^{12}C Reaction

The *non*-observation of deuteron group 7 corresponding to the population of the 4^+ state at 14.08 MeV, may understood by assuming that one-proton transfer is the dominant reaction mechanism:

The ground-state configuration of ^{11}B is shown in Fig. 10.5. The six neutrons couple to 0^+. If the proton is transfered to the $1p_{3/2}$ orbital we obtain the ^{12}C ground state with the six protons also coupling 0^+. If the proton is transfered to the $1p_{1/2}$ orbital, it may couple with the unpaired proton in the $1p_{3/2}$ orbital to give 1^+ and 2^+. If transfered to the $1d_{5/2}$ orbital, it may couple to give 1^-, 2^-, 3^-, 4^-. Thus, we conclude that to obtain a spin-parity of 4^+, we need at least one excited nucleon in addition to the transfered proton, e.g. the configuration $(1p_{3/2})^2(1d_{5/2})^2$, hence the reduced transition probability to the 4^+ state.

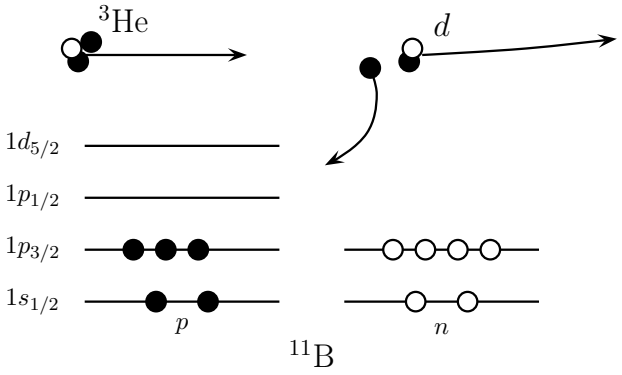

Figure 10.5: Schematic illustration of ^{3}He + ^{11}B → d + ^{12}C one-proton transfer.

10.3 Energies and Widths

The observed width of the peaks in the ^{12}C excitation energy spectrum represents the combined effect of a Breit-Wigner width, Γ, and an experimental (Gaussian) resolution, σ_x. Thus, to extract Γ, we must know σ_x. This becomes particularly important for the 9.64 MeV state for which $\Gamma \approx \sigma_x$.

The experimental resolution, σ_x, is easily obtained from the observed widths of the narrow resonances which are dominated by the experimental resolution ($\Gamma \ll \sigma_x$). As shown in Fig. 10.6, σ_x depends both on the excitation energy and on the proton/deuteron angle. The data points labeled "g.s.", "4.44" and "12.71" were obtained by fitting the corresponding peaks in the ^{12}C spectrum with Gaussians. The dashed curve represents a quadratic interpolation of these data points to 9.64 MeV. The data points labeled "9.64 SIM" were obtained from simulations. They nicely follow the interpolated curve.

The experimental resolution, σ_x, has three contributions: The intrinsic energy resolution of the detectors, the angular resolution of the detectors and the finite area of the beam spot. The latter two are the most significant. The area of the beam spot was determined from the multiplicity-four data set. For each event, the x and y coordinates of the reaction site (i.e. in the plane perpendicular to the beam axis) were found

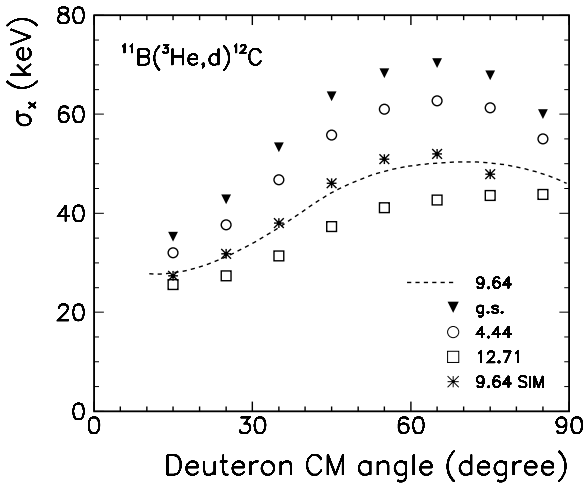

Figure 10.6: Energy and angular dependence of the ^{12}C excitation energy resolution, σ_x, in DSSSD 1 for the ^{11}B(^{3}He, $d\alpha\alpha$) reaction.

by minimizing the momentum deficit:

$$\Delta p = \mid \boldsymbol{p}_{^3\mathrm{He}} - (\boldsymbol{p}_{p,d} + \boldsymbol{p}_{\alpha_1} + \boldsymbol{p}_{\alpha_2} + \boldsymbol{p}_{\alpha_3}) \mid .$$

The resulting (x, y) distribution is well described by a Gaussian function in x times a Gaussian function in y. Simulations assuming a point-like beam spot were used to estimate the contribution to the spread in x and y from the energy and angular resolution of the detectors. With these contributions subtracted, we find $\sigma(x) = 0.97$ mm and $\sigma(y) = 0.75$ mm for ^{3}He + ^{11}B, and $\sigma(x) = 0.72$ mm and $\sigma(y) = 0.52$ mm for ^{3}He + ^{10}B.

The energies, E_x, and widths, Γ, given in Table 10.4, were determined by fitting the peaks with a Breit-Wigner folded with the energy-dependent Gaussian resolution on top of a smooth background. Both multiplicity-three and four data were used. Linear and quadratic forms were used for the background. The energies, E_x, were hardly affected by the choice of background form, while the widths, Γ, showed some dependence which was taken into account in the estimated uncertainties. Due to the angular dependence of σ_x, it was necessary to divide the data into angular bins 10 degree wide and perform fits separately for each angular bin. Similarly, data from different detectors was fitted separately to account for detector-to-detector variations in σ_x. The energies and widths, given in Table 10.4, represent the average over all angular bins and detectors. In general, the energies and widths obtained from different angular bins and detectors were in a good agreement within the statistical uncertainties from the fit. When systematic trends were observed, the uncertainty on the average value was adjusted accordingly. The uncertainty on E_x is dominated by the uncertainty on the energy calibration. The uncertainty on Γ is dominated by the

Table 10.4: Energies and widths of ^{12}C resonances obtained from the present study. Values from the most recent $A = 12$ compilation [AS90] are also given.

State (MeV)	E_x (keV)			Γ (keV)		
	^{10}B	^{11}B	[AS90]	^{10}B	^{11}B	[AS90]
9.64[a]	9 648(5)	9 650(5)	9 641(5)	43(5)	42(5)	34(5)
10.84	10 841(5)	10 852(5)	10 844(16)	271(9)	273(6)	315(25)
11.83	11 832(5)	11 845(6)	11 828(16)	225(9)	241(16)	260(25)
12.71[a]	12 705(5)	12 710(5)	12 710(6)	⋯	⋯	$(18.1 \pm 2.8) \times 10^{-3}$
13.35	⋯	13 305(9)	13 352(17)	⋯	510(40)	374(40)
14.08	14 078(5)	⋯	14 083(15)	273(5)	⋯	258(15)
16.11[a]	16 112(5)	⋯	16 105.8(7)	⋯	⋯	5.3(2)
20.5	20 553(5)	⋯	20 500(100)	245(7)	⋯	300(50)

[a] Used for the internal calibration of the geometry and the E detectors.

modeling of the background, except for the 9.64 MeV state where it is dominated by the uncertainty on the experimental resolution, σ_x.

The agreement with the literature values is generally very good except for a few cases: (i) The width of the 9.64 MeV state, determined to[1] 43(4) keV in the present study, is significantly larger than the literature value of 34(5) keV but agrees with the value of 42(3) keV recently obtained by [Fre09]. (ii) The width of the 10.84 MeV state, determined to[1] 272(5) keV in the present study, is below the literature value of 315(25) keV. (iii) The energy of the 13.35 MeV state, determined to 13 305(9) keV in the present study, is below the literature value of 13 352(17) keV. Its width, determined to 510(40) keV in the present study, is significantly above the literature value of 374(40) keV which, however, represents the weighted average of five very different values: 700(100) [Hin61], 355(50) [Sch65], 430(100) [Bro65b], 290(70) [Wag66] and 500(80) [Rey71].

10.4 Branching Ratios

Natural-parity states in ^{12}C are allowed to decay via the ground state of ^{8}Be. The branching ratio to the ground state, f_{gs} , is determined by the competition with other open channels. Barrier penetrabilities are important to the competition but nuclear structure may also play a role.

We distinguish between f_{peak} which is the branching ratio to the ground-state *peak*, and f_{gs} which is the branching ratio to the ground state as a whole. As discussed in Section 7.6, part of the ground-state decay strength is found *above* the ground-state peak and is referred to as the "ghost". The branching ratio to the ^{8}Be ground-state peak is calculated as:

$$f_{\mathrm{peak}} = \frac{\nu_1}{\nu_1 + \nu_2} ,$$

where ν_1 and ν_2 are the solutions to the matrix equation:

$$\begin{pmatrix} n_1 \\ n_2 \end{pmatrix} = \begin{pmatrix} \varepsilon_{11} & \varepsilon_{12} \\ \varepsilon_{21} & \varepsilon_{22} \end{pmatrix} \begin{pmatrix} \nu_1 \\ \nu_2 \end{pmatrix} .$$

Here, n_1 is the number of decays experimentally observed to proceed via the ^{8}Be ground-state peak at 92 keV and n_2 is the number of decays observed to proceed via other channels. The matrix elements are the detection efficiencies determined from simulations: ε_{11} gives the probability that a decay via the ground-state peak is detected and correctly identified. Similarly, ε_{22} gives the probability that a decay via some other channel but the ground-state peak is detected and correctly identified. The cross terms, ε_{12} and ε_{21}, give the probability that a decay is detected but wrongly identified. They are non-zero due to the finite experimental resolution.

[1] Weighted average of the two values given in the table.

Table 10.5: Branching ratios in α decay of ^{12}C resonances. Statistical and systematical uncertainties on the branching ratios obtained from the present study, f_{peak} and f_{gs}, are given separately.

State (MeV)	f_{peak} (%)	f_{gs} (%)	Δf (stat.) (%)	Δf (syst.)[a] (%)	Literature (%)	Theory[b] (%)
9.64	98.0	100.0	0.05	0.4	97.2[c]	96
10.84	94.3	102.6	0.3	0.8	···	70
14.08	22	25	0.3	3	17(4)[d]	20
16.11	5.8	7.2	0.3	0.8	4.4(8)[e]	[f]

[a] From the estimated 10% uncertainty on the detection efficiencies.
[b] 3α-cluster model of [ÁR08b].
[c] From [Fre07b], uncertainty not given.
[d] From [Cau91]; [Fre07b] gives 17% without quoting the uncertainty.
[e] [AS90] gives Γ_{α_0} = 0.290(45) keV and Γ_{α_1} = 6.3(5) keV.
[f] The 3α-cluster model of [ÁR08b] predicts a 2^+, $T = 0$ state at 13.8 MeV with f_{gs} = 4%.

In the present study, we extract branching ratios for the 9.64, 10.84, 14.08 and 16.11 MeV states. To check for systematic effects, we extract separate branching ratios from the multiplicity-three and four data sets and also individually for the detectors. Generally, good agreement is found when taking into account the estimated 10% uncertainty on the detection efficiencies. The branching ratios given in Table 10.5 are average values. Both branching ratios to the ground-state peak, f_{peak} , and branching ratios to the ground state as a whole, f_{gs} , are given. The calculation of the ghost contribution is described below.

For the 9.64, 14.08 and 16.11 MeV states, our values of f_{peak} are in good agreement with the literature values. It is interesting to note that with the ghost contribution taken into account, the 9.64 MeV state decays exclusively to the ^{8}Be ground state. A Dalitz plot analysis may help confirm/falsify this result. The level of agreement between experiment and the 3α-cluster model of [ÁR08b] is good for the 14.08 MeV state, reasonable for the 9.64 MeV state and rather poor for the 10.84 MeV state. The 16.11 MeV state has spin-parity 2^+ and isospin $T = 1$. Its α decay is attributed to mixing with $T = 0$ states. The 3α-cluster model of [ÁR08b] predicts a 2^+, $T = 0$ state at 13.8 MeV with f_{gs} = 4%, in reasonable agreement with the experimental value.

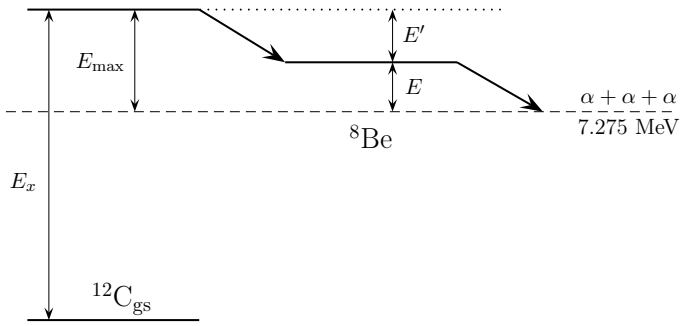

Figure 10.7: Energy diagram showing the sequential decay of an excited state in ^{12}C via ^{8}Be. The excitation energy in ^{12}C is E_x; the excitation energy in ^{8}Be is $E - 92$ keV.

10.4.1 Ghost Contribution

In R-matrix theory, the profile of the ^{8}Be ground state, $\rho_0(E)$, is given by Eq. 7.1 with $E_\lambda = E_{\rm gs} = 92$ keV and $l = 0$. The reduced width, $\gamma_\lambda = \gamma_{\rm gs}$, is obtained from the observed width, $\Gamma_{\rm obs} = 5.57$ eV, through

$$\gamma_{\rm gs}^2 = \frac{\Gamma_{\rm obs}}{2P_0 - \Gamma_{\rm obs}\frac{{\rm d}S_0}{{\rm d}E}} ,$$

where P_0 and $\frac{{\rm d}S_0}{{\rm d}E}$ are the penetrability and the derivative of the shift function evaluated at $E_{\rm gs}$. Then, for a narrow state in ^{12}C with excitation energy E_x, the differential decay rate to the ^{8}Be ground state is

$$\frac{{\rm d}\Gamma_0}{{\rm d}E} = 2P_{l'}(E')\gamma_0^2\,\rho_0(E) ,$$

where $E' = E_x - 7.275\,{\rm MeV} - E$ is the $\alpha + {}^8$Be kinetic energy and l' is the $\alpha + {}^8$Be orbital angular momentum. The energy dependence of the tunneling probability in the $\alpha + {}^8$Be entrance channel is contained in $P_{l'}(E')$. For γ_0 to be interpreted as a reduced width, the ^{8}Be ground-state profile $\rho_0(E)$ must be properly normalized:

$$\int_0^{E_{\max}} \rho_0(E)\,{\rm d}E = 1 , \quad E_{\max} = E_x - 7.275\,{\rm MeV} . \tag{10.1}$$

The exit and entrance-channel radii, $a_{\alpha\alpha}$ and $a_{\alpha{\rm Be}}$, which enter the calculation of the penetrability and shift function, are computed as

$$a_{\alpha\alpha} = r_0(4^{1/3} + 4^{1/3}) = 3.17 r_0 , \quad a_{\alpha{\rm Be}} = r_0'(4^{1/3} + 8^{1/3}) = 3.59 r_0' ,$$

with, typically, $r_0 = r_0' = 1.41$ fm. The integrated decay rate can be separated into that going to the peak and that going to the ghost:

$$\Gamma_0 = \Gamma_{0,{\rm peak}} + \Gamma_{0,{\rm ghost}} = \int_0^{E_{\rm gs}+\delta E} \frac{{\rm d}\Gamma_0}{{\rm d}E}\,{\rm d}E \; + \; \int_{E_{\rm gs}+\delta E}^{E_{\max}} \frac{{\rm d}\Gamma_0}{{\rm d}E}\,{\rm d}E ,$$

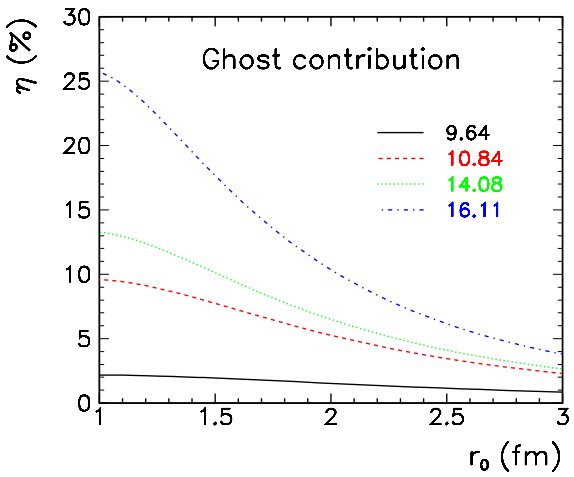

Figure 10.8: Ghost contribution versus r_0 ($3.17r_0$ is the exit-channel radius) in the sequential decay of the 9.64, 10.84, 14.08 and 16.11 MeV states via the ^{8}Be ground state.

where δE is some small number, say $\delta E = 10$ keV, sufficiently large to cover the ground-state peak. The first integral is difficult to compute numerically due to the tiny observed width of the ground-state peak. The integral may be computed by fixing the entrance-channel penetrability, $P_{l'}$, to its value at $E = E_{\rm gs}$ and using the analytical approximation[2]:

$$\int_{E_{\rm gs}-\delta E}^{E_{\rm gs}+\delta E} \rho_0(E)\,{\rm d}E \;\approx\; \frac{1}{1+\gamma_{\rm gs}^2 \frac{{\rm d}S_0}{{\rm d}E}}\,,$$

with $\frac{{\rm d}S_0}{{\rm d}E}$ evaluated at $E_{\rm gs}$.

The ghost contribution, $\eta = \Gamma_{0,\rm ghost}/\Gamma_0$, is shown in Fig. 10.8, with $r_0' = 1.41$ fm fixed and r_0 variable. The ghost contribution is seen to diminish with increasing exit-channel radius consistent with expectations. Naturally, increasing the entrance-channel radius has the opposite effect. The ground-state branching ratio (peak+ghost) is now easily obtained from the branching ratio to the ground-state peak:

$$f_{\rm gs} = \tfrac{1}{1-\eta} f_{\rm peak}$$

The ground-state branching ratios are shown as a function of r_0 in Fig. 10.9; values obtained for $r_0 = 1.41$ fm are given in Table 10.5.

[2]Here, ρ_0 is the ^{8}Be ground-state profile *before* normalization (Eq. 10.1).

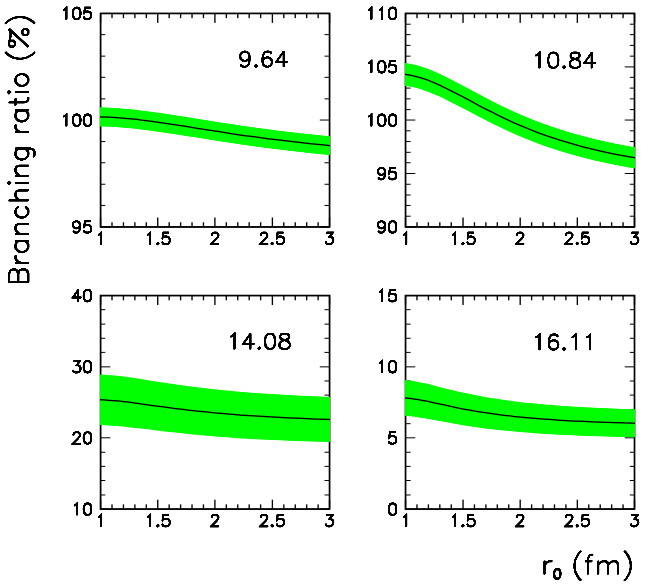

Figure 10.9: Ground-state branching ratios (peak+ghost) versus r_0 ($3.17r_0$ is the exit-channel radius). The green-shaded bands indicate 1σ uncertainties obtained by adding statistical and systematic uncertainties in quadrature.

10.4.2 Reduced Widths

Assuming that the decays not proceeding via the ground state of ^{8}Be proceed via the broad 2^+ state in ^{8}Be, we may compute the reduced widths γ_0 and γ_2 for the two decay channels according to

$$f_{\mathrm{gs}} = \frac{2\langle P\rangle_0\gamma_0^2}{2\langle P\rangle_0\gamma_0^2 + 2\langle P\rangle_2\gamma_2^2}\,, \quad \Gamma_{\mathrm{obs}} = \frac{2\langle P\rangle_0\gamma_0^2 + 2\langle P\rangle_2\gamma_2^2}{1 + \gamma_0^2\langle\frac{\mathrm{dS}}{\mathrm{d}E}\rangle_0 + \gamma_2^2\langle\frac{\mathrm{dS}}{\mathrm{d}E}\rangle_2}\,,$$

where we have defined ($i = 0, 2$),

$$\langle P\rangle_i = \int_0^{E_{\max}} P_{l_i'}(E')\,\rho_i(E)\,\mathrm{d}E\,, \quad \langle\tfrac{\mathrm{dS}}{\mathrm{d}E}\rangle_i = \int_0^{E_{\max}} \tfrac{\mathrm{d}S_{l_i'}}{\mathrm{d}E}(E')\,\rho_i(E)\,\mathrm{d}E\,.$$

The parameters of [Bha06] were used for the profile of the 2^+ state, $\rho_2(E)$. Only the lowest allowed l_2' was used. For the 9.64 and 10.83 MeV states, the results are consistent with a zero branch to the 2^+ state. For the 14.08 and 16.11 MeV states, the ratios of the reduced widths, γ_2^2/γ_0^2, are 3.4(6) and 16(3), respectively.

10.5 Proton Decay to ^{11}B

The proton separation energy in ^{12}C is S_p = 15 957.0(4) keV. Excited states above this energy populated in the ^{3}He + ^{10}B → p + ^{12}C reaction, can decay by proton emission to ^{11}B. This leads to the three-body final state p + p + ^{11}B. Proton decay provides information about the level structure of ^{12}C complementary to α decay, e.g. because the isospin selection rules of proton and α decay are different.

A preliminary analysis of the ^{3}He + ^{10}B data has been performed with the purpose of identifying such proton decays. Three classes of events were considered: (i) Two protons and one ΔE particle[3], (ii) One proton and two ΔE particles and (iii) Two protons. Evidence was found for the existence of proton-decaying states in ^{12}C at the following excitation energies (MeV):

$$16.6,\ 18.3,\ 18.8,\ 19.3,\ 19.6,\ 20.5\ .$$

Decays to the ground state, the first excited state at 2.12 MeV (bound) and the second excited state at 4.44 MeV (bound) in ^{11}B were observed. The states at 16.6, 18.3, 19.3, 19.6 and 20.5 MeV were also observed by [Tem97] in a study of the ^{12}C$(p, p'X)$ reactions with $X = p$ and α. The state at 18.8 MeV was not observed by [Tem97] but has been observed in previous studies [AS90].

The excitation region from 16–21 MeV contains many states, the quantum numbers of which are not well established [AS90]. An analysis of the present experimental data that combines the data from the α and proton channels, would provide valuable information on this excitation region.

[3] By "ΔE particle" is meant a particle that is stopped in the DSSSD.

CHAPTER 11

Indirect Detection of γ Transitions

In the present chapter, we demonstrate how the complete kinematics information allows us to identify γ transitions between unbound states in ^{12}C. We find γ transitions from the 15.11 MeV state to the 12.71, 11.83, 10.3 and 7.65 MeV states. We also find γ transitions from the 12.71 MeV state to the 10.3 and 7.65 MeV states. The states populated in the γ transitions subsequently break up into three α particles. Therefore, we shall call this type of decay "γ-delayed 3α breakup". We are also able to identify γ transitions to the bound states. Finally, we discuss the relation between the γ transitions within ^{12}C and the β decays of ^{12}N and ^{12}B to the same states in ^{12}C.

There is a great amount of overlap between this chapter and [Kir09].

11.1 Introduction

The experimental detection of electromagnetic transitions in nuclei is challenging when the energy distribution of the emitted γ rays is broad, as may happen for transitions between particle-unbound states. In such situations, the γ branches are usually small because they compete with particle decay channels of much larger width. Here we explore an alternative experimental approach where the γ-ray detection is substituted by the measurement of multi-particle breakups in complete kinematics.

γ Transitions provide an experimental window to the excitation region in ^{12}C just above the triple-α threshold with a different selectivity for final states compared to hadronic probes and β decay. As discussed in Section 7.5.1, this excitation region contains several broad levels and is not yet resolved, neither theoretically nor experimentally. Below, we refer to this excitation region as the "10.3 MeV state".

γ Transitions, like β decay, have the advantage of being relatively easy to handle from a theoretical point of view.

The first $T = 1$ state in ^{12}C is situated at 15.11 MeV, about 1 MeV below the threshold for proton emission, and has spin and parity 1^+. It decays predominantly through the emission of γ rays. α Decay is hindered by isospin conservation. Nevertheless, the existence of a small α branch has been established experimentally [Bal74]. The

majority of the γ decays go to the ground state (92%), but γ branches at the percent level to the 12.71, 7.65 and 4.44 MeV states have also been measured [Alb72]. In the present work, γ transitions to broad states in ^{12}C have been detected for the first time. The broad nature of these states explains why previous experiments relying on the detection of the γ rays were not able to separate them from the background.

The decay of the 1^+ $T = 0$ state at 12.71 MeV is dominated by α decay leaving a small γ branch of 2%. Before this work the only known γ transitions were to the ground state (87%) and the 4.44 MeV state (13%). Here we report on the first observation of transitions to unbound states.

11.2 Analysis and Results

11.2.1 γ-Delayed 3α Breakup of the 15.11 MeV State

Given the observation of all four final-state particles, we can determine the excitation energy of the excited state in ^{12}C populated in the ^{3}He + ^{10}B $\rightarrow$ p + ^{12}C reaction by two independent methods. We may either determine the excitation energy from the momentum of the proton using energy and momentum conservation, or we may determine the excitation energy from the momenta of the three α particles using the invariant-mass method. Normally, these two methods bring us to the same result, but if a γ transition precedes the breakup into three α particles, the results no longer agree; the invariant-mass method gives the excitation energy of the state populated in the γ decay, whereas the proton gives the excitation energy of the state initially populated in the ^{3}He + ^{10}B $\rightarrow$ p + ^{12}C reaction. The energy difference is carried away by the unobserved γ ray (neglecting the tiny recoil of the ^{12}C nucleus).

To look for these γ-delayed 3α breakups, we use the two-dimensional spectrum shown in Fig. 11.1 (a). The ^{12}C excitation energy given by the proton, $E_x^{(p)}$, is along the abscissa and the excitation energy given by the invariant-mass method, $E_x^{(3\alpha)}$, is along the ordinate (see also Fig. 9.5). Ordinary 3α breakups follow the diagonal while γ-delayed 3α breakups appear below it. Due to its small α width, the 15.11 MeV state is not visible in the projection (b), even though the single-proton spectrum shows that it is populated in the ^{3}He + ^{10}B $\rightarrow$ p + ^{12}C reaction at a rate comparable to the 16.11 MeV state.

The momentum carried away by the γ ray, E_γ/c, is below the experimental resolution and small compared to all other momenta involved. This fact allows us to impose momentum conservation on the events that we include in Fig. 11.1, thereby significantly reducing the background in the region below the diagonal, see Section 9.3.5.

We use the timing (TDC) information to remove random coincidences with a time window of 100 ns. In the present case, we keep sub-threshold ($\lesssim$ 550 keV) particles

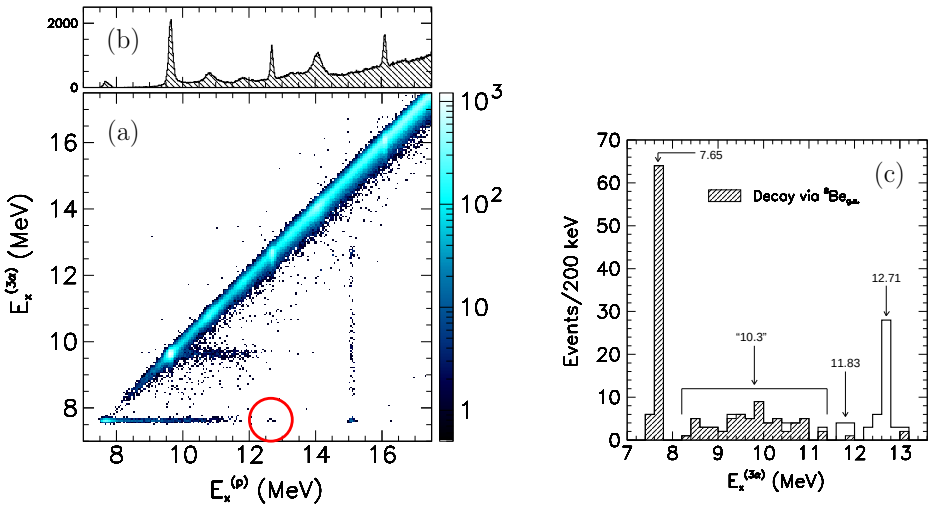

Figure 11.1: (a) Complete kinematics data from the ^{10}B(^{3}He, $p\alpha\alpha\alpha$) reaction. Only events that satisfy momentum conservation and pass the partial time gate (see text for explanation) have been included. The ^{12}C excitation energy calculated from the momentum of the proton, $E_x^{(p)}$, is along the abscissa while the excitation energy calculated from the invariant mass of the three α particles, $E_x^{(3\alpha)}$, is along the ordinate. **(b)** Projection of (a) on the abscissa. **(c)** The deduced γ-decay spectrum of the 15.11 MeV state.

without timing information. Later, when we consider the γ decay of the 12.71 MeV state, we apply a stricter time gate which excludes sub-threshold particles. We refer to these two gates by the names "partial" and "complete", respectively.

The γ transitions from the 15.11 MeV state to lower-lying unbound states form a narrow vertical band at $E_x^{(p)}$ = 15.1 MeV. The background events away from the diagonal are due to random coincidences which happen to survive the partial time gate as well as the requirement of momentum conservation. Close to the diagonal, the experimental response tails also contribute to the background. The two bands that extend horizontally from the Hoyle state and the 9.64 MeV state in direction of increasing excitation energy, are caused by protons that punch through the E detectors. The group of five events indicated by the red circle probably represents the detection of the 12.71 $\rightarrow$ 7.65 transition. However, the punch-through protons prevent any clear conclusions to be drawn. We note that the observed intensity of five events is consistent with the branching ratio of 2.6% obtained in the below study of the ^{11}B(^{3}He, $d\alpha\alpha\alpha$) reaction.

Projecting the 15.11 MeV band onto the ordinate, we obtain the γ spectrum shown in Fig. 11.1 (c). In line with previous observations [Hyl09], the "10.3 MeV state" is

Table 11.1: Details on the γ decay of the 15.11 and 12.71 MeV states in ^{12}C.

Transition	Events	Det. eff. (%)	γ branch [Alb72] (%)	γ branch present (%)
15.11 → 12.71	39	0.74	1.4(4)	1.2(2)
11.83	8	0.57	···	0.32(12)
10.84	<7.3[a]	1.30	···	<0.13
10.3	65	1.09	1.6[b]	1.4(2)
7.65	70	0.36	2.6(7)	4.4(8)
0 and 4.44	40 344	9.9	94(2)	92.7(1.0)
12.71 → 10.3	3	0.40	···	$0.9(^{+6}_{-5})$
7.65	4	0.18	···	$2.6(^{+1.6}_{-1.2})$
0 and 4.44	11 660	13.9	100	$96.6(^{+1.7}_{-1.3})$

[a] Upper limit valid at 90% C. L. .

[b] The 15.11 → 10.3 transition was not observed by [Alb72]. The intensity of 1.6% is an estimate derived from the measured β-decay branching.

seen to decay mainly through the ^{8}Be ground state. The unnatural parity of the 11.83 and 12.71 MeV states prevents them from decaying via the ^{8}Be ground state. This is indeed the case for the group of eight events identified with the 11.83 MeV state, proving that these events do not belong to the high-energy tail of the broad "10.3 MeV state".

The relative γ-ray branching ratios of the 15.11 MeV state derived from the present work are given in Table 11.1 and compared to earlier measurements. The uncertainties given are 1σ confidence intervals and include the uncertainty on the detection efficiency.

11.2.2 Detection Efficiency

The probability that we detect all four charged particles in the γ-delayed 3α breakup of the 15.11 MeV state depends on the decay path. Calculating the probability is complicated and has been done through Monte Carlo simulations (Section 9.4).

The broad "10.3 MeV state" and the Hoyle state are assumed to decay through the narrow ground state of ^{8}Be. Due to the similarity between M1 γ decays and Gamow-Teller β decays, to be discussed in Section 11.3, we may use the β-delayed 3α spectrum measured by [Hyl09] corrected for detection efficiency and phase space to describe the shape of the "10.3 MeV state", provided we scale the spectrum by a factor of E_γ^3 to account for the phase-space factor of M1 γ transitions. The resulting spectrum is consistent with the measured one. For the unnatural-parity states at 12.71 and 11.83 MeV, the detection efficiencies are rather insensitive to the particular

model adopted for the 3α breakup. A phase-space simulation predicts detection efficiencies that differ by less than 5% from those obtained assuming a sequential decay through the broad 2^+ first excited state in ^{8}Be, taking into account all of the effects mentioned in [Fyn03]. This can be understood as the result of (i) the experimental acceptance being fairly uniform throughout the 3α phase space, and (ii) the breakup of the unnatural-parity states covering a large region of the 3α phase space. In contrast, decays via the narrow ground state of ^{8}Be cover a very limited region of phase space. This results in a complete kinematics detection efficiency that is—all other factors taken out—somewhat larger.

By comparison with experimental data, we find that the efficiencies predicted by the simulations are correct within 10%. However, in the particular case of the $12.71 \rightarrow 7.65$ transition we assume an uncertainty of 20% on the efficiency estimate to account for an increased sensitivity to the ADC thresholds. The detection efficiencies are given in Table 11.1.

11.2.3 γ Decay to Bound States

Transitions to the ground state and the 4.44 MeV state can be identified in the experimental data by looking for events where the proton and the ^{12}C nucleus are detected in coincidence. The proton tells us which excited state in ^{12}C was populated. A γ transition to one of the bound states can then be identified as a deficit in the energy balance, $\delta E = Q + E_{\text{beam}} - (E_{p,d} + E_{^{12}\text{C}})$, equal to the excitation energy of the state populated. This method does not distinguish between transitions to the ground state and the 4.44 MeV state.

Due to their low energy and high Z, the ^{12}C ions are easily stopped in the DSSSDs preventing identification by the ΔE-E method. Therefore, a large background due to e.g. $p+\alpha$ coincidences is present. By imposing momentum conservation in the plane normal to the beam axis, the background is significantly reduced. For the 15.11 MeV state, the surviving background is negligible. For the 12.71 MeV state, some background remains (signal-to-background ratio of 3:1) which we are able to reproduce on an absolute level with simulations, as shown in Fig. 11.2 (c).

The γ transitions to the bound states enjoy a much higher detection efficiency than the transitions to the unbound states because their identification only requires the detection of two particles.

11.2.4 γ-Delayed 3α Breakup of the 12.71 MeV State

Very few γ decays are observed from the 12.71 MeV state so we must treat the background due to random coincidences with great care. Timing information is used to separate real coincidences from random ones. If timing information is lacking due

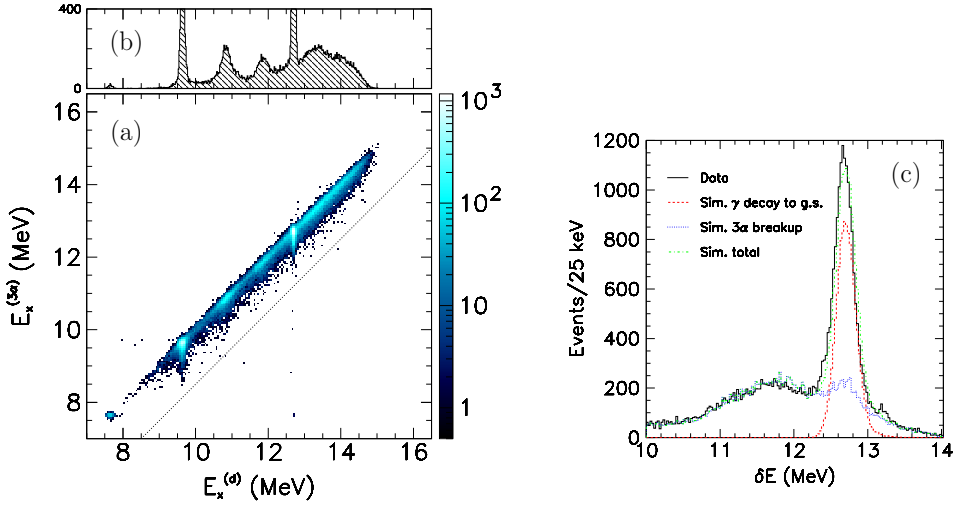

Figure 11.2: (a) Complete kinematics data from the ^{11}B(^{3}He,$d\alpha\alpha\alpha$) reaction. Only events that satisfy momentum conservation and pass the partial time gate have been included. The ^{12}C excitation energy calculated from the momentum of the deuteron, $E_x^{(d)}$, is along the abscissa while the excitation energy calculated from the invariant mass of the three α particles, $E_x^{(3\alpha)}$, is along the ordinate. The dotted line 1.5 MeV below the diagonal marks the extent of the response tails. **(b)** Projection of (a) on the abscissa. **(c)** Energy deficit in d + ^{12}C coincidences gated on the deuteron to single out the 12.71 MeV state.

to sub-threshold particles, event mixing is used to estimate the background due to random coincidences.

The complete kinematics data from the ^{11}B(^{3}He,$d\alpha\alpha\alpha$) reaction is presented in Fig. 11.2 (a). Only $d+3\alpha$ events that satisfy momentum conservation and pass the partial time gate have been included. Due to the reduced Q value, we do not reach as high excitation energies as in the ^{3}He+^{10}B$\rightarrow p+^{12}$C reaction in spite of the increased beam energy. The dotted line 1.5 MeV below the diagonal marks the extent of the response tails. Events in the region below this line are either γ decays to unbound states or random coincidences that happen to satisfy momentum conservation and the requirements of the partial time gate.

We find seven events neatly aligned on a vertical string at $E_x^{(d)} = 12.71$ MeV. Below, we refer to this as the "12.71 MeV string". Four events are clustered together at $E_x^{(3\alpha)} =$ 7.65 MeV, appearing as a single dot in the figure. Two additional events are found below the dotted line, one at $E_x^{(d)} = 11.3$ MeV and another at $E_x^{(d)} = 13.9$ MeV.

If the partial time gate is removed, eleven additional events appear below the dotted line. Together with the single event already present at $E_x^{(d)} = 13.9$ MeV, they form a vertical band about 1 MeV wide centered at $E_x^{(d)} = 14$ MeV. These events originate

from random coincidences between (i) two ΔE particles (ii) a deuteron along with the heavy fragment from one of the following reactions[1]

$$^{3}\mathrm{He} + ^{12}\mathrm{C} \rightarrow d + ^{13}\mathrm{N}(\mathrm{g.s.}) ,$$
$$^{3}\mathrm{He} + ^{10}\mathrm{B} \rightarrow d + ^{11}\mathrm{C}(6.34, 6.48) .$$

If we require all four particles to be inside the 100 ns coincidence window (complete time gate, cf. Section 11.2.1), the eleven events that appeared when the partial time gate was removed obviously disappear, but the single event close to the diagonal remains. If, instead, we require at least one particle to be outside the coincidence window, the number of events grows from one to five. With a data taking window (ADC window) of 2.15 μs and a coincidence window of 100 ns we expect 20.5 times as many random coincidences outside the coincidence window as inside. This is consistent with the observed outcomes of five outside and one inside.

The method of event mixing has been applied to the experimental data to estimate the background rate from random coincidences and yields a number that is consistent with the observed background of twelve events. (The extraction of an unbiased sample of events of type (i), i.e. consisting of two ΔE particles, from the data for use in event mixing was complicated by the fact that the two forward-angle DSSSDs were not included in the trigger. To obtain an unbiased sample it was necessary to consider multiplicity-six events resulting from random coincidences between $d + 3\alpha$ and events of type (i). Energy and momentum conservation was used to separate out the two ΔE particles.)

The single event at $E_x^{(d)} = 11.3$ MeV disappears when the complete time gate is imposed suggesting that it is also a random coincidence.

The three isolated events on the 12.71 MeV string represent the detection of the $12.71 \rightarrow 10.3$ transition. All three events survive the complete time gate making it highly improbable that they should be random coincidences. The 90% confidence limits on the physics signal are 0.869–6.81 [Rol05], showing that the data is consistent with the hypothesis of a non-zero physics signal. The absence of background due to random coincidences is consistent with estimates obtained through event mixing.

The four remaining events of the 12.71 MeV string clustered together at $E_x^{(3\alpha)} = 7.65$ MeV represent the detection of the $12.71 \rightarrow 7.65$ transition. They all disappear when we impose the complete time gate because sub-threshold α particles are present. We would like to stress that all four events survive the partial time gate, i. e. the deuteron and those α particles that do have timing information are indeed inside the coincidence window. We use event mixing to estimate the background due to random coincidences in the region of Fig. 11.2 (a) occupied by the four $12.71 \rightarrow 7.65$ events. We obtain an upper limit of 0.2 at 90% C. L. making it highly improbable that

[1] The ^{11}B target contains 19.8% ^{10}B and rests on a carbon foil.

they should be random coincidences. Using [Rol05], we calculate the 90% confidence limits on the physics signal to 1.40–8.25.

It is worth noting that the seven events of the 12.71 MeV string all survive the ^{8}Be ground-state gate consistent with expectations. The relative γ-ray branching ratios of the 12.71 MeV state derived from the present work are given in Table 11.1.

11.2.5 α Branches

Using detection efficiencies derived from simulations, we convert the observed ratio of α to γ decays of the 12.71 MeV state into branching ratios. The results are Γ_α/Γ = (97.4 ± 0.3)% and Γ_γ/Γ = (2.6 ± 0.4)%, in agreement with the value of Γ_γ/Γ = (2.22 ± 0.14)% adopted in [AS90].

The detection of the isospin-forbidden α decay of the 15.11 MeV state is complicated by a large continuum background. Yet, the p+α coincidence spectrum exhibits a clear signal of 500±100 events on top of a background of about 4 000 events. Only p+α coincidences in which the α particle is emitted at laboratory angles larger than 60°, are considered. This is done to suppress the large signal from p+^{12}C coincidences. Simulations have been used to determine the contribution from the γ-delayed 3α breakups of the 15.11 MeV state. Using the present γ-ray branching ratios, we determine the contribution to 280 ± 30 events, leaving a residual α-decay signal of 220 ± 100 events. This translates into a branching ratio of Γ_α/Γ = (2.8 ± 1.2)%.

The complete kinematics spectrum (Fig. 11.1) does not exhibit a clear peak at 15.11 MeV. However, the large continuum background could easily be hiding a small α-decay signal. Energy conservation is imposed to eliminate the contribution from the γ-delayed 3α breakups. We assume a linear background and establish an upper limit on the Gaussian signal hiding in the background. Correcting for detection efficiencies, we obtain an upper limit of 3.3% on the α branch of the 15.11 MeV state at 90% C. L., in good agreement with the value of (2.8±1.2)% obtained above by considering p+α coincidences.

The value measured by Balamuth *et al.* [Bal74] and adopted in [AS90] is Γ_α/Γ = (4.1±0.9)%. However, the 0.32% γ branch to the 11.83 MeV state and the 1.4% γ branch to the broad "10.3 MeV state" were not accounted for in the analysis of [Bal74]. By subtracting these contributions from their value, one obtains Γ_α/Γ = (2.4 ± 0.9)%, in good agreement with our numbers.

In the framework of two-state mixing, the charge-dependent matrix element connecting the 15.11 and 12.71 MeV states, $\langle H_{\mathrm{CD}} \rangle$, can readily be determined from the α widths [Bal74]. Using our new smaller value of Γ_α(15.11), we obtain $\langle H_{\mathrm{CD}} \rangle$ = 260 ± 60 keV, in better agreement with the results obtained with electromagnetic and pionic probes [NC00].

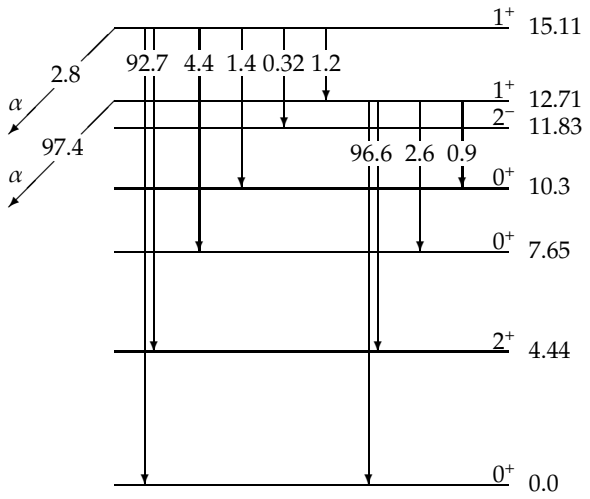

Figure 11.3: Energy-level diagram showing the relative γ-ray branching ratios, in percent of the total γ width, from the 15.11 and 12.71 MeV states in ^{12}C measured in the present work. Uncertainties are given in Table 11.1. Also shown are the α-decay branching ratios, in percent of the total width. Uncertainties are given in the text.

11.3 Connection to β Decay

From the γ-ray branching ratios in Table 11.1, partial γ widths, Γ_γ , can be calculated assuming[2] $\Gamma_{\gamma_0} = (36.9 \pm 0.8)$ eV for the transition to the ground state and using the relative γ-ray branching ratio of (2.3 ± 0.9)% to the 4.44 MeV state measured by [Alb72]. The reduced transition strength, B(M1), can be calculated from Γ_γ through the formula of [Boh69],

$$\Gamma_\gamma = 1.76 \times 10^{13} \hbar\, E_\gamma^3\, B(\mathrm{M1})\,, \tag{11.1}$$

if we assume that the decays are purely M1, as is indeed the case for $1^+ \to 0^+$ transitions. For the $1^+ \to 1^+$ and $1^+ \to 2^+$ transitions, single-particle estimates suggest that the E2 contribution is below one percent. The B(M1) values can be directly compared to theoretical calculations providing a valuable test of the theory, complementary to other observables such as level energies and radii.

Further insight into the relative importance of the spin and orbital terms of the M1 matrix element as well as the importance of meson exchange currents (MEC) can be gained by comparing the B(M1) values to the B(GT) values of the analog Gamow-Teller (GT) β decays of ^{12}B and ^{12}N, which were recently measured by our collabo-

[2] Weighted average of the three most recent measurements, (37.0 ± 1.1) [Che73], (38.5 ± 0.8) [Deu83] and (35.9 ± 0.6) eV [NC00], with the error raised to compensate for the large spread.

ration. The major component of the two transition types (M1 and GT) is the spin term ($\sigma\tau$). In addition, both transitions are equally affected by the Δ-isobar current. For M1 transitions, the orbital term ($l\tau$) also contributes. Finally, both transitions can be affected by MEC; large contributions are expected for M1 transitions, while G-parity conservation strongly suppresses this effect for GT transitions [Tow87]. The combined effect of MEC and the orbital term is measured by the ratio [Ric90],

$$R(\mathrm{M1/GT}) = \frac{B(\mathrm{M1})/2.643\mu_N^2}{B(\mathrm{GT})} \,.$$

In their absence R(M1/GT) is unity.

The ratio R(M1/GT) has been studied for *sd*-shell nuclei. Relying on theoretical calculations of the orbital contribution to R(M1/GT), the MEC contribution was found to be modest [Ric90]. Alternatively, by assuming the MEC contribution known, conclusions can be made regarding the orbital contribution [Fuj03].

In the p-shell, one is limited to the five $T = 0$ nuclei ^{6}Li, ^{8}Be, ^{10}B, ^{12}C and ^{14}N. The low number of states in the β-decay window further limits the number of available cases (though charge-exchange reactions with high-energy radioactive beams may overcome this limitation in the future). The $A = 12$ case is the only one giving the possibility of studying several transitions in the same system. The link between M1 and GT transitions for $A = 12$ was previously explored in [Alb72] where the orbital contribution to the M1 transitions were estimated with the shell model calculations of Cohen and Kurath. The orbital contribution was found to be less than one percent for the transitions to the 12.71 MeV state and the ground state and 10% for the transition to the 4.44 MeV state. The MEC contribution was later calculated for the transition to the ground state and found to account for about 10% of the strength [Gui82].

Recently, new experimental B(GT) values for the decays of both ^{12}B and ^{12}N have become available [Hyl09]. For the 7.65 and 12.71 MeV states, the new B(GT) values are lower than previous measurements by factors of 2–3 which makes it interesting to revisit the $A = 12$ case. In Table 11.2 we give our $B(M1)$ values, the corresponding B(GT) values of [Hyl09] and the ratio R(M1/GT). Results for the bound-state transitions are included for completeness. We also give the theoretical B(M1) predictions of the antisymmetrized molecular dynamics (AMD) approach [KE07] which is suggested to be able to describe both shell-model and cluster-type states.

Evidently, the AMD approach tends to overestimate the transition strength by an overall factor of about two. Tolerating this overall factor, the agreement with the experimental data is reasonable. The AMD approach gives R(M1/GT) ≈ 1, indicating a negligible orbital contribution to the M1 strength (MEC are not included in AMD). For the transitions to the 4.44 MeV state and the "10.3 MeV state", the experimental value of R(M1/GT) is consistent with unity; within 2σ this is also the case for the transition to the Hoyle state. However, for the transitions to the ground state and the

Table 11.2: Comparison of B(GT) and B(M1) values. The experimental B(GT) values are from [Hyl09], the AMD results from Y. Kanada-En'yo, private communication (2010). B(M1) values are in units of μ_N^2. The experimental transition strengths to the broad "10.3 MeV state" have been obtained using the phase-space factor of a narrow state at 10.3 MeV.

Final state	Γ_γ	B(GT)		B(M1)		R	
(MeV, J^π)	(eV)	Exp.	AMD	Exp.	AMD	Exp.	AMD
12.71, 1^+	0.49(10)	0.450(11)	0.85	3.0(6)	2.5	2.6(5)	1.1
10.3, 0^+	0.55(10)	0.154(3)	0.080	0.43(8)	0.19	1.1(2)	0.90
7.65, 0^+	1.8(3)	0.090(2)	0.20	0.37(7)	0.47	1.6(3)	0.89
4.44, 2^+	0.9(4)	0.0270(4)	0.066	0.07(3)	0.19	0.9(4)	1.1
0, 0^+	36.9(8)	0.2952(14)	0.64	0.92(2)	1.5	1.18(3)	0.89

12.71 MeV state, R(M1/GT) deviates significantly from unity. For the ground state the deviation from unity was discussed in [Gui82] where the MEC contribution was calculated and found to account for about 10% of the strength.

It would be interesting to calculate R(M1/GT) for the 15.11 $\rightarrow$ 12.71 transition (and the transitions to the bound states) within the no-core shell-model (NCSM) of [Nav07]. Since the initial and final states both are shell-model-type states, one would expect the NCSM approach to give reliable results. Unfortunately, B(M1) values from this approach are not yet available. It would also be interesting to see the predictions of the fermionic molecular dynamics (FMD) approach, which claims to give an improved handle on shell-model-type states compared to AMD by allowing for a variable width of the Gaussian packets [Che07].

One word of caution regarding the experimental numbers given in Table 11.2: For the transition to the "10.3 MeV state", the B(GT) and B(M1) values were obtained using the phase-space factor of a narrow state at 10.3 MeV even though this state is, as discussed in the beginning of the present chapter, very wide and composed of more than one state [Hyl10b].

11.4 Isoscalar and Isovector Parts of the M1 Decay of the 12.71 MeV State

Ideally, the transitions from the 12.71 MeV state to the "10.3 MeV state", the Hoyle state and the bound states would be purely isoscalar ($\Delta T = 0$). However, large isovector ($\Delta T = 1$) impurities are present due to isospin mixing with the 15.11 MeV state. In the framework of two-state mixing, we may write

$$|12.71\rangle = \alpha|T = 0\rangle + \beta|T = 1\rangle\,, \quad \alpha^2 + \beta^2 = 1\,.$$

Table 11.3: M1 γ decay of the 12.71 MeV state. The AMD results are from Y. Kanada-En'yo, private communication (2010). B(M1) values are in units of μ_N^2. The values enclosed in square brackets are not very meaningful and have only been included for completeness. See the text for explanation.

Final state (MeV, J^π)	Γ_γ (eV)	Exp.		AMD
		$B(\mathrm{M1})_{12.71}$	$\lvert M_0\rvert^2$	
10.3, 0^+	0.0034(21)	0.021(13)	0.013(11)	0.011
7.65, 0^+	0.010(5)	0.007(4)	0.003(2)	0.027
4.44, 2^+	0.048(6)	0.0073(10)	[0.0053(13)]	0.017
0, 0^+	0.32(2)	0.0135(8)	[0.0048(6)]	0.072

The mixing coefficient has been determined to $\beta = +0.0491(34)$ [NC00]. The isovector contribution to the M1 strength is large despite the small amount of mixing because the M1 isovector transition matrix elements are intrinsically faster than isoscalar ones by a factor ≈ 13.7, as argued by [Ade77]. In terms of the pure isoscalar and isovector matrix elements, M_0 and M_1 , we may write

$$B(\mathrm{M1})_{12.71} = |\alpha M_0 + \beta M_1|^2 \,, \quad B(\mathrm{M1})_{15.11} \approx |M_1|^2 \,.$$

Given β and the transition strengths, $B(\mathrm{M1})_{12.71}$ and $B(\mathrm{M1})_{15.11}$, we may solve for the unknown isoscalar strength, $|M_0|^2$.

Experimental and theoretical transition strengths are given in Table 11.3. Note that the theoretical value should be compared to the total strength, i.e. $B(\mathrm{M1})_{12.71}$. The γ widths, Γ_γ , were calculated from the branching ratios of Table 11.1 using the γ width to the ground state $\Gamma_0 = 0.32(2)$ eV given in [NC00] and the ratio $\Gamma_1/\Gamma_0 = 0.150(18)$ given in [Ade77]. $B(\mathrm{M1})_{12.71}$ was calculated from Eq. 11.1. AMD overestimates the transition strength to the ground state by as much as a factor of five. It overestimates the transition strength to the 4.44 MeV state and the Hoyle state by factors of two and three, respectively. Within the experimental uncertainty, AMD gets the transition strength to the "10.3 MeV state" right.

The mixing parameter β was determined from (e, e') measurements of the g.s. $\rightarrow$ 12.71 and g.s. $\rightarrow$ 15.11 transition strengths, relying on a shell-model calculation of the isoscaler contribution [NC00]. Thus, the isoscalar strength to the ground state given in table 11.3 is essentially the shell-model value. For the 4.44 MeV state, the situation gets complicated due to isospin mixing in the *final* state [Ade77], e.g. with the 2^+, $T = 1$ state at 16.11 MeV. For these reasons, the isoscalar strengths obtained for the $12.71 \rightarrow$ g.s. and $12.71 \rightarrow 4.44$ transitions are not very meaningful and have been enclosed in brackets.

11.5 Summary and Perspectives

Detection of multi-particle breakups in complete kinematics allows for the study of electromagnetic transitions between broad particle-unbound nuclear states with an efficiency comparable to standard γ spectroscopy (on the order of 1%), but in an essentially background-free environment.

We have looked at the γ decays of the 15.11 and 12.71 MeV states in ^{12}C to lower-lying states that break up into three α particles. The following transitions were detected: 15.11 $\rightarrow$ 12.71, 11.83, 10.3, 7.65 and 12.71 $\rightarrow$ 10.3, 7.65. The partial γ widths obtained in the present work are in agreement with previous measurements when such exist. The value of $\Gamma_\alpha/\Gamma = (2.8 \pm 1.2)\%$ obtained for the isospin-forbidden α decay of the 15.11 MeV state is in good agreement with the literature value when corrected for the new γ branches.

We have explored the relation between the M1 γ decays of the 15.11 MeV state and the analog β decays of ^{12}B and ^{12}N. The reduced transition strengths have been compared with AMD calculations which, it is found, tend to overestimate the actual strength by a factor of about two. Similar calculations within other frameworks such as NCSM or FMD are desirable. For the 12.71 MeV state, calculations which are able to separate the M1 transition strength into its isoscalar and isovector parts would be of interest. Finally, we note that AMD predicts transitions from the 15.11 and 12.71 MeV states to a lower-lying 2^+_2 state with tiny strengths of $B(\mathrm{GT}) = 0.002\,\mu_N^2$ and $B(\mathrm{M1}) = 0.006\,\mu_N^2$, respectively, which may be the reason why no clear signature of this state is seen in the experiments.

Looking to the future, we see a number of physics cases that could be studied with an experimental method like ours. One nearby example is the 16.11 MeV state in ^{12}C ($J^\pi = 2^+$, $T = 1$) which has γ branches to the 12.71 and 9.64 MeV states at the 10^{-5} level [Ade77], slightly below our sensitivity. Naturally, one would also expect γ branches to the broad states. It is interesting to note that a 2^+, $T = 0$ state should be favored over 0^+ states in γ decays of the 16.11 MeV state because isovector M1 transitions are considerably stronger than isovector E2 transitions, as seen for transitions to bound states. Therefore, γ decays from the 16.11 MeV state provide a promising method to look for the 2^+ rotational excitation of the Hoyle state. Recently, such an experimental study has been undertaken at the 400 keV Van de Graaf accelerator in Aarhus, using the $p + {}^{11}$B reaction to populate the 16.11 MeV state.

Two other examples are the lowest $T = \frac{3}{2}$ levels of ^{9}Be and ^{9}B. They have γ branches of 2.1 and 2.5%, respectively, to the ground state [McD76], but γ transitions to excited states have not been observed yet. (In ^{9}B the $T = \frac{3}{2}$ level is found at $E_x = 14.67$ MeV. It is energetically accessible in the $^3\mathrm{He} + {}^{10}\mathrm{B} \rightarrow \alpha + {}^9\mathrm{B}$ reaction at 4.9 MeV but is not observed due to the reaction being isospin-forbidden.)

Another example is ^{8}Be. The $4^+ \rightarrow 2^+$ transition was recently measured by [Dat05]

who used an experimental technique similar to ours with the additional advantage of also detecting the emitted γ ray. A measurement of the $2^+ \rightarrow 0^+$ transition might be within reach despite an expected branching ratio of only 6×10^{-9}. With the inclusion of γ and neutron detectors in the experimental setup, a wider range of physics cases will become accessible.

CHAPTER 12

Dalitz Plot Analysis of the $^{12}C \rightarrow 3\alpha$ Breakup

In the present chapter, we take a closer look at the $^{12}C \rightarrow 3\alpha$ breakup. We are, in particular, interested in the breakups that do *not* proceed via the ground state of ^{8}Be. The discussion focuses on the three unnatural parity states at 11.83, 12.71 and 13.35 MeV. We make use of complete kinematics data from the $^{11}B(^{3}He, d\alpha\alpha\alpha)$ reaction (multiplicity three and four) which offers the most statistics and the best signal-to-background ratio for these three states.

Dalitz plots will be used to visualize and analyze the data. As we will see, the intensity distribution in the Dalitz plot exhibits zero points characteristic of the total spin and parity of the 3α system, allowing us to determine the spin and parity of the 13.35 MeV state to 4^- in a model-independent way. The Dalitz plot intensity distributions of the 11.83 and 12.71 MeV states will be compared to the predictions of a recent three-body calculation as well as to simpler models. We find that all models are able to reproduce the gross structures of the Dalitz plot intensity distributions, but none give an accurate description of the detailed profile.

There is a great amount of overlap between this chapter and [Kir10].

12.1 Introduction

In two-body decays, the decay fragments are emitted back-to-back, their energies fixed by the conservation laws of energy and momentum. If the decaying nucleus has been prepared in a polarized state, its spin and parity can be inferred from the angular distribution of the decay. However, if the initial spin is randomly oriented or zero, the only measurable quantities holding information on the structure of the initial state are the decay width and, if several decay channels are open, the branching ratios. For three-body decays, the situation is different. The energies of the decay fragments are not fixed but may vary within bounds determined by energy and momentum conservation thereby giving rise to measurable energy distributions which may or may not hold additional information on the structure of the initial state. However,

the interpretation of the measured energy distributions in terms of the initial structure is complicated by final-state interactions of both nuclear and electromagnetic origin.

In the present context, the question we want to ask is: What can the energy distribution of the three α-particles from the decay of ^{12}C teach us about the properties of the initial nuclear state? In particular, we wish to test the hypothesis put forward by [ÁR07] that the energy distribution of the three α-particles is completely determined by the symmetries of the 3α system and the effective forces acting between the α particles. An alternative way to formulate the same hypothesis is to say that the energy distribution is sensitive to the properties of the 3α system that *forms* in the breakup process, while it is *in*sensitive to the structure of the initial nuclear state which does not necessarily resemble that of three interacting α particles.

As noted by J. Hans D. Jensen (1907–1973) in his Nobel lecture from 1963, a similar hypothesis was put forward in the very early days of nuclear physics for ordinary single-α decay:

> It is remarkable that very little information about nuclear structure could be gained from the study of alpha decay. Max von Laue has pointed this out very clearly in a letter to Gamow in 1926; he congratulated Gamow on his explanation of the Geiger-Nuttal law[1] in terms of the tunneling effect and then went on: "however, if the alpha decay is dominated by quantum phenomena in the region outside the nucleus, we obviously cannot learn much about nuclear structure from it." [Jen63]

A few sentences below, Jensen concludes that "the alpha particles obviously only form while emerging from the nucleus."

The 3α-breakup process is not just an obstacle to be overcome in order to glimpse into the structure of ^{12}C but constitutes an interesting case in its own right: The fundamental quantum mechanical phenomena of interference and tunneling are central to the description of the 3α breakup and manifest themselves in the shape of the measured energy distributions in a non-trivial way. Furthermore, the measured energy distributions are sensitive to the effective forces acting between the α particles.

A number of experimental studies of the 3α breakup exist in the literature, see e.g. [Ols65, Bro65a, Wag66, Wit72, Bal74, Fyn03], most of which have focused on the 1^+, $T = 0$ state at 12.71 MeV and the states that can be populated in the $p + {}^{11}\mathrm{B} \rightarrow {}^{12}\mathrm{C}$ reaction. To advance our understanding of the 3α breakup, we must test the theoretical models against other states at different energies and with different constraints from symmetry.

The 3α breakup of the 12.71 MeV state was first measured in complete kinematics in 2003 by [Fyn03] who used the β decay of ^{12}N to populate the 12.71 MeV state.

[1] That is, the fact that the lifetime of an α-emitter changes by 25 powers of ten when the alpha-particle energy increases only by a factor of two.

Dalitz plots were used to analyze the data. The intensity distribution was compared to the predictions of the sequential and the democratic model, cf. Section 12.2. The gross structures were correctly reproduced by both models. When considering the detailed shape of the intensity distribution, the sequential model was found to be in much better agreement with the experimental data than the democratic model. The level of agreement was surprisingly good considering the short life time of the 2^+ resonance in ^{8}Be. It was pointed out that a genuine quantum mechanical three-body calculation is needed to get a complete description of the data. Such calculations have since become available for a number of states in ^{12}C [ÁR08b] and will be compared to our new measurements.

Unbound quantum mechanical three-body systems occur in many realms of physics ranging from molecular to particle physics and attract great interest. One well-known example is the decay of mesonic resonances into three pions [Ams98], which bears many similarities to the 3α breakup.

12.2 Breakup Models: Limiting Cases

Historically, two very different breakup models (and variations thereof) have been employed to describe the experimental data. These are the sequential [Bal74] and the democratic [Kor90] (also called direct) models which represent limiting cases of the possible three-body decay modes.

In the sequential model, the three-body breakup is thought to proceed through an intermediate long-lived two-body resonance thereby effectively reducing the problem to that of a succession of two two-body decays, the only correlations between the two decays being those due to conservation of angular momentum and parity. The central assumption is that of dynamical independence: At the time of the secondary breakup, the particle emitted in the primary decay must have traveled far enough for it not to feel the effects of the secondary breakup. The nuclear force quickly ceases to be important, whereas the effects of the Coulomb force are significant up to at least 100 fm. The usefulness of the sequential model stems from the fact that we know how to deal with nuclear two-body breakups. The appropriate formalism is that of the *R*-matrix theory introduced in Section 7.6. The form of the angular correlations depends on the spins and orbital angular momenta involved in the decay [Bie53]. In the case of the 3α breakup, the decay amplitude must be symmetrized in the coordinates of the three particles as required by Bose statistics causing sizable interference effects.

For the low-lying resonances in ^{12}C, two options exist. These are, as shown in Fig. 12.1, the narrow 0^+ ground state of ^{8}Be and the broad 2^+ first excited state. Due to the long life time of the ^{8}Be ground state ($\Gamma = 5.6\,\mathrm{eV}$, corresponding to

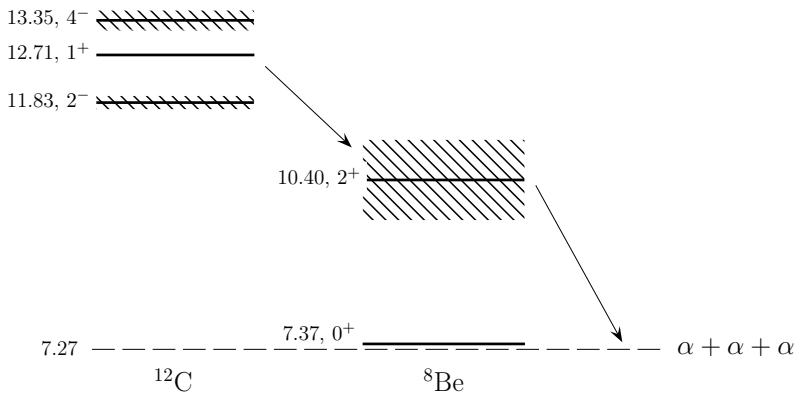

Figure 12.1: Sequential decay via the broad 2^+ resonance in ^{8}Be. Energies are in MeV with respect to the ground state of ^{12}C. Only the three ^{12}C states considered in the present work are shown.

$\tau = \hbar/\Gamma = 1.2 \times 10^{-16}$ s), decays proceeding along this route may be regarded as exclusively sequential. The energies of the α particles are fixed and angular correlations absent due to the ground state having zero spin. Consequently, no dynamical information may be extracted from the ground state channel. The ^{8}Be(2^+) channel is much richer in information. For unnatural-parity states the ground-state route is not allowed because it violates parity conservation.

The short life time of the 2^+ resonance in ^{8}Be ($\Gamma = 1.5$ MeV, corresponding to $\tau = 4.5 \times 10^{-22}$ s) casts serious doubt on the validity of the sequential model. One may estimate the typical distance traveled by the first α particle at the time of the secondary breakup to be only ~ 5 fm, implying a Coulomb energy of ~ 1 MeV. This, clearly, is incompatible with the assumption of dynamical independence. Therefore, we cannot expect perfect agreement between experiment and the predictions of the sequential model. The Coulomb barrier for the secondary breakup ought to be modified from that assumed in the *R*-matrix formalism. One might even argue that the concept of a two-body resonance becomes meaningless due to the strong perturbation caused by the near presence of the third body. In any case great caution must be exerted in the interpretation of the experimental data [Fyn09].

Democratic decays may be regarded as the counterpart of sequential decays. Put somewhat simply, a breakup is characterized as democratic if it does not involve any long-lived intermediate states. The α-α interaction is assumed to play an insignificant role in the breakup, and the decay amplitude is calculated by expanding in hyperspherical harmonics functions (eigenstates of the grand angular momentum operator

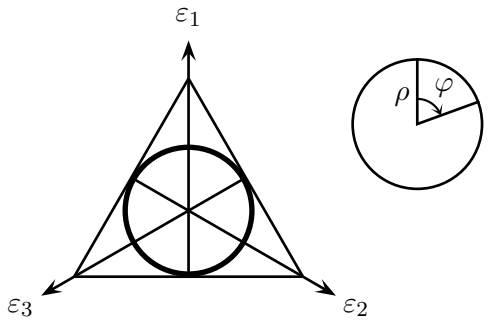

Figure 12.2: The Dalitz plot and associated projections, ρ and φ. ε_i denotes the energy of the i^{th} α particle normalized to the total decay energy, i.e. $\varepsilon_i = E_i / \sum_k E_k$.

of the three-body system, characterized by the hypermomentum K) retaining only the lowest order term permitted by symmetries. This procedure may be regarded as the three-body equivalent of a well-known procedure applied to two-body breakups: Expand the amplitude in spherical harmonics functions (angular momentum eigenstates) and neglect higher-order terms suppressed by the enhanced centrifugal barrier. Since three-body configurations of small relative two-body momentum are associated with large values of the hypermomentum K, such configurations are excluded from the democratic model. The democratic decay amplitude must be symmetrized in the coordinates of the three particles as required by Bose statistics.

12.3 Dalitz Plot Analysis Technique

Assuming an unpolarized initial state, the measurement of two energies, E_1 and E_2, gives complete kinematical information. The data are best visualized in a Dalitz plot [Dal53], see Fig. 12.2. Since the density of final states is proportional to $\mathrm{d}E_1\,\mathrm{d}E_2$, the intensity of the Dalitz plot will be proportional to the matrix element squared. Consequently, pure phase-space decays result in flat distributions. Structures in the Dalitz plot may be manifestations of symmetries of the three-body system, or they may originate from final-state interactions such as a two-body resonance. Two-dimensional plots are ill-suited for visual comparison of experimental and theoretical distributions at the detailed level. For this purpose, one-dimensional projections like the radial (ρ) and angular (φ) projections shown in Fig. 12.2 are much more useful. Other projections may be more instructive depending on the circumstances.

The role of symmetries in three-pion decays was studied by C. Zemach in 1964 [Zem64]. Solely on the grounds of Bose statistics and conservation of spin, isospin and parity, he was able to show that the decay amplitude takes on certain general

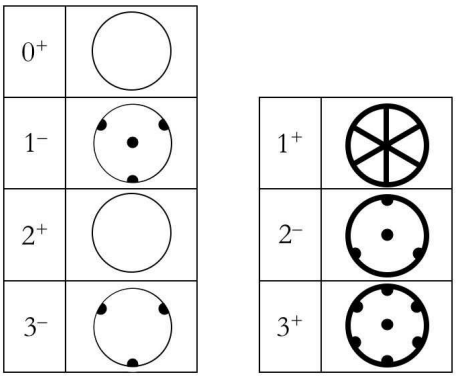

Figure 12.3: Regions of the 3α Dalitz plot where the intensity must vanish (forbidden regions) due to the symmetries of the 3α system, are shown in black. The vanishing is of higher order where the black lines and dots overlap. The pattern for a spin $J + 2n$ ($J \geq 2$ and $n = 1, 2, 3, \ldots$) is identical to the pattern for spin J except that the vanishing at the center is not required for spins ≥ 4.

forms depending on the spin, isospin and parity of the system, forcing the amplitude to vanish in specific regions of the Dalitz plot which we shall refer to as *forbidden* regions. Zemach made no assumptions about the interactions involved except that they have to conserve isospin and parity. Pions and α particles are both spin-zero bosons but have opposite parities (negative and positive, respectively) and, in contrast to α particles, pions posses a non-zero isospin of $T = 1$. The results of Zemach's analysis can readily be applied to the 3α system as long as we account for the difference in parity and restrict ourselves to three-pion systems of total isospin $T = 3$. The regions of the 3α Dalitz plot forbidden by symmetry are shown in Fig. 12.3. In general, the restrictions imposed by the symmetries of the 3α system are more severe for the unnatural-parity states. While severe constrains may facilitate spin-parity assignments, mild constrains make it easier to study the effects of interactions.

In a sequential decay of ^{12}C through a two-body resonance, the first α particle gets two-thirds of the energy released in the primary decay. The center of mass energies of the two secondary α particles depend on the orientation of the secondary breakup relative to the first. Consequently, the intensity of the Dalitz plot will be confined to bands like those shown in Fig. 12.4, whose width and distance to the sides of the triangle reflect the width and energy of the two-body resonance. The lateral intensity distribution of the bands depends on the profile of the two-body resonance as well as the penetrabilities associated with the Coulomb and centrifugal barriers of the entrance ($\alpha + {}^8Be$) and exit ($\alpha + \alpha$) channels, while the longitudinal structure is determined by the angular correlations. Where bands overlap, interference effects

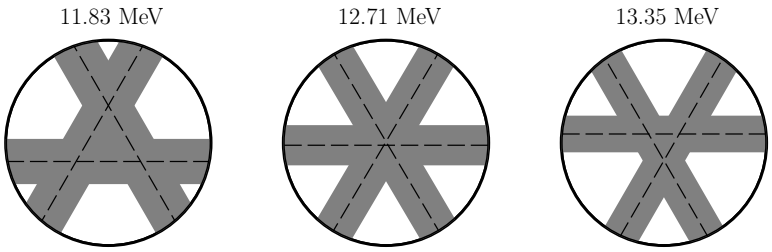

Figure 12.4: Sequential band structure associated with the decay of the three ^{12}C states considered in the present work. The dotted lines indicate the maximum of the band's lateral intensity distribution; the gray area its width (FWHM).

may be expected.

Fig. 12.3 and Fig. 12.4 are useful points of reference when inspecting the two-dimensional Dalitz distributions measured in experiment or calculated from theory. Conceptually, the separation of structures in two distinct groups, namely, those due to the general symmetries of the 3α system and those caused by final-state interactions, is very useful: Any theoretical model possessing the correct symmetries is bound to reproduce the *gross* structures of the Dalitz distribution irrespective of its assumptions about the dynamics of the 3α system. The forbidden regions identified in Fig. 12.3 also have a more "practical" application. As we shall see, they serve as a model-independent spectroscopic tool which allows us to determine or at least impose constraints on the spin-parity of ^{12}C resonances. See [Gas08] for an example of such application in particle physics. Notice that the mere existence of a zero point in the Dalitz plot (i.e. a region of vanishing intensity) cannot be used as conclusive evidence for a particular spin-parity assignment because there could also be dynamical reasons for the suppressed intensity. However, the absence of a zero point can always be used to falsify a proposed spin-parity assignment.

12.4 Results

The ^{12}C excitation spectrum separated into decays that proceed via the ground state of ^{8}Be (dashed) and decays that do not (solid) is shown in Fig. 12.5. The intensity present in addition to the five visible peaks does not constitute background in the usual sense of the term but is understood as broad overlapping resonances in ^{12}C, possibly with contributions from the two very broad 1^+ and 2^+ $T = 0$ states in ^{6}Li through the $^{3}\mathrm{He} + {}^{11}\mathrm{B} \rightarrow {}^{8}\mathrm{Be} + {}^{6}\mathrm{Li} \rightarrow d + 3\alpha$ channel (reactions via the narrow 3^+, $T = 0$ state in ^{6}Li were easily removed by gating on the corresponding peak in the

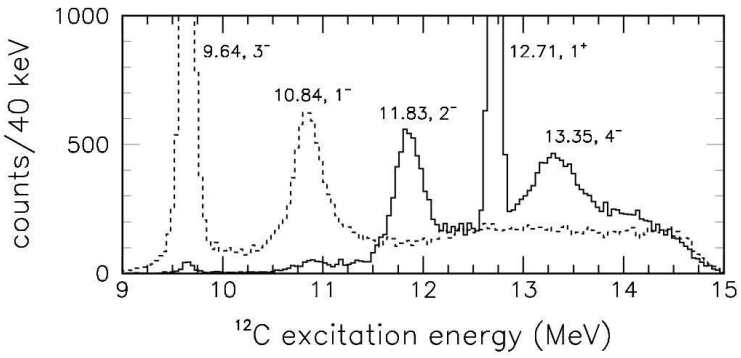

Figure 12.5: ^{12}C Excitation spectrum separated into decays that proceed via the ground state of ^{8}Be (dashed) and decays that do not (solid).

$d + \alpha$ relative energy spectrum). Nonetheless, we shall refer to these broad structures as "background" when we discuss their contribution to the Dalitz plots displayed in Fig. 12.6. We adopt the heuristic approach of using the regions adjacent to the peaks to determine the characteristics of the background below the peak. The background fractions are 11%, 8% and 50% for the 11.83, the 12.71 and the 13.35 MeV state, respectively.

Shown in Fig. 12.6 are the experimental Dalitz distributions obtained by gating on the three unnatural-parity states in Fig. 12.5. Both multiplicity four and multiplicity three events have been used, giving 3.5×10^4 events for the 11.83 MeV state, 1.2×10^5 events for the 12.71 MeV state and 9.9×10^3 events for the 13.35 MeV state.

12.4.1 Spin-Parity Assignment

The Dalitz distributions of the 11.83 and 12.71 MeV states clearly exhibit the forbidden regions dictated by symmetry (Fig. 12.3). What can we say about the spin and parity of the 13.35 MeV state? Since it is not observed to decay via the ground state of ^{8}Be, it is likely to have unnatural parity. The absence of a zero point at the center of the Dalitz plot excludes the spin-parity assignments 1^+, 2^-, 3^+. As noted in the caption of Fig. 12.3, the pattern for a spin $J + 2n$ ($J \geq 2$ and $n = 1, 2, 3, \ldots$) is identical to the pattern for spin J except that the vanishing at the center is not required for spins ≥ 4. Therefore, we conclude that the correct spin-parity assignment for the 13.35 MeV state is 4^- (though spins ≥ 5 cannot be excluded based on the present study alone). The radial projection of the Dalitz distribution is shown in Fig. 12.7 demonstrating with all clarity that the intensity at the center of the Dalitz plot is not

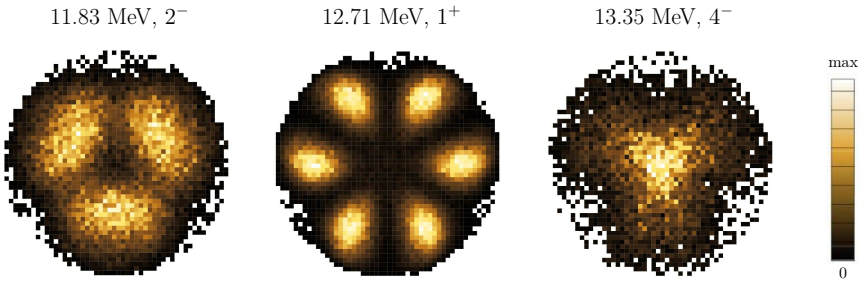

Figure 12.6: Dalitz plots obtained using the experimental data. The spin and parity of the 13.35 MeV state is given as 4^- as established by the present work, contradicting the tentative 2^- assignment that appears in the most recent $A = 12$ compilation [AS90].

due to background, the contribution of which is indicated by the hatched histogram. The radial projection also confirms the vanishing of the intensity at the circumference as expected for all unnatural-parity states.

12.4.2 Model Comparison

The Dalitz distributions of the 11.83 and 12.71 MeV states will now be compared to the predictions of four models: The sequential and democratic models outlined in Section 12.2, a slightly modified version of the sequential model conceived by [Fyn03] and the full three-body calculation of [ÁR08b]. The predictions of the four models are shown in Fig. 12.8. Their radial and angular projections are compared with the experimental data in Fig. 12.9 and 12.10. "Sequential I" refers to the standard formulation of the sequential model [Bal74] and "Sequential II" to the slightly modified version of [Fyn03].

Sequential I. In the sequential model, we use the R-matrix parameters of [Bha06] for the broad 2^+ resonance in ^{8}Be: An excitation energy of $E_0 = 3037 \pm 5$ keV and a reduced width of $\gamma^2 = 1075 \pm 7$ keV. The channel radii were computed as $a = 1.42\,\mathrm{fm}\,(A_1^{1/3} + A_2^{1/3})$. The orbital angular momentum in the secondary breakup is always $l' = 2$. In the primary breakup, l depends on the spin of ^{12}C. For the 12.71 MeV state, only $l = 2$ is compatible with conservation of spin and parity, whereas $l = 1, 3$ are possible for the 11.83 MeV state.

Sequential II. The modification introduced by [Fyn03] consists in adding extra barrier penetrabilities for each of the secondary α particles as an approximate treatment of final-state Coulomb repulsion. Further details are given in [Fyn03].

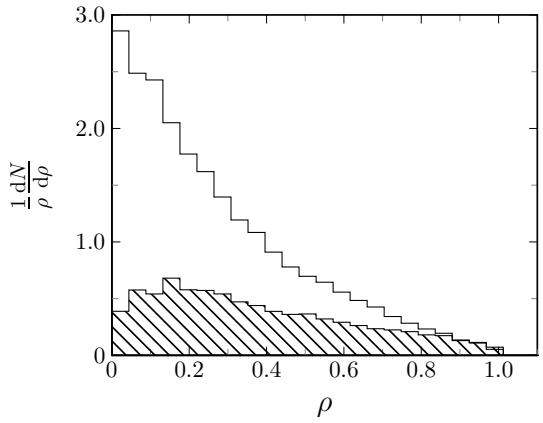

Figure 12.7: Radial projection of the Dalitz plot for the 13.35 MeV state normalized to unit area. The radial coordinate, ρ, runs from 0 (center) to 1 (circumference). The hatched histogram represents the background contribution.

Democratic. The democratic model was briefly reviewed in Section 12.2. For further details, see [Kor90].

Three-body. The full three-body calculation of [ÁR08b] treats ^{12}C as a 3α-cluster system at all distances. The three-body problem is solved in coordinate space using the adiabatic hyperspherical expansion method. The complex scaling method is used to compute resonances. The phenomenological Ali-Bodmer two-body interaction (tuned to reproduce the low-energy two-body scattering phase shifts) is used. In addition, a three-body short-range interaction adjusted to reproduce the correct excitation energies in ^{12}C is included.

To compare model calculations against the data, we must account for experimental effects. For this purpose, Monte Carlo simulations have been employed, see Section 9.4. The simulated distributions contain $\sim 1.5 \times 10^5$ events. Varying the geometry, the detector resolution and the deuteron angular distributions used in the simulation within their respective uncertainties, we find no visible effect on the final distributions.

As discussed in Section 8.3, the ^{12}C resonance formed in the $^3He + ^{11}B \rightarrow d + ^{12}C$ reaction is likely to be polarized to a lesser or larger extent, which may affect the Dalitz distributions since the experiment does not cover full 4π. The form of the polarization is not easily extracted from the measurements. However, through simulations (based on the sequential model) we find that the Dalitz distributions of the 11.83 and 12.71 MeV states are insensitive to polarization, which may be explained

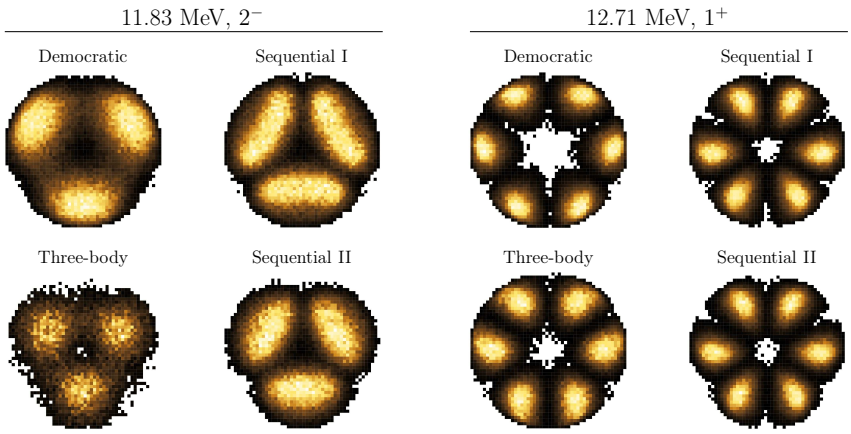

Figure 12.8: Simulations of the Dalitz distribution for the 11.83 and 12.71 MeV states based on four different theoretical models.

as follows: Owing to the small angular momenta involved, only spherical harmonics of low order contribute (see. Eq. 2 in [Fyn03]) whose variation on the angular scale of the detectors is relatively small. For the 13.35 MeV state, the effects of polarization are no longer negligible, which is the reason why we chose to focus on the 11.83 and 12.71 MeV states for the model comparisons.

We note that the statistical uncertainties on the experimental and simulated distributions shown in Fig. 12.9 and 12.10 are essentially zero.

12.4.2.1 The 12.71 MeV State

All models reproduce the forbidden regions dictated by symmetry. However, they all fail in reproducing the detailed shape of the distribution as revealed by the radial and angular projections. The inclusion of final-state Coulomb repulsion in the sequential model is seen to shift the radial projection toward smaller values of ρ, consistent with suppression of coaxial emission[2], whereby perfect agreement with the data is achieved. The angular projection is shifted toward larger values of φ, but the agreement with the data remains rather poor. The deviation is far too large to be accounted for by the uncertainties on the R-matrix parameters.

The three-body model and the democratic model in particular give poor fits to the radial projection. On the other hand, they predict angular projections in reasonable

[2]The circumference of the Dalitz plot corresponds to the situation where all three momenta lie along the same axis.

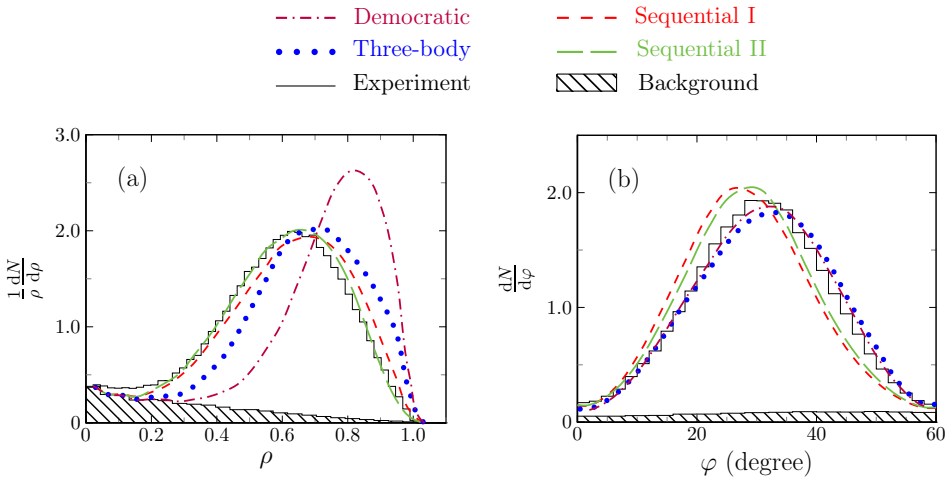

Figure 12.9: Radial and angular projections of the Dalitz plot for the 12.71 MeV state. Owing to the six-fold symmetry of the Dalitz plot, the angular projection only runs from 0 to 60 degrees.

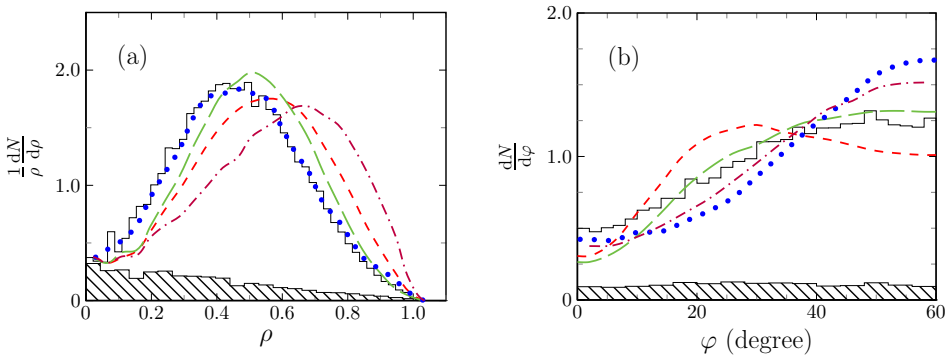

Figure 12.10: Radial and angular projections of the Dalitz plot for the 11.83 MeV state. Owing to the six-fold symmetry of the Dalitz plot, the angular projection only runs from 0 to 60 degrees. For legends, see Fig. 12.9.

agreement with the data even though both are too wide and slightly displaced. As is evident from the sequential band structure of the 12.71 MeV state, cf. Fig. 12.4, the centroid and width of the angular projection directly reflects the energy and width of the two-body resonance, whereas the radial projection is, to a first approximation, independent of these parameters. If we were able to modify the α-α potential used in the three-body calculation so as to increase the energy and simultaneously reduce the width of the two-body resonance, near perfect agreement with the data could probably be achieved for the angular projection. The shifts needed are on the order of 100 keV which is not unrealistic[3]. However, this would not improve the situation in the radial projection.

12.4.2.2 The 11.83 MeV State

It was noted by [Kor90] that the democratic model ought to work better the lower the energy. However, when compared with the data, the democratic model is seen to give bad fits also for the 11.83 MeV state. The three-body model is in perfect agreement with the data in the radial projection, but it gives a poor fit in the angular projection.

An additional complication arises in the sequential model because the α + ^{8}Be breakup may proceed both through a p wave and an f wave. In contrast, the decay of the 12.71 MeV state proceeds exclusively through a d wave. The two amplitudes must be added coherently, i.e. $f = \alpha f_{l=1} \pm \beta f_{l=3}$ with $\alpha^2 + \beta^2 = 1$ and $\alpha, \beta \geq 0$. The two amplitudes may interfere constructively (+) or destructively (−). The best fit to the data is achieved by assuming roughly equal weights, $\alpha \approx \beta \approx 1/\sqrt{2}$, and destructive interference. Note that the f-wave amplitude, $f_{l=3}$, is suppressed by a factor of ≈ 5 relative to the the p-wave amplitude, $f_{l=1}$, due to the increased centrifugal barrier.

The inclusion of final-state Coulomb repulsion in the sequential model is, again, seen to shift the radial distribution towards smaller values of ρ thereby improving the agreement with the data. The fit to the angular projection is also improved though deviations remain.

[3] R. Álvarez-Rodríguez, private communication (2010).

12.5 Final-State Coulomb Repulsion

The importance of final-state Coulomb repulsion may be crudely estimated by numerically solving the classical equations of motion of the 3α system subject only to the Coulomb force from a fixed distance and outwards, see e.g. [Nor68,Tho72]. Given the positions, $\boldsymbol{x}_i(t)$, and the momenta, $\boldsymbol{p}_i(t)$, of the three α particles at a given time, t, we compute the positions and momenta at time $t + \Delta t$ as

$$\begin{aligned} \boldsymbol{p}_i(t + \Delta t) &= \boldsymbol{p}_i(t) + \boldsymbol{F}_i(\boldsymbol{x}_1, \boldsymbol{x}_2, \boldsymbol{x}_3)\, \Delta t \ , \\ \boldsymbol{x}_i(t + \Delta t) &= \boldsymbol{x}_i(t) + \frac{\boldsymbol{p}_i(t + \Delta t)}{m_\alpha}\, \Delta t \ . \end{aligned} \tag{12.1}$$

Here, $\boldsymbol{F}_i(\boldsymbol{x}_1, \boldsymbol{x}_2, \boldsymbol{x}_3)$ is the Coulomb force on the i^{th} α particle, and $\Delta t = 10^{-25}$ s is the chosen time step. Energy conservation is used to check the numerical precision.

First, we look at the Coulomb repulsion between the first emitted α-particle and the secondary α particles in the decay of the 12.71 MeV state in ^{12}C. The three-body energy is $E_{3b} = 12.710 - 7.275 \approx 5.4$ MeV. The two-body energy is fixed to $E_{2b} = 2.4$ MeV. The 3α configuration at the instant of the $^8\text{Be} \rightarrow 2\alpha$ breakup ($t = 0$) is shown in Fig. 12.11 (a). x is the distance between the secondary α particles and y is the distance from their center of mass to the first α particle. The secondary α particles are emitted at angles θ and $180^\circ - \theta$ relative to the recoil axis. At $t = 0$, the energy so far liberated in the form of kinetic energy to the first α particle and the recoiling ^{8}Be nucleus is $E_{3b} - E_{2b} - V_C$, where V_C is the Coulomb energy of the 3α configuration at $t = 0$. Using Eq. 12.1, we calculate the evolution the 3α system out to several thousand fm. The energy shift of the first α particle is shown in Fig. 12.11 (a) for three different choices of starting distance, $y = 10$, 20, 30 fm. Our calculations confirm what one naturally expects: For coaxial emission, the first α particles gets an additional "kick", so its energy increases. For emission angles close to 90°, the Coulomb repulsion weakens because the secondary α particles move apart, so the first α particle gets less energy. Our calculations suggest that for coaxial emission, the extra energy imparted to the first α particle could easily be several hundred keV. Also, the angle measured at infinity could change as much as 10° compared to the actual emission angle.

Second, we look at the Coulomb repulsion between the deuteron and the α particle and the $^8\text{Be}_{gs}$ nucleus in the reaction $^3\text{He} + {}^{11}\text{B} \rightarrow d + {}^{12}\text{C}(10.84) \rightarrow d + \alpha + {}^8\text{Be}_{gs}$. Using numbers from Chapter 8, the three-body energy is computed to $E_{3b} = 9.8$ MeV and the two-body energy to $E_{2b} = 3.5$ MeV. From the width of the 10.84 MeV state ($\Gamma = 272$ keV) and the kinetic energies involved, it is easily shown that, on average, $y \approx 65$ fm at the instant of the $^{12}\text{C}(10.84) \rightarrow \alpha + {}^8\text{Be}_{gs}$ breakup. The result of the calculation is shown in Fig. 12.11 (b). The shift in deuteron energy is on the order of 5–10 keV.

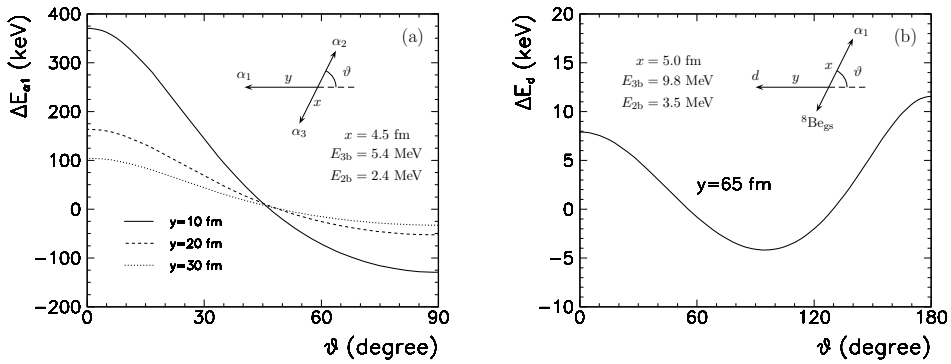

Figure 12.11: (a) Energy shift of the first α particle in the decay of the 12.71 MeV state due to final-state Coulomb repulsion, versus the $^8\mathrm{Be} \rightarrow 2\alpha$ breakup angle, θ, for three choices of the starting distance, y. **(b)** Energy shift of the deuteron from the population of the 10.84 MeV state due to final-state Coulomb repulsion, versus the $^{12}\mathrm{C}(10.84) \rightarrow \alpha + {}^8\mathrm{Be}_{\mathrm{gs}}$ breakup angle, θ, for a realistic choice of starting distance, y.

12.6 Extension to Broad Resonances

It is the presence of very broad states with a strong coupling to the 3α continuum that makes the study of the ^{12}C excitation spectrum interesting as well as challenging. Nevertheless, the present discussion has focused exclusively on three relatively narrow states, while the broad underlying (and as of yet unresolved) structures have been treated merely as a background. The obvious and challenging next step will consist in applying the Dalitz plot analysis technique[4] to the regions *in between* the peaks in Fig. 12.5. In particular, it may be possible to determine or at least constrain the spin and parity of the broad states by examining the gross structures of the Dalitz plot. However, as we consider ^{12}C states of increasing width (and hence shorter life time), we will eventually be confronted with a four-body problem in which dynamical correlations between the deuteron and the three α particles must be taken into account.

One indicator of the necessity of a four-body treatment is the Coulomb energy stored in the $d + {}^{12}\mathrm{C}$ system at the time of the 3α breakup. The distance separating the deuteron and the ^{12}C nucleus at the time of the 3α breakup may be estimated as $v\tau$, where $\tau = \hbar/\Gamma$ is the life time of the excited state in ^{12}C and v is the relative speed of the deuteron and the ^{12}C nucleus at infinite separation. If we require the Coulomb energy to be less than 10% of the energy released in the 3α breakup, we arrive at an

[4]See [Agu80] for an example from particle physics of a systematic approach in which the Dalitz plot intensity distribution is decomposed into certain moments.

upper limit of $\Gamma < 0.6$–1 MeV (for ^{12}C excitation energies in the range 10–14 MeV). Another indicator of the necessity of a four-body treatment is the de Broglie wave length, $\lambda = h/p$, at infinite separation. If we picture the deuteron and the ^{12}C nucleus as freely propagating wave packets, λ gives a measure of their spatial extension. In this naïve picture, a four-body description becomes necessary when λ is comparable to the distance separating the deuteron and the ^{12}C nucleus at the time of the 3α breakup. This happens when Γ exceeds 1–2 MeV.

Even though these estimates are very crude, they demonstrate that dynamical four-body correlations may become important when $\Gamma \gtrsim 1$ MeV. In order to avoid four-body correlations all together, alternative ways of populating excited states in ^{12}C must be found, e.g. through the β decay of ^{12}B and ^{12}N or γ decays from higher-lying states in ^{12}C.

12.7 Summary and Perspectives

The breakup of ^{12}C resonances into three α particles constitutes an interesting and challenging physics case both from the point of view of theory and experiment. The fundamental quantum processes of interference and barrier tunneling play a central role in the breakup, so does the α-α potential, its influence made most evident by the observation of sequential decays proceeding via the narrow ground state of ^{8}Be. They all leave their imprint on the energy distribution of the α particles. The extent to which the structure of the ^{12}C resonance affects the energy distribution is unknown.

The experimental data is best visualized in two-dimensional Dalitz plots which, in the absence of polarization, contain the complete kinematical information. The unique symmetries of the 3α system play a central role in the description of the breakup because they cause the intensity to vanish in certain regions of the Dalitz plot, thereby inducing structures that do not depend on the decay mechanism but are characteristic of the total spin and parity. This provides a model-independent spectroscopic tool that allows us to determine or at least constrain the spin and parity of the 3α system.

Dalitz plots for the three unnatural-parity states at 11.83, 12.71 and 13.35 MeV, which are prevented from decaying sequentially through the narrow ground state of ^{8}Be due to spin-parity conservation, were presented and analyzed. The gross structures of the Dalitz plot, in particular the absence of a zero point at the center, allowed us to assign spin-parity 4^- to the 13.35 MeV state in disagreement with the tentative 2^- assignment of the most recent $A = 12$ compilation [AS90] but in agreement with recent experimental findings [Fre07b] and favored by theoretical considerations.

The Dalitz distributions of the 11.83 and 12.71 MeV states were compared to the predictions of four theoretical models. All were found to reproduce the gross struc-

tures dictated by the symmetries of the 3α system, but none were able to reproduce the detailed shape of the distributions. The sequential model modified to accommodate final-state Coulomb repulsion (Sequential II) gives the best fit to the data. As previously pointed out by [Fyn03], the sequential model in its standard form (Sequential I) gives a surprisingly good fit for the 12.71 MeV state considering the very short life time of the ^{8}Be(2^+) resonance. However, for the 11.83 MeV state we do not find the same high level of agreement. We may understand this as a result of the relaxed constraints from symmetry leaving more room for the dynamics of the breakup process to affect the final energy distribution of the α particles.

We hinted at one possible explanation for why the full three-body computation of [ÁR08b] is unable to give an accurate description of the data, namely, the α-α two-body potential which has been tuned to reproduce the measured α + α scattering phase shifts. Following this procedure, the excitation energy of the ^{8}Be(2^+) state is computed[5] to 2.8 MeV whereas the experimental value is 3.0 MeV. However, we also argued that the discrepancies cannot be explained by this effect alone. This raises the intriguing possibility that we may be seeing the effect of the short-distance twelve-nucleon structure on the energy distribution of the α particles at large distances.

Full three-body computations have also been performed for other states in ^{12}C such as the 13.35 MeV state and the 4^+ state at 14.08 MeV. The latter may prove a particularly interesting case due to the absence of constraints from symmetry. This leaves plenty of room for the dynamics of the breakup to affect the energy distribution of the α particles, providing a most challenging case to theory. However, in view of the present analysis, the need for an improved theoretical model which connects the three-body breakup to an *ab initio* twelve-nucleon description of the resonance structure at small distances, is already clear.

The potential of the experimental data is far from exhausted: The ^{3}He + ^{10}B reaction gives the possibility to study the decay of the 14.08 MeV state as well as the 16.11 and 20.55 MeV states. Another interesting project would be to look at the decay of the 9.64 MeV state through the ghost of the ^{8}Be ground state.

[5] R. Álvarez-Rodríguez, private communication (2010).

CHAPTER 13

Conclusion and Outlook

The results were presented and discussed at length in Chapters 10–12. Summaries were given at the end of Chapters 11 and 12; future perspectives were discussed as well. Below, concluding remarks of a more general character are given.

An experimental investigation of the nuclear reactions induced by few-MeV ^{3}He ions on targets of ^{10}B and ^{11}B has been performed with the purpose of studying the properties of resonances in ^{12}C. The reactions lead to the four-body final states, $p + 3\alpha$ and $d + 3\alpha$, which were measured in complete kinematics using a setup consisting of four finely segmented silicon detectors.

Energies and widths were extracted for a number of resonances in ^{12}C and compared to literature values. In a few cases, inconsistencies were found. α-Decay branching ratios to the ground state of ^{8}Be were determined and compared to the predictions of the α-cluster model of [ÁR08b].

An indirect method to detect γ transitions between unbound states in ^{12}C was described. A number of γ transitions not previously observed were identified. With the present experimental setup, the detection efficiency was on the order of 1% and the background essentially zero. The method is particularly well adapted for detecting γ transitions to broad final states. γ Transitions connecting shell-model states with α-cluster states provide a clean way to study α clustering in that both the initial state and the transition operator are well understood. The measured γ-decay strengths were compared to calculations performed within the microscopic cluster model of [KE07]. If scaled by a factor of 0.5, the calculations are, at best, in reasonable agreement with the measurement. The connection between the γ decays observed in the present study and the β decays of ^{12}B and ^{12}N was explored. The ratio of γ-decay strength to β-decay strength is, in principle, sensitive to the presence of mesons in the nuclear medium, i.e. effects beyond the classical paradigm of nuclear physics.

The Dalitz plot technique was used to study the breakup of ^{12}C resonances to three α particles. Structures in the intensity distribution of the Dalitz plot were divided into two categories: Those due to the general symmetries of the 3α system and those due to final-state interactions. This division was found to be conceptually useful but also had "practical" applications. It allowed us to, in a straightforward and model-independent way, establish the correct spin-parity of a state at 13.35 MeV. The 3α

breakups of two unnatural parity states at 11.83 and 12.71 MeV were studied in detail. Simulations based on four different breakup models were performed, but none of them gave a perfect match to the data. Possible reasons for the discrepancies were given.

No sign of the long-sought 2^+ rotational excitation of the Hoyle state was seen. This, of course, does not rule out its existence. Given its supposedly similar structure to the Hoyle state and the fact that the Hoyle state was clearly observed, the lacking observation of the 2^+ state should probably not be attributed to it being weakly populated in the ^{3}He + ^{10,11}B reactions. More likely, its broad nature makes it extremely difficult to resolve, e.g. from the competing ^{5,6}Li + ^{8}Be channel discussed in Chapter 10. No indication of the 2^+ state being populated in the γ decays was seen either.

The potential of the experimental data is far from exhausted: The $^{12}\mathrm{C} \rightarrow p + {}^{11}\mathrm{B}$ decay branch was only briefly discussed. We barely looked at the $\alpha + {}^9$B channel and the data from the ^{3}He + ^{7}Li reaction was not mentioned at all. We looked at the 3α breakup of the 11.83 and 12.71 MeV states but did not have time to look at the 3α breakup of a number of other states in ^{12}C for which there is also data. The γ-decay study constitutes the only branch of the analysis which, from an experimental point of view, may be considered completed, but from a theoretical point of view, there is still work to do. The results have been compared to calculations performed within the microscopic cluster model of [KE07], but the implications of this comparison for the model are unclear.

To end with, a picture of the $^{12}\mathrm{C} \rightarrow 3\alpha$ breakup:

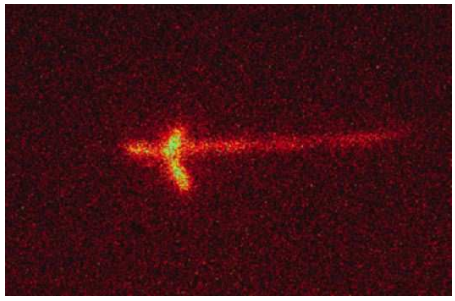

Figure 13.1: CCD camera image of the ionization tracks left by the three α particles from the breakup of ^{12}C following the β decay of ^{12}N (coming in from the right). Adapted from [Mie07].

Bibliography

[Abd94] J. N. Abdurashitov *et al.* (SAGE Collaboration), *Results from SAGE (the Russian-American Gallium Solar-Neutrino Experiment)*. Physics Letters B, **328**, 234–248 (1994). 7

[Abe08] S. Abe *et al.* (KamLAND Collaboration), *Precision Measurement of Neutrino Oscillation Parameters with KamLAND*. Physical Review Letters, **100**, 221803 (2008). 10

[Ade77] E. G. Adelberger, R. E. Marrs, K. A. Snover and J. E. Bussoletti, *Radiative transitions and isospin mixing in ^{12}C*. Physical Review C, **15**, 484–497 (1977). 116, 172, 173

[Ade10] E. G. Adelberger *et al.*, *Solar fusion cross sections II: the pp chain and CNO cycles*. arXiv:1004.2318v2 [nucl-ex] (2010). 79, 87

[Agu80] F. del Aguila, M. Aguilar-Benitez, M. Cerrada, M. G. Doncel and P. Gavillet, *Dalitz Arrays of the ω, ϕ, A_2 and A_1 Resonances*. Zeitschrift für Physik C, **4**, 1–10 (1980). 189

[Agu09] E. F. Aguilera *et al.*, *Reaction cross sections for ^8B, ^7Be, and $^6Li + ^{58}Ni$ near the Coulomb barrier: Proton-halo effects*. Physical Review C, **79**, 021601 (2009). 14

[Aha05] B. Aharmim *et al.* (SNO Collaboration), *Electron energy spectra, fluxes, and day-night asymmetries of ^8B solar neutrinos from measurements with NaCl dissolved in the heavy-water detector at the Sudbury Neutrino Observatory*. Physical Review C, **72**, 055502 (2005). 7, 8

[Aha10] B. Aharmim *et al.* (SNO Collaboration), *Low-energy-threshold analysis of the Phase I and Phase II data sets of the Sudbury Neutrino Observatory*. Physical Review C, **81**, 055504 (2010). 7, 9, 87

[Ahm01] Q. R. Ahmad *et al.* (SNO Collaboration), *Measurement of the Rate of $\nu_e + d \rightarrow p + p + e^-$ Interactions Produced by ^8B Solar Neutrinos at the Sudbury Neutrino Observatory*. Physical Review Letters, **87**, 071301 (2001). 7

[Ahm02] Q. R. Ahmad *et al.* (SNO Collaboration), *Direct Evidence for Neutrino Flavor Transformation from Neutral-Current Interactions in the Sudbury Neutrino Observatory*. Physical Review Letters, **89**, 011301 (2002). 7

[Ahm04] S. N. Ahmed *et al.* (SNO Collaboration), *Measurement of the Total Active ^8B Solar Neutrino Flux at the Sudbury Neutrino Observatory with Enhanced Neutral Current Sensitivity*. Physical Review Letters, **92**, 181301 (2004). 7

[Ahr85] J. Ahrens, *The Total Absorption of Photons by Nuclei*. Nuclear Physics A, **446**, 229c–240c (1985). 109

[Alb72] D. E. Alburger and D. H. Wilkinson, *γ-Ray Decay of the 15.11-MeV T=1 State of ^{12}C*. Physical Review C, **5**, 384–390 (1972). 162, 164, 169, 170

[Alc10] M. Alcorta, *Nuclear Structure of ^{12}C from 3-Body Break-up Studies by Light Ion Reactions in Complete Kinematics*. PhD dissertation, Universidad Complutense de Madrid (2010). 119, 129, 131

[Ams98] C. Amsler, *Proton-antiproton annihilation and meson spectroscopy with the Crystal Barrel*. Reviews of Modern Physics, **70**, 1293–1339 (1998). 177

[Ams08] C. Amsler *et al.* (Particle Data Group), *Review of particle physics*. Physics Letters B, **667**, 1– (2008). 77, 137

[Ans95] P. Anselmann *et al.* (GALLEX Collaboration), *GALLEX Solar-Neutrino Observations - Complete Results for GALLEX-II*. Physics Letters B, **357**, 237–247 (1995). 7

[ÁR07] R. Álvarez-Rodríguez, A. S. Jensen, D. V. Fedorov, H. O. U. Fynbo and E. Garrido, *Energy Distributions from Three-Body Decaying Many-Body Resonances*. Physical Review Letters, **99**, 072503 (2007). 176

[ÁR08a] R. Álvarez-Rodríguez, H. O. U. Fynbo, A. S. Jensen and E. Garrido, *Distinction between Sequential and Direct Three-Body Decays*. Physical Review Letters, **100**, 192501 (2008). 144

[ÁR08b] R. Álvarez-Rodríguez, A. S. Jensen, E. Garrido, D. V. Fedorov and H. O. U. Fynbo, *Momentum distributions of α particles from decaying low-lying ^{12}C resonances*. Physical Review C, **77**, 064305 (2008). 116, 155, 177, 183, 184, 191, 193

[Ara05] T. Araki *et al.* (KamLAND Collaboration), *Measurement of Neutrino Oscillation with KamLAND: Evidence of Spectral Distortion*. Physical Review Letters, **94**, 081801 (2005). 10

[Arp08] C. Arpesella and et al, *Direct Measurement of the ^7Be Solar Neutrino Flux with 192 Days of Borexino Data*. Physical Review Letters, **101**, 091302 (2008). 11

[AS90] F. Ajzenberg-Selove, *Energy levels of light nuclei A=11–12*. Nuclear Physics A, **506**, 1–158 (1990). 114, 115, 144, 147, 148, 153, 155, 159, 168, 183, 190

[Aub83] J. J. Aubert *et al.*, *The ratio of the nucleon structure functions F_2^N for iron and deuterium*. Physics Letters B, **123**, 275–278 (1983). 112

[Aud03] G. Audi, O. Bersillon, J. Blachot and A. H. Wapstra, *The NUBASE evaluation of nuclear and decay properties*. Nuclear Physics A, **729**, 3–128 (2003). 92

[Äys01] J. Äystö, *Development and applications of the IGISOL technique*. Nuclear Physics A, **693**, 477–494 (2001). 20

[Bac07] M. K. Bacrania, N. M. Boyd, R. G. H. Robertson and D. W. Storm, *Search for the second forbidden β decay of ^{8}B to the ground state of ^{8}Be*. Physical Review C, **76**, 055806 (2007). 12

[Bah68] J. N. Bahcall, N. A. Bahcall and G. Shaviv, *Present Status of the Theoretical Predictions for the ^{36}Cl Solar-Neutrino Experiment*. Physical Review Letters, **20**, 1209–1212 (1968). 4

[Bah96] J. N. Bahcall, E. Lisi, D. E. Alburger, L. D. Braeckeleer, S. J. Freedman and J. Napolitano, *Standard neutrino spectrum from ^{8}B decay*. Physical Review C, **54**, 411–422 (1996). 16

[Bah99] J. N. Bahcall, P. I. Krastev and A. Y. Smirnov, *Is a large mixing angle MSW effect the solution of the solar neutrino problems?* Physical Review D, **60**, 093001 (1999). 7, 11

[Bah03] J. N. Bahcall, *Solar Models: An Historical Overview*. Nuclear Physics B (Proc. Suppl.), **118**, 77–86 (2003). 5, 7

[Bah04a] J. N. Bahcall, *Solving the Mystery of the Missing Neutrinos* (2004). http://nobelprize.org/nobel_prizes/physics/articles/bahcall/ 3, 6

[Bah04b] J. N. Bahcall and C. Peña-Garay, *Solar Models and Solar Neutrino Oscillations*. New Journal of Physics, **6**, 63 (2004). 4, 5, 8

[Bal74] D. P. Balamuth, R. W. Zurmühle and S. L. Tabor, *Isospin-forbidden alpha decay of the 15.11-MeV state in ^{12}C*. Physical Review C, **10**, 975–986 (1974). 161, 168, 176, 177, 183

[Bar62] F. C. Barker and P. B. Treacy, *Nuclear levels near thresholds*. Nuclear Physics, **38**, 33–49 (1962). 119

[Bar68] F. C. Barker, H. J. Hay and P. B. Treacy, *0^+ States of ^{8}Be*. Australian Journal of Physics, **21**, 239–257 (1968). 119

[Bar69] F. C. Barker, *2^+ States of ^{8}Be*. Australian Journal of Physics, **22**, 293–316 (1969). 15

[Bar89] F. C. Barker, *Delayed Alpha Spectra from the Beta Decay of ^8Li and ^8B*. Australian Journal of Physics, **42**, 25–39 (1989). 15

[Bec81] F. D. Becchetti, C. A. Fields, R. S. Raymond, H. C. Bhang and D. Overway, *Ghost anomaly in ^8Be studied with $^9Be(p,d)$ at E_p=14.3 and 26.2 MeV*. Physical Review C, **24**, 2401–2408 (1981). 119

[Bet36] H. A. Bethe and R. F. Bacher, *Nuclear Physics. A. Stationary States of Nuclei*. Reviews of Modern Physics, **8**, 82–229 (1936). 111

[Bet56] H. A. Bethe, *Nuclear Many-Body Problem*. Physical Review, **103**, 1353–1390 (1956). 110

[Bet86] H. A. Bethe, *Possible Explanation of the Solar-Neutrino Puzzle*. Physical Review Letters, **56**, 1305–1308 (1986). 6

[Bha02] M. Bhattacharya and E. G. Adelberger, *Reanalysis of $\alpha+\alpha$ scattering and the β-delayed α spectra from ^8Li and ^8B decays*. Physical Review C, **65**, 055502 (2002). 15, 42, 54

[Bha06] M. Bhattacharya, E. G. Adelberger and H. E. Swanson, *Precise study of the final-state continua in ^8Li and ^8B decays*. Physical Review C, **73**, 055802 (2006). 17, 43, 75, 78, 158, 183

[Bie53] L. C. Biedenharn and M. E. Rose, *Theory of Angular Correlation of Nuclear Radiations*. Reviews of Modern Physics, **25**, 729–777 (1953). 141, 177

[Bla52] J. M. Blatt and V. F. Weisskopf, *Theoretical Nuclear Physics*. John Wiley & Sons (1952). 81, 83

[Boh37] N. Bohr and F. Kalckar, *On the transmutation of atomic nuclei by impact of material particles. I. General theoretical remarks*. Det Kongelige Danske Videnskabernes Selskab. Matematisk-fysiske meddelelser, **14**, 10, 1–40 (1937). 110

[Boh39] N. Bohr and J. A. Wheeler, *The Mechanism of Nuclear Fission*. Physical Review, **56**, 426–450 (1939). 110

[Boh69] A. Bohr and B. R. Mottelson, *Nuclear Structure*, volume 1. Benjamin, New York (1969). 169

[Boy07] R. N. Boyd, *An Introduction to Nuclear Astrophysics*. The University of Chicago Press, Chicago and London (2007). 97

[Bro65a] J. D. Bronson, W. D. Simpson, W. R. Jackson and G. C. Phillips, *Three α-Particle Decay of C^{12}*. Nuclear Physics, **68**, 241–269 (1965). 176

[Bro65b] C. P. Browne, W. A. Schier and I. F. Wright, *Isobaric spin selection rule in the $N^{14}(d,\alpha)C^{12}$ reaction*. Nuclear Physics, **66**, 49–64 (1965). 154

[Bro66] G. E. Brown and A. M. Green, *Even parity states of ^{16}O and ^{17}O*. Nuclear Physics, **75**, 401–417 (1966). 114

[Bro07] T. A. D. Brown *et al.*, *Decay studies for states in ^{9}Be up to 11 MeV: Insights into the $n+^{8}Be$ and $\alpha+^{5}He$ cluster structure*. Physical Review C, **76**, 054605 (2007). 144

[Bur57] E. M. Burbidge, G. R. Burbidge, W. A. Fowler and F. Hoyle, *Synthesis of the Elements in Stars*. Reviews of Modern Physics, **29**, 547–650 (1957). 3, 4

[Cam57] A. G. W. Cameron, *Stellar Evolution, Nuclear Astrophysics, and Nucleogenesis*. Atomic Energy of Canada Limited (Report), **CRL-41** (1957). 3, 4

[Cau91] D. D. Caussyn, G. L. Gentry, J. A. Liendo and N. R. Fletcher, *Search for high spin collective states in $^{12}C^{*} \rightarrow 3\alpha$*. Physical Review C, **43**, 205–212 (1991). 155

[Che73] B. T. Chertok, C. Sheffield, J. W. Lightbody, S. Penner and D. Blum, *Low-q^2 Electron Scattering from the 15.109-MeV State of ^{12}C and the Conserved-Vector-Current Test*. Physical Review C, **8**, 23–36 (1973). 169

[Che07] M. Chernykh, H. Feldmeier, T. Neff, P. von Neumann-Cosel and A. Richter, *Structure of the Hoyle State in ^{12}C*. Physical Review Letters, **98**, 032501 (2007). 113, 117, 171

[Cli89] E. T. H. Clifford *et al.*, *The Decay of ^{20}Na: Measurements of isospin mixing and the weak vector coupling constant as well as other new decay data*. Nuclear Physics A, **493**, 293–322 (1989). 22, 42, 55, 89, 90, 92, 93, 95

[Coh65] S. Cohen and D. Kurath, *Effective interactions for the 1p shell*. Nuclear Physics, **73**, 1–24 (1965). 114

[Com92] D. Comedi and J. Davies, *Pulse height response of Si surface barrier detectors to 5–70 MeV heavy ions*. Nuclear Instruments and Methods in Physics Research B, **67**, 93–97 (1992). 101

[Coo57] C. W. Cook, W. A. Fowler, C. C. Lauritsen and T. Lauritsen, *B^{12}, C^{12}, and the Red Giants*. Physical Review, **107**, 508–515 (1957). 113

[Cra08] J. P. Cravens *et al.* (Super-Kamiokande Collaboration), *Solar neutrino measurements in Super-Kamiokande-II*. Physical Review D, **78**, 032002 (2008). 7

[Dal53] R. H. Dalitz, *On the Analysis of τ-Meson Data and the Nature of the τ-Meson*. The Philosophical Magazine, **44**, 1068–1080 (1953). 179

[Dat05] V. M. Datar *et al.*, *Direct Observation of the 4^+-to-2^+ Gamma Transition in ^8Be*. Physical Review Letters, **94**, 122502 (2005). 173

[Dav68] R. Davis, Jr., D. S. Harmer and K. C. Hoffman, *Search for Neutrinos from the Sun*. Physical Review Letters, **20**, 1205–1209 (1968). 4

[Deu83] U. Deutschmann, G. Lahm, R. Neuhausen and J. C. Bergstrom, *Electron Scattering Studies of Magnetic Isovector Transitions in ^{12}C at High Momentum Transfer*. Nuclear Physics A, **411**, 337–356 (1983). 169

[Dig05] C. A. Diget *et al.*, *Properties of the ^{12}C 10 MeV state determined through β-decay*. Nuclear Physics A, **760**, 3–18 (2005). 113

[Dun53] D. N. F. Dunbar, R. E. Pixley, W. A. Wenzel and W. Whaling, *The 7.68-MeV State in ^{12}C*. Physical Review, **92**, 649–650 (1953). 113

[Egu03] K. Eguchi *et al.* (KamLAND Collaboration), *First Results from KamLAND: Evidence for Reactor Antineutrino Disappearance*. Physical Review Letters, **90**, 021802 (2003). 10

[Far60] B. J. Farmer and C. M. Class, *Alpha spectra from the decays of Li^8 and B^8*. Nuclear Physics, **15**, 626–635 (1960). 16

[Fir96] R. B. Firestone and V. S. Shirley, *Table of Isotopes*. John Wiley & Sons, United States of America, 8^{th} edition (1996). 46

[Fir07] R. B. Firestone, *Nuclear Data Sheets for A=23*. Nuclear Data Sheets, **108**, 1–78 (2007). 97

[For09] C. Forssén, E. Caurier and P. Navrátil, *Charge radii and electromagnetic moments of Li and Be isotopes from the ab initio no-core shell model*. Physical Review C, **79**, 021303 (2009). 117

[Fre07a] M. Freer, *The clustered nucleus—cluster structures in stable and unstable nuclei*. Reports on Progress in Physics, **70**, 2149–2210 (2007). 111, 112, 117

[Fre07b] M. Freer *et al.*, *Reexamination of the excited states of ^{12}C*. Physical Review C, **76**, 034320 (2007). 113, 155, 190

[Fre09] M. Freer *et al.*, *2^+ excitation of the ^{12}C Hoyle state*. Physical Review C, **80**, 041303 (2009). 113, 154

[Fro79] A. G. Frodesena, O. Skjeggestad and H. Tøfte, *Probability and Statistics in Particle Physics*. Universitetsførlaget, Bergen-Oslo-Tromsø (1979). 138

[Fuj03] Y. Fujita *et al.*, *Analogous Gamow-Teller and M*1 *transitions in* ^{26}Mg, ^{26}Al, *and* ^{26}Si. Physical Review C, **67**, 064312 (2003). 170

[Fuk98a] Y. Fukuda *et al.* (Super-Kamiokande Collaboration), *Evidence for Oscillation of Atmospheric Neutrinos*. Physical Review Letters, **81**, 1562–1567 (1998). 10

[Fuk98b] Y. Fukuda *et al.* (Super-Kamiokande Collaboration), *Study of the atmospheric neutrino flux in the multi-GeV energy range*. Physics Letters B, **436**, 33–41 (1998). 10

[Fuk01] S. Fukuda *et al.* (Super-Kamiokande Collaboration), *Solar* ^8B *and hep Neutrino Measurements from 1258 Days of Super-Kamiokande Data*. Physical Review Letters, **86**, 5651–5655 (2001). 7

[Fuk02] S. Fukuda *et al.* (Super-Kamiokande Collaboration), *Determination of solar neutrino oscillation parameters using 1496 days of Super-Kamiokande-I data*. Physics Letters B, **539**, 179–187 (2002). 7, 8

[Fur09] N. Furutachi, M. Kimura, A. Dote and Y. Kanada-En'yo, *Structures of Light Halo Nuclei*. Progress of Theoretical Physics, **122**, 865–880 (2009). 14

[Fyn03] H. O. U. Fynbo *et al.*, *Clarification of the Three-Body Decay of* $^{12}C(12.71\ MeV)$. Physical Review Letters, **91**, 082502 (2003). 165, 176, 183, 185, 191

[Fyn05] H. O. U. Fynbo *et al.* (ISOLDE Collaboration), *Revised rates for the stellar triple-*α *process from measurement of* ^{12}C *nuclear resonances*. Nature, **433**, 136–139 (2005). 113

[Fyn09] H. O. U. Fynbo, R. Álvarez-Rodríguez, A. S. Jensen, O. S. Kirsebom, D. V. Fedorov and E. Garrido, *Three-body decays and R-matrix analyses*. Physical Review C, **79**, 054009 (2009). 178

[Gam30] G. Gamow, *Mass defect curve and nuclear constitution*. Proceedings of the Royal Society of London A, **126**, 632–644 (1930). 110

[Gas08] M. Gaspero, B. Meadows, K. Mishra and A. Soffer, *Isospin analysis of* D^0 *decay to three pions*. Physical Review D, **78**, 014015 (2008). 181

[GM58] M. Gell-Mann, *Test of the Nature of the Vector Interaction in* β *Decay*. Physical Review, **111**, 362–365 (1958). 15

[Gre85] L. Grenacs, *Induced Weak Currents in Nuclei*. Annual Review of Nuclear and Particle Science, **35**, 455–499 (1985). 15

[Gui82] P. A. M. Guichon and C. Samour, *Chiral symmetry and axial charge density in the iso vector $0^+ \leftrightarrow 1^+$ transition in the A=12 system*. Nuclear Physics A, **382**, 461–500 (1982). 170, 171

[Haf38] L. R. Hafstad and E. Teller, *The Alpha-Particle Model of the Nucleus*. Physical Review, **54**, 681–692 (1938). 111

[Hax08] W. C. Haxton, *Solar Neutrinos: Models, Observations and New Opportunities*. Publications of the Astronomical Society of Australia, **25**, 44–51 (2008). 4, 7, 11

[Hei32a] W. Heisenberg, *Über den Bau der Atomkerne. I.* Zeitschrift für Physik, **77**, 1–11 (1932). 110

[Hei32b] W. Heisenberg, *Über den Bau der Atomkerne. II.* Zeitschrift für Physik, **78**, 156–164 (1932). 110

[Hei33] W. Heisenberg, *Über den Bau der Atomkerne. III.* Zeitschrift für Physik, **80**, 587–596 (1933). 110

[Hin61] S. Hinds and R. Middleton, *A Study of the ($^3He, d$) Reactions Leading to ^{11}C and ^{12}C*. Proceedings of the Physical Society of London, **78**, 81–91 (1961). 122, 127, 154

[Hir90] S. Hirata *et al.* (Kamiokande Collaboration), *Results from one thousand days of real-time, directional solar-neutrino data*. Physical Review Letters, **65**, 1297–1300 (1990). 7

[Hos06] J. Hosaka *et al.* (Super-Kamiokande Collaboration), *Solar neutrino measurements in Super-Kamiokande-I*. Physical Review D, **73**, 112001 (2006). 7

[Hoy53] F. Hoyle, D. N. F. Dunbar, W. A. Wenzel and W. Whaling, *A State in C^{12} Predicted from Astrophysical Evidence*. Physical Review, **92**, 1095 (1953). 113

[Hua97] W. Huang *et al.*, *Decay study of ^{20}Na and its beta-delayed ^{16}O recoiling*. Science in China A, **40**, 638–643 (1997). 89, 92, 93

[Hyl09] S. Hyldegaard *et al.*, *Precise branching ratios to unbound ^{12}C states from ^{12}N and ^{12}B β-decays*. Physics Letters B, **678**, 459–464 (2009). 163, 164, 170, 171

[Hyl10a] S. Hyldegaard, *β-decay studies of ^8Be and ^{12}C*. PhD dissertation, Aarhus University (2010). 15, 76, 120

[Hyl10b] S. Hyldegaard *et al.*, *R-matrix analysis of the β decays of ^{12}N and ^{12}B*. Physical Review C, **81**, 024303 (2010). 113, 171

[Ike68] K. Ikeda, N. Takigawa and H. Horiuchi, *The Systematic Structure-Change into the Molecule-like Structures in the Self-Conjugate 4n Nuclei*. Supplement of the Progress of Theoretical Physics, Extra Number, 464–475 (1968). 111

[Ito04] M. Itoh *et al.*, *Study of the cluster state at E_x=10.3 MeV in ^{12}C*. Nuclear Physics A, **738**, 268–272 (2004). 113

[Jel09] N. Jelley, A. B. McDonald and R. G. H. Robertson, *The Sudbury Neutrino Observatory*. Annual Review of Nuclear and Particle Science, **59**, 431–465 (2009). 7, 9, 82

[Jen63] J. H. D. Jensen, *Glimpses at the history of the nuclear structure theory*. Nobel Lecture (1963). 110, 176

[Joh03] B. John, Y. Tokimoto, Y.-W. Lui, H. L. Clark, X. Chen and D. H. Youngblood, *Isoscalar electric multipole strength in ^{12}C*. Physical Review C, **68**, 014305 (2003). 113

[Jon04] B. Jonson, *Light dripline nuclei*. Physics Reports, **389**, 1–59 (2004). 13

[Jun03] A. R. Junghans *et al.*, *Precise measurement of the $^7Be(p,\gamma)^8B$ S factor*. Physical Review C, **68**, 065803 (2003). 14

[Jun10] A. R. Junghans, K. A. Snover, E. C. Mohrmann, E. G. Adelberger and L. Buchmann, *Updated S factors for the $^7Be(p,\gamma)^8B$ reaction*. Physical Review C, **81**, 012801(R) (2010). 14

[KE07] Y. Kanada-En'yo, *The Structure of Ground and Excited States of ^{12}C*. Progress of Theoretical Physics, **117**, 655–680 (2007). 117, 170, 193, 194

[Kir08] O. S. Kirsebom, *Experimental studies of reactions induced by ^3He on targets of ^{10}B, ^{11}B, and ^7Li*. Progress report, University of Aarhus (2008). 129

[Kir09] O. S. Kirsebom *et al.*, *Observation of γ-delayed 3α breakup of the 15.11 and 12.71 MeV states in ^{12}C*. Physics Letters B, **680**, 44–49 (2009). 161

[Kir10] O. S. Kirsebom *et al.*, *Breakup of ^{12}C resonances into three α particles*. Physical Review C, **81**, 064313 (2010). 175

[Kno00] G. F. Knoll, *Radiation Detection and Measurement*. John Wiley & Sons, United States of America, 3rd edition (2000). 22, 43, 130

[Kor90] A. A. Korsheninnikov, *Analysis of the properties of three-particle decays of nuclei with A=12 and 16 in the K-harmonics method*. Soviet Journal of Nuclear Physics, **52**, 827–835 (1990). 177, 184, 187

[Lan58] A. M. Lane and R. G. Thomas, *R-Matrix Theory of Nuclear Reactions*. Reviews of Modern Physics, **30**, 257–353 (1958). 118

[Len86] W. N. Lennard, H. Geissel, K. B. Winterbon, D. Phillips, T. K. Alexander and J. S. Forster, *Nonlinear response of Si detectors for low-Z ions*. Nuclear Instruments and Methods in Physics Research A, **248**, 454–460 (1986). 26, 80, 101, 102, 104, 105

[Len87] W. N. Lennard and K. B. Winterbon, *Response of silicon detectors to ^1H and ^4He ions*. Nuclear Instruments and Methods in Physics Research B, **24**, 1035–1038 (1987). 101

[McD76] A. B. McDonald *et al.*, *Isospin-forbidden particle decays in light nuclei (I). $T = \frac{3}{2}$ levels of ^9Be, ^9B*. Nuclear Physics A, **273**, 451–463 (1976). 173

[Mie07] K. Miernik *et al.*, *Optical Time Projection Chamber for imaging nuclear decays*. Nuclear Instruments and Methods in Physics Research A, **581**, 194–197 (2007). 194

[Mik85] S. P. Mikheyev and A. Y. Smirnov, *Resonance Enhancement of Oscillations in Matter and Solar Neutrino Spectroscopy*. Soviet Journal of Nuclear Physics, **42**, 913–917 (1985). 6

[Mil69] P. D. Miller, J. L. Duggan, M. M. Duncan and R. L. Dangle, *$^{11}B(^3He, d)^{12}C$ Spectroscopic Factors*. Nuclear Physics A, **136**, 229–240 (1969). 122, 127

[Mor56] H. Morinaga, *Interpretation of Some of the Excited States of 4n Self-Conjugate Nuclei*. Physical Review, **101**, 254–258 (1956). 113

[Mor66] H. Morinaga, *On the spin of a broad state around 10 MeV in ^{12}C*. Physics Letters, **21**, 78–79 (1966). 113

[Nap87] J. Napolitano, S. J. Freedman and J. Camp, *Beta and neutrino spectra in the decay of ^8B*. Physical Review C, **36**, 298–302 (1987). 16

[Nav07] P. Navrátil, V. G. Gueorguiev, J. P. Vary, W. E. Ormand and A. Nogga, *Structure of A=10–13 Nuclei with Two- Plus Three-Nucleon Interactions from Chiral Effective Field Theory*. Physical Review Letters, **99**, 042501 (2007). 117, 171

[NC00] P. von Neumann-Cosel, H.-D. Gräf, U. Krämer, A. Richter and E. Spamer, *Electroexcitation of isoscalar and isovector magnetic dipole transitions in ^{12}C and isospin mixing*. Nuclear Physics A, **669**, 3–13 (2000). 168, 169, 172

[Nor68] E. Norbeck and F. D. Ingram, *Distortion of Nuclear Spectra by Final-State Coulomb Interactions*. Physical Review Letters, **20**, 1178–1180 (1968). 188

[Oer06] W. von Oertzen, M. Freer and Y. Kanada-En'yo, *Nuclear clusters and nuclear molecules*. Physics Reports, **432**, 43–113 (2006). 117

[Ols65] W. C. Olsen, W. K. Dawson, G. C. Neilson and J. T. Sample, *The Alpha-Particle Breakup of the 12.71 and 11.83 MeV Levels in* C^{12}. Nuclear Physics, **61**, 625–640 (1965). 176

[Ort00] C. E. Ortiz, A. García, R. A. Waltz, M. Bhattacharya and A. K. Komives, *Shape of the* ^8B *Alpha nd Neutrino Spectra*. Physical Review Letters, **85**, 2909–2912 (2000). 9, 16

[Pap07] P. Papka *et al.*, *Decay path measurements for the 2.429 MeV state in* ^9Be*: Implications for the astrophysical* $\alpha + \alpha + n$ *reaction*. Physical Review C, **75**, 045803 (2007). 144

[Per00] K. Peräjärvi *et al.*, *Measurement of the IAS resonance strength in* ^{23}Mg. Physics Letters B, **492**, 1–7 (2000). 22, 85, 98

[Pon67] B. M. Pontecorvo, *Neutrino experiments and the problem of conservation of leptonic charge*. Zh. Exp. Teor. Fiz., **53**, 1717–1725 (1967). 6

[Pre05] Y. Prezado *et al.*, *Low-lying resonance states in the* ^9Be *continuum*. Physics Letters B, **618**, 43–50 (2005). 144

[Rey71] G. M. Reynolds, D. E. Rundquist and R. M. Poichar, *Study of* C^{12} *States Using the* $B^{11}(He^3, d)C^{12}$ *Reaction*. Physical Review C, **3**, 442–447 (1971). 122, 127, 154

[Ric90] A. Richter, A. Weiss, O. Haüsser and B. A. Brown, *New evidence for meson-exchange-current enhancement of isovector M1 strength*. Physical Review Letters, **65**, 2519–2522 (1990). 170

[Rii93] K. Riisager and A. S. Jensen, *The radius of* ^8B *and solar neutrinos*. Physics Letters B, **301**, 6–10 (1993). 14

[Rol05] W. A. Rolke, A. M. López and J. Conrad, *Limits and confidence intervals in the presence of nuisance parameters*. Nuclear Instruments and Methods in Physics Research A, **551**, 493–503 (2005). 167, 168

[Rot04] R. Roth, T. Neff, H. Hergert and H. Feldmeier, *Nuclear structure based on correlated realistic nucleon-nucleon potentials*. Nuclear Physics A, **745**, 3–33 (2004). 117

[Sal90] K. E. Sale *et al.*, *Measurement of the half-life of* ^8Li. Physical Review C, **41**, 2418–2420 (1990). 21

[Sat90] G. R. Satchler, *Introduction to Nuclear Reactions*. MacMillan Education ltd, 2nd edition (1990). 126

[Sch65] W. A. Schier and C. P. Browne, *Alpha-Particle Angular Distributions and Spectra from Deuteron Bombardment of Nitrogen*. Physical Review, **138**, 857–865 (1965). 154

[Sch66] D. Schwalm and B. Povh, *Alpha particles following the β-decay of ^{12}B and ^{12}N*. Nuclear Physics, **89**, 401–411 (1966). 113

[Sch03] S. Schadmand, *Photon-induced reactions*. The European Physical Journal A, **18**, 405–408 (2003). 109

[See09] J. Seely *et al.*, *New Measurements of the European Muon Collaboration Effect in Very Light Nuclei*. Physical Review Letters, **103**, 202301 (2009). 112

[Sig06] P. Sigmund, *Particle Penetration and Radiation Effects*. Springer, Berlin Heidelberg New York (2006). 135

[Sme99] M. H. Smedberg *et al.*, *New results on the halo structure of ^{8}B*. Physics Letters B, **452**, 1–7 (1999). 14

[Smi05] D. Smirnov *et al.*, *Application of a thin double-sided microstrip detector for the registration of β-delayed charge particles: The ^{6}He β decay into the two-body continuum of ^{6}Li*. Nuclear Instruments and Methods in Physics Research A, **547**, 480–489 (2005). 18

[Smy10] M. B. Smy *et al.* (Super-Kamiokande Collaboration), *Low Energy Neutrino Physics at Super-Kamiokande*. Journal of Physics: Conference Series, **203**, 012082 (2010). 7, 9, 87

[Ste96] F. Stegmüller, C. Rolfs, S. Schmidt, W. H. Schulte, H. P. Trautvetter and R. W. Kavanagh, *$^{22}Na(p,\gamma)^{23}Mg$ resonant reaction a low energies*. Nuclear Physics A, **601**, 168–180 (1996). 99

[Sum08] T. Sumikama *et al.*, *Search for the G-parity irregular term in weak nucleon currents extracted from mirror beta decays in the mass 8 system*. Physics Letters B, **664**, 235–240 (2008). 15

[Szc91] A. Szczurek *et al.*, *Ghost anomaly and first excited state of ^{8}Be in the $^{9}Be(d,t\alpha)^{4}He$ reaction at 7 MeV*. Nuclear Physics A, **531**, 77–92 (1991). 119

[Tar04] O. B. Tarasova and D. Bazina, *LISE++ : design your own spectrometer*. Nuclear Physics A, **746**, 411–414 (2004). 20

[Tem97] J. A. Templon *et al.*, *Study of continuum nuclear structure of* ^{12}C *via* $(p, p'X)$ *at intermediate energies*. Physics Letters B, **413**, 253–259 (1997). 159

[Ten04] O. Tengblad, U. C. Bergmann, L. M. Fraile, H. O. U. Fynbo and S. Walsh, *Novel thin window design for a large-area silicon strip detector*. Nuclear Instruments and Methods in Physics Research A, **525**, 458–464 (2004). 22, 34, 130

[Tho72] D. T. Thompson, G. E. Tripard and D. H. Ehlers, *Coulomb Effects in the Final State for Three-Body Reactions*. Physical Review C, **5**, 1174–1180 (1972). 188

[Tig95] R. J. Tighe *et al.*, *Observation of strong isosping mixing in proton emission from the astrophysically interesting isobaric analog state in* ^{23}Mg. Physical Review C, **52**, R2298–R2301 (1995). 85, 97

[Til98] D. R. Tilley, C. M. Cheves, J. H. Kelley, S. Raman and H. R. Weller, *Energy levels of light nuclei, A =20*. Nuclear Physics A, **636**, 249–364 (1998). 31, 42, 46, 89

[Til04] D. R. Tilley *et al.*, *Energy levels of light nuclei A =8,9,10*. Nuclear Physics A, **745**, 155–362 (2004). 13, 21, 147

[Tow87] I. S. Towner, *Quenching of spin matrix elements in nuclei*. Physics Reports, **155**, 263–377 (1987). 170

[Vog04] E. Vogt, *R-Matrix Theory*. Lecture notes from the *R*-Matrix School of the Joint Institute for Nuclear Astrophysics (JINA) at Notre Dame University, South Bend, Indiana (2004). 118

[Wag66] M. A. Waggoner, J. E. Etter, H. D. Holmgren and C. Moazed, *A Study of the Reaction* $^{10}B(^3He, p\alpha\alpha\alpha)$. Nuclear Physics, **88**, 81–127 (1966). 122, 143, 154, 176

[War86] E. K. Warburton, *R-matrix analysis of the* $\beta^{\mp}$*-delayed alpha spectra from the decay of* ^8Li *and* ^8B. Physical Review C, **33**, 303–313 (1986). 15, 120

[Wef37] W. Wefelmeier, *Ein geometrisches Modell des Atomkerns*. Zeitschrift für Physik, **107**, 332–346 (1937). 111

[Wei38] C. F. von Weizsäcker, *Neuere Modellvorstellungen über den Bau der Atomkerne*. Naturwissenschaft, **26**, 209–217, 225–230 (1938). 111

[Whe37] J. A. Wheeler, *Molecular Viewpoints in Nuclear Structure*. Physical Review, **52**, 1083–1106 (1937). 111

[Wil71] D. H. Wilkinson and D. E. Alburger, *β Decay of* ^8Li *and* ^8B*: The Second-Class Current Problem*. Physical Review Letters, **26**, 1127–1130 (1971). 15, 16

[Wil74] D. H. Wilkinson and B. E. F. Macefield, *A parametrization of the phase space factor for allowed β-decay*. Nuclear Physics A, **232**, 58–92 (1974). 83

[Wil95] D. Wilkinson, *Blood, Birds, and the Old Road*. Annual Review of Nuclear and Particle Science, **45**, 1–40 (1995). 109

[Wil00] D. H. Wilkinson, *Limits to second-class nucleonic and mesonic currents*. The European Physical Journal A, **7**, 307–315 (2000). 15

[Win03] W. T. Winter *et al.*, *Determination of the* ^8B *neutrino spectrum*. Physical Review Letters, **91**, 252501 (2003). 17, 106

[Win06] W. T. Winter, S. J. Freedman, K. E. Rehm and J. P. Shiffer, *The* ^8B *neutrino spectrum*. Physical Review C, **73**, 025503 (2006). 11, 17, 75, 78, 81

[Wit72] W. von Witsch, M. Ivanovich, D. Rendic, V. Valkovic and G. C. Phillips, *Decay of* ^{12}C *via the* $^{11}B(p,2\alpha)\alpha$ *Reaction*. Nuclear Physics A, **402**, 402–416 (1972). 176

[Wol78] L. Wolfenstein, *Neutrino oscillations in matter*. Physical Review D, **17**, 2369–2374 (1978). 6

[Yor87] J. Yorkston, A. C. Shotter, D. B. Syme and G. Huxtable, *Interstrip surface effects in oxide passivated ion-implanted silicon strip detectors*. Nuclear Instruments and Methods in Physics Research A, **262**, 353–358 (1987). 39

[Yu03] K. Yu, C. W. Y. Yip, D. Nikezic, J. P. Y. Ho and V. S. Y. Koo, *Comparison among alpha-particle energy losses in air obtained from data of SRIM, ICRU and experiments*. Applied Radiation and Isotopes, **59**, 363–366 (2003). 37

[Zem64] C. Zemach, *Three-Pion Decays of Unstable Particles*. Physical Review, **133**, B1201–B1220 (1964). 179

[Zha02] Y. Zhang, *High-precision measurement of electronic stopping powers for heavy ions using high-resolution time-of-flight spectrometry*. Nuclear Instruments and Methods in Physics Research B, **196**, 1–15 (2002). 24

[Zie08] J. F. Ziegler, J. P. Biersack and M. D. Ziegler, *SRIM - The Stopping and Range of Ions in Matter*. SRIM Co., United States of America, 5^{th} edition (2008). 23, 141

List of Figures

List of Tables